Karlsruher Institut für Technologie

Inverse Scattering Problems and Shape Optimization with Respect to Electromagnetic Chirality for Long Tubular Objects

Zur Erlangung des akademischen Grades eines

Doktors der Naturwissenschaften

von der KIT-Fakultät für Mathematik
des Karlsruher Instituts für Technologie (KIT)
genehmigte

Dissertation

von

Raphael Odin Schurr

Referent:	PD Dr. Tilo Arens
Korreferent:	PD Dr. Frank Hettlich
Tag der mündlichen Prüfung:	5. März 2026

Acknowledgments

An erster Stelle möchte ich mich bei meinem Betreuer, PD Dr. Tilo Arens, bedanken. Zum einen dafür, dass er mir die Möglichkeit gegeben hat, an diesem interessanten und herausfordernden Projekt mitzuwirken. Andererseits für die hervorragende Betreuung und gute Zeit an sich. Die zahlreichen Gespräche und Vorschläge haben mich nicht nur mathematisch vorangetrieben, sondern mich auch in anderen Bereichen substantiell entwickeln lassen und maßgeblich zum Gelingen dieser Arbeit beigetragen.

Ferner möchte ich mich bei meinem Korreferenten, PD Dr. Frank Hettlich, für das Zweitgutachten dieser Arbeit bedanken. Bei ihm habe ich meine ersten Vorlesungen in dieser Arbeitsgruppe gehört und er hat mein Interesse für inverse Probleme und numerische Lösungsverfahren fundamental geprägt. Auch hierfür bin ich dankbar.

Dank gilt auch meinem eigentlichen Chef, Prof. Dr. Roland Griesmaier. Sein ausgeprägtes Fachwissen und humorvoller Charakter haben mich weiter wachsen lassen und dabei stets für gute Laune gesorgt.

Ein großes Dankeschön möchte ich an dieser Stelle nochmal gleichermaßen an Tilo Arens, Frank Hettlich und Roland Griesmaier aussprechen. Dafür, dass sie mir das nötige Vertrauen entgegengebracht haben. Und dafür, dass sie immer ein offenes Ohr für Fragen hatten. Ich konnte immens durch ihre Expertise profitieren und mich fachlich sowie persönlich weiterentwickeln.

Außerdem möchte ich mich bei meinen jetzigen und ehemaligen Kollegen bedanken. Ich hatte stets eine schöne Zeit im Büro und habe mich nicht nur auf meine Arbeit, sondern auch auf mein Umfeld gefreut. Ein paar Kollegen möchte ich an dieser Stelle namentlich erwähnen:

Dr. Marvin Knöller hat mir als Kommilitone vorgeschlagen, Vorlesungen bei Frank Hettlich zu hören. Das war ein guter Vorschlag und die richtige Entscheidung. Als Kollegen waren wir einige Jahre später Teil desselben Projekts und ich konnte extrem von Marvins Fachwissen und seinem Ehrgeiz profitieren. Er hat mich maßgeblich in die Welt des Elektromagnetismus eingewiesen und stand mir stets mit Rat und Tat zur Seite.

Dr. Leonie Fink, Eliane Kummer und Dr. Nasim Shafieeabyaneh haben einige Kapitel dieser Dissertation Korrektur gelesen, wofür ich dankbar bin.

Des Weiteren möchte ich mich bei meinem Bruder, Gabriel, bedanken. Als der Rechencluster unserer Arbeitsgruppe über einen längeren Zeitraum gewartet werden musste, half er mir, eine containerisierte Umgebung aufzubauen, damit ich meine Arbeit während einer rechenintensiven und testlastigen Phase trotzdem fortsetzen konnte. Außerdem konnte ich durch ihn meine Programmierfertigkeiten in den letzten Jahren bedeutend verfeinern.

Besonderer Dank gilt meinen engsten Lieben, Maya und Julia. Durch sie konnte ich mich stets auf meine Zeit außerhalb der Arbeit freuen. Danke für die schöne Zeit, für die Liebe und danke für die Geduld und das Verständnis.

This work has been funded by the Deutsche Forschungsgemeinschaft (DFG, German Research Foundation) – Project-ID 258734477 – SFB 1173, to which I am immensely grateful.

Abstract

We address two distinct but related problems in the field of time-harmonic electromagnetic scattering from both perfectly conducting and penetrable long tubular objects. The first problem is the inverse scattering problem of reconstructing an object from knowledge of the corresponding far-field pattern for a single incident field. The inverse scattering problem can be formulated as a non-linear, ill-posed operator equation, where the operator is the far-field map, which maps the boundary of the scatterer to the far-field pattern of the scattered field exited by one incident field. The shape of the scatterer is reconstructed using a Gauss–Newton minimization procedure for the regularized relative residual of this equation. We establish a characterization of the shape derivative of the far-field map for the class of tubular objects under consideration. The second problem focuses on the shape optimization of scatterers with respect to their electromagnetic chirality properties. A scatterer is called electromagnetically chiral if the scattering response from fields with one pure helicity cannot be reproduced with fields of the opposite helicity. It is called maximally electromagnetically chiral, if it is invisible to fields of one pure helicity. A chirality measure usually requires the far-field operator. We present a general Fréchet differentiability proof for the far-field operator and establish both a characterization of the derivative for tubular objects and an efficient numerical implementation. Numerical examples are provided for both the inverse problem and the shape optimization. The computation of the scattered fields and their domain derivatives is conducted using boundary element methods.

Contents

CHAPTER 1

Introduction

The overarching motif of this dissertation revolves around electromagnetic scattering. Maxwell's equations constitute the foundational theoretical framework that governs the propagation of electromagnetic waves. By only allowing solutions that are periodic in time, we restrict to a time-harmonic Maxwell system. Overall, we are interested in two types of scattering objects: penetrable and perfectly conducting long tubular obstacles. To set up the corresponding frameworks, further interface and boundary conditions have to be imposed. This leads to a transmission and a perfect conductor problem as our reference problems.

On this basis, we address two main goals that we are concerned with in this thesis. On the one hand, we consider an inverse identification problem, where our aim is to determine the shape of a tubular scatterer from measurements of the far-field data corresponding to a given incoming field. On the other hand, we examine scatterers that interact differently with electromagnetic fields of opposite helicity. Such objects are called electromagnetically chiral. Our aim is to optimize the shape of objects in order to maximize their chirality properties, which rely on a measure of electromagnetic chirality depending on corresponding far-field operators.

Electromagnetically chiral scatterers play an important role in a variety of disciplines, such as light-matter interaction, nanoelectronics, and sensing and detection. High chirality properties have been observed for metallic tubular scatterers. For wavelengths in the near to far infrared regime, previous studies have focused on helical shapes [40, 46, 97]. In [3, 42, 69], thin tubular objects with small cross sections have been considered. These lead to asymptotic representation formulae for the scattered field and its far field, such that no Maxwell system has to be solved. This enables an inexpensive shape optimization. However, both helical and thin objects have their disadvantages. They are heavily restrictive on either the course or the cross section of the shape – or both. It turns out that optimal helical objects tend to be extremely small. Thin wires have a minuscule small nature by definition. Consequently, both of them are difficult to realize in practice. In this thesis, we develop shape optimization techniques for thick and long tubular free-form objects. This relieves us from the previously mentioned restrictions, however, the implementation becomes much more expensive.

Both the shape reconstruction and optimization deal with far-field data corresponding to scattering problems. Approaching these problems, one is confronted with the question about the dependence of solutions and their far-field patterns on variations of the boundary of the scatterer. This leads to the notion of the domain derivative of solutions to Maxwell's equations. A shape

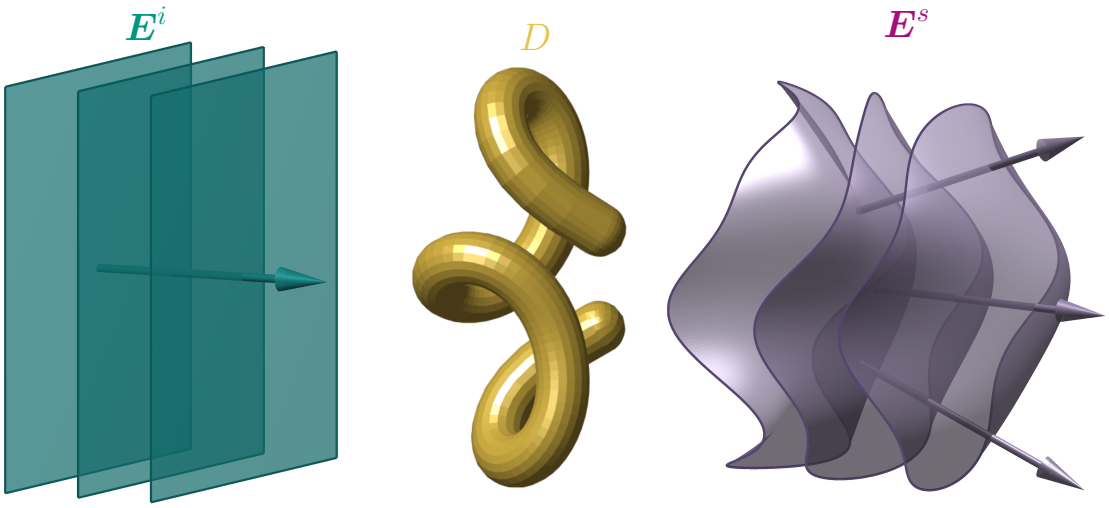

Figure 1.1. Sketch of a scattering problem with an incident electric plane wave $\boldsymbol{E}^i$ (green), the scattering object D (gold), and the corresponding scattered field $\boldsymbol{E}^s$ (purple).

reconstruction algorithm for star-shaped obstacles has been established in [53], by considering an abstract far-field map, which maps the boundary of an obstacle onto the corresponding far-field pattern, and characterizing a Fréchet derivative with respect to perturbations of the domain. The assumption on the geometry being star-shaped implies linear dependence of the boundary parameterization on functions in the domain of the corresponding far-field map. This is not true for the long tubular objects considered in this dissertation. We extend the previously proved results and establish the existence and a characterization of the Fréchet derivative of the far-field map corresponding to tubular objects.

For the shape optimization problem, we need to consider an abstract far-field operator, mapping the boundary of an obstacle onto a linear mapping that, again, maps to a far-field pattern. We also establish the existence and a characterization of the Fréchet derivative of the far-field operator with respect to perturbations of the boundary.

Throughout this work, we assume only homogeneous and isotropic media. This enables an equivalent formulation of the scattering problems as boundary integral equations, which we then solve by boundary element methods.

In conclusion, the main novelties in this work lie in (i) a general existence proof of a domain derivative of the far-field operator, and (ii) the consideration of long free-from tubular objects, which are thick and generally not star-shaped, and an existence proof as well as a characterization of the Fréchet derivative of the corresponding far-field map and operator with respect to perturbations of the boundary. Furthermore, we focus on an efficient numerical computation of such shape derivatives.

1.1. Outline of the Thesis

In Chapter 2 we start by recalling some preliminaries, involving the definition of standard spaces and some notations used throughout this thesis. We proceed by deducing the time-harmonic Maxwell equations from the classical time dependent formulation, which is then complemented by boundary and interface conditions to formulate our reference problems, namely, the scattering of electromagnetic waves by penetrable obstacles and perfect conductors. We then summarize the definition of Sobolev spaces, traces and trace spaces to derive a weak formulation for both of our reference problems. After introducing the notion of electromagnetic chirality and a measure for quantifying it, we formulate the two main goals of this dissertation: the inverse shape identification problem and the shape optimization with respect to electromagnetic chirality.

Since we want to tackle both of these problems with iterative schemes, we need to linearize the occuring non-linear operator equations. For the shape identification, these equations involve far-field maps, which map boundaries ∂D to far-field patterns of the scattered electromagnetic field. For the optimization problem – through the measure of electromagnetic chirality – they involve far-field operators, mapping ∂D to operators that, again, map to far-field patterns of the scattered electromagnetic field. Thus, in Chapter 3, we analyze the behavior of scattering problems and the corresponding far fields with respect to perturbations of the boundary ∂D. We conclude the chapter with a novel result and one of the main theorems of this work, Theorem 3.17, in which we prove differentiability of the far-field operator with respect to perturbations of ∂D.

Then, in Chapter 4, we specify the scatterers that we are concerned with, namely, long tubular objects. We give comprehensive definitions of the associated surface parameterizations. Since these maps do not depend linearly on their defining parameters, we derive linearizations and explicit expressions thereof, which we utilize for the numerical implementation. Finally, we conclude this chapter by two novel and major results, Theorems 4.13 and 4.14, establishing characterizations of the corresponding domain derivatives for long tubular objects.

In Chapter 5, we turn to the shape reconstruction problem. We implement an efficient numerical algorithm using the priorly established characterization of the shape derivative. We start by formulating the occurring boundary value problems as boundary integral equations. We then proceed with a summary on boundary element methods and the relevant boundary element spaces. Then, we regularize and discretize the inverse problem and conclude with several promising numerical examples.

Furthermore, in Chapter 6, we tackle the shape optimization problem, in which we want to optimally design tubular scattering objects, such that they acquire close to maximal chirality properties. After describing the problem, we state a regularized version and apply a BFGS scheme. Furthermore, we illustrate how the far-field operator is discretized. We conclude by presenting numerical examples, where we compare our novel results with significantly dissimilar objects that have been optimized by using different approaches and specifications.

Appendix A provides a brief formulary. For the discretization of tubular objects, we use B-spline curves. In Appendix B, we give a comprehensive summary of these and list important results that are needed in the context of this thesis. In Appendix C, we present a different set of boundary integral equations – for both perfect conductors and penetrable obstacles – than the

ones used in Chapter 5. We use them to generate forward data for the inverse problem. Finally, in Appendix D, we demonstrate a test case, in which we numerically validate the characterizations of the Fréchet derivatives.

1.2. Prior Publication

This dissertation partially includes the content of [5], in which I contributed as an author. In [5], we give a definition of tubular objects (cf. Chapter 4), characterize the domain derivative of the corresponding far-field map (cf. Theorem 4.13), and tackle the inverse shape identification problem (cf. Chapter 5). However, in [5] we use different boundary integral equations and a different approach for solving them. We list these boundary integral formulations in Appendix C. They lead to a different strategy concerning the implementation.

CHAPTER 2

Electromagnetic Scattering

In this work, we are concerned with electromagnetic scattering at bounded obstacles in $\mathbb{R}^3$. We begin with an overview of the basic spaces and notations used throughout this work. Then we introduce the systems that describe the propagation of electromagnetic waves. Subsequently, to obtain proper reference problems, we specify additional spaces, traces and tangential differential operators. At the end, we summarize the notion of electromagnetic chirality and state the two main tasks of this thesis.

2.1. Preliminaries

We briefly summarize some standard definitions and notations employed throughout this work. For a more detailed overview for some of the following results, see, e.g., [82, Chapter 3]. Let $D \subseteq \mathbb{R}^d$, $d \in \{2, 3\}$, be an open and non-empty domain and $k \in \mathbb{N}_0$. We call $\boldsymbol{\beta} = (\beta_1, \dots, \beta_n) \in \mathbb{N}_0^n$ a multi-index with absolute value $|\boldsymbol{\beta}| = \sum_{k=1}^n \beta_k$. We define the differential operator

$$\partial^{\boldsymbol{\beta}} \coloneqq \frac{\partial^{|\boldsymbol{\beta}|}}{\partial^{\beta_1} x_1 \cdots \partial^{\beta_n} x_n} \tag{2.1}$$

and the spaces

$$C^k(D) \coloneqq \{u \colon D \to \mathbb{R} \,:\, \partial^{\boldsymbol{\beta}} u \text{ is continuous for all } |\boldsymbol{\beta}| \leq k\}\,, \tag{2.2}$$

$$C_0^k(D) \coloneqq \{u \in C^k(D) \,:\, \operatorname{supp} u \subset D \text{ compact}\}\,, \tag{2.3}$$

where $\operatorname{supp} u \coloneqq \overline{\{\boldsymbol{x} \in D : u(\boldsymbol{x}) \neq 0\}}$ defines the *support* of u. Furthermore, we define the set of smooth functions

$$C^\infty(D) \coloneqq \bigcap_{m \in \mathbb{N}} C^m(D)\,, \tag{2.4}$$

the set of test functions

$$C_0^\infty(D) \coloneqq \{u \in C^\infty(D) : \operatorname{supp} u \subset D \text{ compact}\}\,, \tag{2.5}$$

and the norm

$$\|u\|_{C^k} = \max_{|\boldsymbol{\beta}|\le k} \sup_{\boldsymbol{x}\in D} |\partial^{\boldsymbol{\beta}} u(\boldsymbol{x})|\,, \qquad u \in C^k(\overline{D})\,, \qquad k \in \mathbb{N}_0\,.$$

For $k = 0$, we usually write $\|\cdot\|_\infty := \|\cdot\|_{C^0} = \|\cdot\|_C$. Furthermore, for $1 \le p \le \infty$, we define the norm

$$\|u\|_{L^p(D)} := \begin{cases} \left(\displaystyle\int_D |u(\boldsymbol{x})|^p \,\mathrm{d}\boldsymbol{x}\right)^{1/p}, & 1 \le p < \infty\,, \\ \operatorname{ess\,sup}\limits_{\boldsymbol{x}\in D} |u(\boldsymbol{x})|\,, & p = \infty\,, \end{cases}$$

and the standard *Lebesgue*[1] *spaces*

$$L^p(D,\mathbb{C}) := \left\{u\colon D \to \mathbb{C} \,:\, u \text{ measurable and } \|u\|_{L^p(D)} < \infty\right\} \big/ \mathcal{N}\,, \qquad 1 \le p \le \infty\,, \tag{2.6}$$

where $\mathcal{N}$ denotes the set of *null functions*, i.e.,

$$\mathcal{N} := \{u\colon D \to \mathbb{C} : u \text{ measurable, } u = 0 \text{ almost everywhere}\}\,.$$

The space $L^2(D)$ with the scalar product

$$\langle u, v\rangle_{L^2(D)} := \int_D u(\boldsymbol{x})\overline{v(\boldsymbol{x})}\,\mathrm{d}\boldsymbol{x}\,, \qquad u, v \in L^2(D)\,,$$

is a Hilbert[2] space. Let $k \in \mathbb{N}_0$. For $\alpha \in (0,1]$ and $u\colon D \to \mathbb{R}$ we define

$$|u|_\alpha = \sup_{\substack{\boldsymbol{x},\boldsymbol{y}\in\overline{D} \\ \boldsymbol{x}\neq\boldsymbol{y}}} \frac{|u(\boldsymbol{x}) - u(\boldsymbol{y})|}{\|\boldsymbol{x} - \boldsymbol{y}\|^\alpha}.$$

Furthermore, for $u \in C^k(\overline{D})$ we define the *Hölder*[3] *norm* by

$$\|u\|_{C^{k,\alpha}(\overline{D})} = \sum_{|\boldsymbol{\beta}|\le k} \|\partial^{\boldsymbol{\beta}} u\|_{C^k} + \sum_{|\boldsymbol{\beta}|=k} |\partial^{\boldsymbol{\beta}} u|_\alpha$$

as well as the (k,α)-*Hölder space* via

$$C^{k,\alpha}(\overline{D}) := \left\{u \in C^k(\overline{D}) : \|u\|_{C^{k,\alpha}(\overline{D})} < \infty\right\}. \tag{2.7}$$

Throughout this work, $\boldsymbol{\nu}$ denotes the exterior unit normal to the surface ∂D – assuming that it is sufficiently smooth. For smooth vector fields $\boldsymbol{V}$, we have

$$\boldsymbol{V} = \boldsymbol{\nu} \times (\boldsymbol{V} \times \boldsymbol{\nu}) + (\boldsymbol{\nu} \cdot \boldsymbol{V})\boldsymbol{\nu}$$

[1] Henri Léon Lebesgue (1875–1941)
[2] David Hilbert (1862–1943)
[3] Ludwig Otto Hölder (1859–1937)

where we also write $\boldsymbol{V}_{\boldsymbol{\nu}} \coloneqq \boldsymbol{\nu} \cdot \boldsymbol{V}$.

Furthermore, we denote the corresponding vector-valued spaces by bold letters, spaces of tangential fields by the subscript "t", and the local spaces by the subscript "loc", e.g.,

$$\boldsymbol{L}^2(D) \coloneqq L^2(D, \mathbb{C}^3) = (L^2(D))^3\,, \tag{2.8}$$

$$\boldsymbol{L}^2_t(\partial D) \coloneqq \{\boldsymbol{u} \in \boldsymbol{L}^2(\partial D) : \boldsymbol{u} \perp \boldsymbol{\nu} \text{ almost everywhere on } \partial D\}\,, \tag{2.9}$$

$$\boldsymbol{L}^2_{\mathrm{loc}}(D) \coloneqq \{\boldsymbol{u}\colon D \to \mathbb{C}^3 : \boldsymbol{u}|_K \in \boldsymbol{L}^2(K) \text{ for any open bounded subset } K \subseteq D\}\,. \tag{2.10}$$

In this case of vector-valued spaces, the corresponding $\boldsymbol{L}^2$-scalar product is given by

$$\langle \boldsymbol{u}, \boldsymbol{v} \rangle_{\boldsymbol{L}^2(D)} \coloneqq \int_D \boldsymbol{u}(\boldsymbol{x}) \cdot \overline{\boldsymbol{v}(\boldsymbol{x})}\, \mathrm{d}\boldsymbol{x}\,, \qquad \boldsymbol{u}, \boldsymbol{v} \in \boldsymbol{L}^2(D)\,.$$

Moreover, we will need the Fréchet[4] differentiability of operators between normed vector spaces, see [6, Definition 5.3.1].

Definition 2.1. *Let $(X, \|\cdot\|_X)$, $(Y, \|\cdot\|_Y)$ open normed vector spaces and $U \subset X$ open. An operator $\phi\colon U \to Y$ is said to be Fréchet differentiable at $x \in U$, if there is a bounded linear operator $\mathrm{d}\phi[x]\colon X \to Y$, such that*

$$\|\phi(x+h) - \phi(x) - \mathrm{d}\phi[x]h\|_Y = \mathcal{O}(\|h\|_X^2)\,, \qquad \|h\|_X \to 0\,.$$

$\mathrm{d}\phi[x]$ is then called Fréchet derivative *of ϕ at x. If the Fréchet derivative exists for all $x \in U$, then we call $\mathrm{d}\phi\colon U \to \{A\colon X \to Y : A \text{ bounded linear operator}\}$ with $x \mapsto \mathrm{d}\phi[x]$ the Fréchet derivative of ϕ on U.*

Remark 2.2. Throughout this work, we will always use a generic constant $C > 0$ for all estimates, even in cases, where the constant may vary from line to line.

2.2. Maxwell's Equations

Denote by $\boldsymbol{\mathcal{E}}$ the *electric field*, by $\boldsymbol{\mathcal{D}}$ the *electric displacement*, by $\boldsymbol{\mathcal{H}}$ the *magnetic field* and by $\boldsymbol{\mathcal{B}}$ the *magnetic flux density*. Furthermore, $\boldsymbol{\mathcal{J}}$ and ρ denote the *current density* and the *charge density*, respectively. With these quantities, the propagation of electromagnetic waves is described by the *Maxwell[5] equations*

$$\frac{\partial \boldsymbol{\mathcal{B}}}{\partial t} + \mathbf{curl}_{\boldsymbol{x}} \boldsymbol{\mathcal{E}} = \boldsymbol{0}\,, \tag{2.11a}$$

$$\frac{\partial \boldsymbol{\mathcal{D}}}{\partial t} - \mathbf{curl}_{\boldsymbol{x}} \boldsymbol{\mathcal{H}} = -\boldsymbol{\mathcal{J}}\,, \tag{2.11b}$$

$$\mathrm{div}_{\boldsymbol{x}} \boldsymbol{\mathcal{D}} = \rho\,, \tag{2.11c}$$

$$\mathrm{div}_{\boldsymbol{x}} \boldsymbol{\mathcal{B}} = 0\,. \tag{2.11d}$$

[4] Maurice René Fréchet (1878–1973)
[5] James Clerk Maxwell (1831–1879)

Equation (2.11a) is *Faraday's*[6] *Law of Induction*, which quantifies how a time-varying magnetic field induces an electric current. Equation (2.11b) is *Ampère's*[7] *Law*, which describes how a magnetic field can be created by both an electric current and a time-varying electric field. Equation (2.11c) is *Gauss'*[8] *Law for Electricity* and implies that electric charges are the sources and sinks of the electric field, where (2.11d), *Gauss' Law for Magnetism*, implies that magnetic monopoles do not exist.

Introducing the electric polarization $\boldsymbol{\mathcal{P}}$ and the magnetization $\boldsymbol{\mathcal{M}}$ of a medium, we consider the model with the constitutive equations (see [113, p. 44])

$$\boldsymbol{\mathcal{D}} = \widetilde{\varepsilon}\,\boldsymbol{\mathcal{E}} + \boldsymbol{\mathcal{P}}\,, \qquad \boldsymbol{\mathcal{H}} = \frac{1}{\mu}\,\boldsymbol{\mathcal{B}} - \boldsymbol{\mathcal{M}}\,,$$

where $\widetilde{\varepsilon}\colon \mathbb{R}^3 \to \mathbb{R}^{3\times 3}$ and $\mu\colon \mathbb{R}^3 \to \mathbb{R}^{3\times 3}$ are the *electric permittivity tensor* and the *magnetic permeability tensor*, respectively. For linear materials the electric polarization and magnetization are neglected, i.e., the constitutive equations reduce to (see [113, p. 45])

$$\boldsymbol{\mathcal{D}} = \widetilde{\varepsilon}\,\boldsymbol{\mathcal{E}}\,, \qquad \boldsymbol{\mathcal{B}} = \mu\,\boldsymbol{\mathcal{H}}\,.$$

Furthermore, in isotropic media these relations do not depend on the spatial directions, such that we can model the constitutive equations with the scalar valued *electric permittivity* $\widetilde{\varepsilon}\colon \mathbb{R}^3 \to \mathbb{R}$ and *magnetic permeability* $\mu\colon \mathbb{R}^3 \to \mathbb{R}$.

If we additionally assume that $\widetilde{\varepsilon}$ and μ are constant, we call the medium *homogeneous*.

Using *Ohm's*[9] *law*, i.e., the linear approximation of the current density

$$\boldsymbol{\mathcal{J}} = \sigma\,\boldsymbol{\mathcal{E}} + \boldsymbol{\mathcal{J}}_{ex}\,, \tag{2.12}$$

with *conductivity* σ and *external current density* $\boldsymbol{\mathcal{J}}_{ex}$, where we always assume $\boldsymbol{\mathcal{J}}_{ex} = \mathbf{0}$, and under the additional assumption that there are no charge distributions, i.e., $\rho = 0$, we arrive at the following formulation of Maxwell's equations:

$$\mu\,\frac{\partial \boldsymbol{\mathcal{H}}}{\partial t} + \mathbf{curl}_{\boldsymbol{x}}\,\boldsymbol{\mathcal{E}} = \mathbf{0}\,, \tag{2.13a}$$

$$\widetilde{\varepsilon}\,\frac{\partial \boldsymbol{\mathcal{E}}}{\partial t} - \mathbf{curl}_{\boldsymbol{x}}\,\boldsymbol{\mathcal{H}} = -\sigma\,\boldsymbol{\mathcal{E}}\,, \tag{2.13b}$$

$$\operatorname{div}_{\boldsymbol{x}}\boldsymbol{\mathcal{E}} = 0\,, \tag{2.13c}$$

$$\operatorname{div}_{\boldsymbol{x}}\boldsymbol{\mathcal{H}} = 0\,. \tag{2.13d}$$

Furthermore, assuming that all fields are periodic with respect to time and have the same *angular frequency* $\omega > 0$, we can separate the temporal and spatial parts, i.e.,

$$\boldsymbol{\mathcal{E}}(\boldsymbol{x},t) = \operatorname{Re}(\mathrm{e}^{-\mathrm{i}\omega t}\boldsymbol{E}(\boldsymbol{x}))\,, \qquad \boldsymbol{\mathcal{H}}(\boldsymbol{x},t) = \operatorname{Re}(\mathrm{e}^{-\mathrm{i}\omega t}\boldsymbol{H}(\boldsymbol{x}))\,,$$

[6] Michael Faraday (1791–1867)
[7] André-Marie Ampère (1775–1836)
[8] Carl Friedrich Gauss (1777–1855)
[9] Georg Simon Ohm (1789–1854)

where $\boldsymbol{E}$ and $\boldsymbol{H}$ are complex valued and the real parts are taken to ensure a physically meaningful solution to the Maxwell system. Consequently, $\boldsymbol{E}$ and $\boldsymbol{H}$ satisfy the following reduced time-harmonic version of Maxwell's equations:

$$\mathbf{curl}\,\boldsymbol{E} - \mathrm{i}\omega\mu\,\boldsymbol{H} = \boldsymbol{0}\,, \qquad \mathbf{curl}\,\boldsymbol{H} + (\mathrm{i}\omega\widetilde{\varepsilon} - \sigma)\,\boldsymbol{E} = \boldsymbol{0}\,. \tag{2.14}$$

It holds

$$\mathrm{i}\omega\widetilde{\varepsilon} - \sigma = \mathrm{i}\omega\left(\widetilde{\varepsilon} - \frac{\sigma}{\mathrm{i}\omega}\right) = \mathrm{i}\omega\left(\widetilde{\varepsilon} + \mathrm{i}\,\frac{\sigma}{\omega}\right).$$

We define $\varepsilon := \widetilde{\varepsilon} + \mathrm{i}\,\sigma/\omega \in \mathbb{C}$ and call ε electric permittivity again. Media with $\sigma = 0$ (or equivalently $\operatorname{Im}\varepsilon = 0$) are called *dielectric*.

Henceforth, we call $\boldsymbol{E}$ the electric and $\boldsymbol{H}$ the magnetic field. The two equations (2.13c), (2.13d), stating that both fields are divergence free, are automatically satisfied due to $\operatorname{div}\mathbf{curl} \equiv 0$.

Summarized, we consider the time-harmonic Maxwell equations

$$\mathbf{curl}\,\boldsymbol{E} - \mathrm{i}\omega\mu\,\boldsymbol{H} = \boldsymbol{0}\,, \qquad \mathbf{curl}\,\boldsymbol{H} + \mathrm{i}\omega\varepsilon\,\boldsymbol{E} = \boldsymbol{0}\,, \tag{2.15}$$

for linear, isotropic media with neither charge distributions nor external current density. With this, let us address scattering problems.

2.3. Reference Problems

In the following definition, for $k \in \{0,1,2\}$ and $\alpha \in (0,1]$, we classify domains in $\mathbb{R}^3$ for which the surface can be represented locally by (k,α)-Hölder continuous functions $\gamma\colon \mathbb{R}^2 \to \mathbb{R}$, see (2.7).

Definition 2.3. *Let $k \in \{0,1,2\}$, $\alpha \in (0,1]$ and $D \subseteq \mathbb{R}^3$ be open. Then, D is called $C^{k,\alpha}$-*smooth *if ∂D is compact and if there are sets $\{U_j\}_{j=1}^m = \{U_j : j \in \{1,\dots,m\}\}$, $\{D_j\}_{j=1}^m = \{D_j : j \in \{1,\dots,m\}\}$, $m \in \mathbb{N}$, with*

(i) $\{U_j\}_{j=1}^m$ is a finite open cover of ∂D, i.e., U_j is open for all $j \in \{1,\dots,m\}$ and $\partial D \subseteq \bigcup_{j=1}^m U_j$,

(ii) for each $j \in \{1,\dots,m\}$ there are transformations T_j, embodying rotations and translations, such that $D_j = T_j(\{\boldsymbol{x} = (x_1,x_2,x_3)^\top : x_3 < \gamma_j(x_1,x_2)\})$, where the functions $\gamma_j\colon \mathbb{R}^2 \to \mathbb{R}$ are (k,α)-Hölder continuous,

(iii) D satisfies $U_j \cap D = U_j \cap D_j$ for each $j \in \{1,\dots,m\}$.

Remark 2.4. As usual, we refer to $C^{0,1}$-smooth domains as *Lipschitz*[10] *domains*. The local parameterizations for Lipschitz domains are almost everywhere differentiable by Rademacher's[11] theorem, see [108, Theorem 10.8 (ii)], and, hence, the exterior unit vector $\boldsymbol{\nu}$ is defined almost everywhere on ∂D. Using a local coordinate system and a corresponding partition of unity, see [68, Theorem A.9], we can also define the function spaces from Section 2.1 on ∂D, see, e.g., [68, Definition A.14] for differentiable functions. Moreover, if we replace the (k,α)-Hölder continuous functions in Definition 2.3 by C^k functions, we call the corresponding domains C^k-smooth.

[10] Rudolf Otto Sigismund Lipschitz (1832–1903)
[11] Hans Adolph Rademacher (1892–1969)

We want to consider scattering problems with some scattering object $D \subseteq \mathbb{R}^3$, which is almost exclusively assumed to be a bounded C^1-smooth domain, such that $\mathbb{R}^3 \setminus \overline{D}$ is connected. We illuminate D by incident fields $\boldsymbol{E}^i$, $\boldsymbol{H}^i$ solving the time-harmonic Maxwell equations (2.15) in $\mathbb{R}^3$, which entails the scattered fields $\boldsymbol{E}^s$, $\boldsymbol{H}^s$, also solving (2.15), where we need to impose additional boundary or interface and radiation conditions in order to obtain a well-posed problem. For the time being, we assume that the occurring fields are sufficiently smooth and, thus, do not yet specify appropriate function spaces for these problems.

2.3.1. Penetrable Obstacle

We consider the following situation: the surface ∂D of the scattering object D separates two different homogeneous media, meaning that the material parameters $\varepsilon \in \mathbb{C}$ and $\mu \in \mathbb{R}$ are in our case piecewise constant, with finite jump across ∂D. Denote the electric permittivity and magnetic permeability of the homogeneous background medium (the exterior domain $\mathbb{R}^3 \setminus \overline{D}$) by ε_+ and μ_+ and those of the homogeneous scattering object (the interior domain D) by ε_- and μ_-. The interface conditions for penetrable obstacles follow naturally from the integral forms of Faraday's law (2.11a) and Ampère's law (2.11b) (which can be readily obtained by using Stoke's[12] theorem, see, e.g., [74, Theorem 16.34])

$$\int_{\partial S} \boldsymbol{\mathcal{E}} \cdot \mathrm{d}\boldsymbol{\ell} = -\int_S \frac{\mathrm{d}\boldsymbol{\mathcal{B}}}{\mathrm{d}t} \cdot \boldsymbol{\nu} \, \mathrm{d}s \qquad \text{and} \qquad \int_{\partial S} \boldsymbol{\mathcal{H}} \cdot \mathrm{d}\boldsymbol{\ell} = \int_S \boldsymbol{\mathcal{J}} \cdot \boldsymbol{\nu} \, \mathrm{d}s + \int_S \frac{\mathrm{d}\boldsymbol{\mathcal{D}}}{\mathrm{d}t} \cdot \boldsymbol{\nu} \, \mathrm{d}s \,, \tag{2.16}$$

respectively, where S is a small curved rectangle somewhere across – and locally perpendicular to – the interface ∂D with two opposite sides, say a, b, parallel to ∂D – where $a \subset D$ and $b \subset \mathbb{R}^3 \setminus \overline{D}$. Eventually, considering the limits of the equations from (2.16) – as the sides of ∂S perpendicular to the interface tend to zero – yields that the tangential components of both the (space-time dependent) electric field $\boldsymbol{\mathcal{E}}$ and magnetic field $\boldsymbol{\mathcal{H}}$ are continuous across the surface.

Next, for $\boldsymbol{x} \in \partial D$ we introduce the notation

$$\boldsymbol{U}|_+(\boldsymbol{x}) \coloneqq \lim_{\substack{\boldsymbol{y} \in \mathbb{R}^3 \setminus \overline{D} \\ \boldsymbol{y} \to \boldsymbol{x}}} \boldsymbol{U}(\boldsymbol{y}) \,, \qquad \boldsymbol{U}|_-(\boldsymbol{x}) \coloneqq \lim_{\substack{\boldsymbol{y} \in D \\ \boldsymbol{y} \to \boldsymbol{x}}} \boldsymbol{U}(\boldsymbol{y}) \tag{2.17}$$

and carry this property to the time-harmonic system, obtaining the transmission interface condition

$$\boldsymbol{E}|_+ \times \boldsymbol{\nu} = \boldsymbol{E}|_- \times \boldsymbol{\nu} \,, \qquad \boldsymbol{H}|_+ \times \boldsymbol{\nu} = \boldsymbol{H}|_- \times \boldsymbol{\nu} \qquad \text{on } \partial D \,, \tag{2.18}$$

for the *total electric* and *magnetic fields*

$$\boldsymbol{E} \coloneqq \begin{cases} \boldsymbol{E}^s|_{\mathbb{R}^3 \setminus \overline{D}} + \boldsymbol{E}^i|_{\mathbb{R}^3 \setminus \overline{D}} & \text{in } \mathbb{R}^3 \setminus \overline{D} \,, \\ \boldsymbol{E}^s|_D & \text{in } D \,, \end{cases} \quad \text{and} \quad \boldsymbol{H} \coloneqq \begin{cases} \boldsymbol{H}^s|_{\mathbb{R}^3 \setminus \overline{D}} + \boldsymbol{H}^i|_{\mathbb{R}^3 \setminus \overline{D}} & \text{in } \mathbb{R}^3 \setminus \overline{D} \,, \\ \boldsymbol{H}^s|_D & \text{in } D \,, \end{cases} \tag{2.19}$$

respectively. Note that in the exterior domain $\mathbb{R}^3 \setminus \overline{D}$, the total fields are a superposition of the incident and scattered fields. By incorporating the scattering object D into the scene, there

[12] Sir George Gabriel Stokes, 1st Baronet (1819–1903)

are effectively no incident fields $\boldsymbol{E}^i, \boldsymbol{H}^i$ throughout D, hence, there the total fields are just the *transmitted* fields, which, for the sake of simplicity, we also denote by $\boldsymbol{E}^s, \boldsymbol{H}^s$. On that note, we also have

$$\boldsymbol{E}^i \times \boldsymbol{\nu} = \boldsymbol{E}^i|_+ \times \boldsymbol{\nu}\,, \qquad \boldsymbol{H}^i \times \boldsymbol{\nu} = \boldsymbol{H}^i|_+ \times \boldsymbol{\nu} \qquad \text{on } \partial D\,.$$

Furthermore, we impose the *Silver–Müller*[13] *radiation condition* (*SMRC*)

$$\lim_{|\boldsymbol{x}|\to\infty} |\boldsymbol{x}|\Big(\sqrt{\mu_+}\,\boldsymbol{H}^s(\boldsymbol{x}) \times \widehat{\boldsymbol{x}} - \sqrt{\varepsilon_+}\,\boldsymbol{E}^s(\boldsymbol{x})\Big) = 0\,, \tag{2.20}$$

uniformly with respect to the direction of observation $\widehat{\boldsymbol{x}} \coloneqq \boldsymbol{x}/|\boldsymbol{x}| \in \mathbb{S}^2 \coloneqq \{\boldsymbol{y} \in \mathbb{R}^3 : |\boldsymbol{y}| = 1\}$, on the scattered fields $\boldsymbol{E}^s, \boldsymbol{H}^s$. This assures that the scattered fields asymptotically behave like electromagnetic dipole fields, emitted by a *Hertzian*[14] *dipole* (see [61, Section 9.2], [99, Subsection 4.3.3]). In particular, they are outgoing and decay as $1/|\boldsymbol{x}|$ as $|\boldsymbol{x}|$ tends to infinity. Such fields are also called *radiating*. All things considered, we state the transmission problem for penetrable obstacles as follows:

Given the incident fields $\boldsymbol{E}^i$, $\boldsymbol{H}^i$ solving

$$\mathbf{curl}\,\boldsymbol{E}^i - \mathrm{i}\omega\mu_+\,\boldsymbol{H}^i = \boldsymbol{0}\,, \qquad \mathbf{curl}\,\boldsymbol{H}^i + \mathrm{i}\omega\varepsilon_+\,\boldsymbol{E}^i = \boldsymbol{0} \quad \text{in } \mathbb{R}^3\,, \tag{2.21}$$

we want to find the corresponding scattered fields $\boldsymbol{E}^s$, $\boldsymbol{H}^s$ that satisfy

$$\left.\begin{aligned} \mathbf{curl}\,\boldsymbol{E}^s - \mathrm{i}\omega\mu_+\,\boldsymbol{H}^s = \boldsymbol{0}\,, \qquad \mathbf{curl}\,\boldsymbol{H}^s + \mathrm{i}\omega\varepsilon_+\,\boldsymbol{E}^s = \boldsymbol{0} \qquad \text{in } \mathbb{R}^3 \setminus \overline{D} \\ \mathbf{curl}\,\boldsymbol{E}^s - \mathrm{i}\omega\mu_-\,\boldsymbol{H}^s = \boldsymbol{0}\,, \qquad \mathbf{curl}\,\boldsymbol{H}^s + \mathrm{i}\omega\varepsilon_-\,\boldsymbol{E}^s = \boldsymbol{0} \qquad \text{in } D \end{aligned}\right\} \tag{2.22a}$$

$$\left.\begin{aligned} \boldsymbol{E}^s|_+ \times \boldsymbol{\nu} - \boldsymbol{E}^s|_- \times \boldsymbol{\nu} = -\boldsymbol{E}^i \times \boldsymbol{\nu} \\ \boldsymbol{H}^s|_+ \times \boldsymbol{\nu} - \boldsymbol{H}^s|_- \times \boldsymbol{\nu} = -\boldsymbol{H}^i \times \boldsymbol{\nu} \end{aligned}\right\} \quad \text{on } \partial D\,, \tag{2.22b}$$

together with the SMRC (2.20).

Remark 2.5. Note that by the prior descriptions, the scattering problem (2.22) together with the SMRC (2.20) is equivalent to the problem in which we want to find the total fields $\boldsymbol{E}, \boldsymbol{H}$ that satisfy (2.22a) and (2.18), where $\boldsymbol{E} - \boldsymbol{E}^i$, $\boldsymbol{H} - \boldsymbol{H}^i$ satisfy (2.20).

2.3.2. Perfect Conductor

A perfect conductor D can be viewed as the limiting case of a penetrable obstacle that models (metallic) objects with infinite conductivity (or, equivalently, zero resistivity), i.e., applying an external electric field causes the object's surface charge to rearrange such that an opposing electric field is induced, cancelling the external electric field throughout the object. In other words: considering $\sigma \to \infty$ in (2.12) while $\boldsymbol{\mathcal{J}}$ remains finite, we expect $\boldsymbol{E} \to \boldsymbol{0}$ within the object. Thus, in this case (2.22b) becomes the boundary condition

$$\boldsymbol{E} \times \boldsymbol{\nu} = \boldsymbol{0} \quad \text{on } \partial D$$

[13] Samuel Silver (1915–1976), Claus Müller (1920–2008)
[14] Heinrich Rudolf Hertz (1857–1894)

for the total electric field $\boldsymbol{E} = \boldsymbol{E}^s + \boldsymbol{E}^i$, and we state the scattering problem for perfect conductors as follows:

Given the incident fields $\boldsymbol{E}^i$, $\boldsymbol{H}^i$ solving

$$\operatorname{\mathbf{curl}} \boldsymbol{E}^i - \mathrm{i}\omega\mu\, \boldsymbol{H}^i = \boldsymbol{0}\,, \qquad \operatorname{\mathbf{curl}} \boldsymbol{H}^i + \mathrm{i}\omega\varepsilon\, \boldsymbol{E}^i = \boldsymbol{0} \qquad \text{in } \mathbb{R}^3\,, \tag{2.23}$$

we want to find the the corresponding scattered fields $\boldsymbol{E}^s$, $\boldsymbol{H}^s$ that satisfy

$$\operatorname{\mathbf{curl}} \boldsymbol{E}^s - \mathrm{i}\omega\mu\, \boldsymbol{H}^s = \boldsymbol{0}\,, \qquad \operatorname{\mathbf{curl}} \boldsymbol{H}^s + \mathrm{i}\omega\varepsilon\, \boldsymbol{E}^s = \boldsymbol{0} \qquad \text{in } \mathbb{R}^3 \setminus \overline{D}\,, \tag{2.24a}$$

$$\boldsymbol{E}^s \times \boldsymbol{\nu} = -\boldsymbol{E}^i \times \boldsymbol{\nu} \qquad \text{on } \partial D\,, \tag{2.24b}$$

together with the SMRC (2.20).

2.4. Sobolev Spaces

Problems (2.22) and (2.24), both together with the SMRC (2.20), are idealized models of how electromagnetic fields propagate and are scattered by penetrable or perfectly conducting objects. However, assuming that a field is sufficiently smooth, such that its curl and divergence exist, is a strong assumption that excludes physically meaningful solutions. Hence, we extend problems (2.22), (2.20) and (2.24), (2.20) to weak formulations on function spaces with less regularity assumptions. In doing so, we obtain a coherent solvability theory for more general solutions in Hilbert spaces.

In the subsequent sections, we provide some requisites and eventually, in Section 2.6, the weak formulations for (2.22), (2.20) as well as (2.24), (2.20) in terms of the scattered electric field $\boldsymbol{E}^s$ as well as the total electric field $\boldsymbol{E}$.

First, we need to define suitable spaces and traces on and with which we also define the required differential operators. Let $D \subseteq \mathbb{R}^3$ be an open, bounded Lipschitz domain. Motivated by the formulae in (A.1) as well as the integral identities from Lemma A.2 we recall the subsequent definition.

Definition 2.6. *We define the following weak differential operators:*

(i) A function $\boldsymbol{U} \in \boldsymbol{L}^2(D)$ possesses a weak divergence *in $L^2(D)$, if there exists a $u \in L^2(D)$ with*

$$\int_D \boldsymbol{U} \cdot \boldsymbol{\nabla}\varphi \,\mathrm{d}\boldsymbol{x} = -\int_D u\,\varphi \,\mathrm{d}\boldsymbol{x} \qquad \text{for all } \varphi \in C_0^\infty(D)\,.$$

We write $\operatorname{div} \boldsymbol{U} = u$.

(ii) A function $u \in L^2(D)$ possesses a weak gradient *in $L^2(D)$, if there exists a $\boldsymbol{U} \in \boldsymbol{L}^2(D)$ with*

$$\int_D u\, \boldsymbol{\nabla}\varphi \,\mathrm{d}\boldsymbol{x} = -\int_D \boldsymbol{U}\,\varphi \,\mathrm{d}\boldsymbol{x} \qquad \text{for all } \varphi \in C_0^\infty(D)\,.$$

We write $\boldsymbol{\nabla} u = \boldsymbol{U}$.

(iii) A function $\boldsymbol{U} \in \boldsymbol{L}^2(D)$ *possesses a* weak curl *in* $\boldsymbol{L}^2(D)$*, if there is a* $\boldsymbol{W} \in \boldsymbol{L}^2(D)$ *with*

$$\int_D \boldsymbol{U} \cdot \mathbf{curl}\, \boldsymbol{\varphi} \, \mathrm{d}\boldsymbol{x} = \int_D \boldsymbol{W} \cdot \boldsymbol{\varphi} \, \mathrm{d}\boldsymbol{x} \qquad \textit{for all } \boldsymbol{\varphi} \in \boldsymbol{C}_0^\infty(D)\,.$$

We write $\mathbf{curl}\, \boldsymbol{U} = \boldsymbol{W}$*.*

Remark 2.7. Denseness of $C_0^\infty(D)$ in $L^2(D)$ and $\boldsymbol{C}_0^\infty(D)$ in $\boldsymbol{L}^2(D)$, see [12, Corollary 4.23], imply uniqueness of these weak derivatives div, $\boldsymbol{\nabla}$ and **curl**, justifying their corresponding operator notation.

With these definitions, we define the standard *Sobolev*[15] *spaces*

$$\begin{aligned} H^1(D) &\coloneqq \left\{ u \in L^2(D) : \boldsymbol{\nabla} u \in \boldsymbol{L}^2(D) \right\}, \\ \boldsymbol{H}^1(D) &\coloneqq \left\{ \boldsymbol{u} \in \boldsymbol{L}^2(D) : \boldsymbol{\nabla} \boldsymbol{u}_j \in \boldsymbol{L}^2(D),\ j \in \{1,2,3\} \right\}, \\ \boldsymbol{H}(\mathbf{curl}, D) &\coloneqq \left\{ \boldsymbol{U} \in \boldsymbol{L}^2(D) : \mathbf{curl}\, \boldsymbol{U} \in \boldsymbol{L}^2(D) \right\}, \end{aligned}$$

which, equipped with the corresponding canonical inner products

$$\begin{aligned} \langle u, v \rangle_{H^1(D)} &\coloneqq \langle u, v \rangle_{L^2(D)} + \langle \boldsymbol{\nabla} u, \boldsymbol{\nabla} v \rangle_{\boldsymbol{L}^2(D)} = \int_D u\, \overline{v} + \boldsymbol{\nabla} u \cdot \boldsymbol{\nabla} \overline{v} \, \mathrm{d}\boldsymbol{x}\,, \\ \langle \boldsymbol{u}, \boldsymbol{v} \rangle_{\boldsymbol{H}^1(D)} &\coloneqq \langle \boldsymbol{u}, \boldsymbol{v} \rangle_{\boldsymbol{L}^2(D)} + \sum_{j=1}^{3} \langle \boldsymbol{\nabla} \boldsymbol{u}_j, \boldsymbol{\nabla} \boldsymbol{v}_j \rangle_{\boldsymbol{L}^2(D)} = \int_D \left[\boldsymbol{u} \cdot \overline{\boldsymbol{v}} + \sum_{j=1}^{3} (\boldsymbol{\nabla} \boldsymbol{u}_j \cdot \boldsymbol{\nabla} \overline{\boldsymbol{v}}_j) \right] \mathrm{d}\boldsymbol{x}\,, \\ \langle \boldsymbol{U}, \boldsymbol{V} \rangle_{\boldsymbol{H}(\mathbf{curl},D)} &\coloneqq \langle \boldsymbol{U}, \boldsymbol{V} \rangle_{\boldsymbol{L}^2(D)} + \langle \mathbf{curl}\, \boldsymbol{U}, \mathbf{curl}\, \boldsymbol{V} \rangle_{\boldsymbol{L}^2(D)} = \int_D \left[\boldsymbol{U} \cdot \overline{\boldsymbol{V}} + \left(\mathbf{curl}\, \boldsymbol{U} \cdot \mathbf{curl}\, \overline{\boldsymbol{V}} \right) \right] \mathrm{d}\boldsymbol{x}\,, \end{aligned}$$

are Hilbert spaces, see [68, Theorem 4.3, p. 178].

Theorem 2.8. *Let* D *be a bounded Lipschitz domain. Then* $\boldsymbol{C}^\infty(\overline{D})$ *is dense in* $\boldsymbol{H}^1(D)$ *with respect to the* $\boldsymbol{H}^1(D)$*-norm and also dense in* $\boldsymbol{H}(\mathbf{curl}, D)$ *with respect to the* $\boldsymbol{H}(\mathbf{curl}, D)$*-norm.*

Proof. See [68, Lemma 5.3] and [68, Lemma 5.19]. ■

Remark 2.9. Analogously as above, a function $u \in L^2(D)$ possesses a *weak derivative of order* $\boldsymbol{\alpha} \in \mathbb{N}^3$, if there is a function $f \in L^2(D)$ such that

$$\int_D u\, \partial^{\boldsymbol{\alpha}} \varphi \, \mathrm{d}\boldsymbol{x} = (-1)^{|\boldsymbol{\alpha}|} \int_D U \varphi \, \mathrm{d}\boldsymbol{x} \qquad \text{for all } \varphi \in C_0^\infty(D)\,.$$

We use the usual notation $\partial^{\boldsymbol{\alpha}} u = U$. Then, we define the Hilbert spaces

$$H^2(D) \coloneqq \left\{ u \in L^2(D) : \partial^{\boldsymbol{\alpha}} u \in \boldsymbol{L}^2(D) \text{ for every multi-index } \boldsymbol{\alpha} \text{ with } |\boldsymbol{\alpha}| \leq 2 \right\},$$

equipped with the inner product

$$\langle u, v \rangle_{H^2(D)} \coloneqq \langle u, v \rangle_{L^2(D)} + \sum_{\substack{\boldsymbol{\alpha} \in \mathbb{N}^3 \\ |\boldsymbol{\alpha}| \leq 2}} \langle \partial^{\boldsymbol{\alpha}} u, \partial^{\boldsymbol{\alpha}} v \rangle_{\boldsymbol{L}^2(D)}\,,$$

[15] Sergei Lwowitsch Sobolew (1908–1989)

and

$$\boldsymbol{H}(\mathbf{curl}^2, D) \coloneqq \left\{ \boldsymbol{U} \in \boldsymbol{L}^2(D) : \mathbf{curl}\, \boldsymbol{U} \in \boldsymbol{L}^2(D)\,,\ \mathbf{curl}\,\mathbf{curl}\, \boldsymbol{U} \in \boldsymbol{L}^2(D) \right\},$$

equipped with the inner product

$$\langle \boldsymbol{U}, \boldsymbol{V} \rangle_{\boldsymbol{H}(\mathbf{curl}^2, D)} \coloneqq \langle \boldsymbol{U}, \boldsymbol{V} \rangle_{\boldsymbol{L}^2(D)} + \sum_{j=1}^{2} \langle \mathbf{curl}^j \boldsymbol{U}, \mathbf{curl}^j \boldsymbol{V} \rangle_{\boldsymbol{L}^2(D)}\,.$$

2.5. Traces, Trace Spaces and Tangential Differential Operators

We start by briefly summarizing some definitions and results on Sobolev spaces of scalar-valued functions on the boundary. For a rigorous construction and definition, see [80, Chapter 3] or [82, Subsection 3.2.1]. We define the fractional Sobolev space over the boundary of a Lipschitz domain D by

$$H^{1/2}(\partial D) \coloneqq \{U \in L^2(\partial D) : \text{there exists } u \in H^1(D) \text{ such that } U = u|_{\partial D}\}$$

with norm

$$\|U\|_{H^{1/2}(\partial D)} \coloneqq \inf\{\|u\|_{H^1(D)} : u \in H^1(D)\,,\ \gamma u = U\}\,.$$

In [80, Theorem 3.37], the trace operator $\gamma\colon C_0^\infty(\overline{D}) \to C_0^\infty(\partial D)$ with $\gamma u \coloneqq u|_{\partial D}$ has been defined and there it has been proved that if D is a Lipschitz domain, γ has a unique extension to a bounded linear operator

$$\gamma\colon H^1(D) \to H^{1/2}(\partial D)\,,$$

where this extension has a continuous right inverse. We denote the dual space of $H^{1/2}(\partial D)$ with respect to the pivot space $L^2(\partial D)$ by $H^{-1/2}(\partial D)$. Since we are dealing with vector-valued functions $\boldsymbol{u}\colon D \to \mathbb{C}^m$, we extend the traces to spaces of such functions as in [82, pp. 106–107], where for spaces of vector-valued functions we also use the bold notation $\boldsymbol{H}^{\pm 1/2}(\partial D) \coloneqq H^{\pm(s-1/2)}(\partial D, \mathbb{C}^3) = (H^{\pm(s-1/2)}(\partial D))^3$ (cf. Section 2.1).

Furthermore, we want to motivate the definitions of those differential operators on the surface ∂D that are relevant for this dissertation. Assume for the moment that D is C^2-smooth. This assures that there are compactly supported extensions $\widetilde{f} \in C^1(\mathbb{R}^3)$, $\widetilde{\boldsymbol{V}} \in \boldsymbol{C}^1(\mathbb{R}^3)$ for every $f \in C^1(\partial D)$, $\boldsymbol{V} \in \boldsymbol{C}_t^1(\partial D)$, respectively, see [68, Lemma A.15]. Let $f \in C^1(\partial D)$, $\boldsymbol{V} \in \boldsymbol{C}_t^1(\partial D)$ and $\widetilde{f} \in C^1(U)$, $\widetilde{\boldsymbol{V}} \in \boldsymbol{C}^1(U)$ be such extensions into U, where $U \subseteq \mathbb{R}^3$ is a neighborhood of ∂D. We define the *surface gradient* $\mathbf{Grad}_{C^2}$ of f as the orthogonal projection of $\boldsymbol{\nabla} \widetilde{f}$ onto the tangential plane, i.e.,

$$\mathbf{Grad}_{C^2} f \coloneqq \boldsymbol{\nu} \times \left(\boldsymbol{\nabla} \widetilde{f} \times \boldsymbol{\nu} \right) = \boldsymbol{\nabla} \widetilde{f} - \boldsymbol{\nu} \frac{\partial \widetilde{f}}{\partial \boldsymbol{\nu}} \qquad \text{on } \partial D\,, \tag{2.25}$$

and the *surface divergence* Div_{C^2} of $\boldsymbol{V}$ by

$$\mathrm{Div}_{C^2} \boldsymbol{V} \coloneqq \operatorname{div} \widetilde{\boldsymbol{V}} - \boldsymbol{\nu} \cdot \mathcal{J}_{\widetilde{\boldsymbol{V}}} \boldsymbol{\nu} \qquad \text{on } \partial D\,,$$

see, e.g., [68, Definition A.16]. Furthermore, we define the *vectorial surface curl*

$$\mathbf{Curl}_{C^2} f \coloneqq \mathbf{Grad}_{C^2} f \times \boldsymbol{\nu} \qquad \text{on } \partial D\,. \tag{2.26}$$

Note that we use the index "C^2" to emphasize that these differential operators are defined for C^2-smooth domains.

Moreover, motivated by the *scalar-valued* $2D$ *curl*

$$\operatorname{curl}_2 \boldsymbol{u} \coloneqq \frac{\partial \boldsymbol{u}_2}{\partial \boldsymbol{x}_1} - \frac{\partial \boldsymbol{u}_1}{\partial \boldsymbol{x}_2} = \operatorname{div}\begin{pmatrix} \boldsymbol{u}_2 \\ -\boldsymbol{u}_1 \end{pmatrix}, \qquad \boldsymbol{u} \in \boldsymbol{C}^1(\partial D, \mathbb{C}^2)\,,$$

we define the *scalar surface curl* Curl as the surface divergence of a rotated vector field

$$\operatorname{Curl}_{C^2} \boldsymbol{V} \coloneqq \operatorname{Div}_{C^2}(\boldsymbol{V} \times \boldsymbol{\nu}) = -\operatorname{Div}_{C^2}(\boldsymbol{\nu} \times \boldsymbol{V}) \qquad \text{on } \partial D\,.$$

By [68, Corollary A.20] it holds that

$$\operatorname{Curl}_{C^2} \boldsymbol{V} = \boldsymbol{\nu} \cdot \mathbf{curl}\, \widetilde{\boldsymbol{V}} \qquad \text{on } \partial D\,.$$

Lemma 2.10. *The following dualities hold for all* $f \in C^1(\partial D), \boldsymbol{V} \in \boldsymbol{C}^1_t(\partial D)$*:*

$$\int_{\partial D} f \operatorname{Div}_{C^2} \boldsymbol{V}\, \mathrm{d}s = -\int_{\partial D} \boldsymbol{V} \cdot \mathbf{Grad}_{C^2} f\, \mathrm{d}s\,,$$
$$\int_{\partial D} f \operatorname{Curl}_{C^2} \boldsymbol{V}\, \mathrm{d}s = \int_{\partial D} \boldsymbol{V} \cdot \mathbf{Curl}_{C^2} f\, \mathrm{d}s\,.$$

Proof. For the first identity see, e.g., [68, Lemma A.18 (c)]. Then, the second identity immediately follows by

$$\boldsymbol{V} \cdot \mathbf{Curl}_{C^2} f = \boldsymbol{V} \cdot (\mathbf{Grad}_{C^2} f \times \boldsymbol{\nu}) = \mathbf{Grad}_{C^2} f \cdot (\boldsymbol{\nu} \times \boldsymbol{V})$$

from the first identity. ∎

By Lemma 2.10 and by $C^1_t(\partial D)$ being dense in $L^2_t(\partial D)$, we can verify that the definitions of $\mathbf{Grad}_{C^2}$ and Div_{C^2} and, thus, of $\mathbf{Curl}_{C^2}$ and $\operatorname{Curl}_{C^2}$ do not depend on the choices of the extensions, see [68, Lemma A.19].

Now, we want to define corresponding surface differential operators for Lipschitz domains $D \subseteq \mathbb{R}^3$ (cf. Definition 2.3 for $k = 0,\ \alpha = 1$). The integration by parts formula

$$\int_D \boldsymbol{u} \cdot \mathbf{curl}\, \boldsymbol{v} - \mathbf{curl}\, \boldsymbol{u} \cdot \boldsymbol{v}\, \mathrm{d}x = -\int_{\partial D} \boldsymbol{u} \cdot (\boldsymbol{v} \times \boldsymbol{\nu})\, \mathrm{d}s = -\int_{\partial D} (\boldsymbol{\nu} \times (\boldsymbol{u} \times \boldsymbol{\nu})) \cdot (\boldsymbol{v} \times \boldsymbol{\nu})\, \mathrm{d}s$$

– see (A.4d) and note that $\boldsymbol{u} = (\boldsymbol{\nu} \times (\boldsymbol{u} \times \boldsymbol{\nu})) + (\boldsymbol{\nu} \cdot \boldsymbol{u})\boldsymbol{\nu}$ – suggests the definition of the tangential traces

$$\boldsymbol{\gamma}_t \colon \boldsymbol{C}^\infty(\overline{D}) \to \boldsymbol{L}^\infty(\partial D)\,, \qquad \boldsymbol{U} \mapsto \boldsymbol{U} \times \boldsymbol{\nu}\,,$$
$$\boldsymbol{\gamma}_T \colon \boldsymbol{C}^\infty(\overline{D}) \to \boldsymbol{L}^\infty(\partial D)\,, \qquad \boldsymbol{U} \mapsto \boldsymbol{\nu} \times (\boldsymbol{U} \times \boldsymbol{\nu})\,.$$

We denote exterior and interior traces by

$$\boldsymbol{\gamma}_t^+ \boldsymbol{U} \coloneqq \boldsymbol{\gamma}_t \left(\boldsymbol{U}|_{\mathbb{R}^3 \setminus \overline{D}} \right) \qquad \text{and} \qquad \boldsymbol{\gamma}_t^- \boldsymbol{U} \coloneqq \boldsymbol{\gamma}_t \left(\boldsymbol{U}|_D \right), \tag{2.27}$$

respectively. In [19, Section 2], it has been argued that such traces can be extended to continuous linear mappings from $\boldsymbol{H}(\mathbf{curl}, D)$ to $\boldsymbol{H}^{-1/2}(\partial D)$. These extensions are obviously not surjective, since the traces $\boldsymbol{\gamma}_t$, $\boldsymbol{\gamma}_T$ are tangential to ∂D, whereas $\boldsymbol{H}^{-1/2}(\partial D)$ contains elements that are not tangential to ∂D. The difficulty for Lipschitz domains is that the Sobolev space of tangential vector fields of order $1/2$ on ∂D can be defined in multiple ways, which are equivalent for smooth domains but different even for piecewise smooth domains, see [18, Section 1]. Furthermore, the unit normal vector $\boldsymbol{\nu}$ is discontinuous, entailing that the scalar product $\boldsymbol{\nu} \cdot \boldsymbol{u}$ is not defined for $\boldsymbol{u} \in \boldsymbol{H}^{-1/2}(\partial D)$.

Following the remedying approach of [18], we introduce the subspaces $\boldsymbol{V}_t \coloneqq \boldsymbol{\gamma}_t(\boldsymbol{H}^1(D)) \subseteq \boldsymbol{L}_t^2(\partial D)$, $\boldsymbol{V}_T \coloneqq \boldsymbol{\gamma}_T(\boldsymbol{H}^1(D)) \subseteq \boldsymbol{L}_t^2(\partial D)$, as well as the antisymmetric bilinear form

$$\langle \cdot, \cdot\cdot \rangle_{t,\partial D} \colon \boldsymbol{L}_t^2(\partial D) \times \boldsymbol{L}_t^2(\partial D) \to \mathbb{C}, \qquad \langle \boldsymbol{U}, \boldsymbol{V} \rangle_{t,\partial D} \coloneqq \int_{\partial D} \boldsymbol{U} \cdot (\boldsymbol{\nu} \times \boldsymbol{V}) \, \mathrm{d}s .$$

Then, we define the corresponding dual spaces $\boldsymbol{V}_t^*$ and $\boldsymbol{V}_T^*$ via extensions of $\langle \cdot, \cdot\cdot \rangle_{t,\partial D}$, see [18, Section 2], [19, Definition 1]. In [18, Definition 3.1], the operators

$$\mathbf{Grad} \colon H^1(\partial D) \to \boldsymbol{L}_t^2(\partial D), \qquad \mathbf{Curl} \colon H^1(\partial D) \to \boldsymbol{L}_t^2(\partial D) \tag{2.28}$$

have been defined by a localization argument, using the Lipschitz continuous maps by which the boundary can be represented. Henceforward, we denote the duality pairings between $H^s(\partial D)$ and $H^{-s}(\partial D)$, with $L^2(\partial D)$ as pivot space, by $\langle \cdot, \cdot\cdot \rangle_{s,\partial D}$ for any s that may occur. Moreover, ${}_{\boldsymbol{V}_T^*}\langle \cdot, \cdot\cdot \rangle_{\boldsymbol{V}_T}$ as well as ${}_{\boldsymbol{V}_t^*}\langle \cdot, \cdot\cdot \rangle_{\boldsymbol{V}_t}$ denote the duality pairings between $\boldsymbol{V}_T^*$ and $\boldsymbol{V}_T$ as well as $\boldsymbol{V}_t^*$ and $\boldsymbol{V}_t$, respectively. The adjoint operators of $-\mathbf{Grad}$ and $\mathbf{Curl}$ are

$$\mathrm{Div} \colon \boldsymbol{L}_t^2(\partial D) \to H^{-1}(\partial D) \qquad \text{and} \qquad \mathrm{Curl} \colon \boldsymbol{L}_t^2(\partial D) \to H^{-1}(\partial D),$$

respectively, and they are defined by the dualities

$$\left.\begin{aligned} \langle \mathrm{Div}\, \boldsymbol{\varphi}, \psi \rangle_{1,\partial D} &\coloneqq -\int_{\partial D} \boldsymbol{\varphi} \cdot \mathbf{Grad}\, \psi \, \mathrm{d}s \\ \langle \mathrm{Curl}\, \boldsymbol{\varphi}, \psi \rangle_{1,\partial D} &\coloneqq \int_{\partial D} \boldsymbol{\varphi} \cdot \mathbf{Curl}\, \psi \, \mathrm{d}s \end{aligned}\right\} \quad \boldsymbol{\varphi} \in \boldsymbol{L}_t^2(\partial D), \ \psi \in H^1(\partial D) \tag{2.29}$$

(cf. Lemma 2.10).

Next, let $H^{3/2}(\partial D) \coloneqq \gamma(H^2(D))$ and its dual space $H^{-3/2}(\partial D)$ with $L^2(\partial D)$ as pivot space as in [17], [18]. Then, in [18, Proposition 3.4], it has been shown that for any $\psi \in H^2(\partial D)$, the expressions $\boldsymbol{\gamma}_T(\boldsymbol{\nabla}\psi)$ and $\boldsymbol{\gamma}_t(\boldsymbol{\nabla}\psi)$ depend only on the trace $\gamma\psi$ on ∂D and consequently that the restrictions of $\mathbf{Grad}$ and $\mathbf{Curl}$ from (2.28) verify

$$\mathbf{Grad}(\gamma\psi) = \boldsymbol{\gamma}_T(\boldsymbol{\nabla}\psi), \qquad \mathbf{Curl}(\gamma\psi) = \boldsymbol{\gamma}_t(\boldsymbol{\nabla}\psi) \qquad \text{for any } \psi \in H^2(D) \tag{2.30}$$

(cf. definitions (2.25) and (2.26)). There, they also have shown that the restrictions of $\mathbf{Grad}$

and **Curl**

$$\mathbf{Grad}\colon H^{3/2}(\partial D) \to \boldsymbol{V}_T\,, \qquad \mathbf{Curl}\colon H^{3/2}(\partial D) \to \boldsymbol{V}_t\,, \tag{2.31}$$

are linear and continuous. We define

$$\mathrm{Div}\colon \boldsymbol{V}_T^* \to H^{-3/2}(\partial D) \qquad \text{and} \qquad \mathrm{Curl}\colon \boldsymbol{V}_t^* \to H^{-3/2}(\partial D) \tag{2.32}$$

by the dualities

$$\langle \mathrm{Div}\,\boldsymbol{\varphi}, \psi\rangle_{3/2,\partial D} \coloneqq -{}_{\boldsymbol{V}_T^*}\langle \boldsymbol{\varphi}, \mathbf{Grad}\,\psi\rangle_{\boldsymbol{V}_T}\,, \qquad \boldsymbol{\varphi} \in \boldsymbol{V}_T^*\,,\ \psi \in H^{3/2}(\partial D)\,, \tag{2.33}$$

$$\langle \mathrm{Curl}\,\boldsymbol{\varphi}, \psi\rangle_{3/2,\partial D} \coloneqq {}_{\boldsymbol{V}_t^*}\langle \boldsymbol{\varphi}, \mathbf{Curl}\,\psi\rangle_{\boldsymbol{V}_t}\,, \qquad \boldsymbol{\varphi} \in \boldsymbol{V}_t^*\,,\ \psi \in H^{3/2}(\partial D)\,. \tag{2.34}$$

Next, the integration by parts formula

$$\int_D \boldsymbol{u}\cdot\mathbf{curl}\,\boldsymbol{v} - \mathbf{curl}\,\boldsymbol{u}\cdot\boldsymbol{v}\,\mathrm{d}x = {}_{\boldsymbol{V}_T^*}\langle \boldsymbol{\gamma}_t\boldsymbol{u}, \boldsymbol{\gamma}_T\boldsymbol{v}\rangle_{\boldsymbol{V}_T} = -{}_{\boldsymbol{V}_t^*}\langle \boldsymbol{\gamma}_T\boldsymbol{u}, \boldsymbol{\gamma}_t\boldsymbol{v}\rangle_{\boldsymbol{V}_t}\,,$$

see [18, Equation (27)], can be used to (i) conclude continuity of the extensions

$$\boldsymbol{\gamma}_t\colon \boldsymbol{H}(\mathbf{curl}, D) \to \boldsymbol{V}_T^*\,, \qquad \boldsymbol{\gamma}_T\colon \boldsymbol{H}(\mathbf{curl}, D) \to \boldsymbol{V}_t^*\,,$$

by surjectivity of $\boldsymbol{\gamma}_t\colon \boldsymbol{H}^1(D) \to \boldsymbol{V}_t$, $\boldsymbol{\gamma}_T\colon \boldsymbol{H}^1(D) \to \boldsymbol{V}_T$ and (ii) deduce that for any $\varphi \in H^1(D)$, the mappings $\varphi \mapsto \boldsymbol{\gamma}_T(\boldsymbol{\nabla}\varphi)$ and $\varphi \mapsto \boldsymbol{\gamma}_t(\boldsymbol{\nabla}\varphi)$ are linear and continuous and that they only depend on the trace of φ on ∂D. In [18, Proposition 3.6], the following extension result is then proved.

Lemma 2.11. *The operators from* (2.31) *and* (2.32) *with the following choice of spaces are linear and continuous:*

$$\mathbf{Grad}\colon H^{1/2}(\partial D) \to \boldsymbol{V}_t^*\,, \qquad \mathbf{Curl}\colon H^{1/2}(\partial D) \to \boldsymbol{V}_T^*\,,$$
$$\mathrm{Div}\colon \boldsymbol{V}_t \to H^{-1/2}(\partial D)\,, \qquad \mathrm{Curl}\colon \boldsymbol{V}_T \to H^{-1/2}(\partial D)\,,$$

where $H^{3/2}(\partial D)$ and $\langle\cdot,\cdot\rangle_{3/2,\partial D}$ are replaced by $H^{1/2}(\partial D)$ and $\langle\cdot,\cdot\rangle_{1/2,\partial D}$, respectively, in (2.30), (2.33), (2.34).

As in [18, Theorem 4.1], we define the following trace spaces.

Definition 2.12. *We define the two subspaces*

$$\boldsymbol{H}^{-1/2}(\mathrm{Div}, \partial D) \coloneqq \{\boldsymbol{V} \in \boldsymbol{V}_T^* : \mathrm{Div}\,\boldsymbol{V} \in H^{-1/2}(\partial D)\}\,,$$
$$\boldsymbol{H}^{-1/2}(\mathrm{Curl}, \partial D) \coloneqq \{\boldsymbol{V} \in \boldsymbol{V}_t^* : \mathrm{Curl}\,\boldsymbol{V} \in H^{-1/2}(\partial D)\}\,.$$

Finally, we have the following results.

Theorem 2.13. *The trace operators $\boldsymbol{\gamma}_t$ and $\boldsymbol{\gamma}_T$ can be extended to surjective, bounded linear operators*

$$\boldsymbol{\gamma}_t\colon \boldsymbol{H}(\mathbf{curl}, D) \to \boldsymbol{H}^{-1/2}(\mathrm{Div}, \partial D)\,, \qquad \boldsymbol{\gamma}_T\colon \boldsymbol{H}(\mathbf{curl}, D) \to \boldsymbol{H}^{-1/2}(\mathrm{Curl}, \partial D)\,.$$

Moreover, $\langle \cdot, \cdot\cdot \rangle_{t,\partial D}$ can be extended to a continuous bilinear form on $\boldsymbol{H}^{-1/2}(\mathrm{Div}, \partial D)$ with respect to which $\boldsymbol{H}^{-1/2}(\mathrm{Div}, \partial D)$ is self-dual.

Proof. See [18, Theorem 4.1] and [18, Lemma 5.6]. ■

Theorem 2.14. *The operators*

$$\begin{aligned} \mathrm{Div}\colon \boldsymbol{L}_t^2(\partial D) &\to \{\xi \in H^{-1}(\partial D) : \langle \xi, 1\rangle_{1,\partial D} = 0\}\,, \\ \mathrm{Curl}\colon \boldsymbol{L}_t^2(\partial D) &\to \{\xi \in H^{-1}(\partial D) : \langle \xi, 1\rangle_{1,\partial D} = 0\} \end{aligned}$$

and their restrictions

$$\begin{aligned} \mathrm{Div}\colon \boldsymbol{V}_t &\to \{\xi \in H^{-1/2}(\partial D) : \langle \xi, 1\rangle_{1/2,\partial D} = 0\}\,, \\ \mathrm{Curl}\colon \boldsymbol{V}_T &\to \{\xi \in H^{-1/2}(\partial D) : \langle \xi, 1\rangle_{1/2,\partial D} = 0\} \end{aligned}$$

are linear, continuous and surjective.

Proof. See [18, Corollary 5.4]. ■

Corollary 2.15. *The restrictions*

$$\mathrm{Div}\colon \boldsymbol{H}^{-1/2}(\mathrm{Div}, \partial D) \to H^{-1/2}(\partial D)\,, \qquad \mathrm{Curl}\colon \boldsymbol{H}^{-1/2}(\mathrm{Curl}, \partial D) \to H^{-1/2}(\partial D)$$

are linear, continuous and surjective.

Proof. By Theorem 2.13, it holds that $\boldsymbol{H}^{-1/2}(\mathrm{Div}, \partial D) = (\boldsymbol{H}^{-1/2}(\mathrm{Curl}, \partial D))^* \subseteq \boldsymbol{V}_t$. Moreover, for any $\boldsymbol{\varphi} \in \boldsymbol{H}^{-1/2}(\mathrm{Div}, \partial D)$, it holds that $\mathrm{Div}\,\boldsymbol{\varphi} \in H^{-1/2}(\partial D)$ by definition and

$$\langle \mathrm{Div}\,\boldsymbol{\varphi}, 1\rangle_{1/2,\partial D} = -_{\boldsymbol{V}_T^*}\langle \boldsymbol{\varphi}, \mathbf{Grad}\, 1\rangle_{\boldsymbol{V}_T} = 0\,.$$

■

2.6. Weak formulations

One fundamental step in deriving the weak formulations of the scattering problems (2.22), (2.20) and (2.24), (2.20), is to reduce these problems to bounded domains in $\mathbb{R}^3$. Hence, we consider an auxiliary open ball B_R centered at zero with radius $R > 0$, such that $\overline{D} \subseteq B_R$, and define

$$\Omega \coloneqq B_R \setminus \overline{D}\,.$$

Additionally, we define the *wave number* $k \coloneqq \omega\sqrt{\varepsilon\mu}$ and the trace operator

$$\boldsymbol{\gamma}_N\colon \boldsymbol{H}(\mathbf{curl}^2, D) \to \boldsymbol{H}^{-1/2}(\mathrm{Div}, \partial D)\,, \qquad \boldsymbol{\gamma}_N \boldsymbol{U} \coloneqq \frac{1}{\mathrm{i}k}\,\boldsymbol{\gamma}_t\,\mathbf{curl}\,\boldsymbol{U}\,.$$

Note that $\boldsymbol{\gamma}_N$ maps an electric field $\boldsymbol{E}$ solving the Maxwell system – up to some scaling – onto the corresponding trace of the magnetic field $\boldsymbol{H}$. Furthermore, we introduce the Calderón operator in order to incorporate the SMRC (2.20) into the weak formulation. Given a tangential field

$\boldsymbol{\varphi} \in \boldsymbol{H}^{-1/2}(\mathrm{Div}, \partial B_R)$, there is a unique radiating electromagnetic field $(\boldsymbol{E}^s, \boldsymbol{H}^s) \in \boldsymbol{H}_{\mathrm{loc}}(\mathbb{R}^3 \setminus \overline{B_R}) \times \boldsymbol{H}_{\mathrm{loc}}(\mathbb{R}^3 \setminus \overline{B_R})$ such that $\boldsymbol{\gamma}_t \boldsymbol{E}^s = \boldsymbol{\varphi}$ on ∂B_R, see [82, Lemma 9.19]. On that note, the Calderón operator $\boldsymbol{\Lambda}\colon \boldsymbol{H}^{-1/2}(\mathrm{Div}, \partial B_R) \to \boldsymbol{H}^{-1/2}(\mathrm{Div}, \partial B_R)$ is defined by

$$\boldsymbol{\Lambda}\boldsymbol{\varphi} \coloneqq \boldsymbol{\gamma}_t \boldsymbol{H}^s = \sqrt{\frac{\varepsilon}{\mu}}\, \boldsymbol{\gamma}_N \boldsymbol{E}^s \qquad \text{on } \partial B_R\,. \tag{2.35}$$

$\boldsymbol{\Lambda}$ is a bounded linear operator, see [82, Theorem 9.21].

With this, we reduce the scattering problem to the bounded domain B_R – which means to $\Omega \subseteq B_R$ in the perfect conductor case – and impose the exact non-local boundary condition

$$\boldsymbol{\Lambda}(\boldsymbol{\gamma}_t \boldsymbol{E}^s) = \boldsymbol{\gamma}_t \boldsymbol{H}^s$$

on the artificial boundary ∂B_R. This ensures that solutions of the truncated problem in B_R are restrictions of outgoing fields satisfying the SMRC (2.20).

2.6.1. Penetrable Obstacle

In order to concisely write down the following calculations, we define

$$\varepsilon \coloneqq \begin{cases} \varepsilon_+ & \text{in } \mathbb{R}^3 \setminus \overline{D}\,, \\ \varepsilon_- & \text{in } D\,, \end{cases} \qquad \mu \coloneqq \begin{cases} \mu_+ & \text{in } \mathbb{R}^3 \setminus \overline{D}\,, \\ \mu_- & \text{in } D\,. \end{cases}$$

Recall the notation for exterior and interior traces from (2.27). With a view to the piecewise definition of the total fields in (2.19), we also use that if we have $\boldsymbol{E}_1 \in \boldsymbol{H}(\mathbf{curl}, D)$ and $\boldsymbol{E}_2 \in \boldsymbol{H}(\mathbf{curl}, B_R \setminus \overline{D})$ such that $\boldsymbol{\gamma}_t^- \boldsymbol{E}_1 = \boldsymbol{\gamma}_t^+ \boldsymbol{E}_2$ on ∂D, then

$$\boldsymbol{E} \coloneqq \begin{cases} \boldsymbol{E}_1 & \text{in } D\,, \\ \boldsymbol{E}_2 & \text{in } B_R \setminus \overline{D} \end{cases} \in \boldsymbol{H}(\mathbf{curl}, B_R)\,.$$

The same holds for $\boldsymbol{H}$.

With that, let $(\boldsymbol{E}^s, \boldsymbol{H}^s) \in (\boldsymbol{C}^\infty(B_R \setminus D) \cup \boldsymbol{C}^\infty(\overline{D})) \times (\boldsymbol{C}^\infty(B_R \setminus D) \cup \boldsymbol{C}^\infty(\overline{D}))$ be a solution of (2.22) in B_R with smooth extension to $\mathbb{R}^3 \setminus \overline{B_R}$ satisfying (2.20), where the corresponding incident field $(\boldsymbol{E}^i, \boldsymbol{H}^i) \in \boldsymbol{C}^\infty(B_R) \times \boldsymbol{C}^\infty(B_R)$ solves (2.21) in B_R. We add $\mathbf{curl}\, \boldsymbol{H}^i + \mathrm{i}\omega\varepsilon_+ \boldsymbol{E}^i = \boldsymbol{0}$ from (2.21) and $\mathbf{curl}\, \boldsymbol{H}^s + \mathrm{i}\omega\varepsilon \boldsymbol{E}^s = \boldsymbol{0}$ from (2.22a) together in Ω to incorporate the requirement for the incident field into the formulation and obtain the equation

$$\mathbf{curl}\, \boldsymbol{H} + \mathrm{i}\omega\varepsilon \boldsymbol{E} = \boldsymbol{0} \qquad \text{in } B_R \setminus \partial D \tag{2.36}$$

for the total field $\boldsymbol{E}$ (cf. (2.19)). After multiplying (2.36) by the complex conjugate of a smooth test function $\boldsymbol{V} \in \boldsymbol{C}^\infty(\overline{B_R})$ and integrating over $B_R \setminus \overline{D}$ as well as D, we can use (A.4d), obtaining

$$\begin{aligned} \int_{B_R} \left(\boldsymbol{H} \cdot \overline{\mathbf{curl}\, \boldsymbol{V}} + \mathrm{i}\omega\varepsilon\, \boldsymbol{E} \cdot \overline{\boldsymbol{V}} \right) \mathrm{d}\boldsymbol{x} - \int_{\partial B_R} (\boldsymbol{H} \times \boldsymbol{\nu}) \cdot \overline{\boldsymbol{V}}\, \mathrm{d}s \\ - \int_{\partial D} (\boldsymbol{H}|_+ \times \boldsymbol{\nu}) \cdot \overline{\boldsymbol{V}}|_+ - (\boldsymbol{H}|_- \times \boldsymbol{\nu}) \cdot \overline{\boldsymbol{V}}|_-\, \mathrm{d}s = 0 \end{aligned} \tag{2.37}$$

(see (2.17) for the notation $[\,\cdot\,]|_\pm$). Note that $\boldsymbol{V} = \boldsymbol{\nu} \times (\boldsymbol{V} \times \boldsymbol{\nu}) + (\boldsymbol{\nu} \cdot \boldsymbol{V})\boldsymbol{\nu}$ and, therefore,

$$\int_{\partial X} (\boldsymbol{H} \times \boldsymbol{\nu}) \cdot \overline{\boldsymbol{V}} \, \mathrm{d}s = \int_{\partial X} (\boldsymbol{H} \times \boldsymbol{\nu}) \cdot (\boldsymbol{\nu} \times (\overline{\boldsymbol{V}} \times \boldsymbol{\nu})) \, \mathrm{d}s \,, \qquad X \in \{\partial D, \partial B_R\} \,.$$

Thus, if we further assume $\boldsymbol{\nu} \times (\boldsymbol{V}|_+ \times \boldsymbol{\nu}) - \boldsymbol{\nu} \times (\boldsymbol{V}|_- \times \boldsymbol{\nu}) = \boldsymbol{0}$ on ∂D and use the interface condition (2.22b) – or equivalently (2.18) for the total fields –, then (2.37) becomes

$$\int_{B_R} \left(\boldsymbol{H} \cdot \overline{\mathbf{curl}\, \boldsymbol{V}} + \mathrm{i}\omega\varepsilon \, \boldsymbol{E} \cdot \overline{\boldsymbol{V}} \right) \mathrm{d}\boldsymbol{x} - \int_{\partial B_R} (\boldsymbol{H} \times \boldsymbol{\nu}) \cdot (\boldsymbol{\nu} \times (\overline{\boldsymbol{V}} \times \boldsymbol{\nu})) \, \mathrm{d}s = 0 \,. \tag{2.38}$$

Next, we want to eliminate $\boldsymbol{H}$ from the equation. The systems (2.21), (2.22a) also provide

$$\boldsymbol{H} = \frac{1}{\mathrm{i}\omega\mu} \, \mathbf{curl}\, \boldsymbol{E} \qquad \text{in } B_R \setminus \partial D \,. \tag{2.39}$$

Furthermore, we employ the Calderón operator $\boldsymbol{\Lambda}$ to incorporate the SMRC (2.20) into the formulation. Using the linearity of $\boldsymbol{\Lambda}$, we split the trace $\boldsymbol{\gamma}_t \boldsymbol{H}$ on ∂B_R into a "known" part of traces of $\boldsymbol{E}^i$ and an "unknown" part of a trace of the total field $\boldsymbol{E}$:

$$\boldsymbol{\gamma}_t \boldsymbol{H} = \boldsymbol{\gamma}_t \boldsymbol{H}^i + \boldsymbol{\gamma}_t \boldsymbol{H}^s = \boldsymbol{\gamma}_t \boldsymbol{H}^i + \boldsymbol{\Lambda}(\boldsymbol{\gamma}_t \boldsymbol{E}^s) = \left[\sqrt{\frac{\varepsilon}{\mu}} \, \boldsymbol{\gamma}_N \boldsymbol{E}^i - \boldsymbol{\Lambda}(\boldsymbol{\gamma}_t \boldsymbol{E}^i) \right] + \boldsymbol{\Lambda}(\boldsymbol{\gamma}_t \boldsymbol{E}) \,. \tag{2.40}$$

Inserting (2.39) and (2.40) into (2.38), moving the "known" terms to the right-hand side, multiplying by $\mathrm{i}\omega\mu$ and using the density of $\boldsymbol{C}^\infty(\overline{B_R})$ in $\boldsymbol{H}(\mathbf{curl}, B_R)$, see Theorem 2.8, yields that the classical smooth solution $\boldsymbol{E}$ satisfies the *variational formulation*

$$\begin{aligned} &\int_{B_R} \left(\mathbf{curl}\, \boldsymbol{E} \cdot \overline{\mathbf{curl}\, \boldsymbol{V}} - \omega^2 \varepsilon\mu \, \boldsymbol{E} \cdot \overline{\boldsymbol{V}} \right) \mathrm{d}\boldsymbol{x} - \mathrm{i}\omega\mu \, \langle \boldsymbol{\Lambda}(\boldsymbol{\gamma}_t \boldsymbol{E}), \boldsymbol{\gamma}_t \boldsymbol{V} \rangle_{t, \partial B_R} \\ &\qquad = \mathrm{i}\omega\mu \left\langle \sqrt{\frac{\varepsilon}{\mu}} \, \boldsymbol{\gamma}_N \boldsymbol{E}^i - \boldsymbol{\Lambda}(\boldsymbol{\gamma}_t \boldsymbol{E}^i), \boldsymbol{\gamma}_t \boldsymbol{V} \right\rangle_{t, \partial B_R} \qquad \text{for all } \boldsymbol{V} \in \boldsymbol{H}(\mathbf{curl}, B_R) \,. \end{aligned} \tag{2.41}$$

A *weak solution* of the scattering problem for a penetrable obstacle is then a total field $\boldsymbol{E} \in \boldsymbol{H}(\mathbf{curl}, B_R)$ solving (2.41).

Remark 2.16. Note that for the incident electric field $\boldsymbol{E}^i \in \boldsymbol{H}_{\mathrm{loc}}(\mathbf{curl}, \mathbb{R}^3)$ (see (2.21)) – which does not satisfy the SMRC (2.20) – it holds that

$$\int_{\mathbb{R}^3} \left(\mathbf{curl}\, \boldsymbol{E}^i \cdot \overline{\mathbf{curl}\, \boldsymbol{V}} - \omega^2 \varepsilon_+ \mu_+ \, \boldsymbol{E}^i \cdot \overline{\boldsymbol{V}} \right) \mathrm{d}\boldsymbol{x} = 0 \qquad \text{for all } \boldsymbol{V} \in \boldsymbol{H}_0(\mathbf{curl}, \mathbb{R}^3) \,,$$

where $\boldsymbol{H}_0(\mathbf{curl}, \mathbb{R}^3)$ denotes the space of compactly supported functions in $\boldsymbol{H}(\mathbf{curl}, \mathbb{R}^3)$.

By [1, Lemma 4.1, Lemma 4.2] the equivalency of the scattering problem (2.22) together with the SMRC (2.20), its truncation to the bounded domain B_R and the variational problem (2.41) is proved – note that in [1] the *Sommerfeld*[16] *radiation condition*, see [105, p. 328, Equation (21)], has been used, however, by [31, Theorem 6.8] the SMRC (2.20) for a radiating field is equivalent to the Sommerfeld radiation condition for every component of the field. The existence of a unique solution has been proved in [1, Lemma 4.3]. However, there the real parts of the

[16] Arnold Sommerfeld (1868–1951)

interior electric permittivity and magnetic permeability are assumed to be strictly positive for the transmission problem. In [69, Theorem 2.21], the statements have been complemented for $\varepsilon_- \in \mathbb{C}$ with $\operatorname{Re}(\varepsilon_-) < 0$, $\operatorname{Im}(\varepsilon_-) > 0$ and $\mu_- > 0$.

Theorem 2.17. *Let $\varepsilon_- > 0$ or $\varepsilon_- \in \mathbb{C}$ with $\operatorname{Re}\varepsilon_- < 0$ and $\operatorname{Im}\varepsilon_- > 0$, and let $\mu_- > 0$, $\varepsilon_+ > 0$, $\mu_+ > 0$. Furthermore, let the incident fields $(\boldsymbol{E}^i, \boldsymbol{H}^i) \in \boldsymbol{H}_{\mathrm{loc}}(\mathbf{curl}, \mathbb{R}^3) \times \boldsymbol{H}_{\mathrm{loc}}(\mathbf{curl}, \mathbb{R}^3)$ be a weak solution of (2.21) with respect to ε_+, μ_+. Then, the scattering problem to find a weak solution $\boldsymbol{E} \in \boldsymbol{H}(\mathbf{curl}, D) \cup \boldsymbol{H}(\mathbf{curl}, B_R \setminus \overline{D})$ of (2.41) is uniquely solvable. There is a unique extension $\boldsymbol{E} \in \boldsymbol{H}(\mathbf{curl}, D) \cup \boldsymbol{H}_{\mathrm{loc}}(\mathbf{curl}, \mathbb{R}^3 \setminus \overline{D})$.*

From the unique solvability of the variational formulation for the total fields, we immediately infer the same result for the corresponding variational formulation for the scattering problem (2.22) together with the SMRC (2.20) (cf. Remark 2.5). To derive such a formulation, on the one hand, we can proceed as for the total field, additionally assuming $\boldsymbol{\nu} \times (\boldsymbol{V}|_+ \times \boldsymbol{\nu}) = \boldsymbol{\nu} \times (\boldsymbol{V}|_- \times \boldsymbol{\nu}) = \mathbf{0}$ on ∂D, where with the interface condition (2.22b), we arrive at the variational formulation

$$\int_{B_R} \left(\mathbf{curl}\, \boldsymbol{E}^s \cdot \overline{\mathbf{curl}\, \boldsymbol{V}} - \omega^2 \varepsilon \mu\, \boldsymbol{E}^s \cdot \overline{\boldsymbol{V}} \right) \mathrm{d}\boldsymbol{x} - \mathrm{i}\omega\mu \, \langle \boldsymbol{\Lambda}(\boldsymbol{\gamma}_t \boldsymbol{E}^s), \boldsymbol{\gamma}_t \boldsymbol{V} \rangle_{t, \partial B_R} = 0$$
$$\text{for all } \boldsymbol{V} \in \boldsymbol{H}(\mathbf{curl}, B_R) \cap \{ \boldsymbol{V} : \boldsymbol{\gamma}_T^+ \boldsymbol{V} = \boldsymbol{\gamma}_T^- \boldsymbol{V} = \mathbf{0} \}\,. \tag{2.42}$$

On the other hand, we can choose extensions $\boldsymbol{f}, \boldsymbol{g} \in \boldsymbol{H}(\mathbf{curl}, B_R)$ of the right-hand sides of the interface conditions (2.22b). Considering $\boldsymbol{E}^s - \boldsymbol{f}$, $\boldsymbol{H}^s - \boldsymbol{g}$, leads again to a problem with zero interface condition and, hence, with the same procedure as for the total fields above, we obtain the formulation

$$\int_{B_R} \left(\mathbf{curl}\, \boldsymbol{E}^s \cdot \overline{\mathbf{curl}\, \boldsymbol{V}} - \omega^2 \varepsilon \mu\, \boldsymbol{E}^s \cdot \overline{\boldsymbol{V}} \right) \mathrm{d}\boldsymbol{x} - \mathrm{i}\omega\mu \, \langle \boldsymbol{\Lambda}(\boldsymbol{\gamma}_t \boldsymbol{E}^s), \boldsymbol{\gamma}_t \boldsymbol{V} \rangle_{t, \partial B_R}$$
$$= \int_{B_R} \left(\mathrm{i}\omega\mu\, \mathbf{curl}\, \boldsymbol{g} \cdot \overline{\boldsymbol{V}} - \omega^2 \varepsilon \mu\, \boldsymbol{f} \cdot \overline{\boldsymbol{V}} \right) \mathrm{d}\boldsymbol{x} \qquad \text{for all } \boldsymbol{V} \in \boldsymbol{H}(\mathbf{curl}, B_R)\,. \tag{2.43}$$

In the case at hand, we have

$$\boldsymbol{\gamma}_t \boldsymbol{f} = -\boldsymbol{\gamma}_t \boldsymbol{E}^i\,, \qquad \boldsymbol{\gamma}_t \boldsymbol{g} = -\boldsymbol{\gamma}_t \boldsymbol{H}^i = -\sqrt{\frac{\varepsilon}{\mu}}\, \boldsymbol{\gamma}_N \boldsymbol{E}^i \qquad \text{on } \partial D\,. \tag{2.44}$$

With $\boldsymbol{f} = -\boldsymbol{E}^i$, $\boldsymbol{g} = -\boldsymbol{H}^i$, we arrive again exactly at (2.42). However, for differing interface conditions, this allows an incorporation of these conditions into the variational formulation.

Corollary 2.18. *Let $\varepsilon_- > 0$ or $\varepsilon_- \in \mathbb{C}$ with $\operatorname{Re}\varepsilon_- < 0$ and $\operatorname{Im}\varepsilon_- > 0$, and let $\mu_- > 0$, $\varepsilon_+ > 0$, $\mu_+ > 0$. Furthermore, let the incident fields $(\boldsymbol{E}^i, \boldsymbol{H}^i) \in \boldsymbol{H}_{\mathrm{loc}}(\mathbf{curl}, \mathbb{R}^3) \times \boldsymbol{H}_{\mathrm{loc}}(\mathbf{curl}, \mathbb{R}^3)$ be a weak solution of (2.21) with respect to ε_+, μ_+. Then, the variational problem to find a weak solution $\boldsymbol{E}^s \in \boldsymbol{H}(\mathbf{curl}, D) \cup \boldsymbol{H}(\mathbf{curl}, B_R \setminus \overline{D})$ of (2.42), is uniquely solvable. There is a unique extension $\boldsymbol{E}^s \in \boldsymbol{H}(\mathbf{curl}, D) \cup \boldsymbol{H}_{\mathrm{loc}}(\mathbf{curl}, \mathbb{R}^3 \setminus \overline{D})$.*

2.6.2. Perfect Conductor

We introduce the closed subspace

$$\boldsymbol{H}_{\mathrm{pc}}(\mathbf{curl},\Omega) \coloneqq \{\boldsymbol{E} \in \boldsymbol{H}(\mathbf{curl},\Omega) : \boldsymbol{\gamma}_t \boldsymbol{E} = 0 \text{ on } \partial D\}$$

and note that $\partial\Omega = \partial B_R \cup \partial D$ and that for $\boldsymbol{H} \in \boldsymbol{C}^\infty(\Omega)$ it holds that

$$\langle \boldsymbol{\gamma}_t \boldsymbol{H}, \boldsymbol{\gamma}_t \boldsymbol{V}\rangle_{t,\partial D} = 0\,, \qquad \boldsymbol{V} \in \boldsymbol{C}^\infty(\overline{\Omega}) \text{ with } \boldsymbol{\nu} \times (\boldsymbol{V} \times \boldsymbol{\nu}) = \mathbf{0} \text{ on } \partial D\,.$$

With that, we proceed similarly as for the transmission problem in the previous Subsection 2.6.1 and obtain the weak formulation of the scattering problem for a perfect conductor:

Find $\boldsymbol{E} \in \boldsymbol{H}_{\mathrm{pc}}(\mathbf{curl},\Omega)$ such that

$$\begin{aligned}\int_\Omega \Big(\mathbf{curl}\, \boldsymbol{E} \cdot \overline{\mathbf{curl}\, \boldsymbol{V}} - \omega^2 \varepsilon_+ \mu_+ \, \boldsymbol{E} \cdot \overline{\boldsymbol{V}} \Big)\, \mathrm{d}\boldsymbol{x} - \mathrm{i}\omega\mu_+ \, \langle \boldsymbol{\Lambda}(\boldsymbol{\gamma}_t \boldsymbol{E}), \boldsymbol{\gamma}_t \boldsymbol{V}\rangle_{t,\partial B_R} \\ = \mathrm{i}\omega\mu_+ \left\langle \sqrt{\frac{\varepsilon}{\mu}}\, \boldsymbol{\gamma}_N \boldsymbol{E}^i - \boldsymbol{\Lambda}(\boldsymbol{\gamma}_t \boldsymbol{E}^i), \boldsymbol{\gamma}_t \boldsymbol{V} \right\rangle_{t,\partial B_R} \qquad \text{for all } \boldsymbol{V} \in \boldsymbol{H}_{\mathrm{pc}}(\mathbf{curl},\Omega)\,. \quad (2.45)\end{aligned}$$

We always assume that $\varepsilon_+, \mu_+ > 0$. Problem (2.45) is uniquely solvable, see [82, Theorem 10.7].

Theorem 2.19. *Let the incident fields $(\boldsymbol{E}^i, \boldsymbol{H}^i) \in \boldsymbol{H}_{\mathrm{loc}}(\mathbf{curl},\mathbb{R}^3) \times \boldsymbol{H}_{\mathrm{loc}}(\mathbf{curl},\mathbb{R}^3)$ be a weak solution of (2.23) with respect to ε_+, μ_+. Then, the problem to find a weak solution $\boldsymbol{E} \in \boldsymbol{H}_{\mathrm{pc}}(\mathbf{curl},\Omega)$ of (2.45) is uniquely solvable. There is a unique extension $\boldsymbol{E} \in \boldsymbol{H}_{\mathrm{pc,loc}}(\mathbf{curl},\mathbb{R}^3\setminus\overline{D})$.*

As in the previous Subsection 2.6.1, we additionally formulate the weak formulation for the scattering problem (2.24) together with the SMRC (2.20), which is

$$\begin{aligned}\int_\Omega \Big(\mathbf{curl}\, \boldsymbol{E}^s \cdot \overline{\mathbf{curl}\, \boldsymbol{V}} - \omega^2 \varepsilon_+ \mu_+ \, \boldsymbol{E}^s \cdot \overline{\boldsymbol{V}} \Big)\, \mathrm{d}\boldsymbol{x} - \mathrm{i}\omega\mu_+ \, \langle \boldsymbol{\Lambda}(\boldsymbol{\gamma}_t \boldsymbol{E}^s), \boldsymbol{\gamma}_t \boldsymbol{V}\rangle_{t,\partial B_R} \\ = \int_\Omega \Big(\mathrm{i}\omega\mu_+ \, \mathbf{curl}\, \boldsymbol{g} \cdot \overline{\boldsymbol{V}} - \omega^2 \varepsilon_+ \mu_+ \, \boldsymbol{f} \cdot \overline{\boldsymbol{V}} \Big)\, \mathrm{d}\boldsymbol{x} \qquad \text{for all } \boldsymbol{V} \in \boldsymbol{H}_{\mathrm{pc}}(\mathbf{curl},\Omega)\,, \quad (2.46)\end{aligned}$$

with extensions $\boldsymbol{f}, \boldsymbol{g} \in \boldsymbol{H}(\mathbf{curl}, D)$ of $\boldsymbol{\gamma}_t \boldsymbol{E}^i, \boldsymbol{\gamma}_t \boldsymbol{H}^i \in \boldsymbol{H}^{-1/2}(\mathrm{Div}, \partial D)$, respectively.

Corollary 2.20. *Let the incident fields $(\boldsymbol{E}^i, \boldsymbol{H}^i) \in \boldsymbol{H}_{\mathrm{loc}}(\mathbf{curl},\mathbb{R}^3) \times \boldsymbol{H}_{\mathrm{loc}}(\mathbf{curl},\mathbb{R}^3)$ be a weak solution of (2.23) with respect to ε_+, μ_+. Then, the variational problem to find $\boldsymbol{E}^s \in \boldsymbol{H}(\mathbf{curl},\Omega)$ that solves (2.46), is uniquely solvable. There is a unique extension $\boldsymbol{E}^s \in \boldsymbol{H}_{\mathrm{loc}}(\mathbf{curl},\mathbb{R}^3 \setminus \overline{D})$.*

2.7. Inverse and Optimization Problem

Recall the definition of the unit sphere in $\mathbb{R}^3$ by $\mathbb{S}^2 = \{\boldsymbol{x} \in \mathbb{R}^3 : |\boldsymbol{x}| = 1\}$. As a consequence of the SMRC (2.20), scattered electric fields can be asymptotically expanded as

$$\boldsymbol{E}^s(\boldsymbol{x}) = \frac{\mathrm{e}^{\mathrm{i}k_+|\boldsymbol{x}|}}{4\pi|\boldsymbol{x}|} \left(\boldsymbol{E}^\infty(\widehat{\boldsymbol{x}}) + \mathcal{O}\left(\frac{1}{|\boldsymbol{x}|}\right)\right) \qquad \text{as } |\boldsymbol{x}| \to \infty\,, \quad (2.47)$$

uniformly with respect to $\widehat{\boldsymbol{x}} = \boldsymbol{x}/|\boldsymbol{x}| \in \mathbb{S}^2$, see [31, Theorem 6.9]. $\boldsymbol{E}^\infty \in \boldsymbol{L}_t^2(\mathbb{S}^2)$ is called the *electric far-field pattern* and it holds that

$$\boldsymbol{E}^\infty(\widehat{\boldsymbol{x}}) = \mathrm{i}k_+ \left\langle \left(\boldsymbol{\gamma}_t \boldsymbol{E} + \boldsymbol{\gamma}_t \boldsymbol{H} \times \widehat{\boldsymbol{x}}\right), \boldsymbol{y} \mapsto \mathrm{e}^{-\mathrm{i}k_+ \widehat{\boldsymbol{x}}\cdot\boldsymbol{y}} \right\rangle_{L^2(\partial D)} \times \widehat{\boldsymbol{x}}\,, \qquad \widehat{\boldsymbol{x}} \in \mathbb{S}^2\,, \tag{2.48}$$

see [31, Theorem 6.9]. The scattered magnetic field $\boldsymbol{H}^s$ has a corresponding asymptotic form and magnetic far-field pattern $\boldsymbol{H}^\infty$ on $\mathbb{S}^2$, however, we can readily compute it by $\boldsymbol{H}^\infty(\widehat{\boldsymbol{x}}) = \widehat{\boldsymbol{x}} \times \boldsymbol{E}^\infty(\widehat{\boldsymbol{x}})$, $\widehat{\boldsymbol{x}} \in \mathbb{S}^2$, if required.

By construction of the Calderón operator $\boldsymbol{\Lambda}$, for solutions $(\boldsymbol{E}, \boldsymbol{H})$ of (2.41) or (2.45), the scattered field $(\boldsymbol{E}^s, \boldsymbol{H}^s)$ can be smoothly extended to radiating electromagnetic fields in $\mathbb{R}^3 \setminus \overline{B_R}$. The electric field in this extension has got the asymptotic representation from (2.47), with electric far-field pattern $\boldsymbol{E}^\infty \in \boldsymbol{L}_t^2(\mathbb{S}^2)$ given by (2.48). At this point, we can make the following definition.

Definition 2.21. *We define the* far-field map $F\colon \partial D \mapsto \boldsymbol{E}^\infty$ *mapping an admissible boundary* ∂D *onto the corresponding far-field pattern* $\boldsymbol{E}^\infty$ *for a fixed incident field* $\boldsymbol{E}^i$*.*

Based on the far-field data, two closely related problems will be treated in this work, namely, an inverse and an optimization problem. For the latter, we first need to introduce the notion of electromagnetic chirality.

2.7.1. Electromagnetic Chirality

The concept of *electromagnetic chirality* (em-chirality) has been much discussed in, e.g., [40, 46, 97]. A measuring tool has been proposed in [40], which has been cast in a mathematical setting in [4]. In the following, we summarize this approach. We start by recalling the definition of *geometrically chiral* objects.

Definition 2.22. *An object* $D \subseteq \mathbb{R}^3$ *is called* geometrically achiral *if there are* $x_0 \in \mathbb{R}^3$ *and an orthogonal matrix* $S \in \mathbb{R}^{3\times 3}$ *with* $\det S = -1$*, such that* $D = x_0 + S(D)$*. Otherwise, it is called geometrically chiral.*

In other words, a geometrically chiral object is defined by the impossibility to coincide with its mirror image along some plane purely by rotations and translations. If this is possible, however, the object is geometrically achiral. Obviously, if D is a sphere, it can be superposed onto any mirror image of itself, whereas other objects may only have certain planes of reflection, where this is possible. Thus, in a sense some objects can be viewed as being more or less geometrically a-/chiral than others, see also [45]. However, Definition 2.22 is merely a binary criterion, since it does not classify *how* chiral an object may be. The em-chirality provides a remedy for this issue. Essentially, it is based on the effect of the scatterer on electromagnetic fields rather than on geometric properties of the scatterer itself.

In order to describe the concept of em-chirality, we first need to start with a general definition of a vector field's *helicity*. Recall the definition of the wave number $k = \omega\sqrt{\varepsilon\mu}$.

Definition 2.23. *A field* $\boldsymbol{U} \in H(\mathbf{curl}, \Omega)$ *is said to have helicity* ± 1 *if it is an eigenfunction of the operator* $1/k\,\mathbf{curl}$ *with eigenvalue* ± 1*. Such fields* $\boldsymbol{U}$ *are also called Beltrami*[17] *vector fields.*

[17] Eugenio Beltrami (1835–1900)

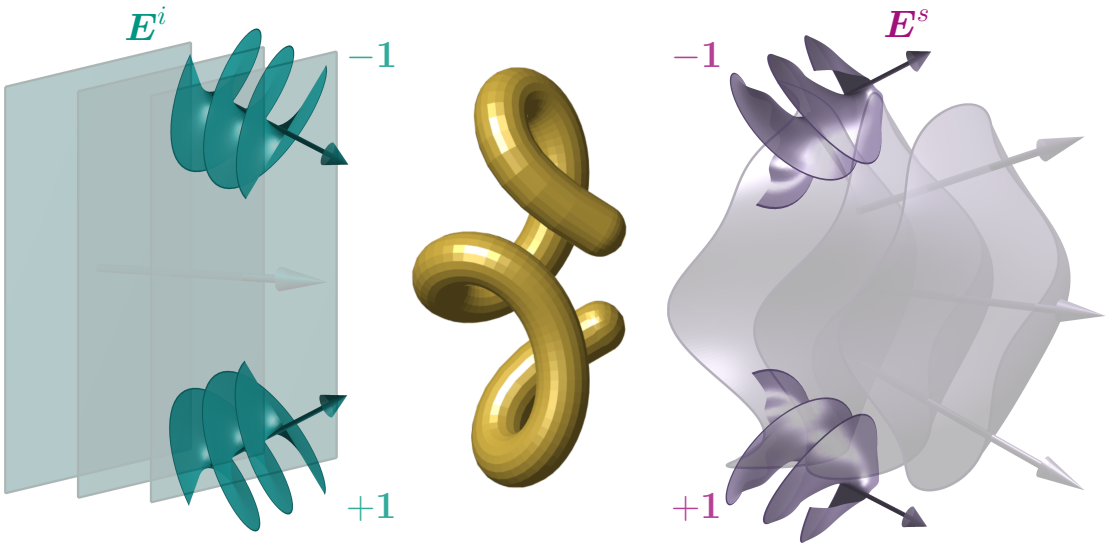

Figure 2.1. Decomposition of an incident electric plane wave $\boldsymbol{E}^i$ and the corresponding scattered field $\boldsymbol{E}^s$ into fields of helicity ± 1. For the former decomposition the anti-/clockwise circular motion of $\operatorname{Re} \boldsymbol{p}$ in the direction of propagation $\boldsymbol{d}$ is emphasized.

The em-chirality of an object now gives us information about how it interacts with incident fields of opposite helicities. In what follows, we argue that the helicity of a plane wave describes its circular polarization state.

We define a *plane wave* $(\boldsymbol{E}^i, \boldsymbol{H}^i)$ with some direction $\boldsymbol{d} \in \mathbb{R}^3$ and polarization $\boldsymbol{p} \in \mathbb{C}^3 \setminus \{\boldsymbol{0}\}$, $\boldsymbol{p} \perp \boldsymbol{d}$, by

$$\boldsymbol{E}^i(\boldsymbol{x}, \boldsymbol{d}, \boldsymbol{p}) \coloneqq \boldsymbol{p}\, \mathrm{e}^{\mathrm{i}k\boldsymbol{d}\cdot\boldsymbol{x}}\,, \qquad \boldsymbol{H}^i(\boldsymbol{x}, \boldsymbol{d}, \boldsymbol{p}) \coloneqq \sqrt{\frac{\varepsilon}{\mu}}\, \boldsymbol{d} \times \boldsymbol{p}\, \mathrm{e}^{\mathrm{i}k\boldsymbol{d}\cdot\boldsymbol{x}}\,, \qquad \boldsymbol{x} \in \mathbb{R}^3\,. \tag{2.49}$$

Such a plane wave is called *left (or right) circularly polarized*, if the real part of the amplitude performs an anticlockwise (or clockwise) circular motion in the direction of propagation $\boldsymbol{d}$. In particular, since the amplitudes of the electric and magnetic fields of a plane wave are perpendicular, a plane wave is left (or right) circularly polarized if and only if the electric field coincides with – up to some scaling – $\mp$ the magnetic field after a quarter of the wavelength λ in the direction of propagation $\boldsymbol{d}$. Thus, by the definition of a plane wave, we find the relation

$$\mathrm{i}\boldsymbol{E}^i(\boldsymbol{x}, \boldsymbol{d}, \boldsymbol{p}) = \boldsymbol{E}^i(\boldsymbol{x} + \lambda/4\, \boldsymbol{d}, \boldsymbol{d}, \boldsymbol{p}) \overset{!}{=} \mp\sqrt{\frac{\mu}{\varepsilon}}\, \boldsymbol{H}^i(\boldsymbol{x}, \boldsymbol{d}, \boldsymbol{p}) = \mp\frac{1}{\mathrm{i}k}\, \operatorname{\mathbf{curl}} \boldsymbol{E}^i(\boldsymbol{x}, \boldsymbol{d}, \boldsymbol{p})\,,$$

indicating that a left (or right) circularly polarized plane wave has helicity ± 1. Furthermore,

$$\boldsymbol{E}^i(\boldsymbol{x}, \boldsymbol{d}, \boldsymbol{p}) = \pm\frac{1}{k}\, \operatorname{\mathbf{curl}} \boldsymbol{E}^i(\boldsymbol{x}, \boldsymbol{d}, \boldsymbol{p}) \quad \Longleftrightarrow \quad \boldsymbol{p}\, \mathrm{e}^{\mathrm{i}k\boldsymbol{x}\cdot\boldsymbol{d}} = \pm\mathrm{i}(\boldsymbol{d} \times \boldsymbol{p})\, \mathrm{e}^{\mathrm{i}k\boldsymbol{x}\cdot\boldsymbol{d}} \quad \Longleftrightarrow \quad \boldsymbol{p} = \pm\mathrm{i}(\boldsymbol{d} \times \boldsymbol{p})\,. \tag{2.50}$$

Hence, a plane wave has helicity ± 1 if and only if $\boldsymbol{p} = \pm \mathrm{i}(\boldsymbol{d} \times \boldsymbol{p})$. This generalizes to arbitrary solutions to the Maxwell system (2.15) in the sense described below.

Definition 2.24. *We define a* Herglotz wave pair $\boldsymbol{V}^i[\boldsymbol{\varphi}] = (\boldsymbol{E}^i[\boldsymbol{\varphi}], \boldsymbol{H}^i[\boldsymbol{\varphi}])$*, consisting of an* electric *and a* magnetic Herglotz wave*, with some density* $\boldsymbol{\varphi} \in L_t^2(\mathbb{S}^2)$ *as a linear superposition of plane waves*

$$\left.\begin{aligned} \boldsymbol{E}^i[\boldsymbol{\varphi}](\boldsymbol{x}) &= \int_{\mathbb{S}^2} \boldsymbol{\varphi}(\boldsymbol{d})\, \mathrm{e}^{\mathrm{i}k\boldsymbol{d}\cdot\boldsymbol{x}}\, \mathrm{d}s(\boldsymbol{d}) \\ \boldsymbol{H}^i[\boldsymbol{\varphi}](\boldsymbol{x}) &= \sqrt{\frac{\varepsilon}{\mu}} \int_{\mathbb{S}^2} \boldsymbol{d} \times \boldsymbol{\varphi}(\boldsymbol{d})\, \mathrm{e}^{\mathrm{i}k\boldsymbol{d}\cdot\boldsymbol{x}}\, \mathrm{d}s(\boldsymbol{d}) \end{aligned}\right\} \quad \boldsymbol{x} \in \mathbb{R}^3 .$$

In any compact subset of $\mathbb{R}^3$, the Herglotz wave pairs form a dense subspace of the solution space for the Maxwell system (2.15) with respect to the $\boldsymbol{H}(\mathbf{curl}, D)$-norm, see [29]. Hence, we can approximate any weak solution to the Maxwell system in any compact subset arbitrarily well by Herglotz wave pairs.

Then, with regard to (2.50), we define the operator $\mathcal{C}\colon L_t^2(\mathbb{S}^2) \to L_t^2(\mathbb{S}^2)$ by

$$\mathcal{C}\boldsymbol{\varphi}(\boldsymbol{d}) \coloneqq \mathrm{i}\,(\boldsymbol{d} \times \boldsymbol{\varphi}(\boldsymbol{d}))\,, \qquad \boldsymbol{d} \in \mathbb{S}^2 . \tag{2.51}$$

With this operator, we have the following characterization for the helicity of Herglotz waves.

Theorem 2.25. *Let* $\boldsymbol{\varphi} \in L_t^2(\mathbb{S}^2)$*. A Herglotz wave pair* $\boldsymbol{V}^i[\boldsymbol{\varphi}]$ *has helicity* ± 1 *if* $\boldsymbol{\varphi}$ *is an eigenfunction with eigenvalue* ± 1 *of the operator* $\mathcal{C}$*.*

Since $\boldsymbol{\varphi} \in L_t^2(\mathbb{S}^2)$, we immediately notice that for $\boldsymbol{d} \in \mathbb{S}^2$, there hold

$$\mathcal{C}^2\boldsymbol{\varphi}(\boldsymbol{d}) = \mathcal{C}(\mathrm{i}\,(\boldsymbol{d} \times \boldsymbol{\varphi}(\boldsymbol{d}))) = -\boldsymbol{d} \times (\boldsymbol{d} \times \boldsymbol{\varphi}(\boldsymbol{d})) = \boldsymbol{\varphi}(\boldsymbol{d}) \tag{2.52}$$

and

$$|\mathcal{C}\boldsymbol{\varphi}(\boldsymbol{d})| = |\mathrm{i}\,(\boldsymbol{d} \times \boldsymbol{\varphi}(\boldsymbol{d}))| = |\boldsymbol{\varphi}(\boldsymbol{d})|\,. \tag{2.53}$$

Moreover, we readily calculate

$$\overline{\boldsymbol{\varphi}(\boldsymbol{d})} \cdot \mathcal{C}\boldsymbol{\varphi}(\boldsymbol{d}) = \overline{\boldsymbol{\varphi}(\boldsymbol{d})} \cdot \mathrm{i}\,(\boldsymbol{d} \times \boldsymbol{\varphi}(\boldsymbol{d})) = -\boldsymbol{\varphi}(\boldsymbol{d}) \cdot \mathrm{i}\,(\boldsymbol{d} \times \overline{\boldsymbol{\varphi}(\boldsymbol{d})}) = -\boldsymbol{\varphi}(\boldsymbol{d}) \cdot \mathcal{C}\overline{\boldsymbol{\varphi}(\boldsymbol{d})} \tag{2.54}$$

as well as

$$\begin{aligned} \overline{\mathcal{C}\boldsymbol{\varphi}(\boldsymbol{d})} &= \overline{\mathrm{i}\,[\boldsymbol{d} \times \mathrm{Re}(\boldsymbol{\varphi}(\boldsymbol{d})) + \mathrm{i}\,(\boldsymbol{d} \times \mathrm{Im}(\boldsymbol{\varphi}(\boldsymbol{d})))]} \\ &= -\mathrm{i}\,(\boldsymbol{d} \times \mathrm{Re}(\boldsymbol{\varphi}(\boldsymbol{d}))) - \boldsymbol{d} \times \mathrm{Im}(\boldsymbol{\varphi}(\boldsymbol{d})) = -\mathcal{C}\overline{\boldsymbol{\varphi}(\boldsymbol{d})}\,. \end{aligned} \tag{2.55}$$

From (2.52) we conclude that the eigenspaces of $\mathcal{C}$ are given by

$$V^{\pm} = \left\{ \boldsymbol{\varphi} \pm \mathcal{C}\boldsymbol{\varphi} : \boldsymbol{\varphi} \in L_t^2(\mathbb{S}^2) \right\}.$$

Furthermore, for $\boldsymbol{\varphi} \in L_t^2(\mathbb{S}^2)$ it holds that

$$\boldsymbol{\varphi} = \frac{1}{2}(\boldsymbol{\varphi} + \boldsymbol{\varphi}) + \frac{1}{2}(\mathcal{C}\boldsymbol{\varphi} - \mathcal{C}\boldsymbol{\varphi}) = \frac{1}{2}(\boldsymbol{\varphi} + \mathcal{C}\boldsymbol{\varphi}) + \frac{1}{2}(\boldsymbol{\varphi} - \mathcal{C}\boldsymbol{\varphi})$$

and (2.53), (2.54) as well as (2.55) imply

$$\int_{\mathbb{S}^2} (\boldsymbol{\varphi} + \mathcal{C}\boldsymbol{\varphi}) \cdot \overline{(\boldsymbol{\varphi} - \mathcal{C}\boldsymbol{\varphi})}\, \mathrm{d}s = \int_{\mathbb{S}^2} |\boldsymbol{\varphi}|^2 + \overline{\boldsymbol{\varphi}} \cdot \mathcal{C}\boldsymbol{\varphi} - \boldsymbol{\varphi} \cdot \overline{\mathcal{C}\boldsymbol{\varphi}} - |\mathcal{C}\boldsymbol{\varphi}|^2 \, \mathrm{d}s = 0\,,$$

i.e., $V^+ \perp V^-$. Therefore, we conclude that $\boldsymbol{L}_t^2(\mathbb{S}^2) = V^+ \oplus V^-$. The orthogonal projections $\mathcal{P}^{\pm}\colon L_t^2(\mathbb{S}^2) \to V^{\pm}$ are naturally given by $\mathcal{P}^{\pm} = 1/2\,(\mathrm{id} \pm \mathcal{C})$. Hence, considering a complete orthonormal system $\mathscr{B}$ of $\boldsymbol{L}_t^2(\mathbb{S}^2) = V^+ \oplus V^-$, the sets

$$\{\boldsymbol{\varphi} + \mathcal{C}\boldsymbol{\varphi} : \boldsymbol{\varphi} \in \mathscr{B}\} \qquad \text{and} \qquad \{\boldsymbol{\varphi} - \mathcal{C}\boldsymbol{\varphi} : \boldsymbol{\varphi} \in \mathscr{B}\} \tag{2.56}$$

form complete orthogonal systems in V^+ and V^-, respectively.

In conclusion, we can represent a Herglotz wave pair with density $\boldsymbol{\varphi} \in L_t^2(\mathbb{S}^2)$ as a sum of two Beltrami fields of opposite helicity being exactly the same as representing it via

$$\boldsymbol{V}^i[\boldsymbol{\varphi}] = \boldsymbol{V}^i[\mathcal{P}^+\boldsymbol{\varphi}] + \boldsymbol{V}^i[\mathcal{P}^-\boldsymbol{\varphi}]\,.$$

Next, we illuminate some bounded scatterer $D \subseteq \mathbb{R}^3$ by $\boldsymbol{V}^i[\boldsymbol{\varphi}]$ and let the total field $\boldsymbol{E}[\boldsymbol{\varphi}]$ be the solution of (2.41) or (2.45). Then, we decompose the corresponding scattered field $\boldsymbol{E}^s[\boldsymbol{\varphi}]$ into the so-called Riemann–Silberstein[18] vectors – or Weber[19] vectors –

$$\boldsymbol{E}^{s,\pm}[\boldsymbol{\varphi}] \coloneqq \boldsymbol{E}^s[\boldsymbol{\varphi}] \pm \mathrm{i}\sqrt{\frac{\mu}{\varepsilon}}\, \boldsymbol{H}^s[\boldsymbol{\varphi}]\,,$$

obtaining

$$\boldsymbol{E}^s[\boldsymbol{\varphi}] = \frac{1}{2}\left(\boldsymbol{E}^{s,+}[\boldsymbol{\varphi}] + \boldsymbol{E}^{s,-}[\boldsymbol{\varphi}]\right).$$

Since

$$\mathbf{curl}\, \boldsymbol{E}^{s,\pm}[\boldsymbol{\varphi}] = \mathbf{curl}\, \boldsymbol{E}^s[\boldsymbol{\varphi}] \pm \mathrm{i}\sqrt{\frac{\mu}{\varepsilon}}\, \mathbf{curl}\, \boldsymbol{H}^s[\boldsymbol{\varphi}] = \mathrm{i}k\sqrt{\frac{\mu}{\varepsilon}}\, \boldsymbol{H}^s[\boldsymbol{\varphi}] \pm k\, \boldsymbol{E}^s[\boldsymbol{\varphi}] = \pm k\, \boldsymbol{E}^{s,\pm}[\boldsymbol{\varphi}]\,,$$

$\boldsymbol{E}^{s,\pm}[\boldsymbol{\varphi}]$ is a field of helicity ± 1.

Moreover, these Beltrami fields $\boldsymbol{E}^{s,\pm}[\boldsymbol{\varphi}]$ adopt the asymptotic behaviour (2.47) from $\boldsymbol{E}^s[\boldsymbol{\varphi}]$, where the corresponding far-field patterns can be characterized with the following theorem.

Theorem 2.26. *Let $\boldsymbol{E}$ be a solution to* (2.41) *or* (2.45) *and $\boldsymbol{E}^s$ be the associated scattered field. The corresponding far-field pattern $\boldsymbol{E}^\infty$ is an element of $V^{\pm}$ if and only if for any bounded open set B with $\overline{B} \subseteq \mathbb{R}^3 \setminus \overline{D}$ we have that $\boldsymbol{E}^s$ is a Beltrami field with eigenvalue ± 1.*

Proof. See [4, Theorem 2.4]. ∎

[18] Georg Friedrich Bernhard Riemann (1826–1866), Ludwik Silberstein (1872–1948)

[19] Heinrich Martin Georg Weber (1842–1913); in [65, Appendix A.1], a historical argument has been presented, supporting the designation of these vectors as Weber vectors.

Concisely, we have

$$\left.\begin{aligned} \boldsymbol{E}^i[\boldsymbol{\varphi}] \text{ has helicity } \pm 1 \quad &\Longleftrightarrow \quad \boldsymbol{\varphi} \in V^{\pm} \\ \boldsymbol{E}^s[\boldsymbol{\varphi}] \text{ has helicity } \pm 1 \quad &\Longleftrightarrow \quad \boldsymbol{E}^{\infty}[\boldsymbol{\varphi}] \in V^{\pm} \end{aligned}\right\} \tag{2.57}$$

and we can decompose such incident electric Herglotz and corresponding scattered fields into fields of helicity ± 1 each (cf. Figure 2.1 for a simplified depiction for a plane wave).

Next, we define the *far-field operator*, which entirely describes the far-field patterns $\boldsymbol{E}^{\infty}[\boldsymbol{\varphi}]$ corresponding to an excitation by electric Herglotz waves $\boldsymbol{E}^i[\boldsymbol{\varphi}]$. Recall the definition of plane waves with direction $\boldsymbol{d}$ and polarization $\boldsymbol{p}$ from (2.49). Let such a plane wave illuminate some scatterer and denote by $\boldsymbol{E}^s(\,\cdot\,, \boldsymbol{d}, \boldsymbol{p})$ the corresponding scattered electric field and by $\boldsymbol{E}^{\infty}(\,\cdot\,, \boldsymbol{d}, \boldsymbol{p})$ the corresponding electric far-field pattern. By superposition, the scattered electric field $\boldsymbol{E}^s[\boldsymbol{\varphi}]$ that corresponds to an incident electric Herglotz wave (cf. Definition 2.24), is given by

$$\boldsymbol{E}^s[\boldsymbol{\varphi}](\boldsymbol{x}) = \int_{\mathbb{S}^2} \boldsymbol{E}^s(\boldsymbol{x}, \boldsymbol{d}, \boldsymbol{\varphi}(\boldsymbol{d}))\, \mathrm{d}s(\boldsymbol{d})\,, \qquad \boldsymbol{x} \in \mathbb{R}^3\,,$$

and its far-field pattern by

$$\boldsymbol{E}^{\infty}[\boldsymbol{\varphi}](\widehat{\boldsymbol{x}}) = \int_{\mathbb{S}^2} \boldsymbol{E}^{\infty}(\widehat{\boldsymbol{x}}, \boldsymbol{d}, \boldsymbol{\varphi}(\boldsymbol{d}))\, \mathrm{d}s(\boldsymbol{d})\,, \qquad \boldsymbol{x} \in \mathbb{R}^3\,.$$

We can now define the far-field operator.

Definition 2.27. *The far-field operator is defined by*

$$\mathcal{F}\colon L_t^2(\mathbb{S}^2) \to L_t^2(\mathbb{S}^2)\,, \qquad \mathcal{F}\boldsymbol{\varphi} \coloneqq \boldsymbol{E}^{\infty}[\boldsymbol{\varphi}]\,.$$

$\mathcal{F}$ is a linear integral operator with smooth kernel, see [31, Theorem 6.9]. Hence, it is a compact operator. On the basis of (2.57), we define the compact operators

$$\mathcal{F}^{pq} \coloneqq \mathcal{P}^p \mathcal{F} \mathcal{P}^q\,, \qquad p, q \in \{+, -\}\,,$$

mapping the part of a density that corresponds to an incident field of helicity $q \in \{+, -\}$ onto the far-field pattern associated to a scattered field of helicity $p \in \{+, -\}$. Then, we decompose the far-field operator into

$$\mathcal{F} = \mathcal{F}^{++} + \mathcal{F}^{+-} + \mathcal{F}^{-+} + \mathcal{F}^{--}\,. \tag{2.58}$$

On that note, we head back to the notion of chirality and define electromagnetically a-/chiral objects.

Definition 2.28. *The scatterer D is called electromagnetically achiral (em-achiral) if there exist unitary operators $\mathcal{U}_j\colon L_t^2(\mathbb{S}^2) \to L_t^2(\mathbb{S}^2)$ with $\mathcal{U}_j\mathcal{C} = -\mathcal{C}\mathcal{U}_j$, $j = 1, \ldots, 4$, such that*

$$\mathcal{F}^{++} = \mathcal{U}_1 \mathcal{F}^{--} \mathcal{U}_2\,, \qquad \mathcal{F}^{+-} = \mathcal{U}_3 \mathcal{F}^{-+} \mathcal{U}_4\,. \tag{2.59}$$

If this is not the case, we call the scatterer D electromagnetically chiral (em-chiral).

This definition does not give an intuitive connection of the geometric and the em-chirality. However, [4, Lemma 3.1] tells us that if there is a unitary operator $\mathcal{U}\colon L_t^2(\mathbb{S}^2) \to L_t^2(\mathbb{S}^2)$ with

$$\mathcal{C}\mathcal{U} = -\mathcal{U}\mathcal{C} \qquad \text{and} \qquad \mathcal{F}\mathcal{U} = \mathcal{U}\mathcal{F}\,, \tag{2.60}$$

then the scattering object (of the corresponding scattering problem) is em-achiral. Furthermore, [4, Theorem 3.2, Theorem 3.3] proof that (2.60) is indeed satisfied for geometrically achiral objects both for perfectly conducting and penetrable scatterers. In conclusion, we have the following result.

Theorem 2.29. *Geometrically achiral objects are also em-achiral in the context of this thesis.*

Next, we examine (2.60). Let $\boldsymbol{\xi} \in V^{\pm}$, i.e., there is a $\boldsymbol{\varphi} \in L_t^2(\mathbb{S}^2)$ such that $\boldsymbol{\xi} = \boldsymbol{\varphi} \pm \mathcal{C}\boldsymbol{\varphi}$. Assuming $\mathcal{U}\mathcal{C} = -\mathcal{C}\mathcal{U}$ for unitary $\mathcal{U}\colon L_t^2(\mathbb{S}^2) \to L_t^2(\mathbb{S}^2)$ implies

$$-\mathcal{C}\mathcal{U}\boldsymbol{\xi} = \mathcal{U}\mathcal{C}\boldsymbol{\xi} = \pm\mathcal{U}\boldsymbol{\xi} \qquad \Longleftrightarrow \qquad \mathcal{C}\mathcal{U}\boldsymbol{\xi} = \mp\mathcal{U}\boldsymbol{\xi}\,,$$

i.e., $\mathcal{U}\boldsymbol{\xi} \in V^{\mp}$. This means that $\mathcal{U}$ maps a density of one helicity to a density of the opposite helicity. Then, together with the condition $\mathcal{F}\mathcal{U} = \mathcal{U}\mathcal{F}$, (2.60) as a whole indicates that an application of $\mathcal{F}$ is equivalent to flipping the input's $V^{\pm}$-components to $V^{\mp}$, applying $\mathcal{F}$ and flipping the result again. Accordingly, Definition 2.28 is a generalization of this property.

From this, in [4], [41] a tool for measuring the degree of how em-chiral an object is, has been specified. Let $\mathcal{G}$ be a compact operator mapping a Hilbert space $(X, (\cdot,\cdot\cdot)_X)$ onto itself. Such $\mathcal{G}$ is called *Hilbert–Schmidt*[20] *operator* if its singular values $(s_n)_{n\in\mathbb{N}}$, see [70, Definition 15.15], form a square-summable sequence. We denote the space of such Hilbert–Schmidt operators by $\mathrm{HS}(X)$ and define the Hilbert–Schmidt norm

$$\|\mathcal{G}\|_{\mathrm{HS}} \coloneqq \left(\sum_{n=1}^{\infty} s_n^2\right)^{1/2}, \qquad \mathcal{G} \in \mathrm{HS}(X)\,.$$

Moreover, let $(g_n)_{n\in\mathbb{N}}$ denote any complete orthogonal system in X. Then, by [111, Satz VI.6.2] it holds that $\mathcal{G} \in \mathrm{HS}(X)$ satisfies

$$\|\mathcal{G}\|_{\mathrm{HS}} = \left(\sum_{n=1}^{\infty} \|\mathcal{G}g_n\|_X^2\right)^{1/2} = \mathrm{tr}(\mathcal{G}^*\mathcal{G})^{1/2} \tag{2.61}$$

and that $\mathrm{HS}(X)$ equipped with the scalar product

$$\langle \mathcal{G}, \mathcal{H}\rangle_{\mathrm{HS}} \coloneqq \sum_{n=1}^{\infty} \langle \mathcal{G}g_n, \mathcal{H}g_n\rangle_X = \mathrm{tr}(\mathcal{H}^*\mathcal{G})\,, \qquad \mathcal{G}, \mathcal{H} \in \mathrm{HS}(X)\,, \tag{2.62}$$

is itself a Hilbert space. $\langle\cdot,\cdot\cdot\rangle_{\mathrm{HS}}$ evidently induces $\|\cdot\|_{\mathrm{HS}}$ by (2.61).

Now, let $p, q \in \{+,-\}$ and recall that the far-field operator $\mathcal{F}$ and its components $\mathcal{F}^{pq}$ are linear integral operators with smooth kernel, entailing an at least exponential decrease of their singular values $(\sigma_n)_n$ and $(\sigma_n^{pq})_n$, respectively [7, Chapter 4]. In particular, $(\sigma_n)_n$, $(\sigma_n^{pq})_n \subseteq \ell^2$,

[20] Erhard Schmidt (1876–1959)

and, hence, $\mathcal{F}$ and $\mathcal{F}^{pq}$ are Hilbert–Schmidt operators. Since $\mathcal{U}_j$, $j = 1, \dots, 4$, are unitary in Definition 2.28, (2.59) implies that

$$\sigma_n^{++} = \sigma_n^{--} \qquad \text{and} \qquad \sigma_n^{+-} = \sigma_n^{-+}, \qquad n \in \mathbb{N}, \tag{2.63}$$

see [4, Section 4]. Thus, measuring the deviation from this property turns out to be a reasonable approach of characterizing how em-chiral an object is, see [4, Definition 4.1], [41, Equation (16)].

Definition 2.30. *For a scattering object D characterized by a far-field operator $\mathcal{F}$, the em-chirality measure $\chi\colon \mathrm{HS}(L_t^2(\mathbb{S}^2)) \to \mathbb{R}_{\geq 0}$ is defined by*

$$\chi(\mathcal{F}) \coloneqq \left(\|(\sigma_n^{++})_{n\in\mathbb{N}} - (\sigma_n^{--})_{n\in\mathbb{N}}\|_{\ell^2}^2 + \|(\sigma_n^{+-})_{n\in\mathbb{N}} - (\sigma_n^{-+})_{n\in\mathbb{N}}\|_{\ell^2}^2 \right)^{1/2}.$$

This definition of a chirality measure has been used in [46], [97] to optimize helical structures with respect to their em-chirality properties, utilizing Bayesian[21] optimization that does not require derivatives of χ, see [100]. We are interested in a differentiable measure, hence, we will use the following smooth relaxation that has been defined in [53, p. 109].

Definition 2.31. *For a scattering object D characterized by a far-field operator $\mathcal{F}$, the modified em-chirality measure $\chi_{\mathrm{HS}}\colon \mathrm{HS}(L_t^2(\mathbb{S}^2)) \to \mathbb{R}_{\geq 0}$ is defined by*

$$\chi_{\mathrm{HS}}(\mathcal{F}) \coloneqq \left[\left(\|\mathcal{F}^{++}\|_{\mathrm{HS}}^2 - \|\mathcal{F}^{--}\|_{\mathrm{HS}}^2 \right)^2 + \left(\|\mathcal{F}^{+-}\|_{\mathrm{HS}}^2 - \|\mathcal{F}^{-+}\|_{\mathrm{HS}}^2 \right)^2 \right]^{1/2}.$$

By the Pythagorean[22] theorem [53, Lemma 5.8] it follows that

$$\chi_{\mathrm{HS}}(\mathcal{F}) = \left[\|\mathcal{F}\|_{\mathrm{HS}}^2 - 2\left(\|\mathcal{F}^{++}\|_{\mathrm{HS}} \|\mathcal{F}^{--}\|_{\mathrm{HS}} + \|\mathcal{F}^{+-}\|_{\mathrm{HS}} \|\mathcal{F}^{-+}\|_{\mathrm{HS}} \right) \right]^{1/2}.$$

Here, we can immediately conclude that $\chi_{\mathrm{HS}}(\mathcal{F})$ is bounded by $\|\mathcal{F}\|_{\mathrm{HS}}$. If a scatterer satisfies

$$\left[\mathcal{F}^{++} = 0 \quad \text{and} \quad \mathcal{F}^{-+} = 0\right] \qquad \text{or} \qquad \left[\mathcal{F}^{--} = 0 \quad \text{and} \quad \mathcal{F}^{+-} = 0\right],$$

then the maximum is attained. The reverse is also true, since (i) if the maximum is attained, there must hold that

$$\left[\mathcal{F}^{++} = 0 \quad \text{or} \quad \mathcal{F}^{--} = 0\right] \qquad \text{and} \qquad \left[\mathcal{F}^{+-} = 0 \quad \text{or} \quad \mathcal{F}^{-+} = 0\right],$$

and (ii) reciprocity implies $\mathcal{F}^{+-} = 0$ if and only if $\mathcal{F}^{-+} = 0$. A scatterer with $\chi_{\mathrm{HS}}(\mathcal{F}) = \|\mathcal{F}\|_{\mathrm{HS}}$ is called *maximally em-chiral* and it is effectively invisible to either fields of helicity $+1$ or -1. In [53, Lemma 5.11, Lemma 5.12], it is shown that χ_{HS} yields the same maximally em-chiral scatterers as χ and that $\chi(\mathcal{F}) = 0$ implies $\chi_{\mathrm{HS}}(\mathcal{F}) = 0$ for any $\mathcal{F} \in \mathrm{HS}(L_t^2(\mathbb{S}^2))$. It is desirable for many applications to have scatterers with χ_{HS} close to its theoretical maximum, which motivates us to find such objects through a shape optimization process. The idea is to employ Newton or quasi-Newton schemes to find scatterers with a high value of the ratio $\chi_{\mathrm{HS}}(\mathcal{F})/\|\mathcal{F}\|_{\mathrm{HS}}$. The

[21] Thomas Bayes (1701–1761)
[22] Pythagoras of Samos (ca. 570–ca. 495 BC)

following formula for the Fréchet derivative (cf. Definition 2.1) can be readily derived from [53, Lemma 5.15] and already has been used in [3, 43].

Lemma 2.32. *Let*

$$\mathcal{D} = \left\{ \mathcal{G} \in \mathrm{HS}(L_t^2(\mathbb{S}^2)) : \chi_{\mathrm{HS}}(\mathcal{G}) \neq 0,\ \|\mathcal{G}^{pq}\|_{\mathrm{HS}} \neq 0,\ p,q \in \{+,-\} \right\}$$

and assume $\mathcal{F} \in \mathcal{D}$. Then χ_{HS} is Fréchet differentiable (see Definition 2.1) at $\mathcal{F}$ with

$$\mathrm{d}\chi_{\mathrm{HS}}[\mathcal{F}]\mathcal{H} = \frac{1}{\chi_{\mathrm{HS}}(\mathcal{F})} \left(\mathrm{Re}\,\langle \mathcal{F}, \mathcal{H} \rangle_{\mathrm{HS}} - \sum_{p,q\in\{+,-\}} \mathrm{Re}\,\langle \mathcal{F}^{pq}, \mathcal{H}^{pq} \rangle_{\mathrm{HS}} \frac{\|\mathcal{F}^{(-p)(-q)}\|_{\mathrm{HS}}}{\|\mathcal{F}^{pq}\|_{\mathrm{HS}}} \right) \tag{2.64}$$

for all $\mathcal{H} \in \mathrm{HS}(L_t^2(\mathbb{S}^2))$.

2.7.2. Shape Reconstruction

In the following two Subsections, we briefly outline the two main problems that are of concern in the context of this thesis.

The first problem focuses on an inverse shape reconstruction, where we want to find an object's shape from the knowledge of the corresponding far-field data for one incident field $(\boldsymbol{E}^i, \boldsymbol{H}^i)$. Thus, the inverse problem reads as follows:

$$\left.\begin{array}{l} \text{Given some far-field data } \boldsymbol{E}^\infty_{\mathrm{data}} \text{ find the corresponding shape } \partial D \\ \text{such that } F(\partial D) = \boldsymbol{E}^\infty_{\mathrm{data}}\,. \end{array}\right\} \tag{2.65}$$

In Chapter 3, we establish the Fréchet differentiability with respect to variations of the surface ∂D for this map. In Chapter 5, we will consider these kind of problems, however, for specific tubular geometries, which will be introduced in Chapter 4.

2.7.3. Shape Optimization

In Chapter 6, we will treat an optimal design problem, in which we want to find shapes ∂D such that the em-chirality properties, described in Subsection 2.7.1, of the corresponding far-field operators are close to maximal. To indicate the dependence on ∂D, we denote by $\mathcal{F}$ the operator mapping an admissible boundary ∂D to a linear operator that maps $\boldsymbol{L}_t^2(\mathbb{S}^2)$ onto itself, i.e., we write

$$\mathcal{F}(\partial D)\colon L_t^2(\mathbb{S}^2) \to L_t^2(\mathbb{S}^2)\,, \qquad \mathcal{F}(\partial D)\boldsymbol{\varphi} = \boldsymbol{E}^\infty[\boldsymbol{\varphi}]\,.$$

In a slight abuse of notation, we call this operator far-field operator again. The optimization problem reads as follows:

$$\text{Find} \qquad \arg\min_{\partial D} \left[-\frac{\chi_{\mathrm{HS}}(\mathcal{F}(\partial D))}{\|\mathcal{F}(\partial D)\|_{\mathrm{HS}}} \right]. \tag{2.66}$$

In Chapter 3, we establish the Fréchet differentiability with respect to perturbations of the surface ∂D for the far-field operator. The differentiability will be carried over to the context of specific tubular geometries in Chapter 4.

CHAPTER 3

Domain Derivatives

In Chapters 5 and 6 we want to apply iterative methods to solve nonlinear equations of the types as in (2.65) and (2.66). These involve mappings of the types $F\colon \partial D \mapsto F(\partial D)$ and $\chi_{\mathrm{HS}} \circ \mathcal{F}$ with $\mathcal{F}\colon \partial D \mapsto \mathcal{F}(\partial D)$ (recall Definition 2.31 of the modified em-chirality measure χ_{HS}). Naturally, a linearization would be useful. Therefore, we are interested in a characterization of the Fréchet derivatives of F and $\mathcal{F}$ with respect to perturbations of the boundary ∂D (the derivative of χ_{HS} can be found in Lemma 2.32). This leads us to the notion of domain derivatives (or shape derivatives) of solutions of boundary value problems. These have been extensively used in literature regarding shape optimization and shape reconstruction problems. For an approach, where the underlying boundary integral equations of the scattering problems are differentiated with respect to perturbations of the boundary, we refer to [92] for the Helmholtz[1] equation and [93] for Maxwell's equations. We use the variational approach that was introduced for the Helmholtz equation in [66] for sound-soft scattering and generalized in [55, 56] for impedance and transmission conditions. For Maxwell's equations it has been studied in [57] for penetrable obstacles and in [52], [53, Chapter 3] for perfect conductors. Our aim is to extend the relevant results from [52, 53, 57] to establish the domain derivative for the operator $\mathcal{F}\colon \partial D \mapsto \mathcal{F}(\partial D)$. To achieve this objective, we first need to investigate the existing convergence results for the map $F\colon \partial D \mapsto F(\partial D)$ and obtain bounds that explicitly depend on the incident field.

We start by introducing some notations. Henceforward, let $D \subseteq \mathbb{R}^3$ be a C^1-smooth domain. Recall that by B_R we denote an open ball of radius $R > 0$ centered at zero and that $\Omega = B_R \setminus \overline{D}$. To quantify differences between domains appropriately, we restrict to geometric perturbations $\boldsymbol{h} \in \boldsymbol{C}^1(\mathbb{R}^3, \mathbb{R}^3)$ that are compactly supported in a neighborhood of ∂D with $\operatorname{supp} \boldsymbol{h} \subseteq B_R$ – which is always possible by choosing R suitably large. Moreover, we choose $\|\boldsymbol{h}\|_{\boldsymbol{C}^1}$ sufficiently small, such that the transformation

$$\boldsymbol{T}\colon D \to \mathbb{R}^3\,, \quad \boldsymbol{x} \mapsto \boldsymbol{T}(\boldsymbol{x}) \coloneqq \boldsymbol{x} + \boldsymbol{h}(\boldsymbol{x})\,,$$

is a diffeomorphism. Consequently, the perturbed domain $D_{\boldsymbol{h}} \coloneqq \boldsymbol{T}(D)$ constitutes again a bounded C^1-smooth domain with boundary $\partial D_{\boldsymbol{h}} = \boldsymbol{T}(\partial D)$ (cf. Figure 3.1).

Denote by J_f the Jacobian of a function f. We will need the following linearizations.

[1] Hermann Ludwig Ferdinand (von) Helmholtz (1821–1894)

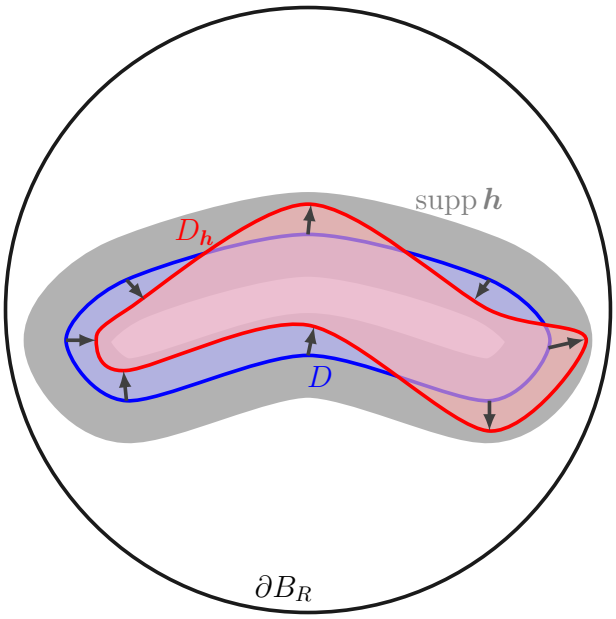

Figure 3.1. Perturbation $D_{\boldsymbol{h}}$ (red) of D (blue) by a sufficiently small vector field $\boldsymbol{h}$ (darkgray arrows) with $\operatorname{supp}\boldsymbol{h}$ (gray) in a neighborhood of ∂D; depicted in $\mathbb{R}^2$.

Lemma 3.1. *It holds that*

$$I - \frac{J_{\boldsymbol{T}}^\top J_{\boldsymbol{T}}}{\det J_{\boldsymbol{T}}} = -(J_{\boldsymbol{h}} + J_{\boldsymbol{h}}^\top - \operatorname{div}\boldsymbol{h}\, I) + \mathcal{O}(\|\boldsymbol{h}\|_{C^1}^2)\,, \tag{3.1a}$$

$$I - J_{\boldsymbol{T}}^{-1} J_{\boldsymbol{T}}^{-\top} \det J_{\boldsymbol{T}} = J_{\boldsymbol{h}} + J_{\boldsymbol{h}}^\top - \operatorname{div}\boldsymbol{h}\, I + \mathcal{O}(\|\boldsymbol{h}\|_{C^1}^2) \tag{3.1b}$$

as $\|\boldsymbol{h}\|_{C^1} \to 0$.

Proof. See, e.g., [53, Lemma 3.2]. ∎

We need to compare solutions $\boldsymbol{E}$ of (2.41) or (2.45) and $\boldsymbol{E}_{\boldsymbol{h}}$ of (2.41) or (2.45) with D replaced by $D_{\boldsymbol{h}}$. This is not directly possible, since the perturbation also changes the function space. Thus, instead of $\boldsymbol{E}_{\boldsymbol{h}}$ we consider the transformed $\boldsymbol{E}_{\boldsymbol{h}} \circ \boldsymbol{T}$. Having the weak formulation (2.41) or (2.45) in mind, a change of variables $\boldsymbol{x} \mapsto \boldsymbol{T}(\boldsymbol{x})$ also concerns $\mathbf{curl}\, \boldsymbol{E}_{\boldsymbol{h}}$. We use the approach of [82, Section 3.9], where it has been argued that the chain rule implies that we must use the transformation

$$\widehat{\boldsymbol{E}}_{\boldsymbol{h}} \coloneqq J_{\boldsymbol{T}}^\top (\boldsymbol{E}_{\boldsymbol{h}} \circ \boldsymbol{T})\,. \tag{3.2}$$

Reference [82, Lemma 3.57] shows that this transformation is indeed **curl**-conserving, i.e., $\boldsymbol{E}_{\boldsymbol{h}} \in \boldsymbol{H}(\mathbf{curl}, D_{\boldsymbol{h}})$ implies $\widehat{\boldsymbol{E}}_{\boldsymbol{h}} \in \boldsymbol{H}(\mathbf{curl}, D)$.

With (3.2), substituting $\boldsymbol{E}, \boldsymbol{V}, \Omega$ by perturbed $\boldsymbol{E}_{\boldsymbol{h}}, \boldsymbol{V}_{\boldsymbol{h}}, \Omega_{\boldsymbol{h}}$ and applying a change of variables $\boldsymbol{x} \mapsto \boldsymbol{T}(\boldsymbol{x})$, we eventually arrive at the following weak formulation for the perturbed problems (cf. [57, Section 3, eq. (9)] for penetrable obstacles and [53, Section 3.1] for perfect conductors):

Transmission problem: Find $\widehat{\boldsymbol{E}}_{\boldsymbol{h}} \in \boldsymbol{H}(\mathbf{curl}, B_R)$ such that

$$\int_{B_R} \left(\mathbf{curl}\, \widehat{\boldsymbol{E}}_{\boldsymbol{h}} \cdot \frac{J_{\boldsymbol{T}}^\top J_{\boldsymbol{T}}}{\det J_{\boldsymbol{T}}} \overline{\mathbf{curl}\, \boldsymbol{V}} - k^2 \widehat{\boldsymbol{E}}_{\boldsymbol{h}} \cdot J_{\boldsymbol{T}}^{-1} J_{\boldsymbol{T}}^{-\top} \overline{\boldsymbol{V}} \det J_{\boldsymbol{T}} \right) \mathrm{d}\boldsymbol{x} - \mathrm{i}\omega\mu \left\langle \boldsymbol{\Lambda}(\boldsymbol{\gamma}_t \widehat{\boldsymbol{E}}_{\boldsymbol{h}}), \boldsymbol{\gamma}_t \boldsymbol{V} \right\rangle_{t,\partial B_R}$$
$$= \mathrm{i}\omega\mu \left\langle \boldsymbol{\gamma}_N \boldsymbol{E}^i - \boldsymbol{\Lambda}(\boldsymbol{\gamma}_t \boldsymbol{E}^i), \boldsymbol{\gamma}_t \boldsymbol{V} \right\rangle_{t,\partial B_R} \qquad \text{for any } \boldsymbol{V} \in \boldsymbol{H}(\mathbf{curl}, B_R)\,. \quad (3.3)$$

Perfect conductor: Find $\widehat{\boldsymbol{E}}_{\boldsymbol{h}} \in \boldsymbol{H}_{\mathrm{pc}}(\mathbf{curl}, \Omega)$ such that

$$\int_{\Omega} \left(\mathbf{curl}\, \widehat{\boldsymbol{E}}_{\boldsymbol{h}} \cdot \frac{J_{\boldsymbol{T}}^\top J_{\boldsymbol{T}}}{\det J_{\boldsymbol{T}}} \overline{\mathbf{curl}\, \boldsymbol{V}} - k_+^2 \widehat{\boldsymbol{E}}_{\boldsymbol{h}} \cdot J_{\boldsymbol{T}}^{-1} J_{\boldsymbol{T}}^{-\top} \overline{\boldsymbol{V}} \det J_{\boldsymbol{T}} \right) \mathrm{d}\boldsymbol{x} - \mathrm{i}\omega\mu_+ \left\langle \boldsymbol{\Lambda}(\boldsymbol{\gamma}_t \widehat{\boldsymbol{E}}_{\boldsymbol{h}}), \boldsymbol{\gamma}_t \boldsymbol{V} \right\rangle_{t,\partial B_R}$$
$$= \mathrm{i}\omega\mu_+ \left\langle \boldsymbol{\gamma}_N \boldsymbol{E}^i - \boldsymbol{\Lambda}(\boldsymbol{\gamma}_t \boldsymbol{E}^i), \boldsymbol{\gamma}_t \boldsymbol{V} \right\rangle_{t,\partial B_R} \qquad \text{for any } \boldsymbol{V} \in \boldsymbol{H}_{\mathrm{pc}}(\mathbf{curl}, \Omega)\,. \quad (3.4)$$

Remark 3.2. Note that the right-hand sides of (3.3) and (3.4) are not affected by the perturbation due to $\boldsymbol{h}$ being compactly supported in a neighborhood of ∂D.

To cover both problems simultaneously, we introduce the following substitute symbols.

Definition 3.3. *Let $\mathfrak{X} \in \{B_R, \Omega\}$ as well as $\mathscr{H} \in \{\boldsymbol{H}(\mathbf{curl}, B_R), \boldsymbol{H}_{\mathrm{pc}}(\mathbf{curl}, \Omega)\}$. Henceforth, the pair $(\mathfrak{X}, \mathscr{H}) = (B_R, \boldsymbol{H}(\mathbf{curl}, B_R))$ corresponds to the transmission problem and the pair $(\mathfrak{X}, \mathscr{H}) = (\Omega, \boldsymbol{H}_{\mathrm{pc}}(\mathbf{curl}, \Omega))$ to the perfect conductor.*

For $\boldsymbol{U}$, $\boldsymbol{V} \in \mathscr{H}$ and admissible perturbations $\boldsymbol{h}$, we define the forms $\mathcal{A}, \mathcal{A}_{\boldsymbol{h}} \colon \mathscr{H} \times \mathscr{H} \to \mathbb{C}$ and $\ell \colon \mathscr{H} \to \mathbb{C}$ with

$$\mathcal{A}(\boldsymbol{U}, \boldsymbol{V}) \coloneqq \int_{\mathfrak{X}} \left(\mathbf{curl}\, \boldsymbol{U} \cdot \overline{\mathbf{curl}\, \boldsymbol{V}} - k^2\, \boldsymbol{U} \cdot \overline{\boldsymbol{V}} \right) \mathrm{d}\boldsymbol{x} - \mathrm{i}\omega\mu \left\langle \boldsymbol{\Lambda}(\boldsymbol{\gamma}_t \boldsymbol{U}), \boldsymbol{\gamma}_t \boldsymbol{V} \right\rangle_{t,\partial B_R},$$

$$\mathcal{A}_{\boldsymbol{h}}(\boldsymbol{U}, \boldsymbol{V}) \coloneqq \int_{\mathfrak{X}} \left(\mathbf{curl}\, \boldsymbol{U} \cdot \frac{J_{\boldsymbol{T}}^\top J_{\boldsymbol{T}}}{\det J_{\boldsymbol{T}}} \overline{\mathbf{curl}\, \boldsymbol{V}} - k^2\, \boldsymbol{U} \cdot J_{\boldsymbol{T}}^{-1} J_{\boldsymbol{T}}^{-\top} \overline{\boldsymbol{V}} \det J_{\boldsymbol{T}} \right) \mathrm{d}\boldsymbol{x}$$
$$- \mathrm{i}\omega\mu \left\langle \boldsymbol{\Lambda}(\boldsymbol{\gamma}_t \boldsymbol{U}), \boldsymbol{\gamma}_t \boldsymbol{V} \right\rangle_{t,\partial B_R},$$

$$\ell(\boldsymbol{V}) \coloneqq \mathrm{i}\omega\mu \left\langle \boldsymbol{\gamma}_N \boldsymbol{E}^i - \boldsymbol{\Lambda}(\boldsymbol{\gamma}_t \boldsymbol{E}^i), \boldsymbol{\gamma}_t \boldsymbol{V} \right\rangle_{t,\partial B_R}.$$

Note that $\mu = \mu_+$ and $k = k_+$ in $\Omega \subseteq \mathbb{R}^3 \setminus \overline{D}$. By this, the weak formulations (2.41), (2.45) become:

Find $\boldsymbol{E} \in \mathscr{H}$ such that

$$\mathcal{A}(\boldsymbol{E}, \boldsymbol{V}) = \ell(\boldsymbol{V}) \qquad \text{for all } \boldsymbol{V} \in \mathscr{H}\,. \quad (3.5)$$

Moreover, (3.3), (3.4) read as:

Find $\widehat{\boldsymbol{E}}_{\boldsymbol{h}} \in \mathscr{H}$ such that

$$\mathcal{A}_{\boldsymbol{h}}(\widehat{\boldsymbol{E}}_{\boldsymbol{h}}, \boldsymbol{V}) = \ell(\boldsymbol{V}) \qquad \text{for all } \boldsymbol{V} \in \mathscr{H} \text{ and all admissible perturbations } \boldsymbol{h}\,. \quad (3.6)$$

Problem (3.6) is also uniquely solvable for every admissible $\boldsymbol{h}$ (see [1, Lemma 4.3], [82, Theorem 10.7]). Note that due to the boundedness of the Calderón operator and the tangential trace

operators we find

$$\|\ell\|_{\mathscr{H}^*} \leq C\|\boldsymbol{E}^i\|_{\boldsymbol{H}(\mathbf{curl},\mathfrak{X})} \tag{3.7}$$

for every incident field $\boldsymbol{E}^i \in \boldsymbol{H}(\mathbf{curl},\mathfrak{X})$.

The Riesz[2] representation theorem [70, Theorem 4.10] implies the existence of bounded linear operators $A, A_{\boldsymbol{h}} \colon \mathscr{H} \to \mathscr{H}$ with

$$\mathcal{A}(\boldsymbol{E},\boldsymbol{V}) = (A\boldsymbol{E},\boldsymbol{V})_{\boldsymbol{H}(\mathbf{curl},\mathfrak{X})}\,, \qquad \mathcal{A}_{\boldsymbol{h}}(\widehat{\boldsymbol{E}}_{\boldsymbol{h}},\boldsymbol{V}) = (A_{\boldsymbol{h}}\widehat{\boldsymbol{E}}_{\boldsymbol{h}},\boldsymbol{V})_{\boldsymbol{H}(\mathbf{curl},\mathfrak{X})}$$

and $L \in \boldsymbol{H}(\mathbf{curl},\mathfrak{X})$ with $\ell(\boldsymbol{V}) = (L,\boldsymbol{V})_{\boldsymbol{H}(\mathbf{curl},\mathfrak{X})}$. With this, the weak formulations (3.5) and (3.6) are equivalent to the operator equations

$$A\boldsymbol{E} = L \qquad \text{and} \qquad A_{\boldsymbol{h}}\widehat{\boldsymbol{E}}_{\boldsymbol{h}} = L\,, \tag{3.8}$$

respectively. Both A and $A_{\boldsymbol{h}}$ have a bounded inverse, since (3.5) and (3.6) are uniquely solvable.

Next, we consider

$$\begin{aligned}\mathcal{A}(\widehat{\boldsymbol{E}}_{\boldsymbol{h}} - \boldsymbol{E},\boldsymbol{V}) &= \mathcal{A}(\widehat{\boldsymbol{E}}_{\boldsymbol{h}},\boldsymbol{V}) - \mathcal{A}(\boldsymbol{E},\boldsymbol{V}) = \mathcal{A}(\widehat{\boldsymbol{E}}_{\boldsymbol{h}},\boldsymbol{V}) - \mathcal{A}_{\boldsymbol{h}}(\widehat{\boldsymbol{E}}_{\boldsymbol{h}},\boldsymbol{V}) \\ &= \int_{\mathfrak{X}} \mathbf{curl}\,\widehat{\boldsymbol{E}}_{\boldsymbol{h}} \cdot \left(I - \frac{J_{\boldsymbol{T}}^\top J_{\boldsymbol{T}}}{\det J_{\boldsymbol{T}}}\right)\overline{\mathbf{curl}\,\boldsymbol{V}} - k^2\widehat{\boldsymbol{E}}_{\boldsymbol{h}} \cdot \left(I - J_{\boldsymbol{T}}^{-1}J_{\boldsymbol{T}}^{-\top}\det J_{\boldsymbol{T}}\right)\overline{\boldsymbol{V}}\,\mathrm{d}\boldsymbol{x}\,.\end{aligned}$$

Therefore, motivated by Lemma 3.1, we define the *material derivative* $\boldsymbol{W} \in \mathscr{H}$ of $\boldsymbol{E}$ with respect to the perturbation $\boldsymbol{h}$ by the unique solution in $\mathscr{H}$ of

$$\begin{aligned}\mathcal{A}(\boldsymbol{W},\boldsymbol{V}) = \int_{\mathfrak{X}} \Big[\mathbf{curl}\,\boldsymbol{E} \cdot \Big(-\Big(J_{\boldsymbol{T}} + J_{\boldsymbol{T}}^\top - \operatorname{div}\boldsymbol{h}\, I\Big)\Big)\overline{\mathbf{curl}\,\boldsymbol{V}} \\ - k^2\boldsymbol{E} \cdot \left(J_{\boldsymbol{T}} + J_{\boldsymbol{T}}^\top - \operatorname{div}\boldsymbol{h}\, I\right)\overline{\boldsymbol{V}}\Big]\,\mathrm{d}\boldsymbol{x}\end{aligned} \tag{3.9}$$

for all $\boldsymbol{V} \in \mathscr{H}$.

In the following lemmas, the assertions are obtained by thoroughly examining the proofs concerning the domain derivative in [53, 57], pursuing a more rigorous statement. There, the convergence has been shown; however, in view of the far-field operator, we need the bounds from the existing theory to be explicitly dependent on the incident field.

We begin with a result stating the continuous dependence of solutions on admissible perturbations $\boldsymbol{h}$ of D.

Lemma 3.4. *Let $\boldsymbol{E}$ be a solution of* (3.5) *and $\widehat{\boldsymbol{E}}_{\boldsymbol{h}}$ a solution of* (3.6)*. It holds that*

$$\big\|\widehat{\boldsymbol{E}}_{\boldsymbol{h}} - \boldsymbol{E}\big\|_{\boldsymbol{H}(\mathbf{curl},\mathfrak{X})} \leq C\,\|\boldsymbol{h}\|_{\boldsymbol{C}^1}\|\boldsymbol{E}^i\|_{\boldsymbol{H}(\mathbf{curl},\mathfrak{X})}\,.$$

Proof. Recall Remark 2.2. We see in the proofs of [57, Theorem 3.2] and [53, Theorem 3.3] that

$$\|A_{\boldsymbol{h}} - A\| \leq C\,\|\boldsymbol{h}\|_{\boldsymbol{C}^1} \tag{3.10}$$

[2] Frigyes Riesz (1880–1956)

is valid and use the boundedness of A^{-1} and (3.7) to obtain

$$\|\boldsymbol{E}\|_{\boldsymbol{H}(\mathbf{curl},\mathfrak{X})} = \|A^{-1}L\|_{\boldsymbol{H}(\mathbf{curl},\mathfrak{X})} \leq \|A^{-1}\|\,\|L\|_{\boldsymbol{H}(\mathbf{curl},\mathfrak{X})} \leq C\,\|\ell\|_{\mathscr{H}^*} \leq C\,\|\boldsymbol{E}^i\|_{\boldsymbol{H}(\mathbf{curl},\mathfrak{X})}\,. \quad (3.11)$$

Since $A_{\boldsymbol{h}}^{-1}$ is bounded for every admissible $\boldsymbol{h}$, we conclude with (3.8), (3.10), and (3.11) that

$$\begin{aligned}\|\widehat{\boldsymbol{E}}_{\boldsymbol{h}} - \boldsymbol{E}\|_{\boldsymbol{H}(\mathbf{curl},\mathfrak{X})} &= \|A_{\boldsymbol{h}}^{-1}A\boldsymbol{E} - A_{\boldsymbol{h}}^{-1}A_{\boldsymbol{h}}\boldsymbol{E}\|_{\boldsymbol{H}(\mathbf{curl},\mathfrak{X})} \leq \|A_{\boldsymbol{h}}^{-1}\|\,\|A - A_{\boldsymbol{h}}\|\,\|\boldsymbol{E}\|_{\boldsymbol{H}(\mathbf{curl},\mathfrak{X})} \\ &\leq C\,\|\boldsymbol{h}\|_{\boldsymbol{C}^1}\,\|\boldsymbol{E}^i\|_{\boldsymbol{H}(\mathbf{curl},\mathfrak{X})}\,.\end{aligned}$$

■

Furthermore, we have the following result regarding differentiability of solutions with respect to admissible perturbations $\boldsymbol{h}$ of D.

Lemma 3.5. *Let $\boldsymbol{E}$ be a solution of* (3.5)*, $\widehat{\boldsymbol{E}}_{\boldsymbol{h}}$ a solution of* (3.6) *and the material derivative $\boldsymbol{W}$ be defined as in* (3.9)*. Then,*

$$\|\widehat{\boldsymbol{E}}_{\boldsymbol{h}} - \boldsymbol{E} - \boldsymbol{W}\|_{\boldsymbol{H}(\mathbf{curl},\mathfrak{X})} \leq C\,\|\boldsymbol{h}\|_{\boldsymbol{C}^1}^2\|\boldsymbol{E}^i\|_{\boldsymbol{H}(\mathbf{curl},\mathfrak{X})}\,.$$

Proof. Recall Remark 2.2. From the proofs of [57, Theorem 3.3] and [53, Theorem 3.4], we obtain

$$\begin{aligned}&|\mathcal{A}(\widehat{\boldsymbol{E}}_{\boldsymbol{h}} - \boldsymbol{E} - \boldsymbol{W}, \boldsymbol{V})| \\ &\qquad \leq C\,\|\boldsymbol{h}\|_{\boldsymbol{C}^1}\Big(\|\boldsymbol{h}\|_{\boldsymbol{C}^1}\|\widehat{\boldsymbol{E}}_{\boldsymbol{h}}\|_{\boldsymbol{H}(\mathbf{curl},\mathfrak{X})} + \|\widehat{\boldsymbol{E}}_{\boldsymbol{h}} - \boldsymbol{E}\|_{\boldsymbol{H}(\mathbf{curl},\mathfrak{X})}\Big)\|\boldsymbol{V}\|_{\boldsymbol{H}(\mathbf{curl},\mathfrak{X})} \quad (3.12)\end{aligned}$$

for any $\boldsymbol{V} \in \mathscr{H}$. For every admissible $\boldsymbol{h}$, the Riesz representation theorem [70, Theorem 4.10] yields a unique bounded linear functional $\widehat{\ell}_{\boldsymbol{h}} \in \mathscr{H}^*$ such that $\widehat{\boldsymbol{E}}_{\boldsymbol{h}} - \boldsymbol{E} - \boldsymbol{W} \in \mathscr{H}$ uniquely solves

$$\mathcal{A}(\widehat{\boldsymbol{E}}_{\boldsymbol{h}} - \boldsymbol{E} - \boldsymbol{W}, \boldsymbol{V}) = \widehat{\ell}_{\boldsymbol{h}}(\boldsymbol{V}) \qquad \text{for all } \boldsymbol{V} \in \mathscr{H}\,.$$

Using (3.12), we conclude with the well-posedness of (3.5) that

$$\begin{aligned}\|\widehat{\boldsymbol{E}}_{\boldsymbol{h}} - \boldsymbol{E} - \boldsymbol{W}\|_{\boldsymbol{H}(\mathbf{curl},\mathfrak{X})} &\leq C\,\|\widehat{\ell}_{\boldsymbol{h}}\|_{\mathscr{H}^*} \\ &\leq C \sup_{\boldsymbol{V}\in\mathscr{H}\setminus\{\boldsymbol{0}\}} \frac{|\mathcal{A}(\widehat{\boldsymbol{E}}_{\boldsymbol{h}} - \boldsymbol{E} - \boldsymbol{W}, \boldsymbol{V})|}{\|\boldsymbol{V}\|_{\boldsymbol{H}(\mathbf{curl},\mathfrak{X})}} \\ &\leq C\,\|\boldsymbol{h}\|_{\boldsymbol{C}^1}\Big(\|\boldsymbol{h}\|_{\boldsymbol{C}^1}\|\widehat{\boldsymbol{E}}_{\boldsymbol{h}}\|_{\boldsymbol{H}(\mathbf{curl},\mathfrak{X})} + \|\widehat{\boldsymbol{E}}_{\boldsymbol{h}} - \boldsymbol{E}\|_{\boldsymbol{H}(\mathbf{curl},\mathfrak{X})}\Big) \\ &\leq C\,\|\boldsymbol{h}\|_{\boldsymbol{C}^1}\Big(\|\boldsymbol{h}\|_{\boldsymbol{C}^1}\|\boldsymbol{E}\|_{\boldsymbol{H}(\mathbf{curl},\mathfrak{X})} + (1 + \|\boldsymbol{h}\|_{\boldsymbol{C}^1})\|\widehat{\boldsymbol{E}}_{\boldsymbol{h}} - \boldsymbol{E}\|_{\boldsymbol{H}(\mathbf{curl},\mathfrak{X})}\Big)\,.\end{aligned}$$

Lemma 3.4 and (3.11) finally yield

$$\begin{aligned}\|\widehat{\boldsymbol{E}}_{\boldsymbol{h}} - \boldsymbol{E} - \boldsymbol{W}\|_{\boldsymbol{H}(\mathbf{curl},\mathfrak{X})} &\leq C\,\|\boldsymbol{h}\|_{\boldsymbol{C}^1}\Big(\|\boldsymbol{h}\|_{\boldsymbol{C}^1}\,\|\boldsymbol{E}^i\|_{\boldsymbol{H}(\mathbf{curl},\mathfrak{X})} + (1 + \|\boldsymbol{h}\|_{\boldsymbol{C}^1})\,\|\boldsymbol{h}\|_{\boldsymbol{C}^1}\,\|\boldsymbol{E}^i\|_{\boldsymbol{H}(\mathbf{curl},\mathfrak{X})}\Big) \\ &\leq C\,\|\boldsymbol{h}\|_{\boldsymbol{C}^1}^2\,\|\boldsymbol{E}^i\|_{\boldsymbol{H}(\mathbf{curl},\mathfrak{X})}\,.\end{aligned}$$

■

With this result and since $\boldsymbol{E} = (I + J_{\boldsymbol{0}}^{\top})\boldsymbol{E}_{\boldsymbol{0}}(\,\cdot + \boldsymbol{0}) = \widehat{\boldsymbol{E}}_{\boldsymbol{0}}$, the material derivative $\boldsymbol{W}$ is equal to the Fréchet derivative (cf. Definition 2.1) of the transformed field with respect to $\boldsymbol{h}$ at zero, i.e.,

$$\boldsymbol{W} = \mathrm{d}\widehat{\boldsymbol{E}}_{\boldsymbol{0}}\boldsymbol{h}\,.$$

Note that we keep the $\boldsymbol{0}$ in the index instead of using the square brackets as in Definition 2.1. Then, looking back at the definition of the material derivative $\boldsymbol{W}$ in (3.9), we see that $\boldsymbol{W}$ depends on $\boldsymbol{h}$ everywhere in $\mathfrak{X}$ and not only on the boundary ∂D, which is something we would expect from a shape derivative. In light of this, we use the statement of Lemma 3.5 and obtain

$$\begin{aligned}\widehat{\boldsymbol{E}}_{\boldsymbol{h}} &= \boldsymbol{E} + \boldsymbol{W} + \mathcal{O}(\|\boldsymbol{h}\|_{\boldsymbol{C}^1}^2)\\ &= \boldsymbol{E} + J_{\boldsymbol{E}}\boldsymbol{h} + J_{\boldsymbol{h}}^{\top}\boldsymbol{E} + (\boldsymbol{W} - J_{\boldsymbol{E}}\boldsymbol{h} - J_{\boldsymbol{h}}^{\top}\boldsymbol{E}) + \mathcal{O}(\|\boldsymbol{h}\|_{\boldsymbol{C}^1}^2)\,, \qquad \|\boldsymbol{h}\|_{\boldsymbol{C}^1} \to 0\,.\end{aligned}$$

It turns out that $\boldsymbol{W} - J_{\boldsymbol{E}}\boldsymbol{h} - J_{\boldsymbol{h}}^{\top}\boldsymbol{E}$ is a radiating solution of Maxwell's equations, which only depends on $\boldsymbol{h}|_{\partial D}$. Hence, we can extract a shape derivative $\boldsymbol{E}'$ defined by

$$\boldsymbol{E}' \coloneqq \boldsymbol{W} - J_{\boldsymbol{E}}\boldsymbol{h} - J_{\boldsymbol{h}}^{\top}\boldsymbol{E}\,, \tag{3.13}$$

which is referred to as the *domain derivative* of $\boldsymbol{E}$. Similarly, we define the domain derivative $\boldsymbol{H}'$ of $\boldsymbol{H}$.

Recall that by the subscript "$\boldsymbol{\nu}$" we indicate the normal component of a vector field. The next theorems show that (3.13) is indeed the appropriate choice to define the domain derivative. Here, in order to avoid notational confusion, we consider the domain derivatives for penetrable obstacles and perfect conductors separately again. For the former, we further introduce the following notation of jumps across the interface:

$$\begin{aligned}[\varphi]_{\partial D} &\coloneqq \varphi|_{\mathbb{R}^3\setminus\overline{D}} - \varphi|_D\,, \qquad \varphi \in \{\varepsilon, \mu\}\,,\\ [\boldsymbol{\gamma}_t\boldsymbol{\varphi}]_{\partial D} &\coloneqq \boldsymbol{\gamma}_t^{+}\boldsymbol{\varphi} - \boldsymbol{\gamma}_t^{-}\boldsymbol{\varphi}\,, \qquad \boldsymbol{\varphi} \in \boldsymbol{H}_{\mathrm{loc}}(\mathbf{curl}, \mathbb{R}^3 \setminus \overline{D}) \cup \boldsymbol{H}(\mathbf{curl}, D)\,.\end{aligned}$$

Theorem 3.6. *It holds that $\boldsymbol{E}', \boldsymbol{H}' \in \boldsymbol{H}(\mathbf{curl}, \Omega) \cup \boldsymbol{H}(\mathbf{curl}, D)$ and they can be uniquely extended to weak radiating solutions $\boldsymbol{E}', \boldsymbol{H}' \in \boldsymbol{H}_{\mathrm{loc}}(\mathbf{curl}, \mathbb{R}^3\setminus\overline{D}) \cup \boldsymbol{H}(\mathbf{curl}, D)$ of* (2.22a) *with transmission condition*

$$\left.\begin{aligned}[\boldsymbol{\gamma}_t\boldsymbol{E}']_{\partial D} &= \mathrm{i}\omega\,[\mu]_{\partial D}\,\boldsymbol{h}_{\boldsymbol{\nu}}\boldsymbol{\gamma}_T\boldsymbol{H} - [\mathbf{Curl}(\boldsymbol{h}_{\boldsymbol{\nu}}\boldsymbol{E}_{\boldsymbol{\nu}})]_{\partial D}\\ [\boldsymbol{\gamma}_t\boldsymbol{H}']_{\partial D} &= -\mathrm{i}\omega\,[\varepsilon]_{\partial D}\,\boldsymbol{h}_{\boldsymbol{\nu}}\boldsymbol{\gamma}_T\boldsymbol{E} - [\mathbf{Curl}(\boldsymbol{h}_{\boldsymbol{\nu}}\boldsymbol{H}_{\boldsymbol{\nu}})]_{\partial D}\end{aligned}\right\} \quad \text{on } \partial D\,, \tag{3.14}$$

where $\boldsymbol{E}$, $\boldsymbol{H}$ are the total fields in the original problem (2.22).

Proof. See [57, Theorem 4.1]. ∎

Theorem 3.7. *It holds that $\boldsymbol{E}', \boldsymbol{H}' \in \boldsymbol{H}(\mathbf{curl}, \Omega)$ and they can be uniquely extended to weak radiating solutions $\boldsymbol{E}', \boldsymbol{H}' \in \boldsymbol{H}_{\mathrm{loc}}(\mathbf{curl}, \mathbb{R}^3 \setminus \overline{D})$ of* (2.24a) *with boundary condition*

$$\boldsymbol{\gamma}_t\boldsymbol{E}' = \mathrm{i}\omega\mu_+\boldsymbol{h}_{\boldsymbol{\nu}}\,\boldsymbol{\gamma}_T\boldsymbol{H} - \mathbf{Curl}\,(\boldsymbol{h}_{\boldsymbol{\nu}}\boldsymbol{E}_{\boldsymbol{\nu}}) \qquad \text{on } \partial D\,, \tag{3.15}$$

where $\boldsymbol{E}$, $\boldsymbol{H}$ *are the total fields in the original problem* (2.24).

Proof. See [53, Theorem 3.6]. ■

Note that (2.43), (2.46) provide a variational formulation for the domain derivative from Theorems 3.6 and 3.7 with interface condition (3.14) and boundary condition (3.15), respectively.

Remark 3.8. We note some important observations:

(i) $\boldsymbol{E}'$ does only depend on the normal projection $\boldsymbol{h}_{\boldsymbol{\nu}}$ of the perturbation $\boldsymbol{h}$ on the boundary. The latter intuitively seems very plausible, since the domains under consideration are C^1-smooth, which means that their surface locally resembles the Euclidean plane $\mathbb{R}^2$. Here, tangential variations, i.e., variations along the plane itself, do not cause any change of the plane, resulting in an impact of solely the normal projection of such perturbations.

(ii) $\boldsymbol{E}'$ is *not* a Fréchet derivative anymore. However, below, we will show that the far-field pattern of $\boldsymbol{E}'$ is indeed the Fréchet derivative of the far-field map.

3.1. The Domain Derivative of the Far-Field Map

In this section, we apply the results from above to obtain the Fréchet derivative of a far-field map F for a fixed incident field (see Definition 2.21). We begin by providing a bound for the far-field pattern that depends on the corresponding field outside of the support of an admissible boundary perturbation $\boldsymbol{h}$.

Lemma 3.9. *We introduce another auxiliary ball* B_ϱ *centered at zero with radius* $\varrho > 0$ *such that* $(D \cup \operatorname{supp} \boldsymbol{h}) \subset B_\varrho \subset B_R$. *For any radiating solution of* (2.41) *or* (2.45) *it holds that*

$$\|\boldsymbol{E}^\infty\|_{\boldsymbol{L}_t^2(\mathbb{S}^2)} \leq C \|\boldsymbol{E}\|_{\boldsymbol{H}(\mathbf{curl}, B_R \setminus \overline{B_\varrho})} .$$

Proof. Recall the notation from Definition 3.3 and let $\boldsymbol{E}^s \in \mathscr{H}$ be a solution of (2.41) or (2.45) with incident field $\boldsymbol{E}^i \in \boldsymbol{H}_{\mathrm{loc}}(\mathbf{curl}, \mathbb{R}^3)$. In both cases, we can uniquely extend $\boldsymbol{E}^s$ to $\mathbb{R}^3 \setminus \overline{B_R}$. Particularly, it holds that $\boldsymbol{E}^i|_{\mathbb{R}^3 \setminus \overline{B_R}}, \boldsymbol{E}^s|_{\mathbb{R}^3 \setminus \overline{B_R}} \in \boldsymbol{H}_{\mathrm{loc}}(\mathbf{curl}, \mathbb{R}^3 \setminus \overline{B_R})$ in any case. Let $\boldsymbol{y} \in \mathbb{R}^3$ and denote the fundamental solution of the Helmholtz equation $\Delta u + k^2 u = 0$ in $\mathbb{R}^3 \setminus \{\boldsymbol{y}\}$ for the wave number k by

$$\Phi_k(\boldsymbol{x}, \boldsymbol{y}) \coloneqq \frac{\mathrm{e}^{\mathrm{i}k|\boldsymbol{x}-\boldsymbol{y}|}}{4\pi|\boldsymbol{x}-\boldsymbol{y}|}, \qquad \boldsymbol{x} \neq \boldsymbol{y} . \tag{3.16}$$

By the *Stratton–Chu*[3] *representation formula*, see [106, Section 8.14], for less regular fields [68, Theorem 5.49], we have for $\boldsymbol{x} \in \mathbb{R}^3 \setminus \overline{B_R}$ that

$$\boldsymbol{E}^s(\boldsymbol{x}) = -\operatorname{\mathbf{curl}} \langle \boldsymbol{\gamma}_t \boldsymbol{E}^s, \Phi(\boldsymbol{x}, \cdot) \rangle_{\partial B_R} + \frac{1}{\mathrm{i}\omega\varepsilon} \operatorname{\mathbf{curl}}^2 \langle \boldsymbol{\gamma}_t \boldsymbol{H}^s, \Phi(\boldsymbol{x}, \cdot) \rangle_{\partial B_R} \tag{3.17}$$

[3] Julius Adams Stratton (1901–1994), Lan Jen Chu (1913–1973)

and

$$0 = \mathbf{curl}\left\langle \boldsymbol{\gamma}_t \boldsymbol{E}^i, \Phi(\boldsymbol{x},\cdot)\right\rangle_{\partial B_R} - \frac{1}{\mathrm{i}\omega\varepsilon}\,\mathbf{curl}^2\left\langle \boldsymbol{\gamma}_t \boldsymbol{H}^i, \Phi(\boldsymbol{x},\cdot)\right\rangle_{\partial B_R}. \tag{3.18}$$

Thus, substracting (3.18) from (3.17), we obtain

$$\boldsymbol{E}^s(\boldsymbol{x}) = -\,\mathbf{curl}\,\langle \boldsymbol{\gamma}_t \boldsymbol{E}, \Phi(\boldsymbol{x},\cdot)\rangle_{\partial B_R} + \frac{1}{\mathrm{i}\omega\varepsilon}\,\mathbf{curl}^2\,\langle \boldsymbol{\gamma}_t \boldsymbol{H}, \Phi(\boldsymbol{x},\cdot)\rangle_{\partial B_R}.$$

As in [31, Theorem 6.9], we obtain the following representation for the far-field pattern:

$$\boldsymbol{E}^\infty(\widehat{\boldsymbol{x}}) = \mathrm{i}k_+\left\langle \left(\boldsymbol{\gamma}_t \boldsymbol{E} + \boldsymbol{\gamma}_t \boldsymbol{H}\times\widehat{\boldsymbol{x}}\right), \boldsymbol{y}\mapsto \mathrm{e}^{-\mathrm{i}k_+\widehat{\boldsymbol{x}}\cdot\boldsymbol{y}}\right\rangle_{\partial B_R}\times\widehat{\boldsymbol{x}}\,.$$

We conclude with $\boldsymbol{\gamma}_t\boldsymbol{E}, \boldsymbol{\gamma}_t\boldsymbol{H} \in \boldsymbol{H}^{-1/2}(\mathrm{Div}, \partial B_R)$, $\boldsymbol{y}\mapsto \mathrm{e}^{\mathrm{i}k\widehat{\boldsymbol{x}}\cdot\boldsymbol{y}} \in \boldsymbol{H}^{-1/2}(\mathrm{Curl}, \partial B_R)$, $\widehat{\boldsymbol{x}}\in\mathbb{S}^2$ – and by using the triangle inequality – that

$$\|\boldsymbol{E}^\infty\|_{\boldsymbol{L}^2_t(\mathbb{S}^2)} \le C\left(\|\boldsymbol{\gamma}_t\boldsymbol{E}\|_{\boldsymbol{H}^{-1/2}(\mathrm{Div},\partial B_R)} + \|\boldsymbol{\gamma}_t\boldsymbol{H}\|_{\boldsymbol{H}^{-1/2}(\mathrm{Div},\partial B_R)}\right). \tag{3.19}$$

Using [24, p.109, Prop. 23], we obtain

$$\|\boldsymbol{\gamma}_t\boldsymbol{H}\|_{\boldsymbol{H}^{-1/2}(\mathrm{Div},\partial B_R)} \le C\,\|\boldsymbol{\gamma}_t\boldsymbol{E}\|_{\boldsymbol{H}^{-1/2}(\mathrm{Div},\partial B_R)}.$$

Hence, with the boundedness of $\boldsymbol{\gamma}_t\colon \boldsymbol{H}(\,\mathbf{curl}, B_R\setminus\overline{B_\varrho}) \to \boldsymbol{H}^{-1/2}(\mathrm{Div}, \partial B_R\cup\partial B_\varrho)$, we conclude

$$\|\boldsymbol{E}^\infty\|_{\boldsymbol{L}^2_t(\mathbb{S}^2)} \le C\|\boldsymbol{\gamma}_t\boldsymbol{E}\|_{\boldsymbol{H}^{-1/2}(\mathrm{Div},\partial B_R)} \le C\|\boldsymbol{E}\|_{\boldsymbol{H}(\mathbf{curl},B_R\setminus\overline{B_\varrho})}.$$

■

Next, we infer Fréchet differentiability of the far-field map and give a bound that explicitly depends on the incident field.

Corollary 3.10. *It holds that*

$$\|F(\partial D_{\boldsymbol{h}}) - F(\partial D) - (\boldsymbol{E}')^\infty\|_{\boldsymbol{L}^2_t(\mathbb{S}^2)} \le C\,\|\boldsymbol{h}\|^2_{C^1}\,\|\boldsymbol{E}^i\|_{\boldsymbol{H}(\mathbf{curl},\Omega)},$$

i.e., the far-field map $\partial D \mapsto F(\partial D) \in \boldsymbol{L}^2_t(\mathbb{S}^2)$ is Fréchet differentiable at ∂D with Fréchet derivative $F'[\partial D]\boldsymbol{h} = (\boldsymbol{E}')^\infty \in \boldsymbol{L}^2_t(\mathbb{S}^2)$.

Proof. Recall Remark 2.2. Even thought the material derivative $\boldsymbol{W}$ is not a solution of (2.41) or (2.45) in the entire exterior of D, it coincides with the domain derivative $\boldsymbol{E}' = \boldsymbol{W} - J_{\boldsymbol{E}}\boldsymbol{h} - J_{\boldsymbol{h}}^\top\boldsymbol{E}$ in the exterior of $D\cup\operatorname{supp}\boldsymbol{h}$, since $\boldsymbol{h}$ is compactly supported in a neighborhood of ∂D. Hence, $\boldsymbol{W}$ is a solution of (2.41) or (2.45) in $\mathbb{R}^3\setminus(\overline{D}\cup\operatorname{supp}\boldsymbol{h})$. Consequently, we obtain the far-field pattern $\boldsymbol{W}^\infty = (\boldsymbol{E}')^\infty$ of $\boldsymbol{W}$.

Furthermore, as in Lemma 3.9, we introduce another auxiliary ball B_ϱ centered at zero with radius $\varrho > 0$ such that $(D\cup\operatorname{supp}\boldsymbol{h}) \subset B_\varrho \subset B_R$. Naturally, $\boldsymbol{E}'$ and $\boldsymbol{W}$ also coincide in the exterior of B_ϱ.

Since $\widehat{\boldsymbol{E}}_{\boldsymbol{h}}, \boldsymbol{E}$ and $\boldsymbol{E}'$ are solutions to (3.6), (3.5) and (2.22) with interface condition (3.14) or (2.24) with boundary condition (3.15), respectively, $\widehat{\boldsymbol{E}}_{\boldsymbol{h}} - \boldsymbol{E} - \boldsymbol{E}'$ is also a solution in both cases. Hence, Lemma 3.9 implies

$$\begin{aligned}\|\widehat{\boldsymbol{E}}_{\boldsymbol{h}}^{\infty} - \boldsymbol{E}^{\infty} - (\boldsymbol{E}')^{\infty}\|_{\boldsymbol{L}_t^2(\mathbb{S}^2)} &\leq C\|\widehat{\boldsymbol{E}}_{\boldsymbol{h}} - \boldsymbol{E} - \boldsymbol{E}'\|_{\boldsymbol{H}(\mathbf{curl},B_R\setminus\overline{B_\varrho})} \\ &= C\|\widehat{\boldsymbol{E}}_{\boldsymbol{h}} - \boldsymbol{E} - \boldsymbol{W}\|_{\boldsymbol{H}(\mathbf{curl},B_R\setminus\overline{B_\varrho})} \leq C\|\widehat{\boldsymbol{E}}_{\boldsymbol{h}} - \boldsymbol{E} - \boldsymbol{W}\|_{\boldsymbol{H}(\mathbf{curl},\Omega)}\,.\end{aligned}$$

Consequently, with Lemma 3.5 and since $F(\partial D_{\boldsymbol{h}}) = \widehat{\boldsymbol{E}}_{\boldsymbol{h}}^{\infty}$, $F(\partial D) = \boldsymbol{E}^{\infty}$, we have

$$\|F(\partial D_{\boldsymbol{h}}) - F(\partial D) - (\boldsymbol{E}')^{\infty}\|_{\boldsymbol{L}_t^2(\mathbb{S}^2)} \leq C\,\|\boldsymbol{h}\|_{C^1}^2\,\|\boldsymbol{E}^i\|_{\boldsymbol{H}(\mathbf{curl},\Omega)}\,.$$

■

3.2. The Domain Derivative of the Far-Field Operator

We now turn to the differentiability of the far-field operator $\partial D \mapsto \mathcal{F}(\partial D)$ described in Subsection 2.7.3. Our aim is to show that

$$\|\mathcal{F}(\partial D_{\boldsymbol{h}}) - \mathcal{F}(\partial D) - \mathcal{F}'[\partial D]\boldsymbol{h}\|_{\mathrm{HS}} \leq C\,\|\boldsymbol{h}\|_{\boldsymbol{C}^1}^2\,,$$

where $\mathcal{F}'[\partial D]\boldsymbol{h}$ is equal to the bounded linear operator $\boldsymbol{\varphi} \mapsto (\boldsymbol{E}'[\boldsymbol{\varphi}])^{\infty}$ in $\mathrm{HS}(\boldsymbol{L}_t^2(\mathbb{S}^2))$. For this purpose, we prove some requisites.

Lemma 3.11. *Let $\boldsymbol{\varphi} \in \boldsymbol{L}_t^2(\mathbb{S}^2)$ be a density. It holds that*

$$\|\mathcal{F}(\partial D_{\boldsymbol{h}})\boldsymbol{\varphi} - \mathcal{F}(\partial D)\boldsymbol{\varphi} - (\boldsymbol{E}'[\boldsymbol{\varphi}])^{\infty}\|_{\boldsymbol{L}_t^2(\mathbb{S}^2)} \leq C\,\|\boldsymbol{h}\|_{\boldsymbol{C}^1}^2\,\|\boldsymbol{E}^i[\boldsymbol{\varphi}]\|_{\boldsymbol{H}(\mathbf{curl},\Omega)}\,.$$

Proof. Let $\boldsymbol{\varphi} \in \boldsymbol{L}_t^2(\mathbb{S}^2)$. Then the assertion follows directly from Corollary 3.10. ■

Next, we introduce the *spherical harmonics* $Y_n^m \in L^2(\mathbb{S}^2)$ for $n \in \mathbb{N}_0,\ m \in \mathbb{Z},\ |m| \leq n$, which form a complete orthonormal system

$$\{Y_n^m : n \in \mathbb{N}_0\,,\ m \in \mathbb{Z}\,,\ |m| \leq n\}$$

in $L^2(\mathbb{S}^2)$, see [84, Theorem 2.4.1]. Based on the spherical harmonics, we define the *vector spherical harmonics* $\boldsymbol{U}_n^m, \boldsymbol{V}_n^m \in \boldsymbol{L}_t^2(\mathbb{S}^2)$ by

$$\boldsymbol{U}_n^m(\widehat{\boldsymbol{x}}) := \frac{1}{\sqrt{n(n+1)}}\,\boldsymbol{\nabla}_{\mathbb{S}^2}\,Y_n^m(\widehat{\boldsymbol{x}})\,, \qquad \boldsymbol{V}_n^m(\widehat{\boldsymbol{x}}) := \widehat{\boldsymbol{x}} \times \boldsymbol{U}_n^m(\widehat{\boldsymbol{x}})\,, \tag{3.20}$$

for $\widehat{\boldsymbol{x}} \in \mathbb{S}^2$, $n \in \mathbb{N}$, $m \in \mathbb{Z}$, $|m| \leq n$, which form a complete orthonormal system

$$\mathscr{B} := \{\boldsymbol{U}_n^m\,,\ \boldsymbol{V}_n^m : n \in \mathbb{N}\,,\ m \in \mathbb{Z}\,,\ |m| \leq n\} \tag{3.21}$$

in $\boldsymbol{L}_t^2(\mathbb{S}^2)$, see [82, Lemma 9.15]. In view of (2.62), we consider the system $\mathscr{B}$ and conclude the following result.

Corollary 3.12. *It holds that*

$$\|\mathcal{F}(\partial D_{\boldsymbol{h}}) - \mathcal{F}(\partial D) - (\boldsymbol{E}'[\,\cdot\,])^{\infty}\|_{\mathrm{HS}}^2 \leq C\|\boldsymbol{h}\|_{\boldsymbol{C}^1}^4 \left(\sum_{n=1}^{\infty} \sum_{m=-n}^{n} \|\boldsymbol{E}^i[\boldsymbol{U}_n^m]\|_{\boldsymbol{L}^2(B_R)}^2 + \|\boldsymbol{E}^i[\boldsymbol{V}_n^m]\|_{\boldsymbol{L}^2(B_R)}^2 \right),$$

if the series on the right-hand side converges.

Proof. From (2.61) and Lemma 3.11 we conclude

$$\begin{aligned}
&\|\mathcal{F}(\partial D_{\boldsymbol{h}}) - \mathcal{F}(\partial D) - (\boldsymbol{E}'[\,\cdot\,])^{\infty}\|_{\mathrm{HS}}^2 \\
&\qquad = \sum_{n=1}^{\infty} \sum_{m=-n}^{n} \| \left(\mathcal{F}(\partial D_{\boldsymbol{h}}) - \mathcal{F}(\partial D) - (\boldsymbol{E}'[\,\cdot\,])^{\infty}\right) \boldsymbol{U}_n^m \|_{\boldsymbol{L}_t^2(\mathbb{S}^2)}^2 \\
&\qquad\qquad + \| \left(\mathcal{F}(\partial D_{\boldsymbol{h}}) - \mathcal{F}(\partial D) - (\boldsymbol{E}'[\,\cdot\,])^{\infty}\right) \boldsymbol{V}_n^m \|_{\boldsymbol{L}_t^2(\mathbb{S}^2)}^2 \\
&\qquad \leq C\|\boldsymbol{h}\|_{\boldsymbol{C}^1}^4 \left(\sum_{n=1}^{\infty} \sum_{m=-n}^{n} \|\boldsymbol{E}^i[\boldsymbol{U}_n^m]\|_{\boldsymbol{H}(\mathbf{curl},B_R)}^2 + \|\boldsymbol{E}^i[\boldsymbol{V}_n^m]\|_{\boldsymbol{H}(\mathbf{curl},B_R)}^2 \right).
\end{aligned}$$

Moreover, for $\boldsymbol{d} \in \mathbb{S}^2$, we have

$$\mathbf{curl}\left(\boldsymbol{U}_n^m(\boldsymbol{d})\,\mathrm{e}^{\mathrm{i}k\boldsymbol{x}\cdot\boldsymbol{d}}\right) = \boldsymbol{\nabla}\mathrm{e}^{\mathrm{i}k\boldsymbol{x}\cdot\boldsymbol{d}} \times \boldsymbol{U}_n^m(\boldsymbol{d}) = \mathrm{i}k\,\boldsymbol{V}_n^m(\boldsymbol{d})\,\mathrm{e}^{\mathrm{i}k\boldsymbol{x}\cdot\boldsymbol{d}}$$

and analogously

$$\mathbf{curl}\left(\boldsymbol{V}_n^m(\boldsymbol{d})\,\mathrm{e}^{\mathrm{i}k\boldsymbol{x}\cdot\boldsymbol{d}}\right) = -\mathrm{i}k\,\boldsymbol{U}_n^m(\boldsymbol{d})\,\mathrm{e}^{\mathrm{i}k\boldsymbol{x}\cdot\boldsymbol{d}}.$$

Thus, it holds that

$$\mathbf{curl}\,\boldsymbol{E}^i[\boldsymbol{U}_n^m] = \mathrm{i}k\,\boldsymbol{E}^i[\boldsymbol{V}_n^m], \qquad \mathbf{curl}\,\boldsymbol{E}^i[\boldsymbol{V}_n^m] = -\mathrm{i}k\,\boldsymbol{E}^i[\boldsymbol{U}_n^m], \tag{3.22}$$

by which the assertion immediately follows. ∎

By Corollary 3.12, it remains to show convergence of

$$\left(\sum_{n=1}^{\infty} \sum_{m=-n}^{n} \|\boldsymbol{E}^i[\boldsymbol{U}_n^m]\|_{\boldsymbol{L}^2(B_R)}^2 \right) \qquad \text{as well as} \qquad \left(\sum_{n=1}^{\infty} \sum_{m=-n}^{n} \|\boldsymbol{E}^i[\boldsymbol{V}_n^m]\|_{\boldsymbol{L}^2(B_R)}^2 \right). \tag{3.23}$$

We will achieve this by explicitly calculating these norms through expansions into vector wave functions. To define the latter, we first denote by j_n and y_n the spherical Bessel[4] functions of the first and second kind and order $n \in \mathbb{N}_0$. The spherical Hankel[5] function of the first kind and order n is then defined by $h_n^{(1)} := j_n + \mathrm{i}y_n$. Furthermore, for $n \in \mathbb{N}_0,\ m \in \mathbb{Z},\ |m| \leq n$, we introduce u_n^m, v_n^m by

$$u_n^m(\boldsymbol{x}) := j_n(kr)\,Y_n^m(\widehat{\boldsymbol{x}}), \qquad v_n^m(\boldsymbol{x}) := h_n^{(1)}(kr)\,Y_n^m(\widehat{\boldsymbol{x}}), \qquad \boldsymbol{x} \in \mathbb{R}^3.$$

[4] Friedrich Wilhelm Bessel (1784–1846)
[5] Hermann Hankel (1839–1873)

Then, for $n \in \mathbb{N},\ m \in \mathbb{Z},\ |m| \leq n$, the *spherical vector wave functions* are defined by

$$\boldsymbol{M}_n^m(\boldsymbol{x}) \coloneqq -j_n(kr)\,\boldsymbol{V}_n^m(\widehat{\boldsymbol{x}})\,, \qquad \boldsymbol{N}_n^m(\boldsymbol{x}) \coloneqq -h_n^{(1)}(kr)\,\boldsymbol{V}_n^m(\widehat{\boldsymbol{x}})\,, \qquad \boldsymbol{x} \in \mathbb{R}^3\,. \tag{3.24}$$

$\boldsymbol{M}_n^m$ and $1/(\mathrm{i}k)\,\mathbf{curl}\,\boldsymbol{M}_n^m$ are solutions of the time-harmonic Maxwell system in $\mathbb{R}^3$ and $\boldsymbol{N}_n^m$ and $1/(\mathrm{i}k)\,\mathbf{curl}\,\boldsymbol{N}_n^m$ are radiating solutions in $\mathbb{R}^3 \setminus \{0\}$, see [31, Theorem 6.26]. In what follows, we will always represent $\boldsymbol{x} \in \mathbb{R}^3$ as $\boldsymbol{x} = r\widehat{\boldsymbol{x}}$ with $\widehat{\boldsymbol{x}} \in \mathbb{S}^2$ and $r \coloneqq |\boldsymbol{x}| > 0$. Moreover, we set

$$\boldsymbol{W}_n^m(\widehat{\boldsymbol{x}}) \coloneqq Y_n^m(\widehat{\boldsymbol{x}})\widehat{\boldsymbol{x}}\,, \qquad \widehat{\boldsymbol{x}} \in \mathbb{S}^2\,,\ n \in \mathbb{N}\,,\ m \in \mathbb{Z}\,,\ |m| \leq n\,. \tag{3.25}$$

Lemma 3.13. *For any $\boldsymbol{x} = r\widehat{\boldsymbol{x}} \in \mathbb{R}^3$ and $n \in \mathbb{N}$, $m \in \mathbb{Z}$, $|m| \leq n$, there hold*

$$\begin{aligned}
\boldsymbol{E}^i[\boldsymbol{U}_n^m](\boldsymbol{x}) &= 4\pi\mathrm{i}^n\,\frac{1}{\mathrm{i}kr}\left(\sqrt{n(n+1)}\,j_n(kr)\,\boldsymbol{W}_n^m(\widehat{\boldsymbol{x}}) + \frac{\mathrm{d}}{\mathrm{d}r}(rj_n(kr))\,\boldsymbol{U}_n^m(\widehat{\boldsymbol{x}})\right),\\
\boldsymbol{E}^i[\boldsymbol{V}_n^m](\boldsymbol{x}) &= 4\pi\mathrm{i}^n\,j_n(kr)\,\boldsymbol{V}_n^m(\widehat{\boldsymbol{x}})\,.
\end{aligned}$$

Proof. Let $n \in \mathbb{N}$, $m \in \mathbb{Z}$, $|m| \leq n$. With [31, Theorem 6.28], we compute the far-field patterns of $\boldsymbol{N}_n^m$ and $\mathbf{curl}\,\boldsymbol{N}_n^m$ by

$$\boldsymbol{N}_n^{m,\infty} = -\frac{4\pi}{k\mathrm{i}^{n+1}}\,\boldsymbol{V}_n^m \qquad \text{and} \qquad (\mathbf{curl}\,\boldsymbol{N}_n^m)^\infty = \frac{4\pi}{\mathrm{i}^n}\,\boldsymbol{U}_n^m\,, \tag{3.26}$$

respectively. Moreover, we consider the gradient in spherical coordinates and use the recurrence relation [79, Equation 10.51.2], obtaining

$$\begin{aligned}
\boldsymbol{\nabla} v_n^m(\boldsymbol{x}) &= \frac{\partial v_n^m(\boldsymbol{x})}{\partial r}\widehat{\boldsymbol{x}} + \frac{1}{r}\,\boldsymbol{\nabla}_{\mathbb{S}^2}\,v_n^m(\boldsymbol{x}) = kh_n^{(1)\prime}(kr)\,\boldsymbol{W}_n^m(\widehat{\boldsymbol{x}}) + \frac{1}{r}h_n^{(1)}(kr)\,\boldsymbol{U}_n^m(\widehat{\boldsymbol{x}})\\
&= \left(-kh_{n+1}^{(1)}(kr) - \frac{n}{r}h_n^{(1)}(kr)\right)\boldsymbol{W}_n^m(\widehat{\boldsymbol{x}}) + \frac{1}{r}h_n^{(1)}(kr)\,\boldsymbol{U}_n^m(\widehat{\boldsymbol{x}})\,.
\end{aligned}$$

With [28, Theorem 2.15], the far-field pattern of $\boldsymbol{x} \mapsto h_{n+1}^{(1)}(k|\boldsymbol{x}|)\,Y_n^m(\widehat{\boldsymbol{x}})$ is given by

$$\left(h_{n+1}^{(1)}(k|\cdot|)\,Y_n^m\left(\frac{\cdot}{|\cdot|}\right)\right)^\infty(\widehat{\boldsymbol{x}}) = \frac{4\pi}{k\mathrm{i}^{n+2}}\,Y_n^m(\widehat{\boldsymbol{x}}) = -\frac{4\pi}{k\mathrm{i}^n}\,Y_n^m(\widehat{\boldsymbol{x}})\,, \qquad \widehat{\boldsymbol{x}} \in \mathbb{S}^2\,.$$

Therefore, we infer that

$$(\boldsymbol{\nabla} v_n^m)^\infty(\widehat{\boldsymbol{x}}) = \frac{4\pi}{\mathrm{i}^n}\,\boldsymbol{W}_n^m(\widehat{\boldsymbol{x}})\,, \qquad \widehat{\boldsymbol{x}} \in \mathbb{S}^2\,. \tag{3.27}$$

Next, recall the definition of the fundamental solution Φ_k of the Helmholtz equation, see (3.16). We consider the *vector addition theorem* in the form of [31, Equation (6.83)] and obtain for any

$\boldsymbol{A} \in \mathbb{C}^3$ that

$$\left.\begin{aligned}\Phi_k(\boldsymbol{x},\boldsymbol{y})\boldsymbol{A} = \mathrm{i}k \sum_{n=1}^{\infty}\sum_{m=-n}^{n} (\boldsymbol{N}_n^m(\boldsymbol{y})\cdot\boldsymbol{A})\,\overline{\boldsymbol{M}_n^m(\boldsymbol{x})} \\ + \frac{\mathrm{i}}{k}\sum_{n=1}^{\infty}\sum_{m=-n}^{n} (\mathbf{curl}\,\boldsymbol{N}_n^m(\boldsymbol{y})\cdot\boldsymbol{A})\,\overline{\mathbf{curl}\,\boldsymbol{M}_n^m(\boldsymbol{x})} \\ + \frac{\mathrm{i}}{k}\sum_{n=1}^{\infty}\sum_{m=-n}^{n} (\boldsymbol{\nabla} v_n^m(\boldsymbol{y})\cdot\boldsymbol{A})\,\overline{\boldsymbol{\nabla} u_n^m(\boldsymbol{x})}\,.\end{aligned}\right\} \tag{3.28}$$

We consider the far-field patterns of the left- and right-hand side of (3.28). With (3.26) and (3.27), this results in

$$\left.\begin{aligned}\boldsymbol{A}\mathrm{e}^{-\mathrm{i}k\boldsymbol{x}\cdot\boldsymbol{d}} = -4\pi\sum_{n=1}^{\infty}\sum_{m=-n}^{n}\frac{1}{\mathrm{i}^n}\,\overline{\boldsymbol{M}_n^m(\boldsymbol{x})}\boldsymbol{V}_n^m(\boldsymbol{d})\cdot\boldsymbol{A} \\ + 4\pi\sum_{n=1}^{\infty}\sum_{m=-n}^{n}\frac{1}{\mathrm{i}^n}\left(\overline{\frac{1}{\mathrm{i}k}\,\mathbf{curl}\,\boldsymbol{M}_n^m(\boldsymbol{x})}\right)\boldsymbol{U}_n^m(\boldsymbol{d})\cdot\boldsymbol{A} \\ + 4\pi\sum_{n=1}^{\infty}\sum_{m=-n}^{n}\frac{1}{k\,\mathrm{i}^{n-1}}\,\overline{\boldsymbol{\nabla} u_n^m(\boldsymbol{x})}\,\boldsymbol{W}_n^m(\boldsymbol{d})\cdot\boldsymbol{A}\,.\end{aligned}\right\} \tag{3.29}$$

Next, we substitute $\boldsymbol{A} = \boldsymbol{\varphi}(\boldsymbol{d})$, $\boldsymbol{\varphi} \in L_t^2(\mathbb{S}^2)$, and take the complex conjugate of equation (3.29). This yields

$$\boldsymbol{\varphi}(\boldsymbol{d})\mathrm{e}^{\mathrm{i}k\boldsymbol{x}\cdot\boldsymbol{d}} = 4\pi\sum_{n=1}^{\infty}\sum_{m=-n}^{n}\mathrm{i}^n\left(\frac{1}{\mathrm{i}k}\,\mathbf{curl}\,\boldsymbol{M}_n^m(\boldsymbol{x})\left(\overline{\boldsymbol{U}_n^m(\boldsymbol{d})}\cdot\boldsymbol{\varphi}(\boldsymbol{d})\right) - \boldsymbol{M}_n^m(\boldsymbol{x})\left(\overline{\boldsymbol{V}_n^m(\boldsymbol{d})}\cdot\boldsymbol{\varphi}(\boldsymbol{d})\right)\right).$$

Then, we integrate over $\mathbb{S}^2$ with respect to $\boldsymbol{d}$, obtaining

$$\int_{\mathbb{S}^2}\boldsymbol{\varphi}(\boldsymbol{d})\mathrm{e}^{\mathrm{i}k\boldsymbol{x}\cdot\boldsymbol{d}}\,\mathrm{d}s(\boldsymbol{d}) = 4\pi\sum_{n=1}^{\infty}\sum_{m=-n}^{n}\mathrm{i}^n\left(\frac{1}{\mathrm{i}k}\,\mathbf{curl}\,\boldsymbol{M}_n^m(\boldsymbol{x})\,(\boldsymbol{\varphi},\boldsymbol{U}_n^m)_{L_t^2(\mathbb{S}^2)} - \boldsymbol{M}_n^m(\boldsymbol{x})\,(\boldsymbol{\varphi},\boldsymbol{V}_n^m)_{L_t^2(\mathbb{S}^2)}\right).$$

Considering $\boldsymbol{\varphi} = \boldsymbol{U}_n^m$ or $\boldsymbol{\varphi} = \boldsymbol{V}_n^m$, we infer by Definition 2.24 of electric Herglotz waves that

$$\left.\begin{aligned}\boldsymbol{E}^i[\boldsymbol{U}_n^m](\boldsymbol{x}) = 4\pi\mathrm{i}^n\,\frac{1}{\mathrm{i}k}\,\mathbf{curl}\,\boldsymbol{M}_n^m(\boldsymbol{x}) \\ \boldsymbol{E}^i[\boldsymbol{V}_n^m](\boldsymbol{x}) = -4\pi\mathrm{i}^n\,\boldsymbol{M}_n^m(\boldsymbol{x})\end{aligned}\right\} \quad \boldsymbol{x}\in\mathbb{R}^3\,. \tag{3.30}$$

Finally, according to [68, Theorem 2.43 (a)], it holds that

$$\begin{aligned}\mathbf{curl}\,\boldsymbol{M}_n^m(\boldsymbol{x}) = j_n(kr)\,\frac{\sqrt{n(n+1)}}{r}\,\boldsymbol{W}_n^m(\widehat{\boldsymbol{x}}) \\ + \left(kj_n'(kr) + \frac{1}{r}\,j_n(kr)\right)\boldsymbol{U}_n^m(\widehat{\boldsymbol{x}})\,, \qquad \boldsymbol{x}\in\mathbb{R}^3\,.\end{aligned} \tag{3.31}$$

Thus, inserting (3.31) and the definition of $\boldsymbol{M}_n^m$ (see (3.24)) into (3.30), we conclude the assertions. ■

With the representations from Lemma 3.13, we can straightforwardly calculate the norms of $\boldsymbol{E}^i[\boldsymbol{U}_n^m]$, $\boldsymbol{E}^i[\boldsymbol{V}_n^m]$.

Lemma 3.14. *Let $n \in \mathbb{N}$, $m \in \mathbb{Z}$, $|m| \leq n$. The $\boldsymbol{L}^2$-norms of the Herglotz wave functions with vector spherical harmonics as densities are given by*

$$\|\boldsymbol{E}^i[\boldsymbol{U}_n^m]\|^2_{\boldsymbol{L}^2(B_R)} = \frac{16\pi^2}{|k|^2} \int_0^R \left(n(n+1)|j_n(kr)|^2 + \left| \frac{\mathrm{d}}{\mathrm{d}r}(rj_n(kr)) \right|^2 \right) \mathrm{d}r \,,$$
$$\|\boldsymbol{E}^i[\boldsymbol{V}_n^m]\|^2_{\boldsymbol{L}^2(B_R)} = 16\pi^2 \int_0^R |rj_n(kr)|^2 \,\mathrm{d}r \,.$$

Proof. Let $n \in \mathbb{N}$, $m \in \mathbb{Z}$, $|m| \leq n$. Recall that $\boldsymbol{W}_n^m(\widehat{\boldsymbol{x}}) = Y_n^m(\widehat{\boldsymbol{x}})\widehat{\boldsymbol{x}}$, $\widehat{\boldsymbol{x}} \in \mathbb{S}^2$ (see (3.25)). We expand $\boldsymbol{E}^i[\boldsymbol{U}_n^m]$, $\boldsymbol{E}^i[\boldsymbol{V}_n^m]$ in the orthonormal system

$$\{\boldsymbol{U}_n^m \,,\ \boldsymbol{V}_n^m \,,\ \boldsymbol{W}_n^m \,:\, n \in \mathbb{N} \,,\ m \in \mathbb{Z} \,,\ |m| \leq n\} \subseteq \boldsymbol{L}^2(B_R) \,.$$

According to [68, Theorem 5.36], the $\boldsymbol{L}^2$-norms are given by

$$\|\boldsymbol{E}^i[\boldsymbol{U}_n^m]\|^2_{\boldsymbol{L}^2(B_R)} = \sum_{n'=1}^{\infty} \sum_{m'=-n'}^{n'} \int_0^R \left(|r\alpha_{n'}^{m'}(r)|^2 + |r\beta_{n'}^{m'}(r)|^2 + |r\gamma_{n'}^{m'}(r)|^2 \right) \mathrm{d}r \,,$$
$$\|\boldsymbol{E}^i[\boldsymbol{V}_n^m]\|^2_{\boldsymbol{L}^2(B_R)} = \sum_{n'=1}^{\infty} \sum_{m'=-n'}^{n'} \int_0^R \left(|ra_{n'}^{m'}(r)|^2 + |rb_{n'}^{m'}(r)|^2 + |rc_{n'}^{m'}(r)|^2 \right) \mathrm{d}r \,,$$

where, due to Lemma 3.13, the expansion coefficients can be readily calculated by

$$\alpha_{n'}^{m'}(r) = 4\pi \mathrm{i}^{n'} \frac{\sqrt{n'(n'+1)}}{\mathrm{i}\overline{k}r} j_{n'}(kr)\delta_{nn'}\delta_{mm'} \,, \qquad \beta_{n'}^{m'}(r) = 4\pi \mathrm{i}^{n'} \frac{1}{\mathrm{i}\overline{k}r} \frac{\mathrm{d}}{\mathrm{d}r}(rj_{n'}(kr))\delta_{nn'}\delta_{mm'} \,,$$
$$\gamma_{n'}^{m'}(r) = 0 \,, \qquad a_{n'}^{m'}(r) = 0 \,, \qquad b_{n'}^{m'}(r) = 0 \,, \qquad c_{n'}^{m'}(r) = 4\pi \mathrm{i}^{n'} j_{n'}(kr)\delta_{nn'}\delta_{mm'} \,,$$

$n, n' \in \mathbb{N}$, $m, m' \in \mathbb{Z}$, $|m| \leq n$, $|m'| \leq n'$, and *Kronecker*[6] *delta* δ_{kl}, $k, l \in \{n, n', m, m'\}$. ∎

The norms of the Herglotz wave functions, which we have derived in Lemma 3.14, implicate that we have to deal with series of polynomials of n times $|j_n|^2$. Therefore, we establish the following convergence result.

Lemma 3.15. *Let $\xi \in \mathbb{N}$. The series*

$$\left(\sum_{n=0}^{\infty} n^{\xi} \, |j_n(z)|^2 \right) \qquad \textit{and} \qquad \left(\sum_{n=0}^{\infty} n^{\xi} \, |j_n'(z)|^2 \right)$$

converge uniformly with respect to z on any compact subset of $\mathbb{C}$.

Proof. Recall Remark 2.2.For $n \in \mathbb{N}_0$, $k \in \mathbb{N}$, it holds that

$$\frac{(n+k)!\,(2n+1)!}{n!\,(2n+2k+1)!} = \frac{1}{2^k\,(2n+2k+1)\cdots(2n+3)} \,.$$

[6] Leopold Kronecker (1823–1891)

Hence, for $z \in \mathbb{C}$, $\xi \in \mathbb{N}$ and $n \in \mathbb{N}_0$, by [79, equation 10.53.1], we have the power series representation

$$\begin{aligned} j_n(z) &= (2z)^n \sum_{k=0}^{\infty} \frac{(-1)^k (n+k)!}{k!\,(2n+2k+1)!}\, z^{2k} \\ &= \frac{2^n n!\, z^n}{(2n+1)!} \left(1 + \sum_{k=1}^{\infty} \frac{(-1)^k}{2^k\, k!\,(2n+2k+1)(2n+2k-1)\cdots(2n+3)}\, z^{2k}\right) \\ &= \frac{2^n n!\, z^n}{(2n+1)!} \left(1 + \frac{1}{n^{\xi+2}} \sum_{k=1}^{\infty} \frac{(-1)^k n^{\xi+2}}{2^k\, k!\,(2n+2k+1)(2n+2k-1)\cdots(2n+3)}\, z^{2k}\right). \end{aligned}$$

The power series

$$\left(\sum_{k=1}^{\infty} \frac{(-1)^k n^{\xi+2}}{2^k\, k!\,(2n+2k+1)(2n+2k-1)\cdots(2n+3)}\, z^{2k}\right)$$

converges on $\mathbb{C}$. Hence, it is bounded on any compact subset. This yields

$$\left| |j_n(z)|^2 - \frac{4^n (n!)^2 |z|^{2n}}{((2n+1)!)^2} \right| \leq \frac{C}{n^{\xi+2}} \tag{3.32}$$

uniformly with respect to z on any compact subset of $\mathbb{C}$. Furthermore, it holds that

$$\frac{(n+1)^\xi 4^{(n+1)} ((n+1)!)^2 |z|^{2n+2}}{((2n+3)!)^2} \frac{((2n+1)!)^2}{n^\xi 4^n (n!)^2 |z|^{2n}} = \frac{1}{(2n+3)^2} \left(\frac{n+1}{n}\right)^\xi |z|^2 \to 0\,, \qquad n \to \infty\,.$$

Therefore, the series

$$\left(\sum_{k=1}^{\infty} n^\xi \frac{4^n (n!)^2 |z|^{2n}}{((2n+1)!)^2}\right)$$

converges for any $z \in \mathbb{C}$ by the ratio test and is, thus, bounded on any compact subset of $\mathbb{C}$. Consequently, by (3.32), it follows for $K \geq |z|$ that

$$\begin{aligned} \sum_{n=0}^{\infty} n^\xi |j_n(z)|^2 &= \sum_{n=0}^{\infty} n^\xi \left[|j_n(z)|^2 - \frac{4^n (n!)^2 |z|^{2n}}{((2n+1)!)^2}\right] + \sum_{n=0}^{\infty} \left[n^\xi \frac{4^n (n!)^2 |z|^{2n}}{((2n+1)!)^2}\right] \\ &\leq C \sum_{n=0}^{\infty} \frac{1}{n^2} + \sum_{n=0}^{\infty} \left[n^\xi \frac{4^n (n!)^2 K^{2n}}{((2n+1)!)^2}\right] \leq C\,. \end{aligned}$$

This is the assertion for the first series.

For the second series we use the recurrence relation [79, equation 10.51.1] and obtain

$$\begin{aligned} |j_n'(z)|^2 &= \left| \frac{n}{2n+1}\, j_{n-1}(z) - \frac{n+1}{2n+1}\, j_{n+1}(z) \right|^2 \\ &= \left(\frac{n}{2n+1}\right)^2 |j_{n-1}(z)|^2 - 2\,\mathrm{Re}\left(\frac{n(n+1)}{(2n+1)^2}\, j_{n-1}(z)\, \overline{j_{n+1}(z)}\right) + \left(\frac{n+1}{2n+1}\right)^2 |j_{n+1}(z)|^2\,. \end{aligned}$$

Since for $u, v \in \mathbb{C}$ it holds that $2\operatorname{Re}(u\overline{v}) \leq |u|^2 + |v|^2$, we have

$$|j_n'(z)|^2 \;\leq\; 2\left(\frac{n}{2n+1}\right)^2 |j_{n-1}(z)|^2 \,+\, 2\left(\frac{n+1}{2n+1}\right)^2 |j_{n+1}(z)|^2 \;\leq\; 2|j_{n-1}(z)|^2 \,+\, 2|j_{n+1}(z)|^2\,.$$

Consequently,

$$\begin{aligned}\sum_{n=0}^{\infty} n^{\xi}\,|j_n'(z)|^2 &= \sum_{n=1}^{\infty} n^{\xi}\,|j_n'(z)|^2 \leq 2\sum_{n=1}^{\infty} n^{\xi}\,|j_{n-1}(z)|^2 + 2\sum_{n=1}^{\infty} n^{\xi}\,|j_{n+1}(z)|^2 \\ &= 2\sum_{n=0}^{\infty}(n+1)^{\xi}\,|j_n(z)|^2 + 2\sum_{n=2}^{\infty}(n-1)^{\xi}\,|j_n(z)|^2 \leq 2^{\xi+2}\sum_{n=0}^{\infty} n^{\xi}\,|j_n(z)|^2\,,\end{aligned}$$

by which the assertion for the second series follows from the convergence of the first one. ■

Finally, we turn to the convergence of the series from (3.23).

Theorem 3.16. *The series*

$$\left(\sum_{n=1}^{\infty}\sum_{m=-n}^{n} \|\boldsymbol{E}^i[\boldsymbol{U}_n^m]\|^2_{\boldsymbol{L}^2(B_R)}\right) \qquad \text{and} \qquad \left(\sum_{n=1}^{\infty}\sum_{m=-n}^{n} \|\boldsymbol{E}^i[\boldsymbol{V}_n^m]\|^2_{\boldsymbol{L}^2(B_R)}\right)$$

converge.

Proof. By Lemma 3.14, we have established

$$\begin{aligned}\sum_{n=1}^{\infty}\sum_{m=-n}^{n} \|\boldsymbol{E}^i[\boldsymbol{U}_n^m]\|^2_{\boldsymbol{L}^2(B_R)} &= \frac{16\pi^2}{|k|^2}\int_0^R \left[\sum_{n=1}^{\infty}(2n+1)\left(n(n+1)|j_n(kr)|^2 + \left|\frac{\mathrm{d}}{\mathrm{d}r}(rj_n(kr))\right|^2\right)\right]\mathrm{d}r\,,\\ \sum_{n=1}^{\infty}\sum_{m=-n}^{n} \|\boldsymbol{E}^i[\boldsymbol{V}_n^m]\|^2_{\boldsymbol{L}^2(B_R)} &= 16\pi^2\int_0^R \left[\sum_{n=1}^{\infty}(2n+1)|rj_n(kr)|^2\right]\mathrm{d}r\,.\end{aligned}$$

Furthermore, there hold

$$\begin{aligned}(2n+1)n(n+1)|j_n(kr)|^2 &\leq 6n^3|j_n(kr)|^2\,,\\ (2n+1)\left|\frac{\mathrm{d}}{\mathrm{d}r}(rj_n(kr))\right|^2 &= (2n+1)|j_n(kr) + krj_n'(kr)|^2\\ &= (2n+1)\left[|j_n(kr)|^2 + 2\operatorname{Re}\left(j_n(kr)\overline{krj_n'(kr)}\right) + |k|^2r^2|j_n'(kr)|^2\right]\\ &\leq 6n\left[|j_n(kr)|^2 + |k|^2R^2|j_n'(kr)|^2\right],\\ (2n+1)|rj_n(kr)|^2 &\leq 3R^2n|j_n(kr)|^2\,.\end{aligned}$$

With Lemma 3.15, we immediately conclude the assertion. ■

We combine the results from above in the main theorem of this section.

Theorem 3.17. *It holds that*

$$\|\mathcal{F}(\partial D_{\boldsymbol{h}}) - \mathcal{F}(\partial D) - (\boldsymbol{E}'[\,\cdot\,])^{\infty}\|_{\mathrm{HS}} \leq C\,\|\boldsymbol{h}\|^2_{\boldsymbol{C}^1}\,, \tag{3.33}$$

i.e., the far-field operator $\partial D \mapsto \mathcal{F}(\partial D) \in \mathrm{HS}(\boldsymbol{L}^2_t(\mathbb{S}^2))$ *is Fréchet differentiable at* ∂D *with Fréchet derivative* $\mathcal{F}'[\partial D]\boldsymbol{h} = (\boldsymbol{E}'[\,\cdot\,])^\infty \in \mathrm{HS}(\boldsymbol{L}^2_t(\mathbb{S}^2))$.

Proof. With Theorem 3.16, we have that

$$\sum_{n=1}^{\infty}\sum_{m=-n}^{n} \|\boldsymbol{E}^i[\boldsymbol{U}_n^m]\|^2_{\boldsymbol{L}^2(B_R)} + \|\boldsymbol{E}^i[\boldsymbol{V}_n^m]\|^2_{\boldsymbol{L}^2(B_R)} \leq C$$

and, therefore, with Corollary 3.12, we infer that

$$\|\mathcal{F}(\partial D_{\boldsymbol{h}}) - \mathcal{F}(\partial D) - (\boldsymbol{E}'[\,\cdot\,])^\infty\|^2_{\mathrm{HS}} \leq C\,\|\boldsymbol{h}\|^4_{\boldsymbol{C}^1}\,.$$

■

CHAPTER 4

Long Tubular Objects and Corresponding Domain Derivatives

In Chapter 3 we have established differentiablilty of the far-field map F and far-field operator $\mathcal{F}$ with respect to perturbations $\boldsymbol{h}$ of the boundary for general C^1-smooth domains D. From this point forward, our focus remains on bounded *tubular* C^1-smooth objects. In the present chapter, we provide a comprehensive definition and construction of such tubular objects. The surface ∂D of these objects will not depend linearly on its defining parameters. Thus, having the inverse identification problem from Chapter 5 and the shape optimization from Chapter 6 in mind, we further need to linearize the surface with respect to perturbations of its defining parameters. Afterwards, we redefine the far-field map F and operator $\mathcal{F}$ on vector spaces, whose elements constitute these parameters representing ∂D. At the end of this chapter, we prove Fréchet differentiability of *these* F and $\mathcal{F}$.

We start by constructing bounded tubular C^1-smooth domains $D \subseteq \mathbb{R}^3$ that follow a central spine curve. The cross section perpendicular to the center curve is assumed to be a circular disk at each point, but the radius may vary along the curve. At the start and end point of the center curve, the tubes are smoothly completed by some caps, such that $\mathbb{R}^3 \setminus \overline{D}$ is connected.

To model such an object, we require a twice continuously differentiable regular curve C, parameterized by some regular $\boldsymbol{z}\colon [0,1] \to \mathbb{R}^3$, with an accompanying continuously differentiable orthogonal frame $(\boldsymbol{t}, \boldsymbol{n}, \boldsymbol{b})$, i.e., $\boldsymbol{t} = \boldsymbol{z}'/|\boldsymbol{z}'|$ on $[0,1]$ and $(\boldsymbol{t}(\tau), \boldsymbol{n}(\tau), \boldsymbol{b}(\tau))$ is an orthonormal basis of $\mathbb{R}^3$ for every $\tau \in [0,1]$. It might seem reasonable to consider the standard accompanying *Frenet*[1] *frame* (cf. [71, 2.4. Definition]); however, the Frenet frame is not defined in any point where the curvature of C vanishes and a continuous extension across such points may also not be possible. As an extreme case, for a straight line the Frenet frame is not defined for any point. Instead, we employ *rotation-minimizing frames* – or Bishop[2] frames –, introduced as *relatively parallel adapted frames* in [10, p. 246], by a vector-valued ordinary differential equation. They are known from applications in computer graphics, see [110].

[1] Jean Frédéric Frenet (1816–1900)
[2] Richard Lawrence Bishop (1931–2019)

Definition 4.1. *Let $\boldsymbol{z}\colon [0,1] \to \mathbb{R}^3$ be a parameterization of a C^2-smooth regular curve C with $|\boldsymbol{z}'| > 0$. A rotation minimizing frame $(\boldsymbol{t}, \boldsymbol{n}, \boldsymbol{b}) \in C^1([0,1], \mathbb{R}^{3\times 3})$ of C is defined through*

$$\boldsymbol{t} = \frac{\boldsymbol{z}'}{|\boldsymbol{z}'|}\,, \qquad \boldsymbol{b} = \boldsymbol{t} \times \boldsymbol{n} \qquad \text{on } [0,1]\,,$$

where $\boldsymbol{n}$ is a solution of the differential-algebraic equations

$$\left.\begin{aligned} \boldsymbol{n}' &= -(\boldsymbol{t}' \cdot \boldsymbol{n})\,\boldsymbol{t} \\ \boldsymbol{t} \cdot \boldsymbol{n} &= 0 \end{aligned}\right\} \qquad \text{on } [0,1]\,, \tag{4.1}$$

together with some initial condition

$$(\boldsymbol{t}(0), \boldsymbol{n}(0), \boldsymbol{b}(0)) = (\boldsymbol{t}_0, \boldsymbol{n}_0, \boldsymbol{b}_0) \in \mathbb{R}^{3\times 3}$$

with $|\boldsymbol{t}_0| = |\boldsymbol{n}_0| = |\boldsymbol{b}_0| = 1$ and $\boldsymbol{t}_0, \boldsymbol{n}_0, \boldsymbol{b}_0$ pairwise orthogonal.

Henceforward, let C be a C^2-smooth regular curve parameterized by some regular parameterization $\boldsymbol{z}\colon [0,1] \to \mathbb{R}^3$. Then, [10, Theorem 1] proves the existence of a uniquely determined C^1-smooth rotation-minimizing frame $(\boldsymbol{t}, \boldsymbol{n}, \boldsymbol{b})$ for every admissible initial condition (see Definition 4.1).

Remark 4.2. Note that the rotation-minimizing frame can be continuously defined for any regular C^1-smooth spine curve, see [110, Definition 1].

We now turn to the definition of the surface of a tubular object as described above. We subdivide such a surface into the surfaces S_{body} of the tubular body, S_{start} of the start cap, and S_{end} of the end cap, and represent it by an atlas of three charts $(S_{\text{body}}, \boldsymbol{x}_{\text{body}})$, $(S_{\text{start}}, \boldsymbol{x}_{\text{start}})$ and $(S_{\text{end}}, \boldsymbol{x}_{\text{end}})$. Keeping in mind that the cross sections of the tubular obstacles are disks, we introduce a strictly positive radius function $r\colon [0,1] \to \mathbb{R}_{>0}$ and the vector

$$\boldsymbol{\zeta}(\tau, \varphi) \coloneqq \cos(\varphi)\,\boldsymbol{n}(\tau) + \sin(\varphi)\,\boldsymbol{b}(\tau)\,, \qquad \tau \in [0,1]\,,\ \varphi \in (-\pi, \pi]\,. \tag{4.2}$$

The map parameterizing the tubular body is given by

$$\boldsymbol{x}_{\text{body}}(\tau, \varphi) \coloneqq \boldsymbol{z}(\tau) + r(\tau)\,\boldsymbol{\zeta}(\tau, \varphi)\,, \qquad \tau \in [0,1]\,,\ \varphi \in (-\pi, \pi]\,. \tag{4.3}$$

Lemma 4.3. *Let $\boldsymbol{z}\colon [0,1] \to \mathbb{R}^3$ be a parameterization of a C^2-smooth regular curve C with $|\boldsymbol{z}'| > 0$, $(\boldsymbol{t}, \boldsymbol{n}, \boldsymbol{b}) \in C^1([0,1], \mathbb{R}^{3\times 3})$ a rotation-minimizing frame of C, and $\psi \coloneqq |\boldsymbol{z}'| - r\,\boldsymbol{t}' \cdot \boldsymbol{\zeta}$. Then*

$$\partial_\varphi \boldsymbol{x}_{\text{body}} \times \partial_\tau \boldsymbol{x}_{\text{body}} = r\,(\psi\,\partial_\varphi \boldsymbol{\zeta} \times \boldsymbol{t} + r'\,\partial_\varphi \boldsymbol{\zeta} \times \boldsymbol{\zeta})\,.$$

Proof. First, we readily calculate

$$\boldsymbol{t}' = \frac{\mathrm{d}}{\mathrm{d}t}\frac{\boldsymbol{z}'}{|\boldsymbol{z}'|} = \frac{\boldsymbol{z}''}{|\boldsymbol{z}'|} - \frac{\boldsymbol{z}'(\boldsymbol{z}' \cdot \boldsymbol{z}'')}{|\boldsymbol{z}'|^3} = \frac{\boldsymbol{z}''}{|\boldsymbol{z}'|} - \frac{\boldsymbol{z}'' \cdot \boldsymbol{t}}{|\boldsymbol{z}'|}\,\boldsymbol{t}\,, \tag{4.4}$$

which also implies $\boldsymbol{t}' \cdot \boldsymbol{t} = 0$. Then, by Definition 4.1, we have

$$\boldsymbol{b}' = \boldsymbol{t}' \times \boldsymbol{n} - (\boldsymbol{t}' \cdot \boldsymbol{n})\,(\boldsymbol{t} \times \boldsymbol{t}) = \boldsymbol{t}' \times (\boldsymbol{b} \times \boldsymbol{t}) = (\boldsymbol{t}' \cdot \boldsymbol{t})\,\boldsymbol{b} - (\boldsymbol{t}' \cdot \boldsymbol{b})\,\boldsymbol{t} = -(\boldsymbol{t}' \cdot \boldsymbol{b})\,\boldsymbol{t}\,. \tag{4.5}$$

Thus, using (4.1) and (4.5), we infer that

$$\partial_\tau \boldsymbol{\zeta}(\tau, \varphi) = -\cos(\varphi)\,(\boldsymbol{t}' \cdot \boldsymbol{n})\,\boldsymbol{t} - \sin(\varphi)\,(\boldsymbol{t}' \cdot \boldsymbol{b})\,\boldsymbol{t} = -(\boldsymbol{t}' \cdot \boldsymbol{\zeta})\,\boldsymbol{t}\,, \qquad \tau \in [0,1]\,,\ \varphi \in (-\pi, \pi]\,.$$

Consequently, using $\boldsymbol{z}' = |\boldsymbol{z}'|\,\boldsymbol{t}$ and recalling that $\psi = |\boldsymbol{z}'| - r\,\boldsymbol{t}' \cdot \boldsymbol{\zeta}$, yields

$$\partial_\tau \boldsymbol{x}_{\text{body}} = \boldsymbol{z}' + r'\,\boldsymbol{\zeta} + r\,\partial_\tau \boldsymbol{\zeta} = \psi\,\boldsymbol{t} + r'\,\boldsymbol{\zeta}\,.$$

With $\partial_\varphi \boldsymbol{x}_{\text{body}} = r\,\partial_\varphi \boldsymbol{\zeta}$ the assertion immediately follows. ■

Next, we want to define the maps $\boldsymbol{x}_{\text{start}}$ and $\boldsymbol{x}_{\text{end}}$ such that the full tubular surface is C^1-smooth, i.e., that the unit normal is continuous across S_{body}, S_{start} and S_{end}. We consider a spherical start cap in the coordinate system with coordinate vectors $(\boldsymbol{b}(0), \boldsymbol{n}(0), -\boldsymbol{t}(0))$ and origin $\boldsymbol{z}(0)$ and a spherical end cap in the coordinate system with coordinate vectors $(\boldsymbol{n}(1), \boldsymbol{b}(1), \boldsymbol{t}(1))$ and origin $\boldsymbol{z}(1)$. Let $\varphi \in (-\pi, \pi]$, $\vartheta \in [0, \pi/2]$. We introduce the vectors

$$\boldsymbol{\xi}_{\text{start}}(\vartheta, \varphi) \coloneqq \cos(\varphi)\sin(\vartheta)\,\boldsymbol{b}(0) + \sin(\varphi)\sin(\vartheta)\,\boldsymbol{n}(0) - \cos(\vartheta)\,\boldsymbol{t}(0)\,, \tag{4.6a}$$

$$\boldsymbol{\xi}_{\text{end}}(\vartheta, \varphi) \coloneqq \cos(\varphi)\sin(\vartheta)\,\boldsymbol{n}(1) + \sin(\varphi)\sin(\vartheta)\,\boldsymbol{b}(1) + \cos(\vartheta)\,\boldsymbol{t}(1)\,. \tag{4.6b}$$

The maps parameterizing the caps' surfaces are given by

$$\boldsymbol{x}_{\text{start}}(\vartheta, \varphi) \coloneqq \boldsymbol{z}(0) + \rho_0(\vartheta, \varphi)\,\boldsymbol{\xi}_{\text{start}}(\vartheta, \varphi)\,, \tag{4.7a}$$

$$\boldsymbol{x}_{\text{end}}(\vartheta, \varphi) \coloneqq \boldsymbol{z}(1) + \rho_1(\vartheta, \varphi)\,\boldsymbol{\xi}_{\text{end}}(\vartheta, \varphi)\,, \tag{4.7b}$$

where ρ_i, $i \in \{0, 1\}$, are chosen to be of the form

$$\rho_i(\vartheta, \varphi) = r(i)\left(1 + f_i(\varphi)\,\vartheta^2\left(\vartheta - \frac{\pi}{2}\right)\right), \qquad i \in \{0, 1\}\,,$$

with f_i, $i \in \{0, 1\}$, being functions that still need to be determined, such that $(S_{\text{body}}, \boldsymbol{x}_{\text{body}})$, $(S_{\text{start}}, \boldsymbol{x}_{\text{start}})$ and $(S_{\text{end}}, \boldsymbol{x}_{\text{end}})$ form the atlas of a C^1-smooth surface (see Figure 4.1 for an illustration).

Assumption 4.4. *We assume that the choice of $(\boldsymbol{z}, r)$ does not lead to self-intersections of the tubular surface parameterized by the maps $\boldsymbol{x}_{\text{body}}$, $\boldsymbol{x}_{\text{start}}$ and $\boldsymbol{x}_{\text{end}}$.*

Under Assumption 4.4, the maps $\boldsymbol{x}_{\text{body}}$, $\boldsymbol{x}_{\text{start}}$ and $\boldsymbol{x}_{\text{end}}$ each are obviously parameterizations of C^1-smooth surfaces in $\mathbb{R}^3$. Furthermore, in the following lemma, we show that the body and the caps are continuously connected.

Lemma 4.5. *$(S_{\text{body}}, \boldsymbol{x}_{\text{body}})$, $(S_{\text{start}}, \boldsymbol{x}_{\text{start}})$ and $(S_{\text{end}}, \boldsymbol{x}_{\text{end}})$ form an atlas of a C^0-smooth surface.*

Proof. We show that the values of the parameterizations of the caps and the body coincide where

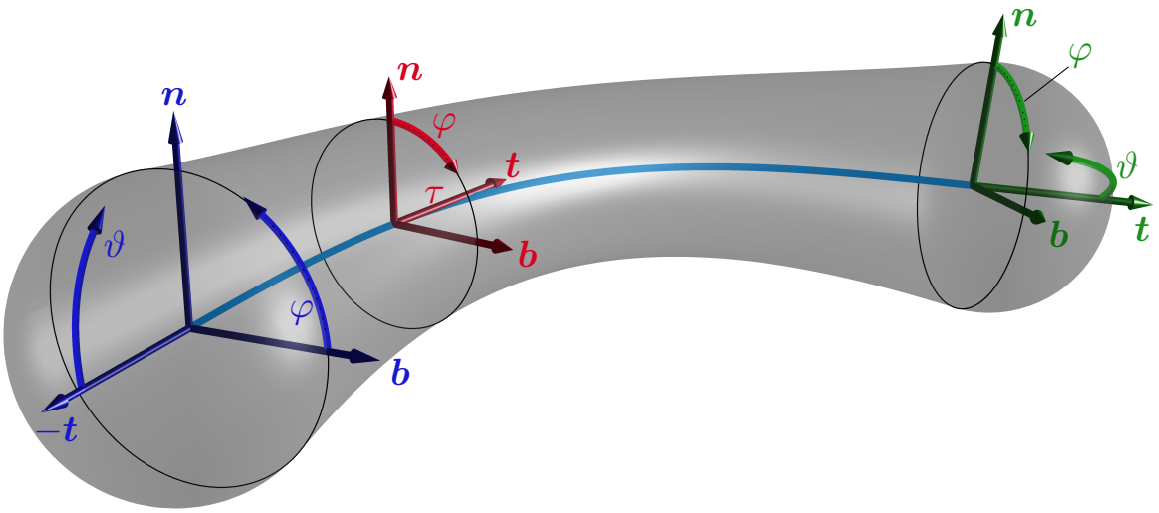

Figure 4.1. Adapted from [5, Figure 1]. Parameters used for the parameterizations $\boldsymbol{x}_{\text{start}}$ (blue), $\boldsymbol{x}_{\text{body}}$ (red) and $\boldsymbol{x}_{\text{end}}$ (green) of the tube surface together with the underlying coordinate systems.

they are connected, i.e., for $\vartheta = \pi/2$ and $\tau \in \{0, 1\}$. It holds that

$$\begin{aligned}
\boldsymbol{x}_{\text{start}}(\pi/2, \varphi) &= \boldsymbol{z}(0) + \rho_0(\pi/2, \varphi)\, \boldsymbol{\xi}_{\text{start}}(\pi/2, \varphi) \\
&= \boldsymbol{z}(0) + r(0)\, (\cos(\varphi)\, \boldsymbol{b}(0) + \sin(\varphi)\, \boldsymbol{n}(0)) \\
&= \boldsymbol{z}(0) + r(0)\, (\sin(\pi/2 - \varphi)\, \boldsymbol{b}(0) + \cos(\pi/2 - \varphi)\, \boldsymbol{n}(0)) \\
&= \boldsymbol{x}_{\text{body}}(0, \pi/2 - \varphi)
\end{aligned}$$

and

$$\begin{aligned}
\boldsymbol{x}_{\text{end}}(\pi/2, \varphi) &= \boldsymbol{z}(1) + \rho_1(\pi/2, \varphi)\, \boldsymbol{\xi}_{\text{end}}(\pi/2, \varphi) \\
&= \boldsymbol{z}(1) + r(1)\, (\cos(\varphi)\, \boldsymbol{n}(1) + \sin(\varphi)\, \boldsymbol{b}(1)) \\
&= \boldsymbol{x}_{\text{body}}(1, \varphi)
\end{aligned}$$

for all $\varphi \in (-\pi, \pi]$. Note that the φ-coordinate is oppositely oriented for the start cap than for the body and the end cap and that there is a phase shift, compensating the opposite orientation. ■

Next, we determine the functions f_i, $i \in \{0, 1\}$, such that $(S_{\text{body}}, \boldsymbol{x}_{\text{body}})$, $(S_{\text{start}}, \boldsymbol{x}_{\text{start}})$ and $(S_{\text{end}}, \boldsymbol{x}_{\text{end}})$ form the atlas of a C^1-smooth surface. For this purpose, we first calculate

$$\partial_\vartheta \boldsymbol{\xi}_{\text{start}}(\vartheta, \varphi) = \cos(\varphi)\cos(\vartheta)\, \boldsymbol{b}(0) + \sin(\varphi)\cos(\vartheta)\, \boldsymbol{n}(0) + \sin(\vartheta)\, \boldsymbol{t}(0)\,,$$

$$\partial_\varphi \boldsymbol{\xi}_{\text{start}}(\vartheta, \varphi) = -\sin(\varphi)\sin(\vartheta)\, \boldsymbol{b}(0) + \cos(\varphi)\sin(\vartheta)\, \boldsymbol{n}(0)\,,$$

$$\partial_\vartheta \boldsymbol{\xi}_{\text{end}}(\vartheta, \varphi) = \cos(\varphi)\cos(\vartheta)\, \boldsymbol{n}(1) + \sin(\varphi)\cos(\vartheta)\, \boldsymbol{b}(1) - \sin(\vartheta)\, \boldsymbol{t}(1)\,,$$

$$\partial_\varphi \boldsymbol{\xi}_{\text{end}}(\vartheta,\varphi) = -\sin(\varphi)\sin(\vartheta)\,\boldsymbol{n}(1) + \cos(\varphi)\sin(\vartheta)\,\boldsymbol{b}(1)\,,$$

$$\partial_\vartheta \rho_i(\vartheta,\varphi) = r(i)\,f_i(\varphi)\left(2\vartheta\left(\vartheta-\frac{\pi}{2}\right)+\vartheta^2\right),$$

$$\partial_\varphi \rho_i(\vartheta,\varphi) = r(i)\,f_i'(\varphi)\,\vartheta^2\left(\vartheta-\frac{\pi}{2}\right),$$

where $i \in \{0,1\}$, $\varphi \in (-\pi,\pi]$ and $\vartheta \in [0,\pi/2]$. Hence,

$$\partial_\vartheta \boldsymbol{\xi}_{\text{start}}(\pi/2,\varphi) = \boldsymbol{t}(0)\,,$$

$$\begin{aligned}\partial_\varphi \boldsymbol{\xi}_{\text{start}}(\pi/2,\varphi) &= -\sin(\varphi)\,\boldsymbol{b}(0) + \cos(\varphi)\,\boldsymbol{n}(0) = \partial_\varphi(\cos(\varphi)\,\boldsymbol{b}(0) + \sin(\varphi)\,\boldsymbol{n}(0)) \\ &= \partial_\varphi\left(\sin(\pi/2-\varphi)\boldsymbol{b}(0) + \cos(\pi/2-\varphi)\boldsymbol{n}(0)\right) = \partial_\varphi \boldsymbol{\zeta}(0,\pi/2-\varphi)\,,\end{aligned}$$

$$\partial_\vartheta \boldsymbol{\xi}_{\text{end}}(\pi/2,\varphi) = -\boldsymbol{t}(1)\,,$$

$$\partial_\varphi \boldsymbol{\xi}_{\text{end}}(\pi/2,\varphi) = -\sin(\varphi)\,\boldsymbol{n}(1) + \cos(\varphi)\,\boldsymbol{b}(1) = \partial_\varphi \boldsymbol{\zeta}(1,\varphi)\,,$$

$$\partial_\vartheta \rho_i(\pi/2,\varphi) = \frac{\pi^2}{4}\,r(i)\,f_i(\varphi)\,,$$

$$\partial_\varphi \rho_i(\pi/2,\varphi) = 0\,,$$

where $i \in \{0,1\}$, $\varphi \in (-\pi,\pi]$. Moreover, it holds that

$$\boldsymbol{\xi}_{\text{start}}(\pi/2,\varphi) = \cos(\varphi)\,\boldsymbol{b}(0) + \sin(\varphi)\,\boldsymbol{n}(0) = \boldsymbol{\zeta}(0,\pi/2-\varphi)\,,$$

$$\boldsymbol{\xi}_{\text{end}}(\pi/2,\varphi) = \cos(\varphi)\,\boldsymbol{n}(1) + \sin(\varphi)\,\boldsymbol{b}(1) = \boldsymbol{\zeta}(1,\varphi)\,,$$

$\varphi \in (-\pi,\pi]$. We can now readily calculate

$$\partial_\vartheta \boldsymbol{x}_{\text{start}}(\pi/2,\varphi) = \frac{\pi^2}{4}\,r(0)\,f_0(\varphi)\,\boldsymbol{\zeta}(0,\pi/2-\varphi) + r(0)\,\boldsymbol{t}(0)\,,$$

$$\partial_\varphi \boldsymbol{x}_{\text{start}}(\pi/2,\varphi) = r(0)\,\partial_\varphi \boldsymbol{\zeta}(0,\pi/2-\varphi)\,,$$

$$\partial_\vartheta \boldsymbol{x}_{\text{end}}(\pi/2,\varphi) = \frac{\pi^2}{4}\,r(1)\,f_1(\varphi)\,\boldsymbol{\zeta}(1,\varphi) - r(1)\,\boldsymbol{t}(1)\,,$$

$$\partial_\varphi \boldsymbol{x}_{\text{end}}(\pi/2,\varphi) = r(1)\,\partial_\varphi \boldsymbol{\zeta}(1,\varphi)\,,$$

and, consequently,

$$\partial_\vartheta \boldsymbol{x}_{\text{start}}(\pi/2,\varphi) \times \partial_\varphi \boldsymbol{x}_{\text{start}}(\pi/2,\varphi) = (r(0))^2\left(\frac{\pi^2}{4}\,f_0(\varphi)\,\boldsymbol{\zeta}(0,\pi/2-\varphi) + \boldsymbol{t}(0)\right) \times \partial_\varphi \boldsymbol{\zeta}(0,\pi/2-\varphi)$$

as well as

$$\partial_\vartheta \boldsymbol{x}_{\mathrm{end}}(\pi/2,\varphi) \times \partial_\varphi \boldsymbol{x}_{\mathrm{end}}(\pi/2,\varphi) = (r(1))^2 \left(\frac{\pi^2}{4} f_1(\varphi)\, \boldsymbol{\zeta}(1,\varphi) - \boldsymbol{t}(1) \right) \times \partial_\varphi \boldsymbol{\zeta}(1,\varphi)\,,$$

for $\varphi \in (-\pi,\pi]$. With a view to Lemma 4.3, we set

$$f_0(\varphi) = \frac{4\,r'(0)}{\pi^2\,\psi(0,\pi/2-\varphi)}\,, \qquad f_1(\varphi) = -\frac{4\,r'(1)}{\pi^2\,\psi(1,\varphi)}\,,$$

obtaining the following result.

Lemma 4.6. *Let $\varphi \in (-\pi,\pi]$. With the given choice of f_i, $i \in \{0,1\}$, it holds that*

$$\begin{aligned}\partial_\vartheta \boldsymbol{x}_{\mathrm{start}}(\pi/2,\varphi) &\times \partial_\varphi \boldsymbol{x}_{\mathrm{start}}(\pi/2,\varphi) \\ &= \frac{r(0)}{\psi(0,\pi/2-\varphi)}\, \partial_\tau \boldsymbol{x}_{\mathrm{body}}(0,\pi/2-\varphi) \times \partial_\varphi \boldsymbol{x}_{\mathrm{body}}(0,\pi/2-\varphi)\,,\end{aligned}$$

$$\partial_\vartheta \boldsymbol{x}_{\mathrm{end}}(\pi/2,\varphi) \times \partial_\varphi \boldsymbol{x}_{\mathrm{end}}(\pi/2,\varphi) = \frac{r(1)}{\psi(1,\varphi)}\, \partial_\varphi \boldsymbol{x}_{\mathrm{body}}(1,\varphi) \times \partial_\tau \boldsymbol{x}_{\mathrm{body}}(1,\varphi)\,.$$

In order to obtain the correct sign in both equations of Lemma 4.6, we impose the following constraint.

Assumption 4.7. *We assume $\|r\|_\infty$ to be sufficiently small, such that $|\boldsymbol{z}'| - r\,\boldsymbol{t}' \cdot \boldsymbol{\zeta} = \psi \geq c > 0$ for some constant c.*

Finally, under Assumption 4.7, we conclude with Lemma 4.6 that the unit normal is continuous across the interfaces of both S_{start} and S_{body} as well as S_{body} and S_{end}. Thus, $(S_{\mathrm{body}}, \boldsymbol{x}_{\mathrm{body}})$, $(S_{\mathrm{start}}, \boldsymbol{x}_{\mathrm{start}})$ and $(S_{\mathrm{end}}, \boldsymbol{x}_{\mathrm{end}})$ yield the atlas of a C^1-smooth surface for the given choice of ρ_i, $i \in \{0,1\}$. Let $\varphi \in (-\pi,\pi]$ and $\vartheta \in [0,\pi/2]$. We define

$$\eta_0(\vartheta,\varphi) \coloneqq \frac{4\,\vartheta^2\,(\vartheta-\pi/2)\,r(0)\,r'(0)}{\pi^2\,\psi(0,\pi/2-\varphi)}\,, \qquad \eta_1(\vartheta,\varphi) \coloneqq -\frac{4\,\vartheta^2\,(\vartheta-\pi/2)\,r(1)\,r'(1)}{\pi^2\,\psi(1,\varphi)} \tag{4.8}$$

and obtain the representation

$$\rho_i(\vartheta,\varphi) \coloneqq r(i) + \eta_i(\vartheta,\varphi)\,, \qquad i \in \{0,1\}\,.$$

In conclusion, we can represent the surface of a bounded, regular, long tubular C^1-smooth object by an element $(\boldsymbol{z}, r)$ of a subset $\mathcal{M}$ of

$$\left\{ (\widehat{\boldsymbol{z}}, \widehat{r}) \,:\, \widehat{\boldsymbol{z}} \in C^2([0,1],\mathbb{R}^3) \text{ and regular}\,,\ \widehat{r} \in C^1([0,1],\mathbb{R})\,,\ \widehat{r} > 0 \right\}, \tag{4.9}$$

where we impose additional restrictions on the curvature of $\boldsymbol{z}$ and the magnitude of r, in the form of Assumptions 4.4 and 4.7.

4.1. Perturbation Formulae for Tubular Objects

The surface of long tubular objects, parameterized by $\boldsymbol{x}_{\text{body}}$, $\boldsymbol{x}_{\text{start}}$, $\boldsymbol{x}_{\text{end}}$ (see (4.3), (4.7)), does not depend linearly on $\boldsymbol{z}$ and r. In view of solving inverse problems and performing optimization schemes, it is required to derive the linearization of each $\boldsymbol{x}_{\text{body}}$, $\boldsymbol{x}_{\text{start}}$, $\boldsymbol{x}_{\text{end}}$, with respect to perturbations $\boldsymbol{u}$ of the curve $\boldsymbol{z}$ and δ of the radius function r.

We follow the approach to linearizing the parameterization of regular curves with respect to a perturbation as in [49]. There, in Equation (15) the following result is stated without proof.

Lemma 4.8. *Let $C_{\boldsymbol{u}}$ be another twice differentiable regular curve with parameterization $\boldsymbol{u}\colon [0,1] \to \mathbb{R}^3$. Then, a continuous orthogonal frame of this curve, parameterized by $\boldsymbol{z}+\boldsymbol{u}$, is $(\boldsymbol{t}_{\boldsymbol{u}}, \boldsymbol{n}_{\boldsymbol{u}}, \boldsymbol{b}_{\boldsymbol{u}})$ with*

$$\begin{aligned}
\boldsymbol{t}_{\boldsymbol{u}} &= \frac{\boldsymbol{z}' + \boldsymbol{u}'}{|\boldsymbol{z}' + \boldsymbol{u}'|}\,, \\
\boldsymbol{n}_{\boldsymbol{u}} &= (\boldsymbol{t}\cdot\boldsymbol{t}_{\boldsymbol{u}})\boldsymbol{n} - \frac{\boldsymbol{b}\cdot\boldsymbol{t}_{\boldsymbol{u}}}{1+\boldsymbol{t}\cdot\boldsymbol{t}_{\boldsymbol{u}}}(\boldsymbol{t}\times\boldsymbol{t}_{\boldsymbol{u}}) - (\boldsymbol{n}\cdot\boldsymbol{t}_{\boldsymbol{u}})\boldsymbol{t}\,, \\
\boldsymbol{b}_{\boldsymbol{u}} &= (\boldsymbol{t}\cdot\boldsymbol{t}_{\boldsymbol{u}})\boldsymbol{b} + \frac{\boldsymbol{n}\cdot\boldsymbol{t}_{\boldsymbol{u}}}{1+\boldsymbol{t}\cdot\boldsymbol{t}_{\boldsymbol{u}}}(\boldsymbol{t}\times\boldsymbol{t}_{\boldsymbol{u}}) - (\boldsymbol{b}\cdot\boldsymbol{t}_{\boldsymbol{u}})\boldsymbol{t}\,.
\end{aligned}$$

Proof. It holds that $|\boldsymbol{t}_{\boldsymbol{u}}| = 1$ and with that also

$$\begin{aligned}
|\boldsymbol{n}_{\boldsymbol{u}}|^2 &= |(\boldsymbol{t}\cdot\boldsymbol{t}_{\boldsymbol{u}})\boldsymbol{n} - (\boldsymbol{n}\cdot\boldsymbol{t}_{\boldsymbol{u}})\boldsymbol{t}|^2 + \left|\frac{\boldsymbol{b}\cdot\boldsymbol{t}_{\boldsymbol{u}}}{1+\boldsymbol{t}\cdot\boldsymbol{t}_{\boldsymbol{u}}}(\boldsymbol{t}\times\boldsymbol{t}_{\boldsymbol{u}})\right|^2 \\
&\quad - 2((\boldsymbol{t}\cdot\boldsymbol{t}_{\boldsymbol{u}})\boldsymbol{n} - (\boldsymbol{n}\cdot\boldsymbol{t}_{\boldsymbol{u}})\boldsymbol{t}) \cdot \left(\frac{\boldsymbol{b}\cdot\boldsymbol{t}_{\boldsymbol{u}}}{1+\boldsymbol{t}\cdot\boldsymbol{t}_{\boldsymbol{u}}}(\boldsymbol{t}\times\boldsymbol{t}_{\boldsymbol{u}})\right) \\
&= |(\boldsymbol{t}\cdot\boldsymbol{t}_{\boldsymbol{u}})\boldsymbol{n}|^2 + |(\boldsymbol{n}\cdot\boldsymbol{t}_{\boldsymbol{u}})\boldsymbol{t}|^2 + \frac{(\boldsymbol{b}\cdot\boldsymbol{t}_{\boldsymbol{u}})^2|\boldsymbol{t}\times\boldsymbol{t}_{\boldsymbol{u}}|^2}{(1+\boldsymbol{t}\cdot\boldsymbol{t}_{\boldsymbol{u}})^2} + 2\,\frac{(\boldsymbol{b}\cdot\boldsymbol{t}_{\boldsymbol{u}})^2(\boldsymbol{t}\cdot\boldsymbol{t}_{\boldsymbol{u}})}{1+\boldsymbol{t}\cdot\boldsymbol{t}_{\boldsymbol{u}}} \\
&= (\boldsymbol{t}\cdot\boldsymbol{t}_{\boldsymbol{u}})^2 + (\boldsymbol{n}\cdot\boldsymbol{t}_{\boldsymbol{u}})^2 + (\boldsymbol{b}\cdot\boldsymbol{t}_{\boldsymbol{u}})^2\left(\frac{1-(\boldsymbol{t}\cdot\boldsymbol{t}_{\boldsymbol{u}})^2 + 2(\boldsymbol{t}\cdot\boldsymbol{t}_{\boldsymbol{u}})(1+\boldsymbol{t}\cdot\boldsymbol{t}_{\boldsymbol{u}})}{(1+\boldsymbol{t}\cdot\boldsymbol{t}_{\boldsymbol{u}})^2}\right) \\
&= (\boldsymbol{t}\cdot\boldsymbol{t}_{\boldsymbol{u}})^2 + (\boldsymbol{n}\cdot\boldsymbol{t}_{\boldsymbol{u}})^2 + (\boldsymbol{b}\cdot\boldsymbol{t}_{\boldsymbol{u}})^2 \\
&= |\boldsymbol{t}_{\boldsymbol{u}}|^2 \\
&= 1
\end{aligned}$$

and analogously $|\boldsymbol{b}_{\boldsymbol{u}}| = 1$. Furthermore,

$$\begin{aligned}
\boldsymbol{t}_{\boldsymbol{u}}\cdot\boldsymbol{n}_{\boldsymbol{u}} &= (\boldsymbol{t}\cdot\boldsymbol{t}_{\boldsymbol{u}})(\boldsymbol{t}_{\boldsymbol{u}}\cdot\boldsymbol{n}) - \frac{\boldsymbol{b}\cdot\boldsymbol{t}_{\boldsymbol{u}}}{1+\boldsymbol{t}\cdot\boldsymbol{t}_{\boldsymbol{u}}}\,\boldsymbol{t}_{\boldsymbol{u}}\cdot(\boldsymbol{t}\times\boldsymbol{t}_{\boldsymbol{u}}) - (\boldsymbol{n}\cdot\boldsymbol{t}_{\boldsymbol{u}})(\boldsymbol{t}_{\boldsymbol{u}}\cdot\boldsymbol{t}) = 0\,, \\
\boldsymbol{t}_{\boldsymbol{u}}\cdot\boldsymbol{b}_{\boldsymbol{u}} &= (\boldsymbol{t}\cdot\boldsymbol{t}_{\boldsymbol{u}})(\boldsymbol{t}_{\boldsymbol{u}}\cdot\boldsymbol{b}) + \frac{\boldsymbol{n}\cdot\boldsymbol{t}_{\boldsymbol{u}}}{1+\boldsymbol{t}\cdot\boldsymbol{t}_{\boldsymbol{u}}}\,\boldsymbol{t}_{\boldsymbol{u}}\cdot(\boldsymbol{t}\times\boldsymbol{t}_{\boldsymbol{u}}) - (\boldsymbol{b}\cdot\boldsymbol{t}_{\boldsymbol{u}})(\boldsymbol{t}_{\boldsymbol{u}}\cdot\boldsymbol{t}) = 0\,.
\end{aligned}$$

By $(\boldsymbol{t}\times\boldsymbol{t}_{\boldsymbol{u}})\cdot\boldsymbol{b} = (\boldsymbol{b}\times\boldsymbol{t})\cdot\boldsymbol{t}_{\boldsymbol{u}} = \boldsymbol{n}\cdot\boldsymbol{t}_{\boldsymbol{u}}$ and analogously $(\boldsymbol{t}\times\boldsymbol{t}_{\boldsymbol{u}})\cdot\boldsymbol{n} = -\boldsymbol{b}\cdot\boldsymbol{t}_{\boldsymbol{u}}$, we also obtain

$$\begin{aligned}
\boldsymbol{n}_{\boldsymbol{u}}\cdot\boldsymbol{b}_{\boldsymbol{u}} &= (\boldsymbol{t}\cdot\boldsymbol{t}_{\boldsymbol{u}})^2(\boldsymbol{n}\cdot\boldsymbol{b}) - \frac{(\boldsymbol{b}\cdot\boldsymbol{t}_{\boldsymbol{u}})(\boldsymbol{t}\cdot\boldsymbol{t}_{\boldsymbol{u}})}{1+\boldsymbol{t}\cdot\boldsymbol{t}_{\boldsymbol{u}}}(\boldsymbol{t}\times\boldsymbol{t}_{\boldsymbol{u}})\cdot\boldsymbol{b} - (\boldsymbol{n}\cdot\boldsymbol{t}_{\boldsymbol{u}})(\boldsymbol{t}\cdot\boldsymbol{t}_{\boldsymbol{u}})(\boldsymbol{t}\cdot\boldsymbol{b}) \\
&\quad + \frac{(\boldsymbol{n}\cdot\boldsymbol{t}_{\boldsymbol{u}})(\boldsymbol{t}\cdot\boldsymbol{t}_{\boldsymbol{u}})}{1+\boldsymbol{t}\cdot\boldsymbol{t}_{\boldsymbol{u}}}(\boldsymbol{t}\times\boldsymbol{t}_{\boldsymbol{u}})\cdot\boldsymbol{n} - \frac{(\boldsymbol{b}\cdot\boldsymbol{t}_{\boldsymbol{u}})(\boldsymbol{n}\cdot\boldsymbol{t}_{\boldsymbol{u}})}{(1+\boldsymbol{t}\cdot\boldsymbol{t}_{\boldsymbol{u}})^2}|\boldsymbol{t}\times\boldsymbol{t}_{\boldsymbol{u}}|^2 - \frac{(\boldsymbol{n}\cdot\boldsymbol{t}_{\boldsymbol{u}})^2}{1+\boldsymbol{t}\cdot\boldsymbol{t}_{\boldsymbol{u}}}(\boldsymbol{t}\times\boldsymbol{t}_{\boldsymbol{u}})\cdot\boldsymbol{t}
\end{aligned}$$

$$
\begin{aligned}
&- (\boldsymbol{t}\cdot\boldsymbol{t}_u)(\boldsymbol{b}\cdot\boldsymbol{t}_u)(\boldsymbol{n}\cdot\boldsymbol{t}) + \frac{(\boldsymbol{b}\cdot\boldsymbol{t}_u)^2}{1+\boldsymbol{t}\cdot\boldsymbol{t}_u}(\boldsymbol{t}\times\boldsymbol{t}_u)\cdot\boldsymbol{t} + (\boldsymbol{n}\cdot\boldsymbol{t}_u)(\boldsymbol{b}\cdot\boldsymbol{t}_u)(\boldsymbol{t}\cdot\boldsymbol{t})\\
&= -\frac{(\boldsymbol{b}\cdot\boldsymbol{t}_u)(\boldsymbol{t}\cdot\boldsymbol{t}_u)}{1+\boldsymbol{t}\cdot\boldsymbol{t}_u}(\boldsymbol{t}\times\boldsymbol{t}_u)\cdot\boldsymbol{b} + \frac{(\boldsymbol{n}\cdot\boldsymbol{t}_u)(\boldsymbol{t}\cdot\boldsymbol{t}_u)}{1+\boldsymbol{t}\cdot\boldsymbol{t}_u}(\boldsymbol{t}\times\boldsymbol{t}_u)\cdot\boldsymbol{n}\\
&\quad - \frac{(\boldsymbol{b}\cdot\boldsymbol{t}_u)(\boldsymbol{n}\cdot\boldsymbol{t}_u)}{(1+\boldsymbol{t}\cdot\boldsymbol{t}_u)^2}|\boldsymbol{t}\times\boldsymbol{t}_u|^2 + (\boldsymbol{n}\cdot\boldsymbol{t}_u)(\boldsymbol{b}\cdot\boldsymbol{t}_u)\\
&= -\frac{2(\boldsymbol{b}\cdot\boldsymbol{t}_u)(\boldsymbol{t}\cdot\boldsymbol{t}_u)(\boldsymbol{n}\cdot\boldsymbol{t}_u)}{1+\boldsymbol{t}\cdot\boldsymbol{t}_u} + (\boldsymbol{n}\cdot\boldsymbol{t}_u)(\boldsymbol{b}\cdot\boldsymbol{t}_u)\left(1-\frac{|\boldsymbol{t}\times\boldsymbol{t}_u|^2}{(1+\boldsymbol{t}\cdot\boldsymbol{t}_u)^2}\right)\\
&= -\frac{2(\boldsymbol{b}\cdot\boldsymbol{t}_u)(\boldsymbol{t}\cdot\boldsymbol{t}_u)(\boldsymbol{n}\cdot\boldsymbol{t}_u)}{1+\boldsymbol{t}\cdot\boldsymbol{t}_u} + (\boldsymbol{n}\cdot\boldsymbol{t}_u)(\boldsymbol{b}\cdot\boldsymbol{t}_u)\frac{2(\boldsymbol{t}\cdot\boldsymbol{t}_u)}{1+\boldsymbol{t}\cdot\boldsymbol{t}_u}\\
&= 0\,.
\end{aligned}
$$

Finally, using

$$
\begin{aligned}
\boldsymbol{t}_u &= (\boldsymbol{t}_u\cdot\boldsymbol{t})\boldsymbol{t} + (\boldsymbol{t}_u\cdot\boldsymbol{n})\boldsymbol{n} + (\boldsymbol{t}_u\cdot\boldsymbol{b})\boldsymbol{b}\,,\\
(\boldsymbol{t}\times\boldsymbol{t}_u) &= ((\boldsymbol{t}\times\boldsymbol{t}_u)\cdot\boldsymbol{t})\boldsymbol{t} + ((\boldsymbol{t}\times\boldsymbol{t}_u)\cdot\boldsymbol{n})\boldsymbol{n} + ((\boldsymbol{t}\times\boldsymbol{t}_u)\cdot\boldsymbol{b})\boldsymbol{b} = (\boldsymbol{n}\cdot\boldsymbol{t}_u)\boldsymbol{b} - (\boldsymbol{b}\cdot\boldsymbol{t}_u)\boldsymbol{n}\,,
\end{aligned}
$$

we conclude

$$
\begin{aligned}
\boldsymbol{t}_u\times\boldsymbol{n}_u &= (\boldsymbol{t}\cdot\boldsymbol{t}_u)(\boldsymbol{t}_u\times\boldsymbol{n}) - \frac{\boldsymbol{b}\cdot\boldsymbol{t}_u}{1+\boldsymbol{t}\cdot\boldsymbol{t}_u}\boldsymbol{t}_u\times(\boldsymbol{t}\times\boldsymbol{t}_u) - (\boldsymbol{n}\cdot\boldsymbol{t}_u)(\boldsymbol{t}_u\times\boldsymbol{t})\\
&= (\boldsymbol{t}\cdot\boldsymbol{t}_u)^2\boldsymbol{b} - (\boldsymbol{t}\cdot\boldsymbol{t}_u)(\boldsymbol{b}\cdot\boldsymbol{t}_u)\boldsymbol{t} - \frac{\boldsymbol{b}\cdot\boldsymbol{t}_u}{1+\boldsymbol{t}\cdot\boldsymbol{t}_u}(\boldsymbol{t}-\boldsymbol{t}_u(\boldsymbol{t}\cdot\boldsymbol{t}_u)) + \frac{(\boldsymbol{n}\cdot\boldsymbol{t}_u)(1+\boldsymbol{t}\cdot\boldsymbol{t}_u)}{1+\boldsymbol{t}\cdot\boldsymbol{t}_u}(\boldsymbol{t}\times\boldsymbol{t}_u)\\
&= \frac{(\boldsymbol{t}\cdot\boldsymbol{t}_u)^2+(\boldsymbol{t}\cdot\boldsymbol{t}_u)^3}{1+\boldsymbol{t}\cdot\boldsymbol{t}_u}\boldsymbol{b} - (\boldsymbol{b}\cdot\boldsymbol{t}_u)\frac{\boldsymbol{t}\cdot\boldsymbol{t}_u+(\boldsymbol{t}\cdot\boldsymbol{t}_u)^2+1}{1+\boldsymbol{t}\cdot\boldsymbol{t}_u}\boldsymbol{t}\\
&\quad + \frac{(\boldsymbol{b}\cdot\boldsymbol{t}_u)(\boldsymbol{t}\cdot\boldsymbol{t}_u)^2}{1+\boldsymbol{t}\cdot\boldsymbol{t}_u}\boldsymbol{t} + \frac{(\boldsymbol{b}\cdot\boldsymbol{t}_u)^2(\boldsymbol{t}\cdot\boldsymbol{t}_u)}{1+\boldsymbol{t}\cdot\boldsymbol{t}_u}\boldsymbol{b} + \frac{(\boldsymbol{b}\cdot\boldsymbol{t}_u)(\boldsymbol{t}\cdot\boldsymbol{t}_u)(\boldsymbol{n}\cdot\boldsymbol{t}_u)}{1+\boldsymbol{t}\cdot\boldsymbol{t}_u}\boldsymbol{n}\\
&\quad + \frac{\boldsymbol{n}\cdot\boldsymbol{t}_u}{1+\boldsymbol{t}\cdot\boldsymbol{t}_u}(\boldsymbol{t}\times\boldsymbol{t}_u) + \frac{(\boldsymbol{n}\cdot\boldsymbol{t}_u)(\boldsymbol{t}\cdot\boldsymbol{t}_u)}{1+\boldsymbol{t}\cdot\boldsymbol{t}_u}((\boldsymbol{n}\cdot\boldsymbol{t}_u)\boldsymbol{b} - (\boldsymbol{b}\cdot\boldsymbol{t}_u)\boldsymbol{n})\\
&= \frac{(\boldsymbol{t}\cdot\boldsymbol{t}_u)^2+(\boldsymbol{t}\cdot\boldsymbol{t}_u)^2(\boldsymbol{t}\cdot\boldsymbol{t}_u)+(\boldsymbol{b}\cdot\boldsymbol{t}_u)^2(\boldsymbol{t}\cdot\boldsymbol{t}_u)+(\boldsymbol{n}\cdot\boldsymbol{t}_u)^2(\boldsymbol{t}\cdot\boldsymbol{t}_u)}{1+\boldsymbol{t}\cdot\boldsymbol{t}_u}\boldsymbol{b}\\
&\quad + \frac{\boldsymbol{n}\cdot\boldsymbol{t}_u}{1+\boldsymbol{t}\cdot\boldsymbol{t}_u}(\boldsymbol{t}\times\boldsymbol{t}_u) - (\boldsymbol{b}\cdot\boldsymbol{t}_u)\frac{\boldsymbol{t}\cdot\boldsymbol{t}_u+1}{1+\boldsymbol{t}\cdot\boldsymbol{t}_u}\boldsymbol{t}\\
&= \frac{(\boldsymbol{t}\cdot\boldsymbol{t}_u)^2+\boldsymbol{t}\cdot\boldsymbol{t}_u}{1+\boldsymbol{t}\cdot\boldsymbol{t}_u}\boldsymbol{b} + \frac{\boldsymbol{n}\cdot\boldsymbol{t}_u}{1+\boldsymbol{t}\cdot\boldsymbol{t}_u}(\boldsymbol{t}\times\boldsymbol{t}_u) - (\boldsymbol{b}\cdot\boldsymbol{t}_u)\boldsymbol{t}\\
&= \boldsymbol{b}_u\,.
\end{aligned}
$$

■

In [49, p. 8], the following result is also provided.

Corollary 4.9. *Taylor's[3] formula yields the asymptotic expansions with respect to the magnitude*

[3] Brook Taylor (1685–1731)

of the perturbation $\boldsymbol{u}$

$$\left.\begin{aligned}
\boldsymbol{t}_{\boldsymbol{u}} &= \boldsymbol{t} + \frac{\boldsymbol{u}'}{|\boldsymbol{z}'|} - \frac{\boldsymbol{u}' \cdot \boldsymbol{t}}{|\boldsymbol{z}'|}\,\boldsymbol{t} + \mathrm{o}(\|\boldsymbol{u}\|_{C^2}) \\
&= \boldsymbol{t} + \frac{1}{|\boldsymbol{z}'|}((\boldsymbol{u}' \cdot \boldsymbol{n})\boldsymbol{n} + (\boldsymbol{u}' \cdot \boldsymbol{b})\boldsymbol{b}) + \mathrm{o}(\|\boldsymbol{u}\|_{C^2})\,, \\
\boldsymbol{n}_{\boldsymbol{u}} &= \boldsymbol{n} - \frac{\boldsymbol{u}' \cdot \boldsymbol{n}}{|\boldsymbol{z}'|}\,\boldsymbol{t} + \mathrm{o}(\|\boldsymbol{u}\|_{C^2})\,, \\
\boldsymbol{b}_{\boldsymbol{u}} &= \boldsymbol{b} - \frac{\boldsymbol{u}' \cdot \boldsymbol{b}}{|\boldsymbol{z}'|}\,\boldsymbol{t} + \mathrm{o}(\|\boldsymbol{u}\|_{C^2})\,.
\end{aligned}\right\} \tag{4.10}$$

Henceforward, we consider perturbations $(\boldsymbol{z} + \boldsymbol{u}, r + \delta) \in \mathcal{M}$ of $(\boldsymbol{z}, r) \in \mathcal{M}$ (definition of $\mathcal{M}$ in (4.9)), such that $(\boldsymbol{z} + \boldsymbol{u}, r + \delta)$ represents again a C^1-smooth tubular object and we denote perturbed quantities by an additional index $(\boldsymbol{u}, \delta)$.

Lemma 4.10. *Let ∂D denote a regular C^1-smooth surface represented by $(\boldsymbol{z}, r) \in \mathcal{M}$. The function $\boldsymbol{h}_{(\boldsymbol{u},\delta)}$ defined on ∂D by*

$$\boldsymbol{h}_{(\boldsymbol{u},\delta)}(\boldsymbol{x}) \coloneqq \boldsymbol{x}_{\ell,(\boldsymbol{u},\delta)}(\boldsymbol{x}_\ell^{-1}(\boldsymbol{x})) - \boldsymbol{x}\,, \qquad \boldsymbol{x} \in S_\ell\,, \quad \ell \in \{\text{body, start, end}\}\,, \tag{4.11}$$

for sufficiently small $\|(\boldsymbol{u}, \delta)\|_{C^2 \times C^1}$, is C^1-smooth on ∂D and depends smoothly on the quantities $\boldsymbol{u}, \boldsymbol{u}', \boldsymbol{u}'', \delta, \delta'$ in $C^1(\partial D)$.

Proof. From (4.3), (4.7), it is clear that in the neighborhood of almost every point on ∂D, with the exceptions of the points $\boldsymbol{z}(0) - r(0)\,\boldsymbol{t}(0)$, $\boldsymbol{z}(1) + r(1)\,\boldsymbol{t}(1)$ on the caps, the charts are diffeomorphisms. Then, for sufficiently small $\|(\boldsymbol{u}, \delta)\|_{C^2 \times C^1}$, by definition, $\boldsymbol{h}_{(\boldsymbol{u},\delta)}$ is C^1-smooth except at these isolated points. In a neighborhood of these points, we may instead use a regular parameterization of the surface, for example by projection on the tangential plane, to extend the definition.

An inspection of the asymptotic formulae in (4.10) together with (4.2), (4.6) and (4.3), (4.7) reveals that $\boldsymbol{x}_{\text{body}}$ depends smoothly on $\boldsymbol{u}$, $\boldsymbol{u}'$ and δ, while $\boldsymbol{x}_{\text{start}}$ and $\boldsymbol{x}_{\text{end}}$ also depend on $\boldsymbol{u}''(0)$, $\delta'(0)$ and $\boldsymbol{u}''(1)$, $\delta'(1)$, respectively. Straightforward calculations then yield that all three charts and their inverses smoothly depend on $\boldsymbol{u}$, $\boldsymbol{u}'$, $\boldsymbol{u}''$, δ, δ'. The same is consequently true for $\boldsymbol{h}_{(\boldsymbol{u},\delta)}$. ∎

In view of the surface linearization, we derive a first order approximation $\boldsymbol{h}$ of $\boldsymbol{h}_{(\boldsymbol{u},\delta)}$ and an explicit formula of the same. To this end, we need to compute asymptotic expansions for the perturbations of the quantities involved in the tubular surface's parameterizations (with respect to the magnitude of the perturbations of $\boldsymbol{z}$ and r).

Lemma 4.11. *Recall the definitions of $\boldsymbol{\zeta}$ from (4.2), ψ from Lemma 4.3, $\boldsymbol{\xi}_\ell$, $\ell \in \{\text{start}, \text{end}\}$, from (4.6), and η_i, $i \in \{0, 1\}$, from (4.8). There hold*

$$\boldsymbol{\zeta}_{\boldsymbol{u}} = \boldsymbol{\zeta} - \frac{\boldsymbol{u}' \cdot \boldsymbol{\zeta}}{|\boldsymbol{z}'|}\,\boldsymbol{t} + \mathrm{o}(\|\boldsymbol{u}\|_{C^1}) \qquad \text{as } \|\boldsymbol{u}\|_{C^1} \to 0\,,$$

as well as

$$\psi_{(\boldsymbol{u},\delta)} = \psi - (\boldsymbol{t}' \cdot \boldsymbol{\zeta})\delta + \boldsymbol{u}' \cdot \boldsymbol{t} - r\left(\frac{\boldsymbol{u}''}{|\boldsymbol{z}'|} - \frac{\boldsymbol{u}' \cdot \boldsymbol{t}}{|\boldsymbol{z}'|^2}\,\boldsymbol{z}'' - \frac{\boldsymbol{z}'' \cdot \boldsymbol{t}}{|\boldsymbol{z}'|^2}\,\boldsymbol{u}'\right) \cdot \boldsymbol{\zeta} + \mathrm{o}(\|\boldsymbol{u}\|_{\boldsymbol{C}^2} + \|\delta\|_{C^1})\,,$$

$$\rho_{i,(\boldsymbol{u},\delta)} = \rho_i + \sum_{j=0}^{1} \mu_{j,i}\,\delta^{(j)}(i) + \sum_{j=1}^{2} \boldsymbol{\nu}_{j,i} \cdot \boldsymbol{u}^{(j)}(i) + \mathrm{o}(\|\boldsymbol{u}\|_{\boldsymbol{C}^2} + \|\delta\|_{C^1})\,, \qquad i \in \{0,1\}\,,$$

as $\|\boldsymbol{u}\|_{\boldsymbol{C}^2}, \|\delta\|_{C^1} \to 0$*, where with*

$$\alpha_i(\varphi) \coloneqq \begin{cases} \pi/2 - \varphi\,, & i = 0\,, \\ \varphi\,, & i = 1\,, \end{cases} \qquad \varphi \in (-\pi, \pi]\,,$$

we define

$$\mu_{0,i}(\vartheta,\varphi) \coloneqq 1 + \frac{\eta_i(\vartheta,\varphi)}{r(i)} + \frac{\eta_i(\vartheta,\varphi)}{\psi(i,\alpha_i(\varphi))}\,\boldsymbol{t}'(i) \cdot \boldsymbol{\zeta}(i,\alpha_i(\varphi))\,, \qquad \mu_{1,i}(\vartheta,\varphi) \coloneqq \frac{\eta_i(\vartheta,\varphi)}{r'(i)}\,,$$

and

$$\boldsymbol{\nu}_{1,i}(\vartheta,\varphi) \coloneqq -\frac{\eta_i(\vartheta,\varphi)}{\psi(i,\alpha_i(\varphi))}\left(\left(1 + \frac{r(i)\,\boldsymbol{z}''(i) \cdot \boldsymbol{\zeta}(i,\alpha_i(\varphi))}{|\boldsymbol{z}'(i)|^2}\right)\boldsymbol{t}(i) + \frac{r(i)\,\boldsymbol{z}''(i) \cdot \boldsymbol{t}(i)}{|\boldsymbol{z}'(i)|^2}\,\boldsymbol{\zeta}(i,\alpha_i(\varphi))\right),$$

$$\boldsymbol{\nu}_{2,i}(\vartheta,\varphi) \coloneqq \frac{r(i)\,\eta_i(\vartheta,\varphi)}{\psi(i,\alpha_i(\varphi))\,|\boldsymbol{z}'(i)|}\,\boldsymbol{\zeta}(i,\alpha_i(\varphi))\,,$$

for $i \in \{0,1\}$*,* $\varphi \in (-\pi,\pi]$ *and* $\vartheta \in [0,\pi/2]$*. Moreover, it holds that*

$$\boldsymbol{\xi}_{\ell,\boldsymbol{u}}(\vartheta,\varphi) = \boldsymbol{\xi}_\ell(\vartheta,\varphi) + (-1)^{i+1}\cos\vartheta\,\frac{\boldsymbol{u}'(i)}{|\boldsymbol{z}'(i)|} - \frac{\boldsymbol{\xi}_\ell(\vartheta,\varphi) \cdot \boldsymbol{u}'(i)}{|\boldsymbol{z}'(i)|}\,\boldsymbol{t}(i) + \mathrm{o}(\|\boldsymbol{u}\|_{\boldsymbol{C}^1})$$

as $\|\boldsymbol{u}\|_{\boldsymbol{C}^1} \to 0$*, for* $(\ell,i) \in \{(\mathrm{start},0),(\mathrm{end},1)\}$*,* $\varphi \in (-\pi,\pi]$ *and* $\vartheta \in [0,\pi/2]$*.*

Proof. With (4.10) we conclude

$$\boldsymbol{\zeta}_{\boldsymbol{u}} = \cos\varphi\left(\boldsymbol{n} - \frac{\boldsymbol{u}' \cdot \boldsymbol{n}}{|\boldsymbol{z}'|}\,\boldsymbol{t}\right) + \sin\varphi\left(\boldsymbol{b} - \frac{\boldsymbol{u}' \cdot \boldsymbol{b}}{|\boldsymbol{z}'|}\,\boldsymbol{t}\right) + \mathrm{o}(\|\boldsymbol{u}\|_{C^1}) = \boldsymbol{\zeta} - \frac{\boldsymbol{u}' \cdot \boldsymbol{\zeta}}{|\boldsymbol{z}'|}\,\boldsymbol{t} + \mathrm{o}(\|\boldsymbol{u}\|_{\boldsymbol{C}^1})$$

as $\|\boldsymbol{u}\|_{\boldsymbol{C}^1} \to 0$. Furthermore, using the linearization formula

$$\frac{1}{|\boldsymbol{x}+\boldsymbol{h}|} = \frac{1}{|\boldsymbol{x}|} - \frac{\boldsymbol{x} \cdot \boldsymbol{h}}{|\boldsymbol{x}|^3} + \mathrm{o}(|\boldsymbol{h}|)\,, \qquad |\boldsymbol{h}| \to 0\,,$$

and (4.10), we obtain

$$\begin{aligned}\boldsymbol{t}'_{\boldsymbol{u}} &= \frac{\boldsymbol{z}'' + \boldsymbol{u}''}{|\boldsymbol{z}' + \boldsymbol{u}'|} - \frac{(\boldsymbol{z}' + \boldsymbol{u}') \cdot (\boldsymbol{z}'' + \boldsymbol{u}'')}{|\boldsymbol{z}' + \boldsymbol{u}'|^3}\,(\boldsymbol{z}' + \boldsymbol{u}') = \frac{\boldsymbol{z}'' + \boldsymbol{u}''}{|\boldsymbol{z}' + \boldsymbol{u}'|} - \left(\boldsymbol{t}_{\boldsymbol{u}} \cdot \frac{\boldsymbol{z}'' + \boldsymbol{u}''}{|\boldsymbol{z}' + \boldsymbol{u}'|}\right)\boldsymbol{t}_{\boldsymbol{u}} \\ &= \boldsymbol{t}' + \frac{\boldsymbol{z}' \cdot \boldsymbol{u}'}{|\boldsymbol{z}'|^3}\,(\boldsymbol{t}(\boldsymbol{z}'' \cdot \boldsymbol{t}) - \boldsymbol{z}'') + \frac{\boldsymbol{u}''}{|\boldsymbol{z}'|} - \frac{\boldsymbol{t} \cdot \boldsymbol{u}''}{|\boldsymbol{z}'|}\,\boldsymbol{t} + \frac{\boldsymbol{z}'' \cdot \boldsymbol{u}'}{|\boldsymbol{z}'|^2}\,\boldsymbol{t} - \frac{\boldsymbol{t} \cdot \boldsymbol{z}''}{|\boldsymbol{z}'|^2}\,\boldsymbol{u}' + 2\,\frac{(\boldsymbol{t} \cdot \boldsymbol{z}'')(\boldsymbol{t} \cdot \boldsymbol{u}')}{|\boldsymbol{z}'|^2}\,\boldsymbol{t} \\ &\quad + \mathrm{o}(\|\boldsymbol{u}\|_{\boldsymbol{C}^2})\end{aligned}$$

$$= \boldsymbol{t}' + \frac{\boldsymbol{u}''}{|\boldsymbol{z}'|} - \frac{\boldsymbol{t}\cdot\boldsymbol{u}'}{|\boldsymbol{z}'|^2}\,\boldsymbol{z}'' - \frac{\boldsymbol{t}\cdot\boldsymbol{z}''}{|\boldsymbol{z}'|^2}\,\boldsymbol{u}' - \left(\frac{\boldsymbol{t}\cdot\boldsymbol{u}''}{|\boldsymbol{z}'|} - \frac{\boldsymbol{u}'\cdot\boldsymbol{z}''}{|\boldsymbol{z}'|^2} - \frac{3(\boldsymbol{t}\cdot\boldsymbol{z}'')(\boldsymbol{t}\cdot\boldsymbol{u}')}{|\boldsymbol{z}'|^2}\right)\boldsymbol{t} + \mathrm{o}(\|\boldsymbol{u}\|_{C^2})$$

as $\|\boldsymbol{u}\|_{C^2} \to 0$. Thus, using $\boldsymbol{t}'\cdot\boldsymbol{t} = 0$ and collecting all higher-order terms, we have the scalar product

$$\boldsymbol{t}'_{\boldsymbol{u}}\cdot\boldsymbol{\zeta}_{\boldsymbol{u}} = \boldsymbol{t}'_{\boldsymbol{u}}\cdot\boldsymbol{\zeta} + \mathrm{o}(\|\boldsymbol{u}\|_{C^2}) = \left(\boldsymbol{t}' + \frac{\boldsymbol{u}''}{|\boldsymbol{z}'|} - \frac{\boldsymbol{t}\cdot\boldsymbol{u}'}{|\boldsymbol{z}'|^2}\,\boldsymbol{z}'' - \frac{\boldsymbol{t}\cdot\boldsymbol{z}''}{|\boldsymbol{z}'|^2}\,\boldsymbol{u}'\right)\cdot\boldsymbol{\zeta} + \mathrm{o}(\|\boldsymbol{u}\|_{C^2})$$

as $\|\boldsymbol{u}\|_{C^2} \to 0$. Then, the linearization formula

$$|\boldsymbol{x}+\boldsymbol{h}| = |\boldsymbol{x}| + \frac{\boldsymbol{x}\cdot\boldsymbol{h}}{|\boldsymbol{x}|} + \mathrm{o}(|\boldsymbol{h}|)\,, \qquad |\boldsymbol{h}| \to 0\,,$$

yields

$$\begin{aligned}
\psi_{(\boldsymbol{u},\delta)} &= |\boldsymbol{z}'| + \frac{\boldsymbol{z}'\cdot\boldsymbol{u}'}{|\boldsymbol{z}'|} - (r+\delta)\,\boldsymbol{t}'_{\boldsymbol{u}}\cdot\boldsymbol{\zeta}_{\boldsymbol{u}} + \mathrm{o}(\|\boldsymbol{u}\|_{C^2} + \|\delta\|_{C^1}) \\
&= |\boldsymbol{z}'| + \boldsymbol{t}\cdot\boldsymbol{u}' - r\left(\boldsymbol{t}' + \frac{\boldsymbol{u}''}{|\boldsymbol{z}'|} - \frac{\boldsymbol{t}\cdot\boldsymbol{u}'}{|\boldsymbol{z}'|^2}\,\boldsymbol{z}'' - \frac{\boldsymbol{t}\cdot\boldsymbol{z}''}{|\boldsymbol{z}'|^2}\,\boldsymbol{u}'\right)\cdot\boldsymbol{\zeta} - \delta(\boldsymbol{t}_{\boldsymbol{u}}\cdot\boldsymbol{\zeta}) + \mathrm{o}(\|\boldsymbol{u}\|_{C^2} + \|\delta\|_{C^1}) \\
&= \psi - \delta(\boldsymbol{t}_{\boldsymbol{u}}\cdot\boldsymbol{\zeta}) + \boldsymbol{t}\cdot\boldsymbol{u}' - r\left(\frac{\boldsymbol{u}''}{|\boldsymbol{z}'|} - \frac{\boldsymbol{t}\cdot\boldsymbol{u}'}{|\boldsymbol{z}'|^2}\,\boldsymbol{z}'' - \frac{\boldsymbol{t}\cdot\boldsymbol{z}''}{|\boldsymbol{z}'|^2}\,\boldsymbol{u}'\right)\cdot\boldsymbol{\zeta} + \mathrm{o}(\|\boldsymbol{u}\|_{C^2} + \|\delta\|_{C^1})
\end{aligned}$$

as $\|\boldsymbol{u}\|_{C^2} + \|\delta\|_{C^1} \to 0$. Next, we define

$$\alpha_i(\varphi) = \begin{cases} \pi/2 - \varphi\,, & i = 0\,, \\ \varphi\,, & i = 1\,, \end{cases} \qquad \varphi \in (-\pi, \pi]\,.$$

Using the linearization formula

$$\frac{1}{x+h} = \frac{1}{x} - \frac{h}{x^2} + \mathrm{o}(h)\,, \qquad \text{as } h \to 0\,,$$

we obtain for $i \in \{0,1\}$, $\varphi \in (-\pi,\pi]$ and $\vartheta \in [0,\pi/2]$ that

$$\begin{aligned}
&\rho_{i,(\boldsymbol{u},\delta)}(\vartheta,\varphi) \\
&= r(i) + \delta(i) + (-1)^i\,\frac{4\vartheta^2\,(\vartheta - \pi/2)\;(r+\delta)(i)\,(r'+\delta')(i)}{\pi^2\,\psi_{(\boldsymbol{u},\delta)}(i,\alpha_i(\varphi))} \\
&= r(i) + \delta(i) + (-1)^i\,\frac{4\vartheta^2\,(\vartheta - \pi/2)}{\pi^2}\left[\frac{r(i)\,r'(i) + r(i)\,\delta'(i) + r'(i)\,\delta(i)}{\psi(i,\alpha_i(\varphi))} - \frac{r(i)\,r'(i)}{\psi^2(i,\alpha_i(\varphi))}\right. \\
&\quad \left(-\delta(i)(\boldsymbol{t}_{\boldsymbol{u}}(i)\cdot\boldsymbol{\zeta}(i,\alpha_i(\varphi))) + \boldsymbol{t}(i)\cdot\boldsymbol{u}'(i) - r(i)\left[\frac{\boldsymbol{u}''(i)}{|\boldsymbol{z}'(i)|} - \frac{\boldsymbol{t}(i)\cdot\boldsymbol{u}'(i)}{|\boldsymbol{z}'(i)|^2}\,\boldsymbol{z}''(i) - \frac{\boldsymbol{t}(i)\cdot\boldsymbol{z}''(i)}{|\boldsymbol{z}'(i)|^2}\,\boldsymbol{u}'(i)\right]\right. \\
&\qquad \left.\left.\cdot\,\boldsymbol{\zeta}(i,\alpha_i(\varphi))\right)\right] + \mathrm{o}(\|\boldsymbol{u}\|_{C^2} + \|\delta\|_{C^1}) \\
&= \rho_i(\vartheta,\varphi) + \left(1 + \frac{\eta_i(\vartheta,\varphi)}{r(i)} + \frac{\eta_i(\vartheta,\varphi)}{\psi(i,\alpha_i(\varphi))}\,\boldsymbol{t}'(i)\cdot\boldsymbol{\zeta}(i,\alpha_i(\varphi))\right)\delta(i) + \frac{\eta_i(\vartheta,\varphi)}{r'(i)}\,\delta'(i)
\end{aligned}$$

$$- \frac{\eta_i(\vartheta,\varphi)}{\psi(i,\alpha_i(\varphi))}\left[\left(1+\frac{r(i)(\boldsymbol{z}''(i)\cdot\boldsymbol{\zeta}(i,\alpha_i(\varphi)))}{|\boldsymbol{z}'(i)|^2}\right)\boldsymbol{t}(i)+\frac{r(i)(\boldsymbol{z}''(i)\cdot\boldsymbol{t}(i))}{|\boldsymbol{z}'(i)|^2}\,\boldsymbol{\zeta}(i,\alpha_i(\varphi))\right]\cdot\boldsymbol{u}'(i)$$

$$+\frac{\eta_i(\vartheta,\varphi)\,r(i)}{\psi(i,\alpha_i(\varphi))\,|\boldsymbol{z}'(i)|}\left(\boldsymbol{\zeta}(i,\alpha_i(\varphi))\cdot\boldsymbol{u}''(i)\right)+\mathrm{o}(\|\boldsymbol{u}\|_{\boldsymbol{C}^2}+\|\delta\|_{C^1})$$

as $\|\boldsymbol{u}\|_{\boldsymbol{C}^2}+\|\delta\|_{C^1}\to 0$.

Finally, with (4.10) we conclude

$$\begin{aligned}\boldsymbol{\xi}_{\mathrm{start},\boldsymbol{u}}(\vartheta,\varphi)&=\boldsymbol{\xi}_{\mathrm{start}}(\vartheta,\varphi)-\cos\vartheta\,\frac{\boldsymbol{u}'(0)}{|\boldsymbol{z}'(0)|}-\cos\varphi\sin\vartheta\,\frac{\boldsymbol{u}'(0)\cdot\boldsymbol{b}(0)}{|\boldsymbol{z}'(0)|}\,\boldsymbol{t}(0)\\&\quad-\sin\varphi\sin\vartheta\,\frac{\boldsymbol{u}'(0)\cdot\boldsymbol{n}(0)}{|\boldsymbol{z}'(0)|}\,\boldsymbol{t}(0)+\cos\vartheta\,\frac{\boldsymbol{u}'(0)\cdot\boldsymbol{t}(0)}{|\boldsymbol{z}'(0)|}\,\boldsymbol{t}(0)+\mathrm{o}(\|\boldsymbol{u}\|_{C^1})\\&=\boldsymbol{\xi}_{\mathrm{start}}(\vartheta,\varphi)-\cos\vartheta\,\frac{\boldsymbol{u}'(0)}{|\boldsymbol{z}'(0)|}-\frac{1}{|\boldsymbol{z}'(0)|}\left(\boldsymbol{u}'(0)\cdot\boldsymbol{\xi}_{\mathrm{start}}(\vartheta,\varphi)\right)\boldsymbol{t}(0)+\mathrm{o}(\|\boldsymbol{u}\|_{\boldsymbol{C}^1})\end{aligned}$$

as $\|\boldsymbol{u}\|_{\boldsymbol{C}^1}\to 0$, for $\varphi\in(-\pi,\pi]$ and $\vartheta\in[0,\pi/2]$. Analogously, this can be carried out for $\boldsymbol{\xi}_{\mathrm{end},\boldsymbol{u}}$. ■

By Lemma 4.11, we can immediately obtain an explicit formula for $\boldsymbol{h}$.

Corollary 4.12. *Let $\tau\in[0,1]$, $\varphi\in(-\pi,\pi]$ and $\vartheta\in[0,\pi/2]$. The first order approximation $\boldsymbol{h}$ of $\boldsymbol{h}_{(\boldsymbol{u},\delta)}$ (see (4.11) for the definition) with respect to $(\boldsymbol{u},\delta)$ is given by*

$$\boldsymbol{h}(\boldsymbol{x})=\begin{cases}\boldsymbol{h}_{\mathrm{body}}(\boldsymbol{x})\,, & \boldsymbol{x}=\boldsymbol{x}_{\mathrm{body}}(\tau,\varphi)\,,\\ \boldsymbol{h}_{\mathrm{start}}(\boldsymbol{x})\,, & \boldsymbol{x}=\boldsymbol{x}_{\mathrm{start}}(\vartheta,\varphi)\,,\\ \boldsymbol{h}_{\mathrm{end}}(\boldsymbol{x})\,, & \boldsymbol{x}=\boldsymbol{x}_{\mathrm{end}}(\vartheta,\varphi)\,,\end{cases}$$

where

$$\begin{aligned}\boldsymbol{h}_{\mathrm{body}}(\boldsymbol{x})&=\boldsymbol{u}(\tau)-\frac{r(\tau)\,\boldsymbol{u}'(\tau)\cdot\boldsymbol{\zeta}(\tau,\varphi)}{|\boldsymbol{z}'(\tau)|}\,\boldsymbol{t}(\tau)+\delta(\tau)\,\boldsymbol{\zeta}(\tau,\varphi)\,,\\ \boldsymbol{h}_{\mathrm{start}}(\boldsymbol{x})&=\boldsymbol{u}(0)-\rho_0(\vartheta,\varphi)\,\frac{\cos(\vartheta)}{|\boldsymbol{z}'(0)|}\,\boldsymbol{u}'(0)-\rho_0(\vartheta,\varphi)\,\frac{\boldsymbol{\xi}_{\mathrm{start}}(\vartheta,\varphi)\cdot\boldsymbol{u}'(0)}{|\boldsymbol{z}'(0)|}\,\boldsymbol{t}(0)\\&\quad+\Big(\sum_{j=0}^{1}\mu_{j,0}(\vartheta,\varphi)\,\delta^{(j)}(0)+\sum_{j=1}^{2}\boldsymbol{\nu}_{j,0}(\vartheta,\varphi)\cdot\boldsymbol{u}^{(j)}(0)\Big)\boldsymbol{\xi}_{\mathrm{start}}(\vartheta,\varphi)\,,\\ \boldsymbol{h}_{\mathrm{end}}(\boldsymbol{x})&=\boldsymbol{u}(1)+\rho_1(\vartheta,\varphi)\,\frac{\cos(\vartheta)}{|\boldsymbol{z}'(1)|}\,\boldsymbol{u}'(1)-\rho_1(\vartheta,\varphi)\,\frac{\boldsymbol{\xi}_{\mathrm{end}}(\vartheta,\varphi)\cdot\boldsymbol{u}'(1)}{|\boldsymbol{z}'(1)|}\,\boldsymbol{t}(1)\\&\quad+\Big(\sum_{j=0}^{1}\mu_{j,1}(\vartheta,\varphi)\,\delta^{(j)}(1)+\sum_{j=1}^{2}\boldsymbol{\nu}_{j,1}(\vartheta,\varphi)\cdot\boldsymbol{u}^{(j)}(1)\Big)\boldsymbol{\xi}_{\mathrm{end}}(\vartheta,\varphi)\,,\end{aligned}$$

with the coefficient functions defined in Lemma 4.11.

Proof. By definition (4.11), it holds that

$$\boldsymbol{x}_{\ell,(\boldsymbol{u},\delta)}\;=\;\boldsymbol{x}_\ell+\boldsymbol{h}\circ\boldsymbol{x}_\ell+\mathrm{o}(\|\boldsymbol{u}\|_{\boldsymbol{C}^2}+\|\delta\|_{C^1}),\qquad \ell\in\{\mathrm{body},\mathrm{start},\mathrm{end}\}\,,$$

as $\|\boldsymbol{u}\|_{\boldsymbol{C}^2}$, $\|\delta\|_{C^1} \to 0$. We have that

$$\begin{aligned}\boldsymbol{x}_{\mathrm{body},(\boldsymbol{u},\delta)}(\tau,\varphi) = \boldsymbol{z}(\tau) + \boldsymbol{u}(\tau) + \delta(\tau)\boldsymbol{\zeta}(\tau,\varphi)\\ + r(\tau)\left(\cos(\varphi)\,\boldsymbol{n}_{\boldsymbol{u}}(\tau) + \sin(\varphi)\,\boldsymbol{b}_{\boldsymbol{u}}(\tau)\right) + \mathrm{o}\big(\|\boldsymbol{u}\|_{\boldsymbol{C}^1} + \|\delta\|_{\infty}\big)\end{aligned}$$

as $\|\boldsymbol{u}\|_{\boldsymbol{C}^1} + \|\delta\|_{\infty} \to 0$, where $\tau \in [0,1]$ and $\varphi \in (-\pi,\pi]$. Inserting the asymptotic expansions from (4.10) then gives the result of the corollary for $\boldsymbol{x} = \boldsymbol{x}_{\mathrm{body}}(\tau,\varphi)$. Likewise, it holds that

$$\begin{aligned}\boldsymbol{x}_{\ell,(\boldsymbol{u},\delta)}(\vartheta,\varphi) = \boldsymbol{x}_{\ell}(\vartheta,\varphi) + \rho_{\tau}(\vartheta,\varphi)\left(\boldsymbol{\xi}_{\ell,\boldsymbol{u}}(\vartheta,\varphi) - \boldsymbol{\xi}_{\ell}(\vartheta,\varphi)\right)\\ + \boldsymbol{\xi}_{\ell}(\vartheta,\varphi)\left(\rho_{\tau,(\boldsymbol{u},\delta)}(\vartheta,\varphi) - \rho_{\tau}(\vartheta,\varphi)\right) + \mathrm{o}\big(\|\boldsymbol{u}\|_{\boldsymbol{C}^2} + \|\delta\|_{C^1}\big)\end{aligned}$$

as $\|\boldsymbol{u}\|_{\boldsymbol{C}^2} + \|\delta\|_{C^1} \to 0$, where $(\ell,\tau) \in \{(\mathrm{start},0),(\mathrm{end},1)\}$, $\vartheta \in [0,\pi/2]$ and $\varphi \in (-\pi,\pi]$. The remaining assertion follows from Lemma 4.11. ■

4.2. Domain Derivatives for Long Tubular Objects

In what follows, we derive a characterization of the Fréchet derivative of the far-field map and operator via the domain derivative (cf. Chapter 3) for boundaries ∂D represented by $(\boldsymbol{z},r) \in \mathcal{M} \subseteq \boldsymbol{C}^2([0,1],\mathbb{R}^3) \times C^1([0,1],\mathbb{R})$ (cf. (4.9)) with respect to perturbations $(\boldsymbol{u},\delta)$. One cannot simply apply Corollary 3.10, because $\boldsymbol{h}_{(\boldsymbol{u},\delta)}$ lives on the boundary and does not satisfy the mandatory conditions. Furthermore, for boundaries ∂D, which are represented by $(\boldsymbol{z},r) \in \mathcal{M}$, the perturbed domain $\partial D_{\boldsymbol{h}}$ may not have such a representation. We avoid this difficulty and stay in the class of admissible domains by directly perturbing $(\boldsymbol{z},r) \in \mathcal{M}$. Thus, we fix an incident field $(\boldsymbol{E}^i,\boldsymbol{H}^i) \in \boldsymbol{H}_{\mathrm{loc}}(\mathbf{curl},\mathbb{R}^3) \times \boldsymbol{H}_{\mathrm{loc}}(\mathbf{curl},\mathbb{R}^3)$ that solves Maxwell's equations and induces the scattered field $(\boldsymbol{E}^s,\boldsymbol{H}^s) \in \boldsymbol{H}(\mathbf{curl},\mathfrak{X}) \times \boldsymbol{H}(\mathbf{curl},\mathfrak{X})$ (cf. Definition 3.3 for the notation), which is a weak solution to the scattering problem (2.22) or (2.24) together with the SMRC (2.20). Then we define the far-field map

$$F\colon \mathcal{M} \to \boldsymbol{L}_t^2(\mathbb{S}^2)\,, \qquad F(\boldsymbol{z},r) = \boldsymbol{E}^{\infty}\,,$$

where $\boldsymbol{E}^{\infty}$ is the far-field pattern of $\boldsymbol{E}^s$ that corresponds to the boundary ∂D represented by $(\boldsymbol{z},r)$. Analogously, we define the far-field operator $\mathcal{F}$, mapping $(\boldsymbol{z},r) \in \mathcal{M}$ to a linear operator that maps $\boldsymbol{L}_t^2(\mathbb{S}^2)$ onto itself, i.e., we have $(\boldsymbol{z},r) \mapsto \mathcal{F}(\boldsymbol{z},r)$ with

$$\mathcal{F}(\boldsymbol{z},r)\colon \boldsymbol{L}_t^2(\mathbb{S}^2) \to \boldsymbol{L}_t^2(\mathbb{S}^2)\,, \qquad \mathcal{F}(\boldsymbol{z},r)\boldsymbol{\varphi} = \boldsymbol{E}^{\infty}[\boldsymbol{\varphi}]\,.$$

Note that – in a slight abuse of notation – we use the same notation for the far-field map and operator as before.

In the next theorem, we show differentiability of the far-field map F.

Theorem 4.13. *Let ∂D denote a regular C^1-surface represented by $(\boldsymbol{z},r) \in \mathcal{M}$ (see (4.9)). Let*

$\boldsymbol{h} \in \boldsymbol{C}^1(\partial D, \mathbb{R}^3)$ denote the linearization of $\boldsymbol{h}_{(\boldsymbol{u},\delta)}$ with respect to $(\boldsymbol{u}, \delta)$, so that

$$\lim_{\|\boldsymbol{u}\|_{\boldsymbol{C}^2}, \|\delta\|_{C^1} \to 0} \frac{\|\boldsymbol{h}_{(\boldsymbol{u},\delta)} - \boldsymbol{h}\|_{\boldsymbol{C}^1}}{\|\boldsymbol{u}\|_{\boldsymbol{C}^2} + \|\delta\|_{C^1}} = 0\,. \tag{4.12}$$

The far-field map F is Fréchet differentiable at $(\boldsymbol{z}, r)$. With $\boldsymbol{h}$ as given above, $F'[\boldsymbol{z}, r](\boldsymbol{u}, \delta)$ is equal to the far-field pattern $\boldsymbol{E}'^{\infty}$ of the weak solution $\boldsymbol{E}'$ of (2.22a) *together with* (3.14) *in the case of a penetrable obstacle and* (2.24a) *together with* (3.15) *in the case of a perfectly conducting obstacle.*

Proof. In order for $F'[\partial D]\boldsymbol{h}_{(\boldsymbol{u},\delta)}$ to exist and to satisfy the formula $F'[\partial D]\boldsymbol{h}_{(\boldsymbol{u},\delta)} = \boldsymbol{E}'^{\infty}_{(\boldsymbol{u},\delta)}$, the vector field $\boldsymbol{h}_{(\boldsymbol{u},\delta)}$ from (4.11) needs to be extended to a compact neighborhood of ∂D. Here, we first extend it constantly to a tubular neighborhood of ∂D and multiply with a smooth cut-off function afterwards so that the extension has compact support. For this purpose, let $I \subset \mathbb{R}$ be a small neighborhood of 0 and denote by $\mathcal{S}_\sigma$ the C^1-smooth surface generated by $(\boldsymbol{z}, r + \sigma)$, for $\sigma \in I$. Then, $\mathcal{U} \coloneqq \bigcup_{\sigma \in I} \mathcal{S}_\sigma$ is an open neighborhood of ∂D. Let

$$\Psi(\boldsymbol{x}, \sigma) \coloneqq \boldsymbol{x} + \boldsymbol{h}_{(\boldsymbol{0},\sigma)}(\boldsymbol{x})\,, \qquad (\boldsymbol{x}, \sigma) \in \partial D \times I\,.$$

For any $(\boldsymbol{x}, \sigma) \in \partial D \times I$, it holds that $\Psi(\boldsymbol{x}, \sigma) \in \mathcal{S}_\sigma$. Moreover, Ψ is continuous. Now, let $\boldsymbol{x}^* \in \partial D$ and $U \subset \partial D$ be a relative open and sufficiently small neighborhood of $\boldsymbol{x}^*$ in ∂D. By the definition of a regular C^1-smooth domain, there exists an open $V \subset \mathbb{R}^2$ and a regular C^1 parameterization $\alpha\colon V \to U$. Now, let $\boldsymbol{y}^* \in V$ be such that $\alpha(\boldsymbol{y}^*) = \boldsymbol{x}^*$. With $\widetilde{\Psi}(\boldsymbol{y}, \sigma) = \Psi(\alpha(\boldsymbol{y}), \sigma)$ for $(\boldsymbol{y}, \sigma) \in V \times I$, we obtain for $\ell \in \{\mathrm{body}, \mathrm{start}, \mathrm{end}\}$

$$\widetilde{\Psi}(\boldsymbol{y}, \sigma) = \alpha(\boldsymbol{y}) + \boldsymbol{h}_{(\boldsymbol{0},\sigma)}(\alpha(\boldsymbol{y})) = \boldsymbol{x}_{\ell,(\boldsymbol{0},\sigma)}(\boldsymbol{x}_\ell^{-1}(\alpha(\boldsymbol{y})))\,, \quad \alpha(\boldsymbol{y}) \in \mathcal{S}_\ell \cap U\,.$$

Then, since $\boldsymbol{h}_{(\boldsymbol{0},0)}$ vanishes, it holds that

$$\begin{aligned}
\frac{\partial \widetilde{\Psi}(\boldsymbol{y}^*, 0)}{\partial y_j} &= \frac{\partial \alpha(\boldsymbol{y}^*)}{\partial y_j}\,,\\
\frac{\partial \widetilde{\Psi}(\boldsymbol{y}^*, 0)}{\partial \sigma} &= \lim_{\sigma \to 0} \frac{\Psi(\boldsymbol{x}^*, \sigma) - \Psi(\boldsymbol{x}^*, 0)}{\sigma} = \lim_{\sigma \to 0} \frac{\boldsymbol{h}_{(\boldsymbol{0},\sigma)}(\boldsymbol{x}^*)}{\sigma} = \lim_{\sigma \to 0} \frac{\widetilde{\boldsymbol{h}}(\boldsymbol{x}^*)}{\sigma}\,,
\end{aligned}$$

where $\widetilde{\boldsymbol{h}}$ denotes the linearization of $\boldsymbol{h}_{(\boldsymbol{0},\sigma)}$ with respect to σ. The regularity of α implies that $\partial_{y_1}\widetilde{\Psi}(\boldsymbol{y}^*, 0) \times \partial_{y_2}\widetilde{\Psi}(\boldsymbol{y}^*, 0) = c\boldsymbol{\nu}$ for some function $c \neq 0$. An inspection of $\widetilde{\boldsymbol{h}}$ in Corollary 4.12, together with the fact that the Jacobian $J_{\widetilde{\Psi}}$ of $\widetilde{\Psi}$ satisfies

$$\det(J_{\widetilde{\Psi}}) = (\partial_{y_1}\widetilde{\Psi}(\boldsymbol{y}^*, 0) \times \partial_{y_2}\widetilde{\Psi}(\boldsymbol{y}^*, 0)) \cdot \widetilde{\boldsymbol{h}} \neq 0\,,$$

yields that $J_{\widetilde{\Psi}}$ is invertible. By the inverse function theorem, Ψ defines a local diffeomorphism around $(\boldsymbol{x}^*, 0)$. Due to the compactness of ∂D, it follows that there exists a sufficiently small I such that $\Psi\colon \partial D \times I \to \mathcal{U}$ is bijective. The constant extension of $\boldsymbol{h}_{(\boldsymbol{u},\delta)}$ to $\mathcal{U}$ is now given by

$$\boldsymbol{h}_{(\boldsymbol{u},\delta)}(\boldsymbol{u}) = \boldsymbol{h}_{(\boldsymbol{u},\delta)}(\boldsymbol{x})\,, \qquad \boldsymbol{u} = \Psi(\boldsymbol{x}, \sigma) \in \mathcal{U}\,.$$

Multiplication of $\boldsymbol{h}_{(\boldsymbol{u},\delta)}$ with a smooth cut-off function provides a compact support in $\mathcal{U}$. For the extended and truncated $\boldsymbol{h}_{(\boldsymbol{u},\delta)}$, we can now apply Corollary 3.10. This yields

$$\lim_{\|\boldsymbol{h}_{(\boldsymbol{u},\delta)}\|_{\boldsymbol{C}^1}\to 0} \frac{\left\|F(\boldsymbol{z}+\boldsymbol{u},r+\delta)-F(\boldsymbol{z},r)-\boldsymbol{E}'^{\infty}_{(\boldsymbol{u},\delta)}\right\|_{\boldsymbol{L}^2_t(\mathbb{S}^2)}}{\|\boldsymbol{h}_{(\boldsymbol{u},\delta)}\|_{\boldsymbol{C}^1}} = 0\,,$$

where $\boldsymbol{E}'_{(\boldsymbol{u},\delta)}$ denotes the solution of (2.22a) together with (3.14) in the case of a penetrable obstacle and (2.24a) together with (3.15) in the case of a perfect conductor, with $\boldsymbol{h}$ – not to be confused with the linearization $\boldsymbol{h}$ – replaced by $\boldsymbol{h}_{(\boldsymbol{u},\delta)}$. From the well-posedness of these exterior boundary value problems, we furthermore conclude

$$\left\|\boldsymbol{E}'^{\infty}_{(\boldsymbol{u},\delta)}-\boldsymbol{E}'^{\infty}\right\|_{\boldsymbol{L}^2_t(\mathbb{S}^2)} \le C\,\|\boldsymbol{h}_{(\boldsymbol{u},\delta)}-\boldsymbol{h}\|_{\boldsymbol{C}^1}\,. \tag{4.13}$$

Thus,

$$\begin{aligned}
&\|F(\boldsymbol{z}+\boldsymbol{u},r+\delta)-F(\boldsymbol{z},r)-\boldsymbol{E}'^{\infty}\|_{\boldsymbol{L}^2_t(\mathbb{S}^2)}\\
&\quad\le \left\|F(\boldsymbol{z}+\boldsymbol{u},r+\delta)-F(\boldsymbol{z},r)-\boldsymbol{E}'^{\infty}_{(\boldsymbol{u},\delta)}\right\|_{\boldsymbol{L}^2_t(\mathbb{S}^2)} + \left\|\boldsymbol{E}'^{\infty}_{(\boldsymbol{u},\delta)}-\boldsymbol{E}'^{\infty}\right\|_{\boldsymbol{L}^2_t(\mathbb{S}^2)}\\
&\quad\le \mathrm{o}\left(\|\boldsymbol{h}_{(\boldsymbol{u},\delta)}\|_{\boldsymbol{C}^1}\right) + C\,\|\boldsymbol{h}_{(\boldsymbol{u},\delta)}-\boldsymbol{h}\|_{\boldsymbol{C}^1}
\end{aligned}$$

as $\|\boldsymbol{h}_{(\boldsymbol{u},\delta)}\|_{\boldsymbol{C}^1}\to 0$. By the definition of $\boldsymbol{h}_{(\boldsymbol{u},\delta)}$ and by (4.12), we see that both terms are of order $\mathrm{o}(\|\boldsymbol{u}\|_{\boldsymbol{C}^2}+\|\delta\|_{C^1})$ as these norms tend to 0, which finishes the proof. ∎

Next, we extend Theorem 4.13 for far-field operators $\mathcal{F}$. For this, we can start analogously as in the proof of Theorem 4.13, however, the analogue of (4.13) – for Herglotz waves and in Hilbert–Schmidt norm (cf. Definition 2.24 and (2.61)) – has to be treated with caution.

Theorem 4.14. *Let ∂D denote a regular C^1-surface represented by $(\boldsymbol{z},r)\in\mathcal{M}$ (see (4.9)). Let $\boldsymbol{h}\in\boldsymbol{C}^1(\partial D,\mathbb{R}^3)$ denote the linearization of $\boldsymbol{h}_{(\boldsymbol{u},\delta)}$ with respect to $(\boldsymbol{u},\delta)$, so that*

$$\lim_{\|\boldsymbol{u}\|_{\boldsymbol{C}^2},\,\|\delta\|_{C^1}\to 0} \frac{\|\boldsymbol{h}_{(\boldsymbol{u},\delta)}-\boldsymbol{h}\|_{\boldsymbol{C}^1}}{\|\boldsymbol{u}\|_{\boldsymbol{C}^2}+\|\delta\|_{C^1}} = 0\,. \tag{4.14}$$

The far-field operator $\mathcal{F}$ is Fréchet differentiable at $(\boldsymbol{z},r)\in\mathcal{M}$. With $\boldsymbol{h}$ given as above, $\mathcal{F}'[\boldsymbol{z},r](\boldsymbol{u},\delta)$ is equal to the operator $\boldsymbol{\varphi}\mapsto(\boldsymbol{E}'[\boldsymbol{\varphi}])^{\infty}$, where for any $\boldsymbol{\varphi}\in\boldsymbol{L}^2_t(\mathbb{S}^2)$ we denote by $(\boldsymbol{E}'[\boldsymbol{\varphi}])^{\infty}$ the far-field pattern of the weak solution $\boldsymbol{E}'[\boldsymbol{\varphi}]$ of (2.22a) together with (3.14) in the case of a penetrable obstacle and (2.24a) together with (3.15) in the case of a perfectly conducting obstacle.

Proof. Recall Remark 2.2. As in the proof of Theorem 4.13, we extend $\boldsymbol{h}_{(\boldsymbol{u},\delta)}$ to a compact neighborhood of the boundary and denote by $\boldsymbol{\varphi}\mapsto(\boldsymbol{E}'_{(\boldsymbol{u},\delta)}[\boldsymbol{\varphi}])^{\infty}$ the domain derivative of the far-field operator, i.e., $\boldsymbol{E}'_{(\boldsymbol{u},\delta)}[\boldsymbol{\varphi}]$ is a solution with respect to the perturbation $\boldsymbol{h}_{(\boldsymbol{u},\delta)}$ of (2.22a) together with (3.14) in the case of a penetrable obstacle and (2.24a) together with (3.15) in the case of a perfect conducting obstacle for any $\boldsymbol{\varphi}\in L^2_t(\mathbb{S}^2)$. Thus, by Theorem 3.17 we have

$$\left\|\mathcal{F}(\boldsymbol{z}+\boldsymbol{u},r+\delta)-\mathcal{F}(\boldsymbol{z},r)-(\boldsymbol{E}'_{(\boldsymbol{u},\delta)}[\,\cdot\,])^{\infty}\right\|_{\mathrm{HS}} = \mathrm{o}(\|\boldsymbol{h}_{(\boldsymbol{u},\delta)}\|_{\boldsymbol{C}^1})\,,\qquad \|\boldsymbol{h}_{(\boldsymbol{u},\delta)}\|_{\boldsymbol{C}^1}\to 0\,.$$

Next, similarly as in the proof of Lemma 3.4, we find that

$$\left\|(\boldsymbol{E}'_{(\boldsymbol{u},\delta)}[\boldsymbol{\varphi}])^{\infty} - (\boldsymbol{E}'[\boldsymbol{\varphi}])^{\infty}\right\|_{\boldsymbol{L}^2_t(\mathbb{S}^2)} \leq C\,\|\boldsymbol{h}_{(\boldsymbol{u},\delta)} - \boldsymbol{h}\|_{\boldsymbol{C}^1}\|(\boldsymbol{E}'_{(\boldsymbol{u},\delta)}[\boldsymbol{\varphi}])^{\infty}\|_{\boldsymbol{L}^2_t(\mathbb{S}^2)}\,,$$

and as in (3.19), we conclude

$$\|(\boldsymbol{E}'_{(\boldsymbol{u},\delta)}[\boldsymbol{\varphi}])^{\infty}\|_{\boldsymbol{L}^2_t(\mathbb{S}^2)} \leq C\left(\|\boldsymbol{\gamma}_t\boldsymbol{E}'_{(\boldsymbol{u},\delta)}[\boldsymbol{\varphi}]\|_{\boldsymbol{H}^{-1/2}(\mathrm{Div},\partial D)} + \|\boldsymbol{\gamma}_t\boldsymbol{H}'_{(\boldsymbol{u},\delta)}[\boldsymbol{\varphi}]\|_{\boldsymbol{H}^{-1/2}(\mathrm{Div},\partial D)}\right)$$

for all $\boldsymbol{\varphi} \in \mathscr{B}$ (defined in (3.21)). Hence, it holds that

$$\begin{aligned}
&\left\|(\boldsymbol{E}'_{(\boldsymbol{u},\delta)}[\,\cdot\,])^{\infty} - (\boldsymbol{E}'[\,\cdot\,])^{\infty}\right\|_{\mathrm{HS}} \\
&= \left(\sum_{n=1}^{\infty}\sum_{m=-n}^{n}\left\|(\boldsymbol{E}'_{(\boldsymbol{u},\delta)}[\boldsymbol{U}_n^m])^{\infty} - (\boldsymbol{E}'[\boldsymbol{U}_n^m])^{\infty}\right\|^2_{\boldsymbol{L}^2_t(\mathbb{S}^2)} + \left\|(\boldsymbol{E}'_{(\boldsymbol{u},\delta)}[\boldsymbol{V}_n^m])^{\infty} - (\boldsymbol{E}'[\boldsymbol{V}_n^m])^{\infty}\right\|^2_{\boldsymbol{L}^2_t(\mathbb{S}^2)}\right)^{1/2} \\
&\leq C\,\|\boldsymbol{h}_{(\boldsymbol{u},\delta)} - \boldsymbol{h}\|_{\boldsymbol{C}^1}\left(\sum_{n=1}^{\infty}\sum_{m=-n}^{n}\left\|\boldsymbol{\gamma}_t\boldsymbol{E}'_{(\boldsymbol{u},\delta)}[\boldsymbol{U}_n^m]\right\|^2_{\boldsymbol{H}^{-1/2}(\mathrm{Div},\partial D)} + \left\|\boldsymbol{\gamma}_t\boldsymbol{E}'_{(\boldsymbol{u},\delta)}[\boldsymbol{V}_n^m]\right\|^2_{\boldsymbol{H}^{-1/2}(\mathrm{Div},\partial D)}\right. \\
&\qquad\qquad \left. + \left\|\boldsymbol{\gamma}_t\boldsymbol{H}'_{(\boldsymbol{u},\delta)}[\boldsymbol{U}_n^m]\right\|^2_{\boldsymbol{H}^{-1/2}(\mathrm{Div},\partial D)} + \left\|\boldsymbol{\gamma}_t\boldsymbol{H}'_{(\boldsymbol{u},\delta)}[\boldsymbol{V}_n^m]\right\|^2_{\boldsymbol{H}^{-1/2}(\mathrm{Div},\partial D)}\right)^{1/2}.
\end{aligned}$$

Reference [24, p.109, Prop. 23] implies that

$$\left\|\boldsymbol{\gamma}_t\boldsymbol{H}'_{(\boldsymbol{u},\delta)}[\boldsymbol{\varphi}]\right\|_{\boldsymbol{H}^{-1/2}(\mathrm{Div},\partial D)} \leq C\left\|\boldsymbol{\gamma}_t\boldsymbol{E}'_{(\boldsymbol{u},\delta)}[\boldsymbol{\varphi}]\right\|_{\boldsymbol{H}^{-1/2}(\mathrm{Div},\partial D)}$$

for all $\boldsymbol{\varphi} \in \mathscr{B}$. Furthermore, using the boundary condition (3.14) (transmission) or (3.15) (perfect conductor) and the continuity of all therein occurring surface differential operators and traces, see Lemma 2.11 and Theorem 2.13, and by

$$\boldsymbol{E}_{\boldsymbol{\nu}} = -\frac{1}{\mathrm{i}\omega\varepsilon}\boldsymbol{\nu}\cdot\mathbf{curl}\,\boldsymbol{H} = -\frac{1}{\mathrm{i}\omega\varepsilon}\,\mathrm{Curl}\,\boldsymbol{H} = -\frac{1}{\mathrm{i}\omega\varepsilon}\,\mathrm{Div}(\boldsymbol{H}\times\boldsymbol{\nu})\,, \tag{4.15}$$

which must be interpreted formally, we conclude

$$\left\|\boldsymbol{\gamma}_t\boldsymbol{E}'_{(\boldsymbol{u},\delta)}[\boldsymbol{\varphi}]\right\|_{\boldsymbol{H}^{-1/2}(\mathrm{Div},\partial D)} \leq C\,\|\boldsymbol{h}_{(\boldsymbol{u},\delta)}\|_{\boldsymbol{C}^1}\|\boldsymbol{H}[\boldsymbol{\varphi}]\|_{\boldsymbol{H}(\mathbf{curl},\Omega)} \leq C\,\|\boldsymbol{h}_{(\boldsymbol{u},\delta)}\|_{\boldsymbol{C}^1}\|\boldsymbol{H}^i[\boldsymbol{\varphi}]\|_{\boldsymbol{H}(\mathbf{curl},B_R)}$$

for all $\boldsymbol{\varphi} \in \mathscr{B}$. Additionally, we know that

$$\boldsymbol{H}^i[\boldsymbol{\varphi}] = \frac{1}{\mathrm{i}\omega\mu}\,\mathbf{curl}\,\boldsymbol{E}^i[\boldsymbol{\varphi}] \quad \text{as well as} \quad \mathbf{curl}\,\boldsymbol{H}^i[\boldsymbol{\varphi}] = -\mathrm{i}\omega\varepsilon\boldsymbol{E}^i[\boldsymbol{\varphi}] \quad \text{for all } \boldsymbol{\varphi} \in \mathscr{B}\,,$$

and by (3.22), we have that $\mathbf{curl}\,\boldsymbol{E}^i[\boldsymbol{U}_n^m] = \mathrm{i}k\boldsymbol{E}^i[\boldsymbol{V}_n^m]$. Thus, it holds that

$$\begin{aligned}
\left\|\boldsymbol{H}^i[\boldsymbol{U}_n^m]\right\|^2_{\boldsymbol{H}(\mathbf{curl},B_R)} &= \left\|\boldsymbol{H}^i[\boldsymbol{U}_n^m]\right\|^2_{\boldsymbol{L}^2(B_R)} + \left\|\mathbf{curl}\,\boldsymbol{H}^i[\boldsymbol{U}_n^m]\right\|^2_{\boldsymbol{L}^2(B_R)} \\
&= \frac{\varepsilon}{\mu}\left\|\boldsymbol{E}^i[\boldsymbol{V}_n^m]\right\|^2_{\boldsymbol{L}^2(B_R)} + \omega^2\varepsilon^2\left\|\boldsymbol{E}^i[\boldsymbol{U}_n^m]\right\|^2_{\boldsymbol{L}^2(B_R)}\,.
\end{aligned}$$

Likewise, we obtain a similar expression for $\|\boldsymbol{H}^i[\boldsymbol{V}_n^m]\|^2_{\boldsymbol{H}(\mathbf{curl},B_R)}$. With these considerations, we

use Theorem 3.16 and conclude

$$\begin{aligned}
&\left\|(\boldsymbol{E}'_{(\boldsymbol{u},\delta)}[\,\cdot\,])^{\infty} - (\boldsymbol{E}'[\,\cdot\,])^{\infty}\right\|_{\mathrm{HS}} \\
&\qquad \leq C\,\|\boldsymbol{h}_{(\boldsymbol{u},\delta)} - \boldsymbol{h}\|_{\boldsymbol{C}^1}\|\boldsymbol{h}_{(\boldsymbol{u},\delta)}\|_{\boldsymbol{C}^1}\left(\sum_{n=1}^{\infty}\sum_{m=-n}^{n}\left\|\boldsymbol{H}^i[\boldsymbol{U}_n^m]\right\|^2_{\boldsymbol{H}(\mathbf{curl},B_R)} + \left\|\boldsymbol{H}^i[\boldsymbol{V}_n^m]\right\|^2_{\boldsymbol{H}(\mathbf{curl},B_R)}\right)^{1/2} \\
&\qquad \leq C\,\|\boldsymbol{h}_{(\boldsymbol{u},\delta)} - \boldsymbol{h}\|_{\boldsymbol{C}^1}\,.
\end{aligned}$$

Consequently, we infer

$$\begin{aligned}
&\|\mathcal{F}(\boldsymbol{z}+\boldsymbol{u}, r+\delta) - \mathcal{F}(\boldsymbol{z}, r) - (\boldsymbol{E}'[\,\cdot\,])^{\infty}\|_{\mathrm{HS}} \\
&\qquad\qquad \leq \left\|\mathcal{F}(\boldsymbol{z}+\boldsymbol{u}, r+\delta) - \mathcal{F}(\boldsymbol{z}, r) - (\boldsymbol{E}'_{(\boldsymbol{u},\delta)}[\,\cdot\,])^{\infty}\right\|_{\mathrm{HS}} + \left\|(\boldsymbol{E}'_{(\boldsymbol{u},\delta)}[\,\cdot\,])^{\infty} - (\boldsymbol{E}'[\,\cdot\,])^{\infty}\right\|_{\mathrm{HS}} \\
&\qquad\qquad \leq \mathrm{o}(\|\boldsymbol{h}_{(\boldsymbol{u},\delta)}\|_{\boldsymbol{C}^1}) + C\,\|\boldsymbol{h}_{(\boldsymbol{u},\delta)} - \boldsymbol{h}\|_{\boldsymbol{C}^1}
\end{aligned}$$

as $\|\boldsymbol{h}_{(\boldsymbol{u},\delta)}\|_{\boldsymbol{C}^1} \to 0$. By the definition of $\boldsymbol{h}_{(\boldsymbol{u},\delta)}$ and by assumption (4.14), we see that both terms are of order $\mathrm{o}(\|\boldsymbol{u}\|_{\boldsymbol{C}^2} + \|\delta\|_{C^1})$ as $\|\boldsymbol{u}\|_{\boldsymbol{C}^2} + \|\delta\|_{C^1} \to 0$, yielding the assertion. ■

CHAPTER 5

Shape Reconstruction

The central step in solving the inverse identification problem and, particularly, to optimizing the shape of objects with respect to their em-chirality properties, is the characterization and efficient numerical computation of the shape derivative. A characterization has been established in Chapter 3 and specified for tubular objects in Section 4.2. In the present chapter, we derive and implement an efficient algorithm to solve an inverse scattering problem. To be more precise, we identify pairs $(\boldsymbol{z}, r) \in \mathcal{M}$ (cf. (4.9)) representing surfaces ∂D of long tubular objects from measurements of the far field for just one incident field of a plane wave $(\boldsymbol{E}^i, \boldsymbol{H}^i) \in \boldsymbol{H}_{\mathrm{loc}}(\mathbf{curl}, \mathbb{R}^3) \times \boldsymbol{H}_{\mathrm{loc}}(\mathbf{curl}, \mathbb{R}^3)$. Here, we always assume a priori knowledge about the material parameters ε, μ and the single incident field $(\boldsymbol{E}^i, \boldsymbol{H}^i)$. Hence, the inverse problem (cf. (2.65)) now reads as:

$$\left.\begin{array}{l} \text{Given some far-field data } \boldsymbol{E}^{\infty}_{\mathrm{data}}, \text{ find the corresponding pair } (\boldsymbol{z}, r) \in \mathcal{M} \\ \text{such that } F(\boldsymbol{z}, r) = \boldsymbol{E}^{\infty}_{\mathrm{data}}\,. \end{array}\right\} \tag{5.1}$$

This can be regarded as a preliminary step to the optimization problem, although it is a challenging task in its own right.

Inverse scattering theory has a long history spreading over the last half-century. Reference [30] gives a retrospection of parts of the progress and development made, especially for acoustic waves. The principal approach to solving an inverse scattering problem by an iterative Gauss–Newton[1] type algorithm is well-established, see [66]. Impressive results regarding the shape reconstruction – also in a setting governed by the time-harmonic Maxwell's system – can be found in [51], [53, Subsection 6.3.1], for star-shaped obstacles (using a Newton iteration and applying Tikhonov[2] regularization), and in [23], [69, Section 4.3], for dielectric thin tubes and metallic nanowires (using a regularized Gauss–Newton algortihm with a golden section line search). In the latter two publications, which extend the results from [2, 48], the consideration of thin tubes leads to asymptotic formulae for the scattered field $\boldsymbol{E}^s$ and the corresponding far-field pattern $\boldsymbol{E}^{\infty}$ as the radius of the tube's cross-section tends to zero, see [69, Theorem 3.6]. This carries over to the assembly of the associated far-field map and its Fréchet derivative, such that not a single Maxwell system has to be solved for the inverse scattering problems. However, since we consider free-form tubes with thickness as established in Chapter 4, we do not profit from such efficiency gains.

[1] Johann Carl Friedrich Gauß (1777–1855), Sir Isaac Newton (1643–1727)
[2] Andrey Nikolayevich Tikhonov (1906–1993)

The underlying operator equation in (5.1) is ill-posed, which is why regularization thereof is required. It remains unresolved whether problem (5.1) possesses a solution or if it would be unique. For perfectly conducting balls, unique solvability has been shown for finitely many far-field data in [59]. For rectangular obstacles (in 2D), a uniqueness result can be found in [58] and for coated polyhedral scatterers (in 3D), in [60].

In order to implement a Gauss–Newton type method, we need to calculate the Fréchet derivative of the far-field map F. Hence, we use Theorem 4.13, where we have to solve the boundary value problem (2.22a) together with (3.14) in the case of a penetrable obstacle and (2.24a) together with (3.15) for perfect conductors. We numerically solve these problems by using boundary element methods. To this end, we start by formulating the boundary value problems as boundary integral equations.

5.1. Integral Equations for the Scattering Problems

Let $\boldsymbol{y} \in \mathbb{R}^3$ and recall the fundamental solution of the Helmholtz equation $\Delta u + k^2 u = 0$ in $\mathbb{R}^3 \setminus \{\boldsymbol{y}\}$ for the wave number k, given by

$$\Phi_k(\boldsymbol{x}, \boldsymbol{y}) = \frac{\mathrm{e}^{\mathrm{i}k|\boldsymbol{x}-\boldsymbol{y}|}}{4\pi|\boldsymbol{x}-\boldsymbol{y}|}\,, \qquad \boldsymbol{x} \neq \boldsymbol{y}\,,$$

(cf. (3.16)). Furthermore, we reduce the Maxwell system (2.15) to

$$\mathbf{curl}^2 \boldsymbol{E} - k^2 \boldsymbol{E} = \boldsymbol{0}\,.$$

Note that a weak solution $\boldsymbol{E} \in \boldsymbol{H}(\mathbf{curl}, D)$ or $\boldsymbol{E} \in \boldsymbol{H}_{\mathrm{loc}}(\mathbf{curl}, \mathbb{R}^3 \setminus \overline{D})$ of the Maxwell systems naturally satisfies $\boldsymbol{E} \in \boldsymbol{H}(\mathbf{curl}^2, D)$ or $\boldsymbol{E} \in \boldsymbol{H}_{\mathrm{loc}}(\mathbf{curl}^2, \mathbb{R}^3 \setminus \overline{D})$, respectively.

Next, for a smooth scalar- and vector-valued density φ and $\boldsymbol{\varphi}$, the scalar- and vector-valued single layer potentials SL_k and $\mathbf{SL}_k$ are given by

$$\left.\begin{aligned} \mathrm{SL}_k\,\varphi(\boldsymbol{x}) &\coloneqq \int_{\partial D} \Phi_k(\boldsymbol{x}, \boldsymbol{y})\varphi(\boldsymbol{y})\,\mathrm{d}s(\boldsymbol{y}) \\ \mathbf{SL}_k\,\boldsymbol{\varphi}(\boldsymbol{x}) &\coloneqq \int_{\partial D} \Phi_k(\boldsymbol{x}, \boldsymbol{y})\boldsymbol{\varphi}(\boldsymbol{y})\,\mathrm{d}s(\boldsymbol{y}) \end{aligned}\right\} \quad \boldsymbol{x} \in \mathbb{R}^3 \setminus \partial D\,.$$

These potentials extend to continuous operators from $H^{-1/2}(\partial D, \mathbb{C}^m)$ to $H^1_{\mathrm{loc}}(\mathbb{R}^3, \mathbb{C}^m)$ both for $m = 1$ and $m = 3$, see [34, Theorem 1]. The electric and magnetic potentials

$$\left.\begin{aligned} \boldsymbol{\mathcal{E}}_k\,\boldsymbol{\varphi} &\coloneqq \mathrm{i}k\;\mathbf{SL}_k\,\boldsymbol{\varphi} - \frac{1}{\mathrm{i}k}\;\boldsymbol{\nabla}\mathrm{SL}_k(\mathrm{Div}\,\boldsymbol{\varphi}) \\ \boldsymbol{\mathcal{H}}_k\,\boldsymbol{\varphi} &\coloneqq \mathbf{curl}\,\mathbf{SL}_k\,\boldsymbol{\varphi} \end{aligned}\right\} \quad \boldsymbol{\varphi} \in \boldsymbol{H}^{-1/2}(\mathrm{Div}, \partial D) \tag{5.2}$$

mapping from $\boldsymbol{H}^{-1/2}(\mathrm{Div}, \partial D)$ to $\boldsymbol{H}_{\mathrm{loc}}(\mathbf{curl}^2, D \cup \mathbb{R}^3 \setminus \overline{D})$, are both well-defined, continuous linear operators, see [19, Theorem 5]. Subsequently, the electromagnetic boundary operators $\mathbf{S}_k$, $\mathbf{C}_k \colon \boldsymbol{H}^{-1/2}(\mathrm{Div}, \partial D) \to \boldsymbol{H}^{-1/2}(\mathrm{Div}, \partial D)$ are obtained by averaging tangential traces of the

potentials,

$$\mathbf{S}_k \coloneqq \frac{1}{2}\left(\boldsymbol{\gamma}_t^+ \boldsymbol{\mathcal{E}}_k + \boldsymbol{\gamma}_t^- \boldsymbol{\mathcal{E}}_k\right), \qquad \mathbf{C}_k \coloneqq \frac{1}{2}\left(\boldsymbol{\gamma}_t^+ \boldsymbol{\mathcal{H}}_k + \boldsymbol{\gamma}_t^- \boldsymbol{\mathcal{H}}_k\right).$$

Continuity of $\mathbf{S}_k$ and $\mathbf{C}_k$ has been shown in [20, Corollary 3.4]. Here, the superscript "+" indicates a trace taken from the exterior $\mathbb{R}^3 \setminus \overline{D}$, while the superscript "−" indicates a trace taken from inside D (cf. (2.27)). The boundary operators satisfy the jump relations (see [19, Theorem 7])

$$\boldsymbol{\gamma}_t^{\pm} \boldsymbol{\mathcal{E}}_k = \mathbf{S}_k\,, \qquad \boldsymbol{\gamma}_N^{\pm} \boldsymbol{\mathcal{E}}_k = \mp\frac{1}{2} I + \mathbf{C}_k\,, \qquad \boldsymbol{\gamma}_t^{\pm} \boldsymbol{\mathcal{H}}_k = \mp\frac{1}{2} I + \mathbf{C}_k\,, \qquad \boldsymbol{\gamma}_N^{\pm} \boldsymbol{\mathcal{H}}_k = \mathbf{S}_k\,. \tag{5.3}$$

With the electric single- and double layer potentials, we can employ the Stratton–Chu representation formula for electric fields in the following form ([19, Theorem 6], [22, Section 3]):

$$\boldsymbol{\mathcal{E}}_k \boldsymbol{\gamma}_t^- \boldsymbol{H} + \boldsymbol{\mathcal{H}}_k \boldsymbol{\gamma}_t^- \boldsymbol{E} = \begin{cases} \boldsymbol{E}\,, & \text{in } D\,, \\ \mathbf{0}\,, & \text{in } \mathbb{R}^3 \setminus \overline{D}\,, \end{cases} \tag{5.4}$$

for weak solutions $(\boldsymbol{E}, \boldsymbol{H}) \in \boldsymbol{H}(\mathbf{curl}^2, D) \times \boldsymbol{H}(\mathbf{curl}^2, D)$ of (2.15) and

$$-\boldsymbol{\mathcal{E}}_k \boldsymbol{\gamma}_t^+ \boldsymbol{H} - \boldsymbol{\mathcal{H}}_k \boldsymbol{\gamma}_t^+ \boldsymbol{E} = \begin{cases} \mathbf{0}\,, & \text{in } D\,, \\ \boldsymbol{E}\,, & \text{in } \mathbb{R}^3 \setminus \overline{D}\,, \end{cases} \tag{5.5}$$

for weak solutions $(\boldsymbol{E}, \boldsymbol{H}) \in \boldsymbol{H}_{\mathrm{loc}}(\mathbf{curl}^2, \mathbb{R}^3 \setminus \overline{D}) \times \boldsymbol{H}_{\mathrm{loc}}(\mathbf{curl}^2, \mathbb{R}^3 \setminus \overline{D})$ of (2.15) that satisfy the Silver–Müller radiation condition (2.20). We will now first consider the perfect conductor.

5.1.1. Perfect Conductor

To compute the scattered field from (2.24) together with the SMRC (2.20) and its domain derivative $\boldsymbol{E}'$ for the perfect conductor problem, we first observe – as in the proof of Lemma 3.9 – that we can combine the Stratton–Chu representation formulae (5.4), (5.5) to infer the following representation for the scattered field $\boldsymbol{E}^s \in \boldsymbol{H}_{\mathrm{loc}}(\mathbf{curl}, \mathbb{R}^3 \setminus \overline{D})$ in the exterior domain in terms of tangential traces of the corresponding total field:

$$\boldsymbol{E}^s = -\boldsymbol{\mathcal{E}}_k \boldsymbol{\gamma}_t^+ \boldsymbol{H} - \boldsymbol{\mathcal{H}}_k \boldsymbol{\gamma}_t^+ \boldsymbol{E} \qquad \text{in } \mathbb{R}^3 \setminus \overline{D}\,. \tag{5.6}$$

With (5.6) we make the plausible indirect ansatz

$$\boldsymbol{E}^s = -\boldsymbol{\mathcal{E}}_k \boldsymbol{\lambda} \qquad \text{or} \qquad \boldsymbol{E}' = -\boldsymbol{\mathcal{E}}_k \boldsymbol{\lambda} \qquad \text{in } \mathbb{R}^3 \setminus \overline{D}\,, \tag{5.7}$$

for some unknown density $\boldsymbol{\lambda} \in \boldsymbol{H}^{-1/2}(\mathrm{Div}, \partial D)$. We apply $\boldsymbol{\gamma}_t$ to both sides of each equation in (5.7), exploit the perfect conductor boundary conditions (2.24b) or (3.15), and use the jump relations (5.3), which results in the indirect *electric field integral equation* (EFIE)

$$\mathbf{S}_k \boldsymbol{\lambda} = \begin{cases} \boldsymbol{\gamma}_t^+ \boldsymbol{E}^i\,, & \text{for the scattering problem}\,, \qquad \text{(5.8a)} \\ -\mathrm{i}\omega\mu_+ \boldsymbol{h}_{\boldsymbol{\nu}} \boldsymbol{\gamma}_T \boldsymbol{H} + \mathbf{Curl}\,(\boldsymbol{h}_{\boldsymbol{\nu}} \boldsymbol{E}_{\boldsymbol{\nu}})\,, & \text{for the domain derivative}\,. \qquad \text{(5.8b)} \end{cases}$$

Solving (5.8) for $\boldsymbol{\lambda}$ then yields $\boldsymbol{E}^s$ or $\boldsymbol{E}'$ by the ansatz (5.7). The corresponding far-field pattern can be obtained by

$$\boldsymbol{E}^\infty(\widehat{\boldsymbol{x}}) = -(\boldsymbol{\mathcal{E}}_k^\infty \boldsymbol{\lambda})(\widehat{\boldsymbol{x}}) \qquad \text{or} \qquad (\boldsymbol{E}')^\infty(\widehat{\boldsymbol{x}}) = -(\boldsymbol{\mathcal{E}}_k^\infty \boldsymbol{\lambda})(\widehat{\boldsymbol{x}})\,, \qquad \widehat{\boldsymbol{x}} \in \mathbb{S}^2\,, \tag{5.9}$$

where for $\boldsymbol{\mathcal{E}}_k^\infty$ we replace the fundamental solution with its far-field pattern in the definition of $\boldsymbol{\mathcal{E}}_k$ (see (5.2)). Note that using the perfect conductor boundary condition (2.24b) in (5.6), it immediately follows that $\boldsymbol{\lambda} = \boldsymbol{\gamma}_t^+ \boldsymbol{H}$ for the scattering problem.

We are looking for solutions in $\boldsymbol{H}^{-1/2}(\mathrm{Div}, \partial D)$ and, thus, (5.8) has to be understood in the variational sense, see [15]. The corresponding sesquilinearform fails to be coercive, however, in [17, Theorem 5] it has been shown that, under the assumption that the wave number k is not an *interior eigenvalue*, see [19, Definition 4], (5.8) admits a unique solution $\boldsymbol{\lambda} \in \boldsymbol{H}^{-1/2}(\mathrm{Div}, \partial D)$, where we have continuous dependence on the data. There, a generalized inf-sup condition has been proved to recover coercivity with respect to a *Hodge*[3] *decomposition* of $\boldsymbol{H}^{-1/2}(\mathrm{Div}, \partial D)$, see [17, Theorem 2]. Since there exists at most a countable sequence of interior eigenvalues and the only possible accumulation point is infinity, see [67, Theorem 4.5], the assumption that k is not in this sequence is relatively mild. However, in Appendix C.1, we also outline a regularized *combined field integral equation* (CFIE) that does not need this requirement. There, also more references on interior resonances can be found.

5.1.2. Penetrable Obstacle

We proceed similarly for penetrable obstacles. Having definition (2.19) in mind, let the scattered fields $\boldsymbol{E}^s, \boldsymbol{H}^s \in \boldsymbol{H}_{\mathrm{loc}}(\mathbf{curl}, \mathbb{R}^3)$ be solutions to (2.22), (2.20), with corresponding incident fields $\boldsymbol{E}^i$, $\boldsymbol{H}^i \in \boldsymbol{H}_{\mathrm{loc}}(\mathbf{curl}, \mathbb{R}^3)$. Note that $\boldsymbol{E}^s|_D$ is not radiating. Hence, by the Stratton–Chu representation formula (5.4) – now also including $\boldsymbol{H}^s$, which can be obtained in a similar manner as in [68, Theorem 3.27] – we have the representations

$$\left.\begin{aligned} \boldsymbol{E}^s &= \boldsymbol{\mathcal{E}}_{k_-} \boldsymbol{\gamma}_t^- \boldsymbol{H}^s + \boldsymbol{\mathcal{H}}_{k_-} \boldsymbol{\gamma}_t^- \boldsymbol{E}^s \\ \boldsymbol{H}^s &= -\boldsymbol{\mathcal{E}}_{k_-} \boldsymbol{\gamma}_t^- \boldsymbol{E}^s + \boldsymbol{\mathcal{H}}_{k_-} \boldsymbol{\gamma}_t^- \boldsymbol{H}^s \end{aligned}\right\} \quad \text{in } D\,, \tag{5.10}$$

as well as

$$\left.\begin{aligned} \boldsymbol{E}^s &= -\boldsymbol{\mathcal{E}}_{k_+} \boldsymbol{\gamma}_t^+ \boldsymbol{H}^s - \boldsymbol{\mathcal{H}}_{k_+} \boldsymbol{\gamma}_t^+ \boldsymbol{E}^s \\ \boldsymbol{H}^s &= \boldsymbol{\mathcal{E}}_{k_+} \boldsymbol{\gamma}_t^+ \boldsymbol{E}^s - \boldsymbol{\mathcal{H}}_{k_+} \boldsymbol{\gamma}_t^+ \boldsymbol{H}^s \end{aligned}\right\} \quad \text{in } \mathbb{R}^3 \setminus \overline{D}\,, \tag{5.11}$$

for the scattered fields. Analogously, representations (5.10), (5.11) hold, if $\boldsymbol{E}^s, \boldsymbol{H}^s$ are substituted by the domain derivatives $\boldsymbol{E}', \boldsymbol{H}'$.

We make the indirect ansatz

$$\left.\begin{aligned} \boldsymbol{E}^s &= \boldsymbol{\mathcal{E}}_{k_-} \boldsymbol{\lambda}_2 + \boldsymbol{\mathcal{H}}_{k_-} \boldsymbol{\lambda}_1 \\ \boldsymbol{H}^s &= -\boldsymbol{\mathcal{E}}_{k_-} \boldsymbol{\lambda}_1 + \boldsymbol{\mathcal{H}}_{k_-} \boldsymbol{\lambda}_2 \end{aligned}\right\} \quad \text{in } D\,, \tag{5.12}$$

[3] Sir William Vallance Douglas Hodge (1903–1975)

$$\left.\begin{aligned} \boldsymbol{E}^s &= -\boldsymbol{\mathcal{E}}_{k_+}\boldsymbol{\lambda}_2 - \boldsymbol{\mathcal{H}}_{k_+}\boldsymbol{\lambda}_1 \\ \boldsymbol{H}^s &= \boldsymbol{\mathcal{E}}_{k_+}\boldsymbol{\lambda}_1 - \boldsymbol{\mathcal{H}}_{k_+}\boldsymbol{\lambda}_2 \end{aligned}\right\} \quad \text{in } \mathbb{R}^3 \setminus \overline{D}\,, \tag{5.13}$$

for some unknown densities $\boldsymbol{\lambda}_1, \boldsymbol{\lambda}_2 \in \boldsymbol{H}^{-1/2}(\mathrm{Div}, \partial D)$. Using the jump relations (5.3) on (5.12) and (5.13), we conclude

$$\left.\begin{aligned} \gamma_t^- \boldsymbol{E}^s &= \mathbf{S}_{k_-}\boldsymbol{\lambda}_2 + \left(\frac{1}{2}\boldsymbol{I} + \mathbf{C}_{k_-}\right)\boldsymbol{\lambda}_1 \\ \gamma_t^- \boldsymbol{H}^s &= -\mathbf{S}_{k_-}\boldsymbol{\lambda}_1 + \left(\frac{1}{2}\boldsymbol{I} + \mathbf{C}_{k_-}\right)\boldsymbol{\lambda}_2 \end{aligned}\right\} \quad \text{on } \partial D\,, \tag{5.14}$$

$$\left.\begin{aligned} \gamma_t^+ \boldsymbol{E}^s &= -\mathbf{S}_{k_+}\boldsymbol{\lambda}_2 + \left(\frac{1}{2}\boldsymbol{I} - \mathbf{C}_{k_+}\right)\boldsymbol{\lambda}_1 \\ \gamma_t^+ \boldsymbol{H}^s &= \mathbf{S}_{k_+}\boldsymbol{\lambda}_1 + \left(\frac{1}{2}\boldsymbol{I} - \mathbf{C}_{k_+}\right)\boldsymbol{\lambda}_2 \end{aligned}\right\} \quad \text{on } \partial D\,. \tag{5.15}$$

Thus, with the multitrace operator

$$\mathbf{A}_k \colon (\boldsymbol{H}^{-1/2}(\mathrm{Div}, \partial D))^2 \to (\boldsymbol{H}^{-1/2}(\mathrm{Div}, \partial D))^2\,, \qquad \mathbf{A}_k \coloneqq \begin{pmatrix} \mathbf{C}_k & \mathbf{S}_k \\ -\mathbf{S}_k & \mathbf{C}_k \end{pmatrix},$$

we can rewrite (5.14) and (5.15), obtaining

$$\left(\frac{1}{2}\boldsymbol{I} + \mathbf{A}_{k_-}\right)\begin{pmatrix}\boldsymbol{\lambda}_1 \\ \boldsymbol{\lambda}_2\end{pmatrix} = \begin{pmatrix}\gamma_t^- \boldsymbol{E}^s \\ \gamma_t^- \boldsymbol{H}^s\end{pmatrix} \tag{5.16}$$

and

$$\left(\frac{1}{2}\boldsymbol{I} - \mathbf{A}_{k_+}\right)\begin{pmatrix}\boldsymbol{\lambda}_1 \\ \boldsymbol{\lambda}_2\end{pmatrix} = \begin{pmatrix}\gamma_t^+ \boldsymbol{E}^s \\ \gamma_t^+ \boldsymbol{H}^s\end{pmatrix}, \tag{5.17}$$

respectively. Subtracting (5.17) from (5.16) yields the (indirect) modified PMCHWT[4] integral equation

$$(\mathbf{A}_{k_-} + \mathbf{A}_{k_+})\begin{pmatrix}\boldsymbol{\lambda}_1 \\ \boldsymbol{\lambda}_2\end{pmatrix} = \begin{pmatrix}\gamma_t^- \boldsymbol{E}^s - \gamma_t^+ \boldsymbol{E}^s \\ \gamma_t^- \boldsymbol{H}^s - \gamma_t^+ \boldsymbol{H}^s\end{pmatrix} = \begin{pmatrix}\gamma_t^+ \boldsymbol{E}^i \\ \gamma_t^+ \boldsymbol{H}^i\end{pmatrix} \tag{5.18a}$$

for the scattering problem and analogously

$$(\mathbf{A}_{k_-} + \mathbf{A}_{k_+})\begin{pmatrix}\boldsymbol{\lambda}_1 \\ \boldsymbol{\lambda}_2\end{pmatrix} = \begin{pmatrix}\gamma_t^- \boldsymbol{E}' - \gamma_t^+ \boldsymbol{E}' \\ \gamma_t^- \boldsymbol{H}' - \gamma_t^+ \boldsymbol{H}'\end{pmatrix} = \begin{pmatrix}-\mathrm{i}\omega\,[\mu]_{\partial D}\,\boldsymbol{h}_{\boldsymbol{\nu}}\gamma_T \boldsymbol{H} + [\mathbf{Curl}(\boldsymbol{h}_{\boldsymbol{\nu}}\boldsymbol{E}_{\boldsymbol{\nu}})]_{\partial D} \\ \mathrm{i}\omega\,[\varepsilon]_{\partial D}\,\boldsymbol{h}_{\boldsymbol{\nu}}\gamma_T \boldsymbol{E} + [\mathbf{Curl}(\boldsymbol{h}_{\boldsymbol{\nu}}\boldsymbol{H}_{\boldsymbol{\nu}})]_{\partial D}\end{pmatrix} \tag{5.18b}$$

for the domain derivative. Here, we have exploited the interface conditions (2.22b) and (3.14). Solving (5.18) for $(\boldsymbol{\lambda}_1, \boldsymbol{\lambda}_2)$ then yields $(\boldsymbol{E}^s, \boldsymbol{H}^s)$ or $(\boldsymbol{E}', \boldsymbol{H}')$ by the ansatz (5.12), (5.13). The corresponding far-field patterns can be obtained by replacing $(\boldsymbol{\mathcal{E}}_k,\ \boldsymbol{\mathcal{H}}_k)$ by $(\boldsymbol{\mathcal{E}}_k^\infty,\ \boldsymbol{\mathcal{H}}_k^\infty)$ in the

[4] A. J. Poggio, Edmund K. Miller, Y. Chang, Roger Fuller Harrington (b. 1925), Te-Kao Wu (b. 1948), Leonard L. Tsai

ansatz, where – as in (5.9) – the latter can be computed by substituting the fundamental solution by its far-field pattern in the definition of $(\boldsymbol{\mathcal{E}}_k, \boldsymbol{\mathcal{H}}_k)$ (see (5.2)). Note that for the scattering problem it readily follows that $(\boldsymbol{\lambda}_1, \boldsymbol{\lambda}_2) = (\boldsymbol{\gamma}_t^+ \boldsymbol{E}^s, \boldsymbol{\gamma}_t^+ \boldsymbol{H}^s)$ by (2.18). The variational formulation of the modified PMCHWT (5.18) in $\boldsymbol{H}^{-1/2}(\mathrm{Div}, \partial D) \times \boldsymbol{H}^{-1/2}(\mathrm{Div}, \partial D)$ is straightforward. The unique solvability has been shown in [19, Theorem 12], [21, Corollary 6.4].

5.2. Boundary Element Methods

The discretization of the boundary integral equations (5.8), (5.18) is carried out using the `Bempp-cl` boundary element method library for the Galerkin[5] discretization (see [9] and `https://bempp.com`). In this library, the function spaces $\boldsymbol{H}^{-1/2}(\mathrm{Div}, \partial D)$ and $\boldsymbol{H}^{-1/2}(\mathrm{Curl}, \partial D)$ are discretized using the Rao–Wilton–Glisson[6] (RWG), scaled Nédélec[7] (SNC), Buffa–Christiansen[8] (BC), and rotated Buffa–Christiansen (RBC) finite element families as detailed in [103]. Implementations of all the integral operators that have been introduced in Section 5.1 are available. We refer to [19, Sections 8, 9] for more on boundary element spaces and Galerkin discretization and corresponding error estimates. In what follows, we present an overview of the definition of basis functions on the boundary.

We approximate the surface ∂D through a polyhedral surface defined by a triangular mesh $\mathcal{T}_h$ with mesh size h, i.e., $h = \max_{T \in \mathcal{T}_h} \sup_{\boldsymbol{x}, \boldsymbol{y} \in T} |\boldsymbol{x} - \boldsymbol{y}|$. For each pair of different triangles $T, \widehat{T} \in \mathcal{T}_h$, their intersection is either exactly one corner, one edge, or empty. Hereinafter, the degrees of freedom (DOF) correspond to the edges of the triangulation. On the ith edge E_i, shared by the triangles $T_i^- \in \mathcal{T}_h$ and $T_i^+ \in \mathcal{T}_h$, for $\boldsymbol{x} \in \bigcup_{T \in \mathcal{T}_h} T$ the Raviart–Thomas[9] (RT) (see [96] for the original definition and [13, Section III.3] for a thorough introduction) and Nédélec (NC) (see [83]) order 0 basis functions are defined by

$$\mathbf{RT}_i(\boldsymbol{x}) \coloneqq \begin{cases} -\dfrac{1}{2 \int_{T_i^-} \mathrm{d}\boldsymbol{y}} (\boldsymbol{x} - \boldsymbol{v}_i^-), & \boldsymbol{x} \in T_i^-, \\ \dfrac{1}{2 \int_{T_i^+} \mathrm{d}\boldsymbol{y}} (\boldsymbol{x} - \boldsymbol{v}_i^+), & \boldsymbol{x} \in T_i^+, \\ \mathbf{0}, & \text{else}, \end{cases} \qquad \text{and} \qquad \mathbf{NC}_i(\boldsymbol{x}) \coloneqq \boldsymbol{\nu}(\boldsymbol{x}) \times \mathbf{RT}_i(\boldsymbol{x}),$$

where $\boldsymbol{v}_i^\pm$ are the vertices of $T_i^\pm$ with $\boldsymbol{v}_i^\pm \notin T_i^\mp$ (cf. Figure 5.1). Note that $\boldsymbol{\nu}$ is constant on each triangle. Scaling the RT and NC basis functions by the length l_i of the shared edge E_i leads to the Div-conforming RWG (see [95]) and Curl-conforming SNC order 0 basis functions

$$\mathbf{RWG}_i \coloneqq l_i \, \mathbf{RT}_i \qquad \text{and} \qquad \mathbf{SNC}_i \coloneqq l_i \, \mathbf{NC}_i = \boldsymbol{\nu} \times \mathbf{RWG}_i .$$

Note that a basis function is Div-conforming if its normal components are continuous across the edges and Curl-conforming if its tangential components are continuous across the edges.

[5] Boris Grigorjewitsch Galjorkin (1871–1945)
[6] Sadasiva M. Rao, Donald Robert Wilton (b. 1942), Allen W. Glisson
[7] Jean-Claude Nédélec (b. 1943)
[8] Annalisa Buffa (b. 1973), Snorre Harald Christiansen (b. 1975)
[9] Pierre-Arnauld Raviart (b. 1939), Jean-Marie Thomas

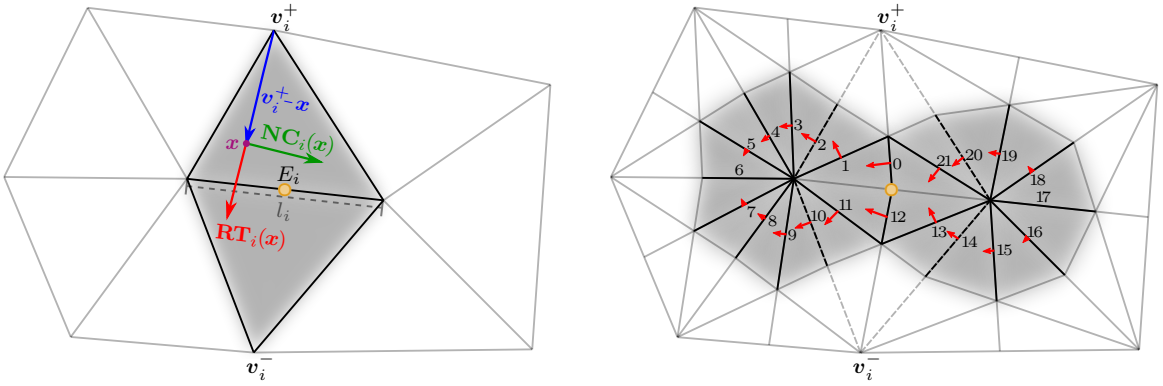

Figure 5.1. *Left*: Exemplary definition of an RT and an NC basis function – red and green, respectively – in $\boldsymbol{x} \in T_i^+$ (purple), where T_i^+ (top triangle) and T_i^- (bottom triangle) are colored gray. Also featured are the shared edge E_i of $T_i^\pm$ and its length l_i. They are associated with the midpoint of E_i highlighted in orange.
Right: Exemplary depiction of a BC basis function associated with the same midpoint of E_i as the RT and NC basis function on the unrefined mesh on the left-hand side – again highlighted in orange. The relevant triangles, on which the BC basis function on the barycentrically refined mesh is supported, are shaded gray. The numbering of the edges for this example is portrayed. The weightings and directions of the corresponding RWG basis functions are exemplary featured by red arrows. Dashed lines implicate the triangles that are supported for the corresponding RT and NC basis functions, associated to the same edge on the unrefined mesh (cf. left image).

The problem is now that by [27, Proposition 3.1], the space spanned by the RWG basis functions has a subspace U for which

$$\limsup_{h\to 0} \sup_{\substack{\boldsymbol{u}\in U\\ \boldsymbol{u}\neq\boldsymbol{0}}} \sup_{\substack{\boldsymbol{u}'\in\operatorname{span}\{\mathbf{SNC}_j\}\\ \boldsymbol{u}'\neq\boldsymbol{0}}} \frac{\langle \boldsymbol{u}, \boldsymbol{u}'\rangle_{t,\partial D}}{\|\boldsymbol{u}\|_{\boldsymbol{H}^{-1/2}(\mathrm{Div},\partial D)}\,\|\boldsymbol{u}'\|_{\boldsymbol{H}^{-1/2}(\mathrm{Curl},\partial D)}}\, h^{-1/2} < \infty\,.$$

Therefore, we conclude that

$$\inf_{\substack{\boldsymbol{u}\in U\\ \boldsymbol{u}\neq\boldsymbol{0}}} \sup_{\substack{\boldsymbol{u}'\in\operatorname{span}\{\mathbf{SNC}_j\}\\ \boldsymbol{u}'\neq\boldsymbol{0}}} \frac{\langle \boldsymbol{u}, \boldsymbol{u}'\rangle_{t,\partial D}}{\|\boldsymbol{u}\|_{\boldsymbol{H}^{-1/2}(\mathrm{Div},\partial D)}\,\|\boldsymbol{u}'\|_{\boldsymbol{H}^{-1/2}(\mathrm{Curl},\partial D)}}$$

behaves at least like $h^{1/2}$ as $h \to 0$. Thus, the discrete inf-sup condition (see [11, (12.5.1) Lemma])

$$\inf_{\substack{\boldsymbol{u}\in U\\ \boldsymbol{u}\neq\boldsymbol{0}}} \sup_{\substack{\boldsymbol{u}'\in\operatorname{span}\{\mathbf{SNC}_j\}\\ \boldsymbol{u}'\neq\boldsymbol{0}}} \frac{\langle \boldsymbol{u}, \boldsymbol{u}'\rangle_{t,\partial D}}{\|\boldsymbol{u}\|_{\boldsymbol{H}^{-1/2}(\mathrm{Div},\partial D)}\,\|\boldsymbol{u}'\|_{\boldsymbol{H}^{-1/2}(\mathrm{Curl},\partial D)}} =: \alpha > 0$$

is *not* satisfied for sufficiently small mesh sizes h. This results in an almost singular mass matrix and, thus, an ill-conditioned discretization of everything that involves calculations of the L^2-identity. To re-establish the inf-sup stability, in [16] the BC basis functions have been defined.

In what follows, we summarize their assembly. First, we perform a barycentric refinement of the mesh, i.e., we add new vertices at the barycenter of each triangle and at the center of each edge, obtaining a refined mesh with a sixfold increase in the number of elements. Then, the BC basis function $\mathbf{BC}_i$, associated with the ith edge of the original coarse grid, is defined as a linear combination of RWG basis functions, associated with edges of the barycentric refinement (cf. Figure 5.1). This linear combination is almost tangential across the ith edge of the original coarse mesh. Therefore, the BC basis functions behave like Curl-conforming functions across the ith edge, while being Div-conforming as a linear combination of Div-conforming RWG basis functions. In [16, Proposition 3.14], the inf-sup condition, i.e., there is a $C > 0$ such that for all mesh sizes h it holds that

$$\inf_{\substack{\boldsymbol{u}\in\operatorname{span}\{\mathbf{RWG}_j\}\\ \boldsymbol{u}\neq\mathbf{0}}} \sup_{\substack{\boldsymbol{u}'\in\operatorname{span}\{\mathbf{BC}_j\}\\ \boldsymbol{u}'\neq\mathbf{0}}} \frac{\langle \boldsymbol{u}, \boldsymbol{u}'\rangle_{t,\partial D}}{\|\boldsymbol{u}\|_{\boldsymbol{H}^{-1/2}(\mathrm{Div},\partial D)}\,\|\boldsymbol{u}'\|_{\boldsymbol{H}^{-1/2}(\mathrm{Curl},\partial D)}} \geq \frac{1}{C}\,,$$

is proved. The RBC basis functions are then defined by

$$\mathbf{RBC}_i \coloneqq \boldsymbol{\nu} \times \mathbf{BC}_i\,.$$

The violation of the discrete inf-sup condition causes numerical instabilities for any equation involving an identity. Since there is no identity in the EFIE (5.8) and the modified PMCHWT (5.18), we can solve the perfect conductor scattering problem (2.24) together with the SMRC (2.20) and the transmission problem (2.22) together with the SMRC (2.20), using just the RWG and SNC basis functions for discretizing the given function spaces. However, for computing the domain derivatives, in both cases we stumble across the ill-conditioning when implementing the operations and surface differential operators occurring in the right-hand sides of (3.15) and (3.14), which are not all readily available in `Bempp-cl`. For these, we have to calculate the Gram[10] matrix, which is almost singular as well. Therefore, we need to incorporate discretizations with BC and RBC basis functions. However, `Bempp-cl` does not allow solving (5.8) and (5.18) using a direct solver upon using a DOF transformation, which is needed when we barycentrically refine all the other occurring spaces (products and other operations between two functions on the grid are only possible on the same grid – hence, using BC basis functions, we need to barycentrically refine all occurring spaces). In this case, only iterative solvers, such as GMRES, are implemented in `Bempp-cl`.

This brings us to our main issue: using GMRES, for typical structures and material parameters used in this thesis, the iteration number was observed to be quite large. Even computing the solution for the scattering problem for a silver helix with, e.g., two turns, took so long that using this approach even for an inverse problem is out of question. Hence, a direct solver is required – more particularly in view of the optimization in Chapter 6, where even more Maxwell problems have to be solved and where such problematic objects include the ones of interest to us. Direct solvers avoid the problem of high iteration counts and are thus much faster than iterative solvers for these structures in practice.

In order to enable the utilization of a direct solver in conjunction with `Bempp-cl` for the

[10] Jørgen Pederson Gram (1850–1916)

implementation, we perform calculations on the barycentrically refined mesh when necessary, i.e., when the mass or Gram matrix need to be calculated, and projecting the resulting traces to a non-refined mesh, using only RWG and SNC basis functions for the discretizations. This way, we can use a direct solver, such as the LU decomposition, for solving the linear system that results from discretizing (5.8), (5.18), despite the restrictions by `Bempp-cl`. For this projection approach, it is crucial to choose the right spaces and the correct discretizations for the corresponding dual spaces. We briefly outline the approach and which spaces are suitable. First, we note that for sufficiently smooth fields there hold

$$\mathbf{Curl}\,(\boldsymbol{h}_{\boldsymbol{\nu}}\boldsymbol{E}_{\boldsymbol{\nu}}) = \mathbf{Grad}(\boldsymbol{h}_{\boldsymbol{\nu}}\boldsymbol{E}_{\boldsymbol{\nu}}) \times \boldsymbol{\nu} \qquad \text{and} \qquad \boldsymbol{E}_{\boldsymbol{\nu}} = -\frac{1}{\mathrm{i}\omega\varepsilon}\operatorname{Div}(\boldsymbol{H} \times \boldsymbol{\nu})\,,$$

see (2.30) and (4.15), respectively. Thus, we can compute all quantities occurring in the transmission and boundary conditions (3.14), (3.15) from the total fields of the corresponding scattering problem, implementing only the surface gradient **Grad**, the surface divergence Div, the rotation operators $\boldsymbol{\nu} \times \cdot$ as well as $\cdot \times \boldsymbol{\nu}$ and products of two functions on the boundary. The surface gradient is implicitly implemented as an operator in `Bempp-cl`, while the surface divergence can be represented in weak form via the partial integration formula

$$\int_{\partial D} v \operatorname{Div} \boldsymbol{U}\,\mathrm{d}s = -\int_{\partial D} \boldsymbol{U} \cdot \mathbf{Grad}\, v\,\mathrm{d}s\,,$$

see Section 2.5. The rotation operator and the product of two boundary functions are implemented using suitable projections on the relevant boundary element spaces.

Below and in Algorithm 1, we denote vector space discretizations of the original grid by RWG and SNC, where on the barycentrically refined grids, they are denoted by RWG_b and SNC_b as well as BC and RBC, corresponding to the basis functions with the same designation. Scalar space discretizations with continuous, piecewise linear functions on the original and barycentrically refined grid are denoted by P1 and $\mathrm{P1}_b$, respectively. Let us recapitulate the mapping properties of the relevant operators described in Section 2.5. We have

$$\begin{aligned} \boldsymbol{\gamma}_t &\colon \boldsymbol{H}(\mathbf{curl}, \Omega) \to \boldsymbol{H}^{-1/2}(\operatorname{Div}, \partial D)\,, & \mathbf{Grad} &\colon H^{1/2}(\partial D) \to \boldsymbol{H}^{-1/2}(\operatorname{Curl}, \partial D)\,, \\ \boldsymbol{\gamma}_T &\colon \boldsymbol{H}(\mathbf{curl}, \Omega) \to \boldsymbol{H}^{-1/2}(\operatorname{Div}, \partial D)\,, & \operatorname{Div} &\colon \boldsymbol{H}^{-1/2}(\operatorname{Div}, \partial D) \to H^{-1/2}(\partial D)\,. \end{aligned}$$

Thus, the tangential traces of the electric field $\boldsymbol{E}$ – and hence of $\boldsymbol{E}^i$ and $\boldsymbol{E}^s$ – are defined in $\boldsymbol{H}^{-1/2}(\operatorname{Div}, \partial D)$. Recall that the L^2-dual space of $\boldsymbol{H}^{-1/2}(\operatorname{Div}, \partial D)$ is $\boldsymbol{H}^{-1/2}(\operatorname{Curl}, \partial D)$, see Theorem 2.13.

We discretize $\boldsymbol{H}^{-1/2}(\operatorname{Div}, \partial D)$ by using RWG, RWG_b and BC basis functions. The dual $\boldsymbol{H}^{-1/2}(\operatorname{Curl}, \partial D)$ is then discretized by the use of SNC, SNC_b and RBC basis functions, respectively. A discretization of $\boldsymbol{\gamma}_t\boldsymbol{H}$ or $(\boldsymbol{\gamma}_t\boldsymbol{E}, \boldsymbol{\gamma}_t\boldsymbol{H})$ is obtained by solving (5.8a) or (5.18a), which for the scattering problem can be done on the original mesh as mentioned above. Then, we project $\boldsymbol{\gamma}_t\boldsymbol{H}$ onto RWG_b and discretize $\boldsymbol{\gamma}_T\boldsymbol{H}$ on BC. Finally, we assemble the functions $\mathrm{i}k\boldsymbol{h}_{\boldsymbol{\nu}}\boldsymbol{\gamma}_T\boldsymbol{H}$ (on BC) and $\operatorname{Curl}(\boldsymbol{h}_{\boldsymbol{\nu}}\boldsymbol{E}_{\boldsymbol{\nu}})$ (on RWG_b) and project them both onto RWG.

We employ the following discretizations:

$$\cdot \times \boldsymbol{\nu}\,(\hat{=}\,\boldsymbol{\gamma}_t)\colon \mathrm{RBC} \to \mathrm{RWG}_b\,, \qquad \mathbf{Grad}\colon \mathrm{P1}_b \to \mathrm{RBC}\,,$$
$$\boldsymbol{\nu} \times \cdot\,(\hat{=}\,\boldsymbol{\gamma}_T)\colon \mathrm{RWG}_b \to \mathrm{BC}\,, \qquad \mathrm{Div}\colon \mathrm{RWG}_b \to \mathrm{P1}_b\,.$$

The projection procedure is outlined in Algorithm 1 for some perturbation $\boldsymbol{h}$ of $(\boldsymbol{z}, r)$ representing some perfect conductor. We proceed similarly for transmission problems.

Algorithm 1 Projection approach in `Bempp-cl`: Domain derivative for some perturbation $\boldsymbol{h}$ – perfect conductor

Require: RWG, SNC, BC, RBC, RWG_b, SNC_b; discretization of $\boldsymbol{\gamma}_t\boldsymbol{H}$ on RWG
Ensure: Solve system (5.8b) to obtain density $\boldsymbol{\lambda}$ in RWG
1 Project $\boldsymbol{\gamma}_t\boldsymbol{H}$ to RWG_b
2 Compute $\boldsymbol{h}_{\boldsymbol{\nu}}$ on P1 by Corollary 4.12
3 Project $\boldsymbol{h}_{\boldsymbol{\nu}}$ to $\mathrm{P1}_b$
4 Assemble $\mathrm{i}k\boldsymbol{h}_{\boldsymbol{\nu}}\boldsymbol{\gamma}_T\boldsymbol{H}$ and $\mathrm{Curl}(\boldsymbol{h}_{\boldsymbol{\nu}}\boldsymbol{E}_{\boldsymbol{\nu}})$ from right-hand of (3.15)
5 Project $\mathrm{i}k\boldsymbol{h}_{\boldsymbol{\nu}}\boldsymbol{\gamma}_T\boldsymbol{H}$ and $\mathrm{Curl}(\boldsymbol{h}_{\boldsymbol{\nu}}\boldsymbol{E}_{\boldsymbol{\nu}})$ onto RWG
6 Assemble right-hand side of (3.15)
7 Solve discretized EFIE with LU decomposition

Remark 5.1. `Bempp-cl` provides the method `self.barycentric_representation()` to obtain a barycentric representation of a discrete space `self`. In order to work correctly, we needed to modify the implementation for the P1 spaces, which can be found under

`bempp.api.space.scalar_spaces.p1_barycentric_continuous_function_space()`

in `Bempp-cl 0.3.1`. The modified version of `p1_barycentric_continuous_function_space()` can be found in our provided code in the script `correct_space.py`.

5.3. Numerical Implementation of the Inverse Problem

We fix material parameters ε, μ, an incident field $(\boldsymbol{E}^i, \boldsymbol{H}^i) \in \boldsymbol{H}_{\mathrm{loc}}(\mathbf{curl}, \mathbb{R}^3) \times \boldsymbol{H}_{\mathrm{loc}}(\mathbf{curl}, \mathbb{R}^3)$, and recall the definition of $\mathcal{M}$ containing pairs $(\boldsymbol{z}, r)$ which represent boundaries ∂D of C^1-smooth domains (cf. (4.9)). Then, inspired by previous works using asymptotic scattering models for thin tubular objects [3, 23, 69], to solve the inverse problem (5.1), we focus on the minimization problem

$$\|F(\boldsymbol{z}, r) - \boldsymbol{E}^{\infty}_{\mathrm{data}}\|^2_{\boldsymbol{L}^2_t(\mathbb{S}^2)} \to \min\,, \tag{5.19}$$

for $(\boldsymbol{z}, r) \in \mathcal{M}$.

5.3.1. The Regularized Problem

We cope with the ill-posed nature of (5.1) by introducing three regularization terms that penalize unfavorable behavior of $\boldsymbol{z}$ and r. The first regularization term is the total curvature of the spine curve $\boldsymbol{z}$, which is given by Ψ_1 with

$$\Psi_1(\boldsymbol{z}) \coloneqq \int_0^1 \kappa^2(\tau)|\boldsymbol{z}'(\tau)| \,\mathrm{d}\tau\,,$$
$$\text{with curvature } \kappa(\tau) = \frac{|\boldsymbol{z}'(\tau) \times \boldsymbol{z}''(\tau)|}{|\boldsymbol{z}'(\tau)|^3}\,, \qquad \tau \in [0,1]\,, \tag{5.20}$$

and regularizes the curvature of the curve the tube is based upon (cf. [69, Equation (4.18)]). Hence, Ψ_1 prevents too strong entanglement of the tubular object. For the second penalty term we choose $n \in \mathbb{N}$ knots $t_j \in [0,1]$, $j = 1, \ldots, n$, with $0 = t_1 < t_2 < \ldots < t_n = 1$. The term is then defined by Ψ_2 with

$$\Psi_2(\boldsymbol{z}) \coloneqq \sum_{j=1}^{n-1} \left| \frac{1}{n-1} \int_0^1 |\boldsymbol{z}'(\tau)| \,\mathrm{d}\tau - \int_{t_j}^{t_{j+1}} |\boldsymbol{z}'(\tau)| \,\mathrm{d}\tau \right|^2 \tag{5.21}$$

and aims at forcing a close to uniform segmentation of the parameter interval $[0,1]$ (cf. [69, p. 86]). Note that Ψ_1 and Ψ_2 solely regularize the center curve the tube is based upon. Finally, we introduce a third term Ψ_3 defined by

$$\Psi_3(r) \coloneqq \int_0^1 |r'(\tau)|^2 \,\mathrm{d}\tau\,, \tag{5.22}$$

which penalizes large variations of the radius function r.

With these terms, the minimization problem (5.19) becomes the regularized minimization problem

$$J(\boldsymbol{z}, r) \coloneqq \|F(\boldsymbol{z}, r) - \boldsymbol{E}^\infty\|^2_{\boldsymbol{L}^2_t(\mathbb{S}^2)} + \alpha_1 \Psi_1(\boldsymbol{z}) + \alpha_2 \Psi_2(\boldsymbol{z}) + \alpha_3 \Psi_3(r) \to \min\,, \tag{5.23}$$

for $(\boldsymbol{z}, r) \in \mathcal{M}$ with regularization parameters $\alpha_j > 0$, $j = 1, 2, 3$.

We solve (5.23) by employing a Gauss–Newton scheme, see, e.g., [85, Section 10.3], where we start with an initial guess $(\boldsymbol{z}_0, r_0)$ and in each iteration, an update $(\boldsymbol{z}_{n+1}, r_{n+1})$ to the current iterate $(\boldsymbol{z}_n, r_n)$, $n \in \mathbb{N}_0$, is computed. In this update step, we further incorporate the *tubular neighborhood condition*

$$\|r\|_{C[0,1]} \|\kappa\|_{C[0,1]} < 1\,. \tag{5.24}$$

As described in [76, Theorem 1], this condition on the curvature κ and radius function r prevents local self-intersections of the tubular object, i.e., it ensures that the update satisfies Assumption 4.4 locally. The tubular neighborhood condition has already been used in [5], [69].

Remark 5.2. Note that (5.24) only guarantees that there is no *local* self-intersection of the tube. Global self-intersections are still possible. In [86], the O'Hara Möbius energy has been introduced that blows up if the underlying curve in $\mathbb{R}^2$ has self-intersections. In [73], an analogous energy term for k-dimensional submanifolds in $\mathbb{R}^n$ has been proposed. This would provide us with a penalty term for preventing global self-intersections. However, we did not include this term in our algorithm, since in practice we rarely faced this particular problem of non-local self-intersections.

Applying the Gauss–Newton method to solve problem (5.23), requires the computation of the Fréchet derivative of the functional J. In Theorem 4.13, we have shown that F is Fréchet

differentiable at $(\boldsymbol{z}, r)$ and that the Fréchet derivative is equal to the far-field pattern $\boldsymbol{E}'^{\infty}$ of the domain derivative $\boldsymbol{E}'$. This can be obtained by solving (2.22a) together with the interface condition (3.14) for a penetrable scatterer and (2.24a) together with the boundary condition (3.15) in the case of a perfectly conducting scatterer. For the penalty terms in the context of the Gauss–Newton scheme, we have the following results.

Lemma 5.3. *Let $(\boldsymbol{z}, r) \in \mathcal{M}$ (cf. (4.9)) and $(\boldsymbol{u}, \delta)$ be a perturbation, such that $(\boldsymbol{z}+\boldsymbol{u}, r+\delta) \in \mathcal{M}$. Furthermore, let $\mathcal{M}_{\boldsymbol{z}} \coloneqq \{\boldsymbol{z} : (\boldsymbol{z}, r) \in \mathcal{M}\}$, $\mathcal{M}_r \coloneqq \{r : (\boldsymbol{z}, r) \in \mathcal{M}\}$. It holds that*

$$\kappa^2 |\boldsymbol{z}'| = \left| \frac{\boldsymbol{z}''}{|\boldsymbol{z}'|^{3/2}} - \frac{\boldsymbol{z}' \cdot \boldsymbol{z}''}{|\boldsymbol{z}'|^{7/2}} \boldsymbol{z}' \right|^2 . \tag{5.25}$$

We define the mappings $\psi_1 \colon \mathcal{M}_{\boldsymbol{z}} \to \mathbb{R}^3$, $\psi_{2,j} \colon \mathcal{M}_{\boldsymbol{z}} \to \mathbb{R}$, $\psi_3 \colon \mathcal{M}_r \to \mathbb{R}$ by

$$\begin{aligned}
\psi_1(\boldsymbol{z}) &\coloneqq \frac{\boldsymbol{z}''}{|\boldsymbol{z}'|^{3/2}} - \frac{\boldsymbol{z}' \cdot \boldsymbol{z}''}{|\boldsymbol{z}'|^{7/2}} \boldsymbol{z}' , \\
\psi_{2,j}(\boldsymbol{z}) &\coloneqq \frac{1}{n-1} \int_0^1 |\boldsymbol{z}'(\tau)| \, \mathrm{d}\tau - \int_{t_j}^{t_{j+1}} |\boldsymbol{z}'(\tau)| \, \mathrm{d}\tau , \qquad j \in \{1, \dots, n-1\} , \\
\psi_3(r) &\coloneqq r' .
\end{aligned}$$

ψ_1, $\psi_{2,j}$, $j \in \{1, \dots, n-1\}$, and ψ_3 are Fréchet differentiable at $(\boldsymbol{z}, r)$. It holds that

$$\mathrm{d}\psi_1[\boldsymbol{z}]\boldsymbol{u} = \frac{\boldsymbol{u}''}{|\boldsymbol{z}'|^{3/2}} - \frac{3}{2} \frac{\boldsymbol{z}' \cdot \boldsymbol{u}'}{|\boldsymbol{z}'|^{7/2}} \boldsymbol{z}'' - \frac{\boldsymbol{z}'' \cdot \boldsymbol{z}'}{|\boldsymbol{z}'|^{7/2}} \boldsymbol{u}' - \left(\frac{\boldsymbol{z}'' \cdot \boldsymbol{u}'}{|\boldsymbol{z}'|^{7/2}} + \frac{\boldsymbol{u}'' \cdot \boldsymbol{z}'}{|\boldsymbol{z}'|^{7/2}} - \frac{7}{2} \frac{(\boldsymbol{z}'' \cdot \boldsymbol{z}')(\boldsymbol{z}' \cdot \boldsymbol{u}')}{|\boldsymbol{z}'|^{11/2}} \right) \boldsymbol{z}' , \tag{5.26}$$

$$\mathrm{d}\psi_{2,j}[\boldsymbol{z}]\boldsymbol{u} = \frac{1}{n-1} \int_0^1 \frac{\boldsymbol{z}'(\tau) \cdot \boldsymbol{u}'(\tau)}{|\boldsymbol{z}'(\tau)|} \, \mathrm{d}\tau - \int_{t_j}^{t_{j+1}} \frac{\boldsymbol{z}'(\tau) \cdot \boldsymbol{u}'(\tau)}{|\boldsymbol{z}'(\tau)|} \, \mathrm{d}\tau , \qquad j \in \{1, \dots, n-1\} , \tag{5.27}$$

$$\mathrm{d}\psi_3[r]\delta = \delta' . \tag{5.28}$$

Proof. (5.25) and the Fréchet derivatives of ψ_1, $\psi_{2,j}$, $j \in \{1, \dots, n-1\}$, have been proved in [69, Lemma 4.5]. The Fréchet derivative of ψ_3 is straightforward. ∎

5.3.2. Discretization of the Inverse Problem

In our reconstruction algorithm, we always discretize $\boldsymbol{z}$ by a third-degree B-spline curve $\boldsymbol{z}_M$ – see Appendix B – defined by M control points $\boldsymbol{c}^{(1)}, \dots, \boldsymbol{c}^{(M)}$, collected in $\vec{\boldsymbol{c}} \in \mathbb{R}^{3M}$, and the radius function r by a cubic spline r_M, interpolating the radius values $\vec{r} \in \mathbb{R}^{M-2}$, using the distinct knots of $\boldsymbol{z}_M$ as interpolation points. With this information, we can represent ∂D by these M control points and $M-2$ radius values. In order to generate a corresponding rotation-minimizing frame, instead of directly solving the differential-algebraic equation (4.1), we apply the double-reflection method proposed in [110]. Note that the discrete inverse problem (cf. (5.1)) is now to find the control points $\vec{\boldsymbol{c}} \in \mathbb{R}^{3M}$ and radius values $\vec{r} \in \mathbb{R}^{M-2}$ such that $F(\boldsymbol{z}_M, r_M) = \boldsymbol{E}^{\infty}_{\mathrm{data}}$.

The electric far-field pattern $\boldsymbol{E}^{\infty}$ corresponding to this pair of incident plane waves is evaluated

Algorithm 2 Solving the inverse problem

Require: Incident field, its direction and polarization. Noisy far-field data F_{exact} corresponding to some tubular object T_{exact} represented by M control points $\vec{\boldsymbol{c}}_{\text{exact}}$ and $M-2$ radii $\vec{r}_{\text{exact}}$

Ensure: Reconstruction T_{approx}, represented by M control points $\vec{\boldsymbol{c}}_{\text{approx}}$ and $M-2$ radius values $\vec{r}_{\text{approx}}$, of exact object T_{exact} and corresponding far field F_{approx}

$(\vec{\boldsymbol{c}}_{\text{approx}}, \vec{r}_{\text{approx}}) \leftarrow$ initial guess
$F_{\text{approx}} \leftarrow$ far field of T_{approx} represented by $(\vec{\boldsymbol{c}}_{\text{approx}}, \vec{r}_{\text{approx}})$
while relative $\boldsymbol{L}_t^2$-residual > some tolerance and the update sufficiently big **do**
    Define the discrete boundary spaces on the current grid `# Bempp-cl function spaces`
    Define the functions $\gamma_t \boldsymbol{E}^i$ (and $\gamma_t \boldsymbol{H}^i$) on the grid `# Bempp-cl Gridfunctions`
    Set up the boundary operators for the EFIE or modified PMCHWT integral equation
    $\boldsymbol{\mathcal{J}}_{K_N} \leftarrow$ initialize Jacobian of K_N
    for $i = 0$ to $M-1$ **do**
        for $j = 1$ to 3 **do**
            Perturb jth coordinate of (i+1)th control point
            Solve EFIE / modified PMCHWT to obtain a corresponding $\boldsymbol{E}'$
            Obtain far field F' of $\boldsymbol{E}'$
            Compute domain derivatives ψ_1', ψ_2' of ψ_1, ψ_2 by (5.26), (5.27)
            F', ψ_1', $\psi_{2,j}' \leftarrow$ incorporate quadrature weights and regularization parameters
            $\boldsymbol{\mathcal{J}}_{K_N}[\ldots, 3*i+j] \leftarrow (F', \psi_1', \psi_2')$
        end for
    end for
    for $i = 1$ to $M-2$ **do**
        Perturb ith radius value
        Solve EFIE / modified PMCHWT to obtain a corresponding $\boldsymbol{E}'$
        Obtain far field F' of $\boldsymbol{E}'$
        Compute domain derivative ψ_3' of ψ_3 by (5.28)
        F', $\psi_3' \leftarrow$ incorporate quadrature weights and regularization parameters
        $\boldsymbol{\mathcal{J}}_{K_N}[\ldots, 3*M+i] \leftarrow (F', \psi_3')$
    end for
    Apply a Gauss–Newton step with Jacobian $\boldsymbol{\mathcal{J}}_{K_N}$ to get `update` $= \boldsymbol{g}_k$ by (5.31)
    Step size $\lambda \leftarrow$ initialize by 1
    Reduce λ until (5.24) is satisfied and all radius values are greater than some tolerance
    $(\vec{\boldsymbol{c}}_{\text{approx}}, \vec{r}_{\text{approx}}) \leftarrow (\vec{\boldsymbol{c}}_{\text{approx}}, \vec{r}_{\text{approx}}) + \lambda *$ `update`
    $F_{\text{approx}} \leftarrow$ far field of T_{approx} represented by $(\vec{\boldsymbol{c}}_{\text{approx}}, \vec{r}_{\text{approx}})$
end while

in $2N(N-1)$ discrete directions

$$\boldsymbol{y}_{j\ell} = \begin{pmatrix} \sin(\pi\, j/N)\, \cos(\pi\, \ell/(2N)) \\ \sin(\pi\, j/N)\, \sin(\pi\, \ell/(2N)) \\ \cos(\pi\, j/N) \end{pmatrix} \in \mathbb{S}^2\,, \qquad j = 1, \ldots, N-1, \quad \ell = 0, \ldots, 2N-1\,. \tag{5.29}$$

We discretize the $\boldsymbol{L}_t^2$-norm in (5.23) and all the integrals over the interval $[0,1]$, which occur in the penalty terms Ψ_i, $i \in \{1,2,3\}$, and their Fréchet derivatives, by using a composite trapezoidal

rule. For the integrals over $[t_j, t_{j+1}]$ in (5.21) and (5.27), we use a simple trapezoidal rule. Hence, we obtain an approximation J_N of the functional J from (5.23), given by

$$\left.\begin{aligned} J_N(\boldsymbol{z}_M, r_M) = \frac{\pi^2}{N^2} \sum_{j=1}^{N-1} \sum_{\ell=0}^{2N-1} |(F(\boldsymbol{z}_M, r_M) - \boldsymbol{E}^\infty)(\boldsymbol{y}_{j\ell})|^2 \sin(\pi\, j/N) \\ + \alpha_1 \sum_{j=1}^{m} w_j \kappa^2(\tau_j) |\boldsymbol{z}'_M(\tau_j)| \\ + \alpha_2 \sum_{i=1}^{n-1} \left| \frac{1}{n-1} \sum_{j=1}^{m} w_j |\boldsymbol{z}'_M(\tau_j)| - \frac{1}{2}(t_{i+1} - t_i)(|\boldsymbol{z}'_M(\tau_{i+1})| + |\boldsymbol{z}'_M(\tau_i)|) \right|^2 \\ + \alpha_3 \sum_{j=1}^{m} w_j |r'_M(\tau_j)|^2 \,, \end{aligned}\right\} \tag{5.30}$$

with a uniform partition $\{0 = \tau_1 < \tau_2 < \ldots < \tau_m = 1\} \subset [0,1]$ and weights w_j, $j \in \{1, \ldots, m\}$, according to the composite trapezoidal rule. With ψ_1, $\psi_{2,j}$, $j \in \{1, \ldots, n-1\}$, ψ_3 from Lemma 5.3 and by keeping in mind that the far-field pattern and ψ_1 are vector-valued, we can interpret (5.30) as

$$J_N(\boldsymbol{z}_M, r_M) = |K_N(\vec{\boldsymbol{c}}, \vec{r})|^2 \,,$$

for some $K_N \colon \mathbb{R}^{3M+(M-2)} \to \mathbb{R}^{3\cdot 2N(N-1)+3m+(n-1)+m}$. The kth search direction $\boldsymbol{g}_k$ for the Gauss–Newton iteration is then the solution of

$$\boldsymbol{\mathcal{J}}_{K_N}^\top(\vec{\boldsymbol{c}}_k, \vec{r}_k)\, \boldsymbol{\mathcal{J}}_{K_N}(\vec{\boldsymbol{c}}_k, \vec{r}_k)\, \boldsymbol{g}_k = -\, \boldsymbol{\mathcal{J}}_{K_N}^\top(\vec{\boldsymbol{c}}_k, \vec{r}_k) K_N(\vec{\boldsymbol{c}}_k, \vec{r}_k) \,, \tag{5.31}$$

where $\boldsymbol{\mathcal{J}}_{K_N}$ is the discrete Jacobian of K_N with respect to perturbations of the control points and the radius values. To assemble this Jacobian $\boldsymbol{\mathcal{J}}_{K_N}$, we need to compute

(i) the Jacobian of F, using Theorem 4.13 together with (5.8) or (5.18), where the far-field pattern of the domain derivative may be computed by the Stratton–Chu formula as described in (5.9) and at the end of Subsection 5.1.2,

(ii) the Jacobians of $\psi_1,\ \psi_{2,j},\ \psi_3,\ j \in \{1, \ldots, m\}$, using Lemma 5.3.

A pseudocode representation of the implementation is given in Algorithm 2.

Remark 5.4. Note that, besides self-intersections being the cause, an update of $(\boldsymbol{z}, r)$ may also not be in $\mathcal{M}$, if the radius attains negative values. We tackle this issue by reducing the step size for the update, until the radius is greater than some positive tolerance. However, we note that this only poses a problem, if we consider particularly "challenging" or exceedingly "small" radii. For the numerical examples, which we have investigated, this usually has not been an issue. Below, in Example 5.1, we show a case, where the problem did occur.

Remark 5.5. For a thorough discussion on regularized iterative schemes and convergence results under additional assumptions, we refer to [63].

5.4. Numerical Examples

For our numerical experiments, we consider the scattering of a plane wave

$$(\boldsymbol{E}^i(\boldsymbol{x}), \boldsymbol{H}^i(\boldsymbol{x})) = \left(\boldsymbol{p}, \sqrt{\frac{\varepsilon_+}{\mu_+}}\, \boldsymbol{d} \times \boldsymbol{p}\right) \mathrm{e}^{\mathrm{i}k_+ \boldsymbol{x}\cdot\boldsymbol{d}}, \qquad \boldsymbol{d} = \frac{1}{\sqrt{3}} \begin{pmatrix} 1 \\ 1 \\ 1 \end{pmatrix}, \quad \boldsymbol{p} = \begin{pmatrix} 1 \\ 0 \\ -1 \end{pmatrix},$$

from a tubular obstacle D. The vector $\boldsymbol{d} \in S^2$ is the direction of propagation and the vector $\boldsymbol{p} \in \mathbb{C}^3 \setminus \{0\}$ with $\boldsymbol{p} \perp \boldsymbol{d}$ denotes the polarization of the plane wave (cf. (2.49)). The electric far-field pattern $\boldsymbol{E}^\infty_{\mathrm{data}}$ corresponding to this pair of incident plane waves is evaluated in 180 discrete points given by (5.29) for $N = 10$. To prevent an inverse crime, cf. [31, p. 179], we use another solver to generate the given forward far-field data than for solving the inverse problem. We accomplish this by solving the scattering problem for the exact object via the CFIE (C.5) (perfect conductor) or the PMCHWT (C.8) (penetrable obstacle). To approximate the solution of the system of linear equations that is obtained by discretizing the CFIE / PMCHWT integral equation, we employ the iterative generalized minimal residual (GMRES) method [98, 109], with tolerance 1e–5 and without restarts. Additionally, we use a different discretization for the iterates during the reconstruction than in the simulation for the true scattering object D. Afterwards, we perturb the resulting electric far-field pattern $\boldsymbol{E}^\infty_{\mathrm{data}}$ by some additive complex-valued random noise with noise level $\delta > 0$. Thus, for some complex-valued matrix $\boldsymbol{M}$ with the same size as $\boldsymbol{E}^\infty_{\mathrm{data}}$ and uniformly distributed random numbers $a + \mathrm{i}b$, with $a, b \in [-1/2, 1/2)$, as entries, we define the given noisy far-field data for the reconstruction by $\boldsymbol{E}^{\infty,\delta} := \boldsymbol{E}^\infty_{\mathrm{data}} + \delta \|\boldsymbol{E}^\infty_{\mathrm{data}}\|_{\boldsymbol{L}^2_t(\mathbb{S}^2)} \boldsymbol{M} / \|\boldsymbol{M}\|_{\boldsymbol{L}^2_t(\mathbb{S}^2)}$. This noisy data satisfies

$$\frac{\|\boldsymbol{E}^\infty_{\mathrm{data}} - \boldsymbol{E}^{\infty,\delta}\|_{\boldsymbol{L}^2_t(\mathbb{S}^2)}}{\|\boldsymbol{E}^\infty_{\mathrm{data}}\|_{\boldsymbol{L}^2_t(\mathbb{S}^2)}} = \delta\,.$$

For the discretization of the $\boldsymbol{L}^2_t(\mathbb{S}^2)$-norms, we use a composite trapezoidal rule, as in (5.30). For all the examples that follow, we set $\delta = 5\%$. For pairs $(\boldsymbol{z}, r) \in \mathcal{M}$, $\boldsymbol{z}$ is discretized by third-degree B-spline spine curves (see Appendix B) and r by a cubic spline with the distinct knots of the B-spline as the interpolation points, as detailed in the examples below. The actual goal is to minimize the reconstruction error of the shape of an object. Since such an error is impractical to define, the Gauss–Newton iteration terminates, when either the relative $\boldsymbol{L}^2$-residual becomes smaller than the applied noise level, i.e.,

$$\frac{\|\boldsymbol{E}^\infty_{\mathrm{data}} - \boldsymbol{E}^\infty_{\mathrm{approx}}\|_{\boldsymbol{L}^2_t(\mathbb{S}^2)}}{\|\boldsymbol{E}^\infty_{\mathrm{data}}\|_{\boldsymbol{L}^2_t(\mathbb{S}^2)}} < \delta\,,$$

or when the relative movement of the control points and the relative change of the radius function – which are computed by the norm of the respective update divided by the norm of the corresponding previous data – fall below a given tolerance. In all subsequent examples, we select a tolerance of 1% for both the relative movement of the control points and the relative radius change. The regularization parameters $\alpha_1, \alpha_2, \alpha_3$ are determined based on experiential knowledge.

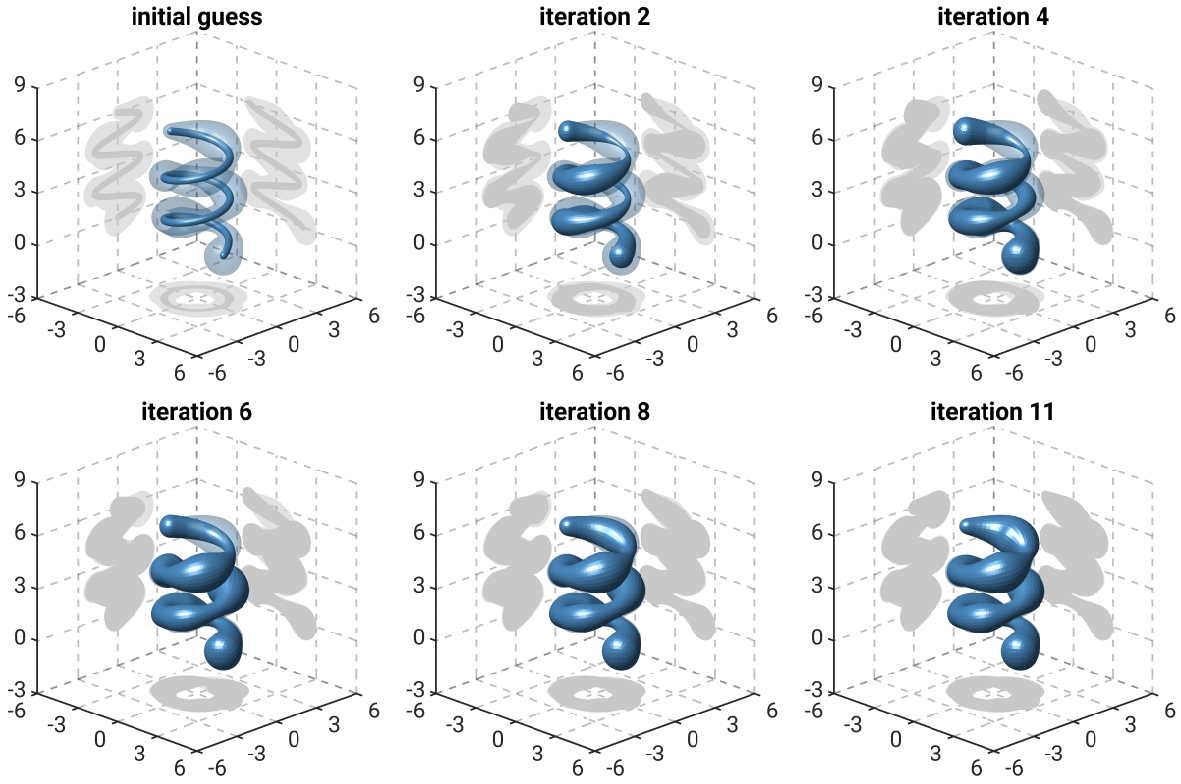

Figure 5.2. Excerpts from the convergence history of Example 5.1. The exact obstacle is displayed slightly transparent as a comparison for each iteration.

For each example we provide a convergence history – for Example 5.4 together with a graph of the relative residual plotted against the iteration number. Here, we highlight only the values of some iterations. Each plot of the convergence history features the true scatterer, slightly transparent and in faded blue, together with projections onto the shifted coordinate planes in faded gray. The current iterate is visualized in solid blue with its projections in solid gray.

Example 5.1. We start with a mere reconstruction of the radius function of a perfectly conducting obstacle D defined by a third-degree B-spline curve with control points

$$\boldsymbol{c}_j = 2 \begin{pmatrix} \cos(5\pi\, j/20) \\ \sin(5\pi\, j/20) \\ 3\, j/20 \end{pmatrix}, \qquad j = 0, \dots, 19\,.$$

The radius function $r = \sin^2(10\,\cdot\,) + \cos^{12}(10\,\cdot\,)$ is represented by a cubic spline with the distinct knots of the B-spline as the interpolation points. We choose the material parameters $\varepsilon_+ = \mu_+ = 1$ and the angular frequency $\omega = 2$. Discretizing the surface leads to a mesh and a corresponding RWG finite element space with 27744 DOF.

For the reconstruction, we choose a B-spline spine curve of degree 3 defined by 19 control

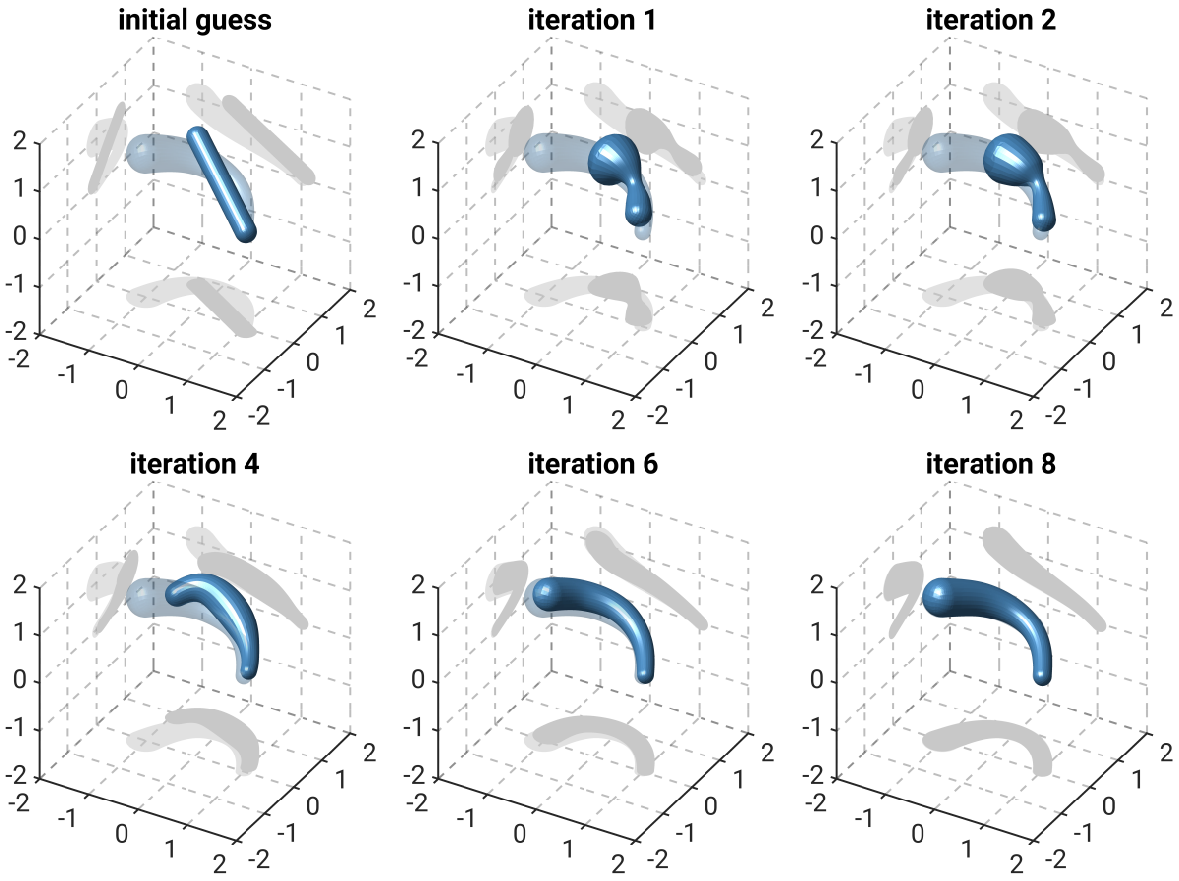

Figure 5.3. Excerpts from the convergence history of Example 5.2. The exact obstacle is displayed slightly transparent as a comparison for each iteration.

points

$$\widetilde{\boldsymbol{c}}_j = 2 \begin{pmatrix} \cos(5\pi\, j/19) \\ \sin(5\pi\, j/19) \\ 3\, j/19 \end{pmatrix}, \qquad j = 0, \dots, 18\,,$$

and knots $t_j = j/19$, $j = 0, \dots, 18$. Note that we induce a systematic error by choosing one control point less than for the exact scatterer. Hence, due to the object's helical shape and the cross sections along the curve being circles, an exact reconstruction is not possible. The radial function is represented by a cubic spline with t_j as the interpolation points. For the initial guess, the radius function is chosen constant as $r \equiv 0.2$. In each iteration, the RWG space discretization of the corresponding mesh has 21546 DOF. The regularization parameter is chosen as $\alpha_3 = 2.5\text{e}{-3}$. Starting with a relative residual of approximately 87.67% the Gauss–Newton iteration terminates after 11 iterations with a relative residual of around 11.05% due to the update being too small. The results for the reconstruction are shown in Figure 5.2.

We note that if we choose the same control points for the reconstruction as for the exact shape, the iteration terminates after 9 steps, due to the relative residual dropping below $2.8\% < 5\% = \delta$.

In iteration 2 (and also 4) of Figure 5.2, we can see the radius getting very small. This can become problematic, especially when radius values become negative. To prevent this from

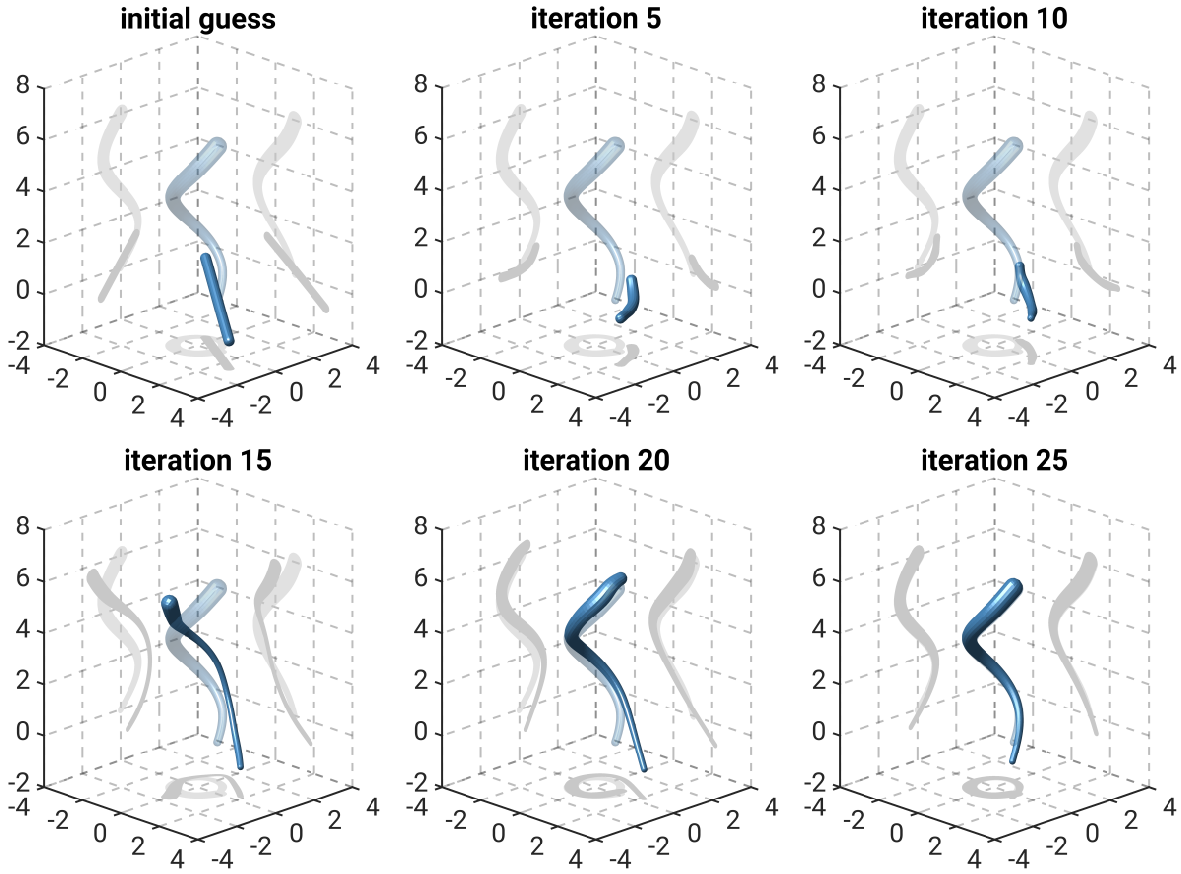

Figure 5.4. The initial guess, samples of the reconstruction and the final reconstruction for Example 5.3 are depicted. The exact obstacle is displayed slightly transparent as a comparison for each iteration.

happening, we reduce the step size as long as any radius value is below an a priori known value (in this example 0.01), see Remark 5.4.

Example 5.2. We continue with a full reconstruction of a perfectly conducting obstacle D defined by a third-degree B-spline curve with control points

$$\boldsymbol{c}_j = \begin{pmatrix} \cos(\pi\, j/5) \\ \sin(\pi\, j/5) \\ j/5 \end{pmatrix}, \qquad j = 0, \dots, 4\,.$$

The radius function $r = 0.15 \exp(\sin(\,\cdot\,))$ is represented by a cubic spline with the distinct knots of the B-spline as the interpolation points. We choose the material parameters $\varepsilon_+ = \mu_+ = 1$ and the angular frequency $\omega = 2$. Discretizing the surface leads to a mesh and a corresponding RWG finite element space with 10464 DOF.

For the reconstruction, we choose a B-spline spine curve of degree 3 defined by 7 control points and knots $t_j = j/6$, $j = 0, \dots, 6$. The radial function is represented by a cubic spline with these points t_j as the interpolation points. For the initial guess, the spine curve is chosen

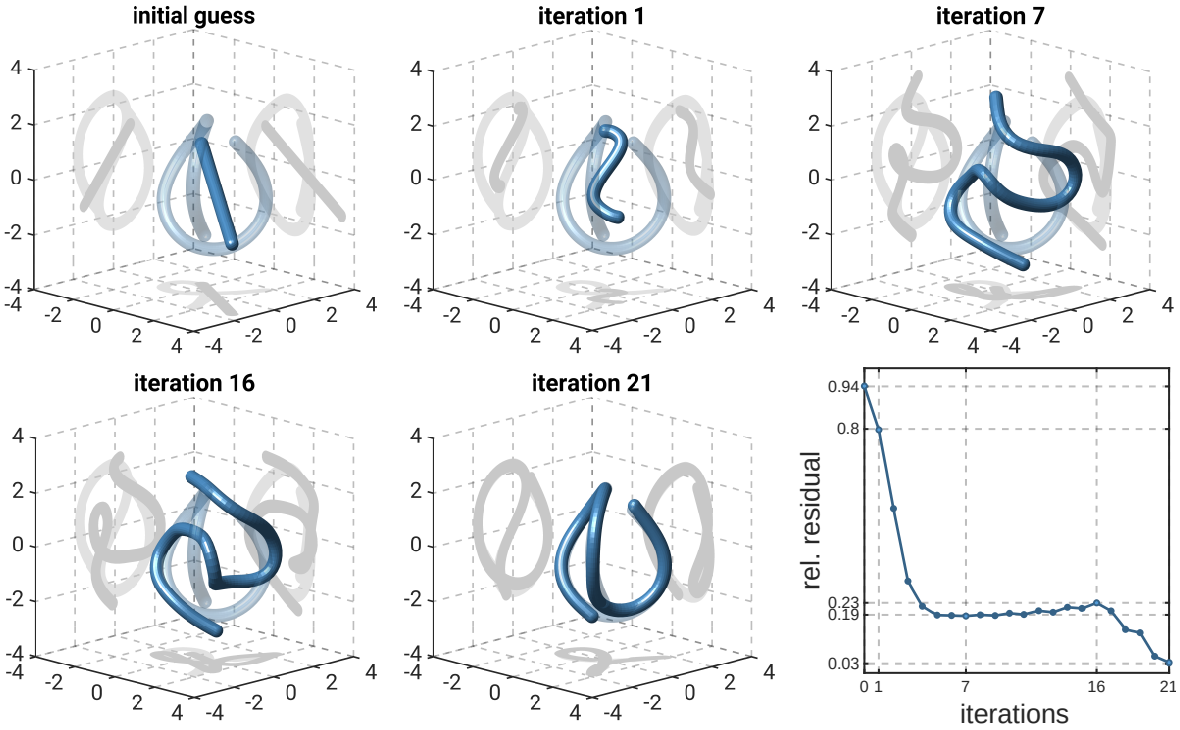

Figure 5.5. *Top-left to bottom-center*: The initial guess, samples of the reconstruction and the final reconstruction for Example 5.4 are depicted. The exact obstacle is displayed slightly transparent as a comparison for each iteration. *Bottom-right*: The relative residual plotted against the corresponding iteration.

straight and the radius function constant as $r \equiv 0.2$. In each iteration, the RWG space discretization of the corresponding mesh has 8106 DOF. The regularization parameters are chosen as $\alpha_1 = 6.25$, $\alpha_2 = 64$, $\alpha_3 = 16$. Starting with a relative residual of approximately 82.36%, the Gauss–Newton iteration terminates after 8 iterations with a relative residual of around $2.39\% < 5\% = \delta$. The results for the reconstruction are shown in Figure 5.3.

Example 5.3. We consider another full reconstruction, this time of a penetrable obstacle D defined by a third-degree B-spline curve with control points

$$\boldsymbol{c}_j = \begin{pmatrix} \cos(\pi\, j/5) \\ \sin(\pi\, j/5) \\ 3\, j/5 \end{pmatrix}, \qquad j = 0, \dots, 9\,.$$

The radius function $r = 0.15 \exp(\sin(\,\cdot\,))$ is represented by a cubic spline with the distinct knots of the B-spline as the interpolation points. We choose the material parameters $\varepsilon_+ = 1$, $\varepsilon_- = -4.42 + 0.21\mathrm{i}$, $\mu_+ = \mu_- = 1$ and the angular frequency $\omega = 1$. Note that for a wavelength of 400 nm, these are the dielectric constants for silver (Ag) in vacuum, see [54], [91]. Consequently, the given object models a scatterer measuring approximately 413.8 nm in height, with a minimum radius of 9.5 nm and a maximum radius of roughly 22.2 nm. Discretizing the surface leads to a mesh and a corresponding RWG finite element space with 13380 DOF.

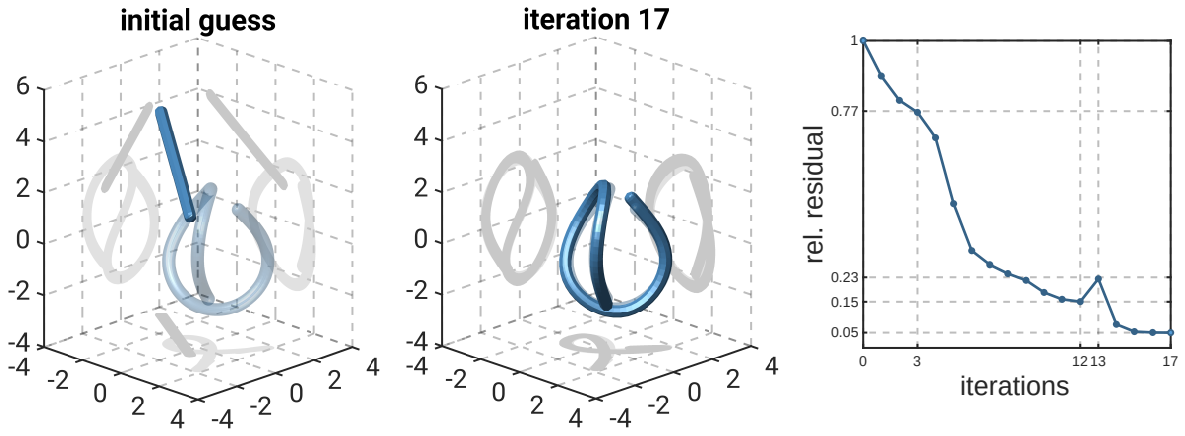

Figure 5.6. The initial guess the final reconstruction and the relative residuals. We use 5% random noise on the given far-field data and 10 control points for the reconstruction, where the course of the true scatterer's center curve has been meticulously reproduced. Here, we start with a different straight tube than in the prior examples. The regularization parameters are $\alpha_1 = 9\text{e}{-2}$, $\alpha_2 = 9$. The finite element spaces of RWG and BC functions, which are used throughout the iteration, have 4032 DOF in total.

For the reconstruction, we choose a B-spline spine curve of degree 3 defined by 13 control points and knots $t_j = j/12$, $j = 0, \dots, 12$. The radial function is represented by a cubic spline with these points t_j as the interpolation points. For the initial guess, the spine curve is chosen as a straight line and the radius function constant as $r \equiv 0.2$. In each iteration, the RWG space discretization of the corresponding mesh has 8544 DOF. The regularization parameters are chosen as $\alpha_1 = 2.25$, $\alpha_2 = 100$, $\alpha_3 = 25$. Starting with a relative residual of approximately 108.37% the Gauss–Newton iteration terminates after 25 iterations with a relative residual of around $3.33\% < 5\% = \delta$. The results for the reconstruction are shown in Figure 5.4.

Example 5.4. As a final example, we present a very challenging problem due to the complicated and involved shape of the object. The example first shows a negative result in that our algorithm will converge to a local minimum of the objective functional if the parameters are unfavorably chosen. We consider a penetrable obstacle with material parameters $\varepsilon_- = 2$, $\mu_- = 1$, i.e., $\varepsilon_r = 2$, $\mu_r = 1$, and the angular frequency is chosen as $\omega = 1$. In this example, $\boldsymbol{z}$ is a third-degree B-spline curve with 20 control points $\boldsymbol{c}_j$, $j = 0, \dots, 19$. We consider a constant radius function $r = 0.24$, which is represented by a cubic spline with the distinct knots of the B-spline as the interpolation points. The shape of this object – depicted in the images of Figure 5.5 – is motivated by Example 6.1 from the optimization in Chapter 6. The object is rather entangled and the caps of the tube are quite close to parts of its body. The finite element space of RWG and BC functions, which is used for computing the exact far-field data, has 22176 DOF in total.

To represent the domains in the reconstruction, we use 30 control points and the knots $t_j = j/29$, $j = 0, \dots, 29$. The finite element spaces of RWG and BC functions, which are used throughout the iteration process, have 15780 DOF in total. As the reconstruction of the shape alone already constitutes a very challenging problem in this example, we assume the radius of the

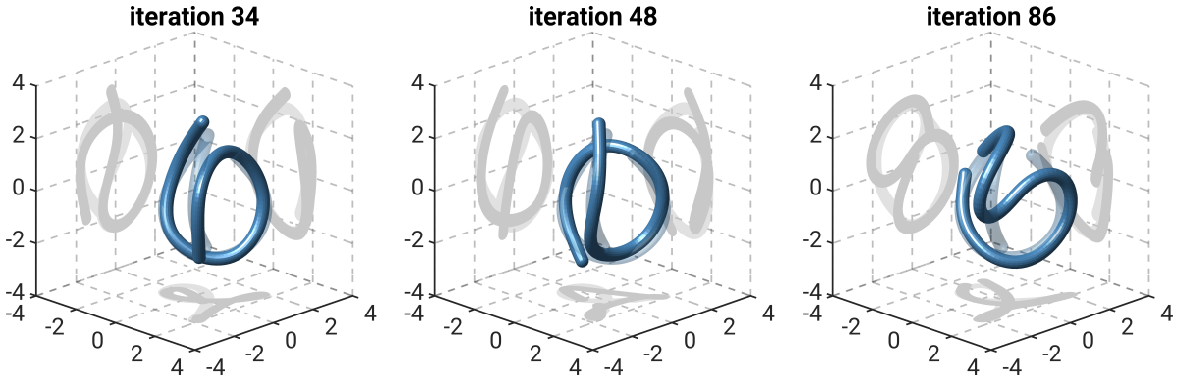

Figure 5.7. Final reconstructions from three distinct iteration processes with either a different initial guess (left) or a different number of control points and regularization parameters (right). In each case, despite connecting the wrong components, most parts of the true scatterer are accurately reconstructed.
Left: Relative residual $\approx 8.7\%$ after 34 steps. 10 control points, $\alpha_1 = 0.25$, $\alpha_2 = 9$.
Middle: Relative residual $\approx 8.3\%$ after 48 steps. 10 control points, $\alpha_1 = 0.25$, $\alpha_2 = 9$.
Right: Relative residual $\approx 7.1\%$ after 86 steps. 25 control points, $\alpha_1 = 306.25\text{e}{-4}$, $\alpha_2 = 56.25\text{e}{-2}$.

tube to be known. The regularization parameters are chosen as $\alpha_1 = 4\text{e}{-2}$, $\alpha_2 = 56.25\text{e}{-2}$. The Gauss–Newton iteration starts with a relative residual of approximately 94.1% and terminates after 21 iterations with a relative residual of around $3.3\% < 5\% = \delta$. In Figure 5.5, samples of the reconstruction are depicted.

It was necessary to choose the regularization parameters significantly smaller than in the previous examples in order to obtain a convergent reconstruction process. This is due to the entwined structure of this object. On the other hand, such a choice allows for high curvatures of the spine curve and possible violations of the tubular neighborhood condition (5.24), which prevents local self-intersections.

Another difficulty in this problem is that due to the closeness of the caps to parts of the body, there exist other tubular objects with a quite different course of the spine curve that produce a very similar far field. To illustrate this challenge, we have simulated several positive and negative examples, one of the former depicted in Figure 5.6 and one of the latter in Figure 5.7, where we vary the resolution of the discretization, the number of control points and regularization parameters, and the initial guess.

We will conclude this example with a brief observation. As large sections of the original object are accurately reconstructed in each negative example (Figures 5.5 and 5.7), the resulting shapes are expected to represent local minima of the objective functional. The algorithm seemingly converges to these local minima in this configuration, nicely illustrating one of the key difficulties in designing iterative reconstruction algorithms for inverse scattering problems. In the error plots of Figures 5.5 and 5.6, we observe that the relative residual has to increase in order to escape the assumed local minimum in such scenarios. In the first (negative) case (see Figure 5.5), the iteration seemingly approaches another *local* instead of the *global* minimum, however, the relative residual still becomes smaller than $5\%(= \delta)$. In the second (postitive) example (see Figure 5.6),

we obtain a very good reconstruction of the true scatterer, which also terminates with a relative residual smaller than 5%.

CHAPTER 6

Optimization with Respect to Electromagnetic Chirality

In the final chapter, we turn to the optimization of tubular objects as defined in Chapter 4 with respect to their em-chirality properties. Such objects are represented by $(\boldsymbol{z}, r) \in \mathcal{M}$ (cf. (4.9)) with a spine curve $\boldsymbol{z}$ and a radius function r. The notion of em-chirality has been summarized in Subsection 2.7.1 and a measure for quantifying em-chirality properties of an object has been introduced in Definition 2.31. We normalize this measure, hence, we consider the bounded objective functional

$$\mathcal{J}_{\mathrm{HS}} \colon \mathcal{M} \to [0,1]\,, \qquad \mathcal{J}_{\mathrm{HS}}(\boldsymbol{z}, r) = \frac{\chi_{\mathrm{HS}}(\mathcal{F}(\boldsymbol{z}, r))}{\|\mathcal{F}(\boldsymbol{z}, r)\|_{\mathrm{HS}}}\,. \tag{6.1}$$

We proceed silimarly to [3], [69, Chapter 5], where the optimization of thin tubular scatterers has been realized. There – as described at the beginning of Chapter 5 – the consideration of thin tubes has led to asymptotic formulae for the scattered field and the corresponding far field, such that not a single Maxwell system had to be solved to compute the far-field operator and a corresponding Fréchet derivative. The resulting tubular objects turned out to be rather complicated and non-intuitive in shape, which in addition to their small cross section, makes them difficult to realize in practice. Therefore, our goal is to develop optimization techniques for thick and long tubular objects, i.e., our aim is to solve the following minimization problem:

$$\text{Find} \qquad \operatorname*{arg\,min}_{(\boldsymbol{z}, r) \in \mathcal{M}} \big[- \mathcal{J}_{\mathrm{HS}}(\boldsymbol{z}, r) \big]\,. \tag{6.2}$$

6.1. Implementation of the Optimization

We will introduce regularization terms to obtain a regularized version of (6.2). One of these terms already assumes that we are considering a discretization of $\boldsymbol{z}$ by a B-spline curve (see Appendix B) and regularizes the corresponding control points. In this case, $(\boldsymbol{z}, r)$ is discretized by a B-spline curve with n control points $\vec{\boldsymbol{c}}_n = (\boldsymbol{c}^{(1)}, \ldots, \boldsymbol{c}^{(n)}) \in \mathbb{R}^{3\times n},\ n \in \mathbb{N}$, and a cubic spline with the distinct knots of the B-spline as the interpolation points. We denote the subset of $\mathcal{M}$ containing such discretizations by $\mathcal{M}_n$.

6.1.1. The Regularized Optimization Problem

To cope with the ill-posedness of (6.2), we introduce four additional penalty terms Ψ_j, $j \in \{1,2,3,4\}$. For Ψ_1, Ψ_3, Ψ_4, we assume that $(\boldsymbol{z}, r) \in \mathcal{M}$. For Ψ_2, we assume that $(\boldsymbol{z}, r) \in \mathcal{M}_n$.

The first regularization term, Ψ_1, has already been defined in (5.20):

$$\Psi_1(\boldsymbol{z}) = \int_0^1 \kappa^2(\tau)|\boldsymbol{z}'(\tau)| \,\mathrm{d}\tau \quad \text{with} \quad \kappa(\tau) = \frac{|\boldsymbol{z}'(\tau) \times \boldsymbol{z}''(\tau)|}{|\boldsymbol{z}'(\tau)|^3}\,, \qquad \tau \in [0,1]\,.$$

It penalizes a high entanglement of $\boldsymbol{z}$. For the second penalty term, $\boldsymbol{z}$ is discretized by a B-spline with n control points $\vec{\boldsymbol{c}}_n = (\boldsymbol{c}^{(1)}, \dots, \boldsymbol{c}^{(n)}) \in \mathbb{R}^{3\times n}$, $n \in \mathbb{N}$. The second term is then defined by

$$\Psi_2(\vec{\boldsymbol{c}}) = \sum_{j=1}^{n-1} \left(\left(\frac{1}{n-1} \sum_{i=1}^{n-1} \left| \boldsymbol{c}^{(i+1)} - \boldsymbol{c}^{(i)} \right| \right) - \left| \boldsymbol{c}^{(j+1)} - \boldsymbol{c}^{(j)} \right| \right)^2 . \tag{6.3}$$

Ψ_2 promotes a uniform distribution of the control points. Note that this term differs from the second regularization term (5.21) for the shape reconstruction in Chapter 5. It has a similar effect, however, it directly penalizes the control points for non-optimal movement in the update and is, thus, easier controllable. The third term, Ψ_3, has been defined in (5.22):

$$\Psi_3(r) = \int_0^1 |r'(\tau)|^2 \,\mathrm{d}\tau\,.$$

It penalizes high variations of r. In Remark 5.4, we have already mentioned that an update of $(\boldsymbol{z}, r)$ in an iterative scheme may not be in $\mathcal{M}$ (see (4.9)) if the updated radius function attains negative values. To prevent this, we fix a radius value $r_{\min}$, below which the radius function should not fall, and some value $l < r_{\min}$. Then, we define the function

$$f^l_{r_{\min}}(\rho) = \begin{cases} \dfrac{1}{2\pi l}\,, & \rho \in (-\infty, r_{\min} - l]\,, \\ \dfrac{1}{2\pi l} \exp\left(-\dfrac{(\rho + l - r_{\min})^2}{2l^2} \right), & \rho \in (r_{\min} - l, \infty)\,, \end{cases}$$

and with that the fourth regularization term

$$\Psi_4(r) = \int_0^1 f^l_{r_{\min}}(r(\tau)) \,\mathrm{d}\tau\,. \tag{6.4}$$

Ψ_4 is small if ρ is greater than $r_{\min}$ and it rapidly ascends to $1/(2\pi l)$ if ρ becomes smaller than $r_{\min}$. The value l determines how steep the ascent is and how grave the punishment for being to close to or below $r_{\min}$.

With these terms and regularization parameters $\alpha_j > 0$, $j \in \{1,2,3,4\}$, we assemble the regularized objective functional

$$\Phi(\boldsymbol{z}, r) \coloneqq -\frac{\chi_{\mathrm{HS}}(\mathcal{F}(\boldsymbol{z}, r))}{\|\mathcal{F}(\boldsymbol{z}, r)\|_{\mathrm{HS}}} + \alpha_1\Psi_1(\boldsymbol{z}) + \alpha_2\Psi_2(\vec{\boldsymbol{c}}) + \alpha_3\Psi_3(r) + \alpha_4\Psi_4(r) \tag{6.5}$$

and state the regularized optimization problem:

$$\text{Find} \qquad \underset{(\boldsymbol{z},r)\in\mathcal{M}_n}{\arg\min}\, \Phi(\boldsymbol{z},r)\,. \tag{6.6}$$

Note that in (6.5) and (6.6), we assume $(\boldsymbol{z},r)$ being discretized by a B-spline curve and a cubic spline, due to the restriction from introducing the second regularization term Ψ_2.

We next establish that all penalty terms are Fréchet differentiable. For Ψ_1, Ψ_3, Ψ_4, we assume that $(\boldsymbol{z},r)\in\mathcal{M}$ and consider perturbations $(\boldsymbol{u},\delta)$, such that $(\boldsymbol{z}+\boldsymbol{u},r+\delta)\in\mathcal{M}$. For the second term Ψ_2, let $(\boldsymbol{z},r)\in\mathcal{M}_n$ and consider perturbations $(\boldsymbol{u},\delta)$, such that $(\boldsymbol{z}+\boldsymbol{u},r+\delta)\in\mathcal{M}_n$. Here, the perturbation $\boldsymbol{u}$ is assumed to be a B-spline curve defined by n control points $\vec{\boldsymbol{q}} = (\boldsymbol{q}^{(1)},\dots,\boldsymbol{q}^{(n)})\in\mathbb{R}^{3\times n}$ and δ is a cubic spline with the distinct knots of $\boldsymbol{u}$ as the interpolation points.

Lemma 6.1. *Let $\boldsymbol{z}$, r, $\vec{\boldsymbol{c}}$, $\boldsymbol{u}$, δ, $\vec{\boldsymbol{q}}$ be defined as above. The penalty terms Ψ_i, $i\in\{1,2,3,4\}$, are Fréchet differentiable at $\boldsymbol{z}$, r or $\vec{\boldsymbol{c}}$. It holds that*

$$\begin{aligned}\mathrm{d}\Psi_1[\boldsymbol{z}]\boldsymbol{u} = \int_0^1 \Bigg(& 2\,\frac{\boldsymbol{z}''(\tau)\cdot\boldsymbol{u}''(\tau)}{|\boldsymbol{z}'(\tau)|^3} - 3\,|\boldsymbol{z}''(\tau)|^2\,\frac{\boldsymbol{z}'(\tau)\cdot\boldsymbol{u}'(\tau)}{|\boldsymbol{z}'(\tau)|^5} \\ & - 2\left(\boldsymbol{z}'(\tau)\cdot\boldsymbol{u}''(\tau)+\boldsymbol{z}''(\tau)\cdot\boldsymbol{u}'(\tau)\right)\frac{\boldsymbol{z}'(\tau)\cdot\boldsymbol{z}''(\tau)}{|\boldsymbol{z}'(\tau)|^5} \\ & + 5\boldsymbol{z}'(\tau)\cdot\boldsymbol{u}'(\tau)\,\frac{(\boldsymbol{z}'(\tau)\cdot\boldsymbol{z}''(\tau))^2}{|\boldsymbol{z}'(\tau)|^7}\Bigg)\,\mathrm{d}\tau\,,\end{aligned} \tag{6.7}$$

$$\begin{aligned}\mathrm{d}\Psi_2[\vec{\boldsymbol{c}}]\vec{\boldsymbol{q}} = 2\sum_{j=1}^{n-1}\Bigg[& \left(\frac{1}{n-1}\sum_{i=0}^{n-1}\left|\boldsymbol{c}^{(i+1)}-\boldsymbol{c}^{(i)}\right|\right) - \left|\boldsymbol{c}^{(j+1)}-\boldsymbol{c}^{(j)}\right| \Bigg] \\ & \Bigg[\left(\frac{1}{n-1}\sum_{i=1}^{n-1}\frac{(\boldsymbol{c}^{(i+1)}-\boldsymbol{c}^{(i)})\cdot(\boldsymbol{q}^{(i+1)}-\boldsymbol{q}^{(i)})}{|\boldsymbol{c}^{(i+1)}-\boldsymbol{c}^{(i)}|}\right) \\ & - \frac{(\boldsymbol{c}^{(j+1)}-\boldsymbol{c}^{(j)})\cdot(\boldsymbol{q}^{(j+1)}-\boldsymbol{q}^{(j)})}{|\boldsymbol{c}^{(j+1)}-\boldsymbol{c}^{(j)}|}\Bigg]\,,\end{aligned} \tag{6.8}$$

as well as

$$\mathrm{d}\Psi_3[r]\delta = 2\int_0^1 r'(\tau)\,\delta'(\tau)\,\mathrm{d}\tau\,. \tag{6.9}$$

Furthermore, we have

$$\mathrm{d}\Psi_4[r]\delta = \int_0^1 \mathrm{d}f^l_{r_{\min}}[r(\tau)]\delta(\tau)\,\mathrm{d}\tau \tag{6.10}$$

with

$$\mathrm{d}f^l_{r_{\min}}[r(t)]\delta(t) = \begin{cases} 0\,, & r(t) \leq r_{\min} - l\,, \\ -\dfrac{1}{2\pi l^3}\,\delta(t)(r(t)+l-r_{\min})\,\exp\left(-\dfrac{(r(t)+l-r_{\min})^2}{2\,l^2}\right), & r(t) > r_{\min} - l\,, \end{cases} \tag{6.11}$$

for $t \in [0,1]$.

Proof. For the Fréchet derivative of Ψ_1, see [69, Lemma 5.21]. The Fréchet derivative of the second regularization term Ψ_2 follows from

$$\mathrm{d}(|\cdot|)[\boldsymbol{x}]\boldsymbol{u} = \frac{\boldsymbol{x}\cdot\boldsymbol{u}}{|\boldsymbol{x}|}$$

and the Fréchet derivative of Ψ_3 from $\mathrm{d}((\cdot)^2)[r']\delta = 2\,r'\,\delta'$. Moreover, let δ be an admissible and sufficiently small perturbation of r. Then, with $\mathrm{d}f^l_{r_{\min}}[r(t)]\delta(t)$ defined as in (6.11), it holds that

$$\begin{aligned} &f^l_{r_{\min}}(r(t)+\delta(t)) - f^l_{r_{\min}}(r(t)) - \mathrm{d}f^l_{r_{\min}}[r(t)]\delta(t) \\ &\quad = \frac{1}{2\pi l}\,\exp\left(-\frac{(r(t)+l-r_{\min})^2}{2\,l^2}\right) \\ &\qquad \left[\exp\left(-\frac{\delta^2(t)+2\delta(t)(r(t)+l-r_{\min})}{2\,l^2}\right) - 1 + \frac{1}{l^2}\delta(t)(r(t)+l-r_{\min})\right] \end{aligned}$$

for $t \in [0,1]$. Therefore, considering $\|\delta\|_{1,\infty} \to 0$ leads to

$$\begin{aligned} &f^l_{r_{\min}}(r(t)+\delta(t)) - f^l_{r_{\min}}(r(t)) - \mathrm{d}f^l_{r_{\min}}[r(t)]\delta(t) \\ &\quad = \frac{1}{2\pi l}\,\exp\left(-\frac{(r(t)+l-r_{\min})^2}{2\,l^2}\right) \\ &\qquad \left[-\frac{\delta^2(t)}{2l^2} - \frac{1}{l^2}\delta(t)(r(t)+l-r_{\min}) + \mathcal{O}(\delta^2(t)) + \frac{1}{l^2}\delta(t)(r(t)+l-r_{\min})\right] \\ &\quad = \mathcal{O}(\delta^2(t)) \end{aligned}$$

for $t \in [0,1]$, which finishes the proof. ∎

6.1.2. The BFGS scheme

We can now apply a BFGS[1] scheme, see [14, 44, 47, 104] and [85, Section 6.1], with a cautious update rule from [75] and the Armijo[2] line search [85, Equation (3.4)] to the optimization problem (6.6). Here, we assume that $\boldsymbol{z}$ is discretized by a third-order B-spline curve with n control points $\vec{\boldsymbol{c}}_n = (\boldsymbol{c}^{(1)}, \ldots, \boldsymbol{c}^{(n)}) \in \mathbb{R}^{3\times n}$, $n \in \mathbb{N}$. As a consequence, the radius function, which is discretized

[1] Charles George Broyden (1933–2011), Roger Fletcher (1939–2016), Donald Goldfarb (b. 1941), David Francis Shanno (1938–2019)

[2] Larry Armijo

by a cubic spline with the distinct knots as the interpolation points, can be represented by $n-2$ radius values $\vec{r}_n = (r_1, \dots, r_{n-2}) \in \mathbb{R}^{n-2}$. We define the jth iterate $\boldsymbol{X}_j$ of the BFGS scheme to be a collection of n control points $\vec{\boldsymbol{c}}_n$ and $n-2$ radius values $\vec{r}_n$, stored in one vector, i.e., $\boldsymbol{X}_j \in \mathbb{R}^{3n+(n-2)}$. In this quasi-Newton scheme, the Hessian is approximated and this approximation is updated in each iteration step. Only a gradient has to be calculated. Denoting by $\boldsymbol{\nabla}_{\mathrm{CP}}$ the gradient of the objective function Φ with respect to the control points and by $\boldsymbol{\nabla}_{\mathrm{rad}}$ with respect to the radius values, we obtain the full gradient of Φ by

$$\boldsymbol{\nabla}\Phi = \begin{pmatrix} \boldsymbol{\nabla}_{\mathrm{CP}}\,\Phi \\ \boldsymbol{\nabla}_{\mathrm{rad}}\,\Phi \end{pmatrix} \in \mathbb{R}^{3n+(n-2)}\,. \tag{6.12}$$

Furthermore, we denote by $\boldsymbol{H}_j \in \mathbb{R}^{(3n+(n-2))\times(3n+(n-2))}$ the jth iterate of a symmetric positive matrix approximation for the true Hessian of Φ. Then, we consider the convex quadratic model of Φ at the current iterate $\boldsymbol{X}_j$

$$q_j(\boldsymbol{d}_{\texttt{BFGS}}) = \Phi(\boldsymbol{X}_j) + \boldsymbol{\nabla}\Phi(\boldsymbol{X}_j)\cdot\boldsymbol{d}_{\texttt{BFGS}} + \frac{1}{2}\,\boldsymbol{d}_{\texttt{BFGS}}\cdot\boldsymbol{H}_j\boldsymbol{d}_{\texttt{BFGS}}\,,$$

which is minimized by

$$\boldsymbol{d}_{\texttt{BFGS},j} = -\boldsymbol{H}_j^{-1}\,\boldsymbol{\nabla}\Phi(\boldsymbol{X}_j)\,.$$

We use this minimizer as the search direction, obtaining the $(j+1)$th iterate

$$\boldsymbol{X}_{j+1} \coloneqq \boldsymbol{X}_j + \lambda_j \boldsymbol{d}_{\texttt{BFGS},j}\,. \tag{6.13}$$

For the cautious update rule of $\boldsymbol{H}_j \in \mathbb{R}^{(3n+(n-2))\times(3n+(n-2))}$, we initiate the iteration with the identity $\boldsymbol{H}_0 = \boldsymbol{I}_M$ and define

$$\boldsymbol{S}_j \coloneqq \boldsymbol{X}_{j+1} - \boldsymbol{X}_j = \lambda_j \boldsymbol{d}_{\texttt{BFGS},j}\,, \qquad \boldsymbol{Y}_j \coloneqq \boldsymbol{\nabla}\Phi(\boldsymbol{X}_{j+1}) - \boldsymbol{\nabla}\Phi(\boldsymbol{X}_j)\,,$$

and an update of $\boldsymbol{H}_j$ through

$$\boldsymbol{H}_{j+1} \coloneqq \boldsymbol{H}_j - \frac{\boldsymbol{H}_j\boldsymbol{Y}_j\boldsymbol{Y}_j^\top\boldsymbol{H}_j}{\boldsymbol{Y}_j^\top\boldsymbol{H}_j\boldsymbol{Y}_j} + \frac{\boldsymbol{S}_j\boldsymbol{S}_j^\top}{\boldsymbol{Y}_j^\top\boldsymbol{S}_j} \qquad \text{if } \frac{\boldsymbol{Y}_j^\top\boldsymbol{S}_j}{|\boldsymbol{S}_j|^2} > \varepsilon_{\texttt{BFGS}}|\,\boldsymbol{\nabla}\Phi(\boldsymbol{X}_j)|\,, \tag{6.14}$$

for some parameter $\varepsilon_{\texttt{BFGS}} > 0$. Hence, we perform the classical BFGS update, if a stronger curvature condition than $\boldsymbol{Y}_j^\top\boldsymbol{S}_j > 0$ is satisfied. However, we leave $\boldsymbol{H}_j$ unaltered otherwise. This ensures positive definiteness of $\boldsymbol{H}_j$ for any $j \in \mathbb{N}_0$.

Furthermore, we use the Armijo condition for a backtracking line search to determine the step size λ_j in (6.13): for given $\sigma_{\texttt{BFGS}} \in (0,1)$, $\delta_{\texttt{BFGS}} \in (0,1)$, we want to find the smallest exponent $m \in \mathbb{N}_0$, such that $\delta_{\texttt{BFGS}}^m$ gives sufficient decrease in the sense that

$$\Phi(\boldsymbol{X}_j + \delta_{\texttt{BFGS}}^m\,\boldsymbol{d}_{\texttt{BFGS},j}) \le \Phi(\boldsymbol{X}_j) + \sigma_{\texttt{BFGS}}\,\delta_{\texttt{BFGS}}^m\,\boldsymbol{\nabla}\Phi(\boldsymbol{X}_j)\cdot\boldsymbol{d}_{\texttt{BFGS},j}\,. \tag{6.15}$$

We then set $\lambda_j \coloneqq \delta_{\texttt{BFGS}}^m$. As in Section 5.4, we further reduce the step size until the tubular

neighborhood condition (5.24) is satisfied and until the updated radius does not fall below a certain positive minimal value.

In order to obtain the gradient (6.12) of the objective function

$$\Phi(\boldsymbol{z}, r) = -\frac{\chi_{\mathrm{HS}}(\mathcal{F}(\boldsymbol{z}, r))}{\|\mathcal{F}(\boldsymbol{z}, r)\|_{\mathrm{HS}}} + \alpha_1 \Psi_1(\boldsymbol{z}) + \alpha_2 \Psi_2(\vec{\boldsymbol{c}}) + \alpha_3 \Psi_3(r) + \alpha_4 \Psi_4(r)$$

from (6.5), we need to compute its derivative with respect to perturbations of each control point and radius value. The derivatives for the penalty terms can be obtained by Lemma 6.1. The Fréchet derivative of $\mathcal{J}_{\mathrm{HS}}$ (see (6.1)) with respect to some admissible perturbation $\boldsymbol{h}$ is readily given by

$$\mathrm{d}\mathcal{J}_{\mathrm{HS}}[\boldsymbol{z}, r]\boldsymbol{h} = \frac{\mathrm{d}\chi_{\mathrm{HS}}[\mathcal{F}(\boldsymbol{z}, r)](\mathrm{d}\mathcal{F}[\boldsymbol{z}, r]\boldsymbol{h})}{\|\mathcal{F}(\boldsymbol{z}, r)\|_{\mathrm{HS}}} - \frac{\chi_{\mathrm{HS}}(\mathcal{F}(\boldsymbol{z}, r))\ \mathrm{Re}\langle \mathcal{F}(\boldsymbol{z}, r), \mathrm{d}\mathcal{F}[\boldsymbol{z}, r]\boldsymbol{h}\rangle_{\mathrm{HS}}}{\|\mathcal{F}(\boldsymbol{z}, r)\|_{\mathrm{HS}}^3} \tag{6.16}$$

by the chain and product rule. The derivative $\mathrm{d}\mathcal{F}[\boldsymbol{z}, r]\boldsymbol{h}$ has been characterized in Theorem 4.14 in terms of the operator $\boldsymbol{\varphi} \mapsto (\boldsymbol{E}'[\boldsymbol{\varphi}])^\infty$, mapping densities to far-field patterns of the domain derivative $\boldsymbol{E}'[\boldsymbol{\varphi}]$. Thus, as in Chapter 5 for the inverse shape identification problem, we have to deal with scattering problems, which can be solved by the EFIE (5.8) or the modified PMCHWT integral equation (5.18). Furthermore, in order to compute the Hilbert–Schmidt norm and scalar product as well as the chirality measure of $\mathcal{F}(\boldsymbol{z}, r)$, we need to assemble the discrete far-field operator.

Remark 6.2. We do not expect our objective functional Φ to be convex. Hence, global convergence results as in [85, Chapter 6] cannot be applied. Moreover, translations of $(\boldsymbol{z}, r)$ – and thus of ∂D – do not change the em-chirality, nor do they influence the regularization terms. Thus, the level sets $\{(\boldsymbol{z}, r) \in \mathcal{M}_n : \Phi(\boldsymbol{z}, r) \leq \Phi(\boldsymbol{z}_0, r_0)\}$, where $(\boldsymbol{z}_0, r_0)$ denotes an initial guess, are unbounded. Consequently, we cannot use the global convergence result from [75], since they assume boundedness of these level sets. Note that the boundedness could be achieved by modifying the regularization terms. However, this has not been considered in this thesis.

6.1.3. Discretization of the Far-Field Operator

Recall the definition of the far-field operator for some scattering obstacle D by

$$\mathcal{F}(\partial D)\colon L_t^2(\mathbb{S}^2) \to L_t^2(\mathbb{S}^2)\,, \qquad \mathcal{F}(\partial D)\boldsymbol{\varphi} = \boldsymbol{E}^\infty[\boldsymbol{\varphi}]$$

(cf. Subsection 2.7.3). In order to compute the em-chirality measure $\chi_{\mathrm{HS}}(\mathcal{F}(\partial D))$ of $\mathcal{F}(\partial D)$ (cf. Definition 2.31), we start by discretizing the far-field operator by considering some truncation parameter $N \in \mathbb{N}$ and the $(2N^2 + 4N)$-dimensional ordered basis

$$\begin{aligned}\mathscr{B}_N &\coloneqq \{\boldsymbol{U}_n^m,\, \boldsymbol{V}_n^m : n \in \mathbb{N},\ n \leq N,\ m \in \mathbb{Z},\ |m| \leq n\} \\ &= \left\{\boldsymbol{U}_1^{-1},\, \boldsymbol{U}_1^0,\, \boldsymbol{U}_1^1,\, \boldsymbol{U}_2^{-2},\, \ldots,\, \boldsymbol{U}_N^N,\, \boldsymbol{V}_1^{-1},\, \boldsymbol{V}_1^0,\, \boldsymbol{V}_1^1,\, \boldsymbol{V}_2^{-2},\, \ldots,\, \boldsymbol{V}_N^N\right\}.\end{aligned}$$

An element $\boldsymbol{\varphi}_N \in \operatorname{span} \mathscr{B}_N \subseteq \boldsymbol{L}_t^2(\mathbb{S}^2)$ is given by the truncated expansion into vector spherical harmonics

$$\boldsymbol{\varphi}_N = \sum_{n=1}^{N} \sum_{m=-n}^{n} a_n^m \boldsymbol{U}_n^m + b_n^m \boldsymbol{V}_n^m$$

with coefficients $a_n^m \coloneqq \langle \boldsymbol{\varphi}_N, \boldsymbol{U}_n^m \rangle_{\boldsymbol{L}_t^2} \in \mathbb{C},\ b_n^m \coloneqq \langle \boldsymbol{\varphi}_N, \boldsymbol{V}_n^m \rangle_{\boldsymbol{L}_t^2} \in \mathbb{C}$, $n \in \mathbb{N}\,,\ n \leq N\,,\ m \in \mathbb{Z}\,,\ |m| \leq n$. Accordingly, it holds that

$$\mathcal{F}\boldsymbol{\varphi}_N = \sum_{n=1}^{N} \sum_{m=-n}^{n} \alpha_n^m \boldsymbol{U}_n^m + \beta_n^m \boldsymbol{V}_n^m$$

with coefficients

$$\left.\begin{aligned} \alpha_n^m &\coloneqq \langle \mathcal{F}\boldsymbol{\varphi}_N, \boldsymbol{U}_n^m \rangle_{\boldsymbol{L}_t^2} = \sum_{n=1}^{N} \sum_{m=-n}^{n} a_n^m \langle \mathcal{F}\boldsymbol{U}_n^m, \boldsymbol{U}_n^m \rangle_{\boldsymbol{L}_t^2} + b_n^m \langle \mathcal{F}\boldsymbol{V}_n^m, \boldsymbol{U}_n^m \rangle_{\boldsymbol{L}_t^2}\,, \\ \beta_n^m &\coloneqq \langle \mathcal{F}\boldsymbol{\varphi}_N, \boldsymbol{V}_n^m \rangle_{\boldsymbol{L}_t^2} = \sum_{n=1}^{N} \sum_{m=-n}^{n} a_n^m \langle \mathcal{F}\boldsymbol{U}_n^m, \boldsymbol{V}_n^m \rangle_{\boldsymbol{L}_t^2} + b_n^m \langle \mathcal{F}\boldsymbol{V}_n^m, \boldsymbol{V}_n^m \rangle_{\boldsymbol{L}_t^2}\,, \end{aligned}\right\} \tag{6.17}$$

$n \in \mathbb{N}\,,\ n \leq N\,,\ m \in \mathbb{Z}\,,\ |m| \leq n$. Thus, assembling the discretized far-field operator $\mathcal{F}_N = \mathcal{F}_N(\partial D)\colon \operatorname{span} \mathscr{B}_N \to \operatorname{span} \mathscr{B}_N$ leads to

$$\mathcal{F}_N \coloneqq \begin{pmatrix} (\boldsymbol{U}\boldsymbol{U})^{(N)} & (\boldsymbol{V}\boldsymbol{U})^{(N)} \\ (\boldsymbol{U}\boldsymbol{V})^{(N)} & (\boldsymbol{V}\boldsymbol{V})^{(N)} \end{pmatrix} \in \mathbb{C}^{(2N^2+4N)\times(2N^2+4N)}$$

with block matrices

$$(\boldsymbol{X}\boldsymbol{Y})^{(N)} \coloneqq \begin{pmatrix} \left\langle \mathcal{F}\boldsymbol{X}_1^{-1}, \boldsymbol{Y}_1^{-1} \right\rangle_{\boldsymbol{L}_t^2} & \dots & \left\langle \mathcal{F}\boldsymbol{X}_N^{N}, \boldsymbol{Y}_1^{-1} \right\rangle_{\boldsymbol{L}_t^2} \\ \vdots & \ddots & \vdots \\ \left\langle \mathcal{F}\boldsymbol{X}_1^{-1}, \boldsymbol{Y}_N^{N} \right\rangle_{\boldsymbol{L}_t^2} & \dots & \left\langle \mathcal{F}\boldsymbol{X}_N^{N}, \boldsymbol{Y}_N^{N} \right\rangle_{\boldsymbol{L}_t^2} \end{pmatrix} \in \mathbb{C}^{(N^2+2N)\times(N^2+2N)}\,,$$

where $\boldsymbol{X}, \boldsymbol{Y}$ need to be replaced accordingly by $\boldsymbol{U}$ or $\boldsymbol{V}$.

To compute the modified em-chirality measure, we further have to decompose the discretized far-field operator into

$$\widetilde{\mathcal{F}}_N = \begin{pmatrix} \mathcal{F}_N^{++} & \mathcal{F}_N^{+-} \\ \mathcal{F}_N^{-+} & \mathcal{F}_N^{--} \end{pmatrix}, \tag{6.18}$$

see (2.58). To this end, recall the definition of the operator $\mathcal{C}$ from (2.51) by

$$\mathcal{C}\colon L_t^2(\mathbb{S}^2) \to L_t^2(\mathbb{S}^2)\,, \qquad \mathcal{C}\boldsymbol{\varphi}(\boldsymbol{d}) = \mathrm{i}\,(\boldsymbol{d} \times \boldsymbol{\varphi}(\boldsymbol{d}))\,, \qquad \boldsymbol{d} \in \mathbb{S}^2\,.$$

From the definition of $\boldsymbol{U}_n^m,\ \boldsymbol{V}_n^m$, see (3.20), we readily conclude

$$\mathcal{C}\boldsymbol{U}_n^m(\boldsymbol{d}) = \mathrm{i}\boldsymbol{V}_n^m(\boldsymbol{d})\,. \tag{6.19}$$

Hence, by (2.56) and (6.19), (6.18) is a representation of $\mathcal{F}$ with respect to the basis

$$\widetilde{\mathscr{B}}_N \coloneqq \{\boldsymbol{U}_n^m + \mathrm{i}\boldsymbol{V}_n^m,\ \boldsymbol{U}_n^m - \mathrm{i}\boldsymbol{V}_n^m : n \in \mathbb{N},\ n \leq N,\ m \in \mathbb{Z},\ |m| \leq n\}\ .$$

A basis change matrix from $\mathscr{B}_N$ to $\widetilde{\mathscr{B}}_N$ and its inverse are given by

$$\boldsymbol{M} \coloneqq \begin{pmatrix} \boldsymbol{I} & \boldsymbol{I} \\ \mathrm{i}\boldsymbol{I} & -\mathrm{i}\boldsymbol{I} \end{pmatrix}, \qquad \boldsymbol{M}^{-1} = \frac{1}{2}\begin{pmatrix} \boldsymbol{I} & -\mathrm{i}\boldsymbol{I} \\ \boldsymbol{I} & \mathrm{i}\boldsymbol{I} \end{pmatrix}.$$

Therefore, we have

$$\boldsymbol{M}^{-1}\mathcal{F}_N\boldsymbol{M} = \widetilde{\mathcal{F}}_N = \begin{pmatrix} \mathcal{F}_N^{++} & \mathcal{F}_N^{+-} \\ \mathcal{F}_N^{-+} & \mathcal{F}_N^{--} \end{pmatrix}. \tag{6.20}$$

We are now in a position to compute the modified em-chirality measure χ_{HS} from Definition 2.31 as well as the Hilbert–Schmidt scalar product (2.62) and norm (2.61) for the derivative (6.16). We can further calculate the singular values of $\widetilde{\mathcal{F}}_N$ and compute the original em-chirality measure χ from Definition 2.30.

However, computing $\mathcal{F}_N(\boldsymbol{\varphi})$ for every $\boldsymbol{\varphi} \in \mathscr{B}_N$ requires solving the EFIE (5.8) or the modified PMCHWT (5.18) $2N^2 + 4N$ times. Thus, assembling the gradient $\boldsymbol{\nabla}\Phi$ from (6.12) for the BFGS scheme, requires solving $(2N^2 + 4N) \cdot (\#\,\text{perturbations})$ scattering problems. For instance, consider an optimization of $n = 30$ control points defining a B-spline curve of degree 3 and $n - 2 = 28$ corresponding radius values for a cubic spline curve, as well as setting the truncation parameter to $N = 3$. This necessitates solving the EFIE (5.8) or the modified PMCHWT (5.18) $30 \cdot (3 \cdot 30 + 28) = 3540$ times. Considering $n = 20$ and $N = 2$ instead, still requires solving it 1248 times to compute one gradient.

Thus, it is of utmost interest being able to solve the scattering problems as efficiently as possible. As already described in Section 5.4, in [5] instead of the EFIE (5.8) and modified PMCHWT (5.18) we have used a CFIE and PMCHWT, respectively, see Appendix C, solving the systems of linear equations via the GMRES method.

Here, for the optimization, the CFIE and the PMCHWT are out of question due to their high computational time, especially for complicated material parameters and structures (e.g., silver tubes) – which are particularly interesting for the optimization – where the GMRES method could need hundreds of iterations to converge, as mentioned in Section 5.2. The work-around to this problem and its implementation are also described in Section 5.2, see Algorithm 1. Only because of that, performing the optimization is feasible. We provide a pseudocode for solving the optimization problem in Algorithm 3. A simple numerical example for validating the implementation of the far-field operator and its Fréchet derivative, can be found in Appendix D.

Remark 6.3. The coefficients α_n^m, β_n^m from the expansion of the far-field operator in vector spherical harmonics (6.17) only contribute significantly to the result for $n, |m| \lesssim kR$ and decay rapidly as $n, |m| \gtrsim kR$, where R is the radius of a ball centered at zero, such that $D \subseteq B_R$, see [50]. Thus, we always choose the expansion order $N \gtrsim kR$.

Algorithm 3 Solving the optimization problem

Require: Initial guess of some tube T_0 represented by n control points $\vec{c}_n$ and $n-2$ radii $\vec{r}_n$ stored in $\boldsymbol{X}_0$, truncation parameter $N > kR$

Ensure: Optimized tube T_{opt}, represented by n control points and $n-2$ radii stored in $\boldsymbol{X}_M$

$\boldsymbol{H}_0 \leftarrow \boldsymbol{I}$ `# initialize Hessian with identity`
while relative $\chi_{\text{HS}}(\widetilde{\mathcal{F}}_N)/\|\widetilde{\mathcal{F}}_N\|_{\text{HS}} <$ some tolerance and update sufficiently big **do**
  Compute far-field operator $\widetilde{\mathcal{F}}_N$ by (6.20)
  Compute penalty terms $\Psi_1, \Psi_2, \Psi_3, \Psi_4$
  Assemble objective functional $\Phi(\boldsymbol{X}_j)$ from (6.5)
  Compute $\boldsymbol{\nabla}\Phi(\boldsymbol{X}_j)$ from (6.12)
  $\boldsymbol{d}_{\texttt{BFGS},j} \leftarrow -\boldsymbol{H}_j^{-1}\,\boldsymbol{\nabla}\Phi(\boldsymbol{X}_j)$
  Determine step size λ_j via (6.15) `# Armijo condition`
  Further reduce step size until (5.24) is satisfied and all radius values > some tolerance
  $\boldsymbol{X}_{j+1} \coloneqq \boldsymbol{X}_j + \lambda_j \boldsymbol{d}_{\texttt{BFGS},j}$
  Compute $\boldsymbol{\nabla}\Phi(\boldsymbol{X}_{j+1})$
  Update Hessian $\boldsymbol{H}_{j+1}$ via (6.14) `# cautious update rule`
end while
$T_{\text{opt}} \leftarrow$ tube represented by points and radii stored in last $\boldsymbol{X}_{j+1}$

6.2. Numerical Examples

For our simulations, we consider perfectly conducting and penetrable obstacles. To obtain objects made of specific materials – as silver (Ag) or gold (Au) –, we need to use the correct combination of wavelengths, material parameters, and scaling. We start with a note on the necessary scaling of objects. Denote by ε_0 and μ_0 the *vacuum electric permittivity* and *vacuum magnetic permeability*, respectively (see [107]). It holds that the *speed of light* is given by $c = 1/\sqrt{\varepsilon_0\mu_0} \approx 299\,792\,458\,\mathrm{m\,s^{-1}}$, see [87, Equation (10–43)], [107]. Usually, the electric permittivity is given relatively compared to the vacuum electric permittivity (analogously for the magnetic permeability), i.e., we consider the *relative electric permittivity* $\varepsilon_r \coloneqq \varepsilon/\varepsilon_0$ and *relative magnetic permeability* $\mu_r \coloneqq \mu/\mu_0$. Thus, it holds that

$$k = \omega\sqrt{\varepsilon\mu} = \omega\sqrt{\varepsilon_0\varepsilon_r\mu_0\mu_r} = \frac{\omega}{c}\sqrt{\varepsilon_r\mu_r} \tag{6.21}$$

and consequently, since $\omega = 2\pi f$, where f denotes the *frequency*,

$$\lambda = \frac{2\pi}{k} = \frac{c}{f\sqrt{\varepsilon_r\mu_r}}\,. \tag{6.22}$$

Henceforth, we assume $\mu_r = 1$ and we always scale the *vacuum wave number* to $k_0 = 1$ – and, therefore, the *vacuum wavelength* to $\lambda_0 = 2\pi/k_0 = 2\pi$. By (6.22), the original vacuum wavelength is $\widetilde{\lambda}_0 = c/f$. With this, a simulated ("big") object needs to be scaled by

$$s_{\blacktriangledown,f}\colon x \mapsto \left(\frac{1}{2\pi}\frac{c}{f}\right) x \cdot 10^6 \tag{6.23}$$

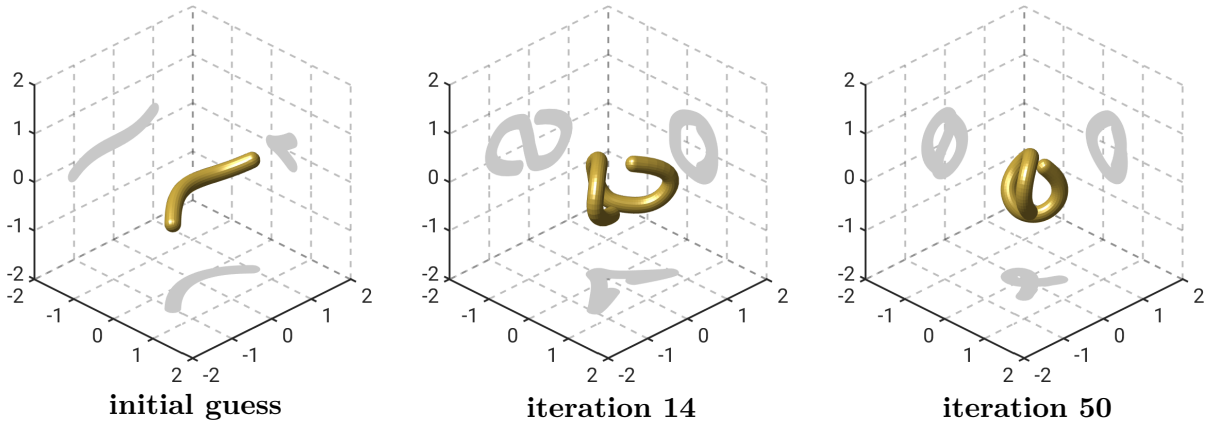

Figure 6.1. The initial guess, one excerpt and the final result from the optimization in Example 6.1.

and the actual size ("small" object) has to be scaled by

$$s_{\blacktriangle,f} : y \mapsto \left(2\pi \frac{f}{c}\right) y \cdot 10^{-6} . \tag{6.24}$$

If, e.g., the frequency f is given, we obtain specific materials by choosing the material parameters corresponding to the original vacuum wavelength $\widetilde{\lambda}_0$.

For both perfectly conducting and penetrable obstacles, we compare with helices as reference objects. We describe these by four parameters, namely, the minor radius r_{minor} of the tube's circular cross sections, the major radius r_{major} describing the radius of the windings around the winding axis, the total winding number n_{turns}, and the pitch p, describing the axial distance between two consecutive windings.

As before, the tubular objects D are represented by $(\boldsymbol{z}, r) \in \mathcal{M}$ (see (4.9)), where $\boldsymbol{z}$ is discretized by a third-order B-spline curve with n control points and r by a cubic spline with the distinct knots of the B-spline curve as the interpolation points. The optimization terminates if the relative movement of the control points and the relative change of the radius function (norm of the update divided by norm of the previous data) fall below a given tolerance or if the relative chirality becomes greater than 99%. In all following examples, the parameters $\varepsilon_{\texttt{BFGS}}$ and $\sigma_{\texttt{BFGS}}$ for the BFGS scheme and Armijo-type line search are chosen as in [69, p. 126], i.e., $\varepsilon_{\texttt{BFGS}} = 1\text{e}{-5}$ and $\sigma_{\texttt{BFGS}} = 1\text{e}{-4}$, and we set $\delta_{\texttt{BFGS}} = 0.5$. The regularization parameters α_j, $j \in \{1, 2, 3, 4\}$, are chosen based on experiential knowledge. We also always start the iteration with a slightly twisted tube instead of just using a straight tube, since the latter one's symmetry would imply em-achirality, see Theorem 2.29, i.e., the corresponding em-chirality value is 0. However, we need to divide by the em-chirality measure for calculating its derivative, see (2.64).

6.2.1. Optimization of Perfect Conductors

The following objects are optimized for the wavelength $\lambda = 200\,\mu\text{m}$. The reason for this is that the numerical study [41, Section VII] has been conducted with respect to this wave number. This

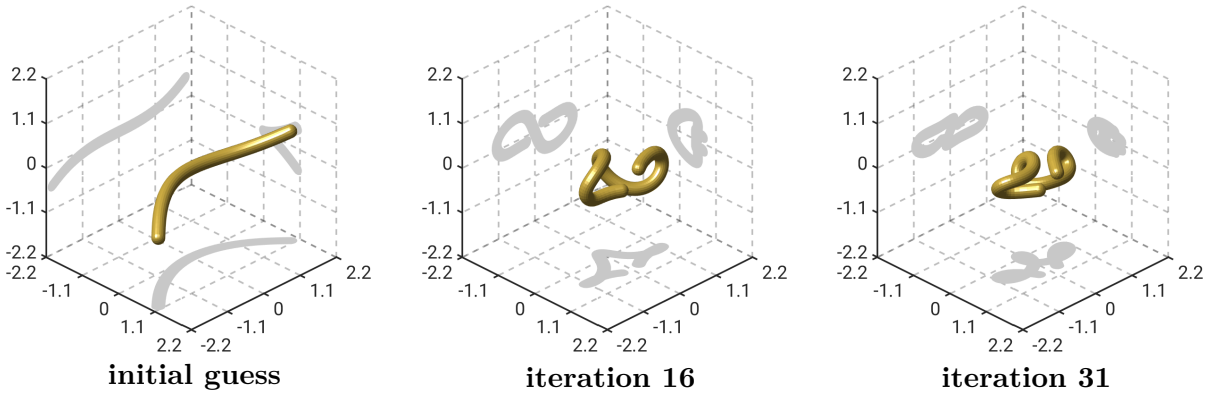

Figure 6.2. The initial guess, one excerpt and the final result from the optimization in Example 6.2.

gives us a basis for comparison. For the first three examples the radii are assumed to be constant.

Example 6.1. We initiate the optimization with a perfectly conducting obstacle D defined by a third-degree B-spline curve with control points

$$\boldsymbol{c}_j = 2 \begin{pmatrix} (j/20 - 1/2)^2 \\ j/20 - 1/2 \\ (j/20 - 1/2)^3 \end{pmatrix}, \qquad j = 0, \dots, 19\,.$$

The radius function is set constant to $r \equiv 0.15$. We choose the material parameters $\varepsilon_0 = \mu_0 = 1$ and the angular frequency $\omega = 1$. Discretizing the surface leads to a mesh and a corresponding RWG finite element space with 6690 DOF.

The regularization parameters are chosen as $\alpha_1 = 5\text{e}{-3},\ \alpha_2 = 1\text{e}{-2}$. Starting with a relative modified em-chirality of approximately 2.67%, the BFGS scheme terminates after 50 iterations, yielding an object with a relative modified em-chirality of around 88.63%. The results for the optimization are shown in Figure 6.1.

Example 6.2. We initiate the optimization with a perfectly conducting obstacle D defined by a third-degree B-spline curve with control points

$$\boldsymbol{c}_j = 4 \begin{pmatrix} (j/20 - 1/2)^2 \\ j/20 - 1/2 \\ (j/20 - 1/2)^3 \end{pmatrix}, \qquad j = 0, \dots, 19\,.$$

The radius function is set constant to $r \equiv 0.15$. We choose the material parameters $\varepsilon_0 = \mu_0 = 1$ and the angular frequency $\omega = 1$. Discretizing the surface leads to a mesh and a corresponding RWG finite element space with 6690 DOF.

The regularization parameters are chosen as $\alpha_1 = 2.5\text{e}{-3},\ \alpha_2 = 1\text{e}{-2}$. Moreover, we set $N = 3$. Starting with a relative modified em-chirality of approximately 2.8%, the BFGS scheme terminates after 31 iterations, yielding an object with a relative modified em-chirality of around 93.61%. The results for the optimization are shown in Figure 6.2. In Figure 6.5, we compare this

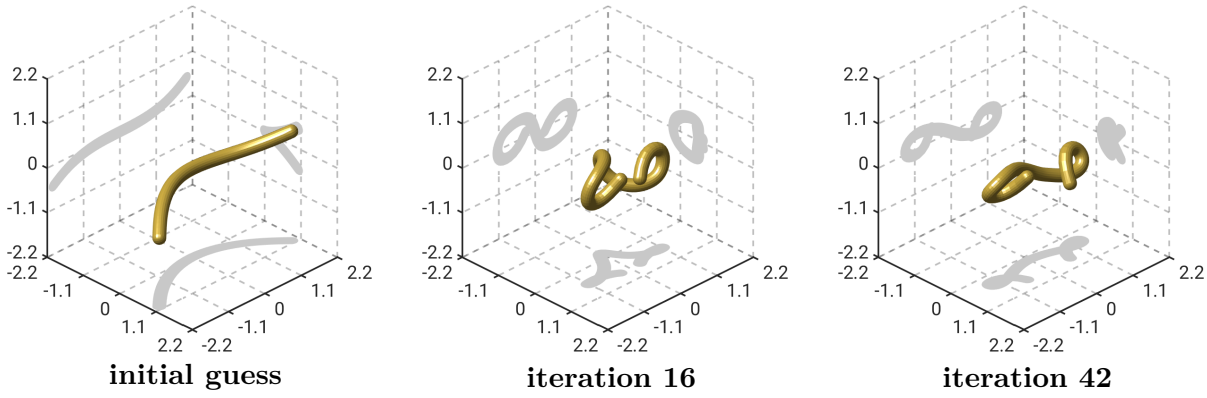

Figure 6.3. The initial guess, one excerpt and the final result from the optimization in Example 6.3.

optimized object to the silver helix that also has been optimized for a wavelength $\lambda = 200\,\mu\text{m}$ in [41]. The helix has a relative modified em-chirality measure of approximately 92.04%. Moreover, if we compare the relative em-chirality values (*not* modified, cf. Definition 2.30), we even have a greater difference: approximately 92.07% for the helix and 94.52% for the optimized object. Note that for this wavelength, it holds that $\varepsilon_r = -1.8404\text{e+}5 + 5.5024\text{e+}5\text{i}$ for silver and $\varepsilon_r = -21378 + 1.9710\text{e+}5\text{i}$ for gold [54]. This implies high absorption, suggesting that the perfect conductor is indeed a good model, particularly for silver – but also for gold – objects for $\lambda = 200\,\mu\text{m}$. This suggestion is also supported by numerical tests. Furthermore, the relative em-chirality of 92.07% fits the information of [41, p. 9], where they indicate a value of 92%.

Example 6.3. We initiate the optimization with a perfectly conducting obstacle D defined by a third-degree B-spline curve with the same control points and with the same radius as in Example 6.2. We choose the material parameters $\varepsilon_0 = \mu_0 = 1$ and the angular frequency $\omega = 1$. Discretizing the surface leads to a mesh and a corresponding RWG finite element space with 6690 DOF. The regularization parameters are chosen as $\alpha_1 = 3\text{e}{-3},\ \alpha_2 = 1\text{e}{-2}$. Starting with a relative modified em-chirality of approximately 2.67%, the BFGS scheme terminates after 42 iterations, yielding an object with a relative modified em-chirality of around 93.91%. The results for the optimization are shown in Figure 6.3.

The final results from Examples 6.1–6.3 show a similar pattern near the start and end cap, whereas, depending on the initial guess and the regularization, primarily the body of the tube seems to be more stretched or compressed. Note that none of these shapes are helical. Since they are larger in size and can attain higher em-chirality values than the reference helix, cf. Example 6.2 as well as Figures 6.5 and 6.6, they seem to constitute a reasonable alternative. Particularly, they are considerably regular in shape, which seems to make them a well-suited candidate for possible practical realizations. Additionally, for these free-form optimized objects, not only the em-chirality values are larger but also the Hilbert–Schmidt norm $\|\mathcal{F}\|_{\text{HS}}$, see Figure 6.6. The square of this value is sometimes called the interaction cross-section and it indicates the degree of how much the corresponding object interacts with incident fields. It is favorable to have high chirality values, while maintaining large interaction cross-sections.

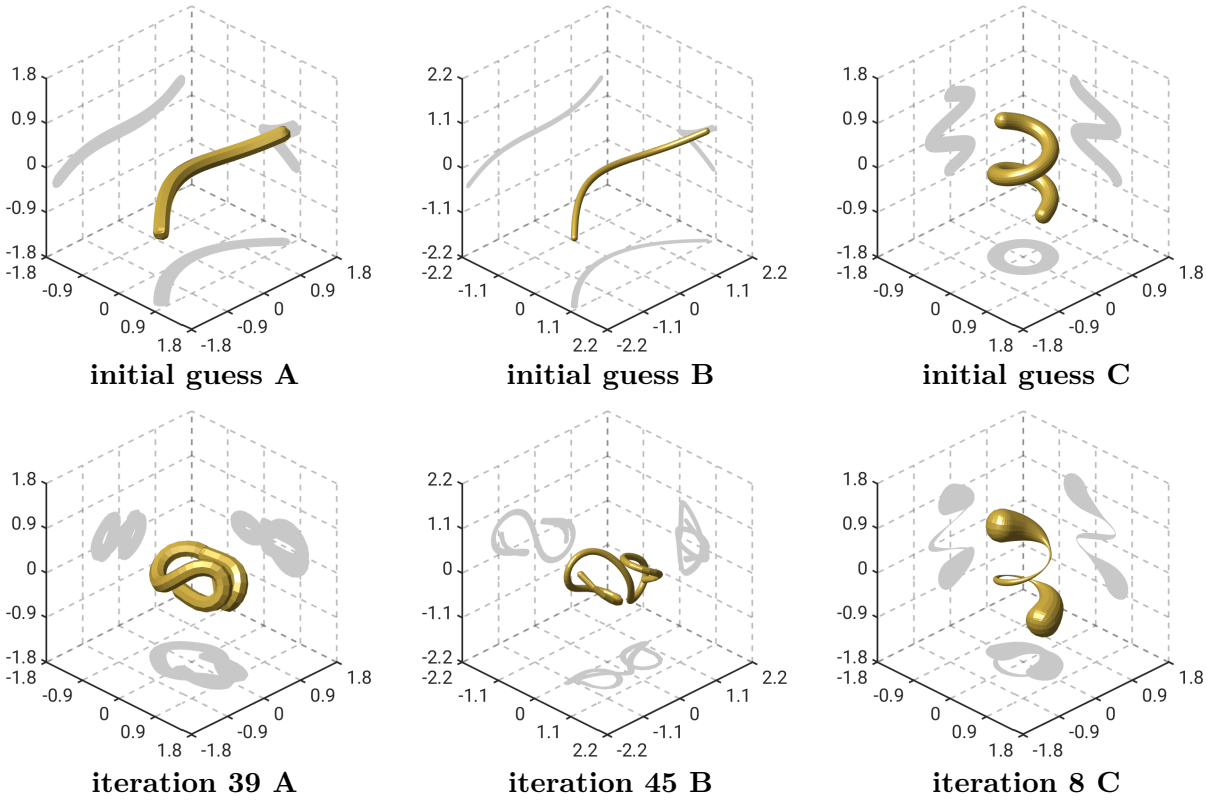

Figure 6.4. *Top row*: The initial guesses for cases A, B, C. *Bottom row*: The final results of the optimization for cases A, B, C.

In the next example, we show some additional optimization results. It should be noted that we do not include examples for a full (control points and radius) optimization as these are delicate to regularize and the optimization schemes often terminate prematurely, yielding objects with only low em-chirality.

Example 6.4. We present two cases (A and B) optimizing the control points only, where the final iteration is slightly more entangled than in the previous Examples 6.1–6.3, see Figure 6.4. For these objects, we start with similar control points as in Example 6.1. For object A, the radius is set to $r \equiv 0.15$ and $\alpha_1 = 6.25\text{e}{-5}$, $\alpha_2 = 6.25\text{e}{-4}$. For object B, we set $r \equiv 7.5\text{e}{-2}$ and $\alpha_1 = 9\text{e}{-6}$, $\alpha_2 = 1\text{e}{-4}$. The final iterations seem to break the pattern, which we observe in Examples 6.1–6.3 slightly, however, especially at the start and end cap, they exhibit a similar behavior, see Figure 6.4. The iteration for object A starts with a relative modified em-chirality of around 2.69% and terminates at roughly 93.45%. Object B starts with approximately 0.95% and terminates at around 93.71%. Furthermore, with object C of Figure 6.4, we show an optimization result with respect to the radius function only. We start with a helix of radius $r \equiv 0.15$ that has a relative modified em-chirality of around 2.23% and set $\alpha_3 = 1\text{e}{-2}$, $\alpha_4 = 0$. During the optimization, the start and end caps get bigger and the body gets "thinned out" and, eventually, we arrive at a relative modified em-chirality of around 72.28%.

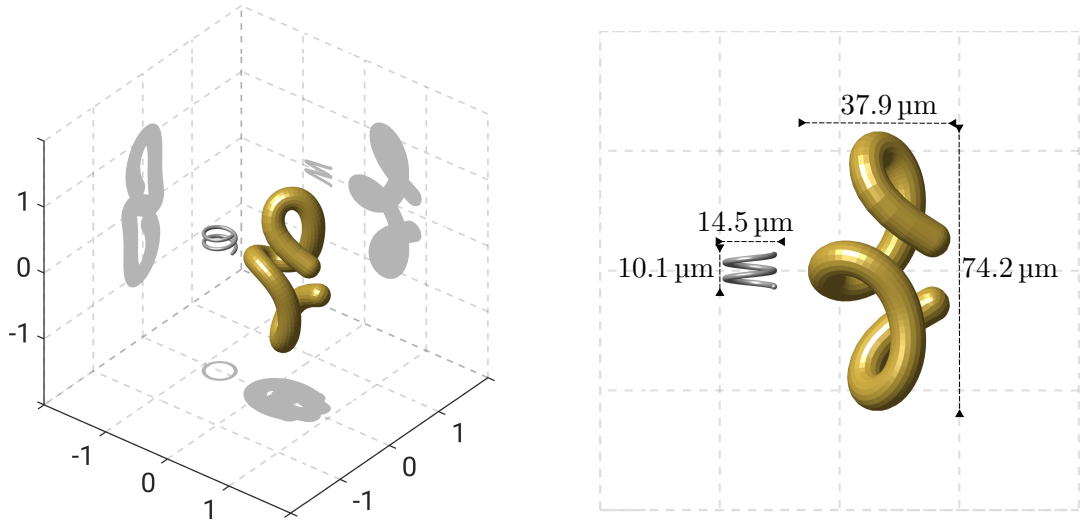

Figure 6.5. Size comparison of the optimized non-helical object from Example 6.2 and the silver helix from [41]. In the depicted configuration the vertical height of the former is more than 7.3 times greater than of the latter and it has a radius that is roughly six times larger (approximately 4.8 µm versus 0.8 µm).

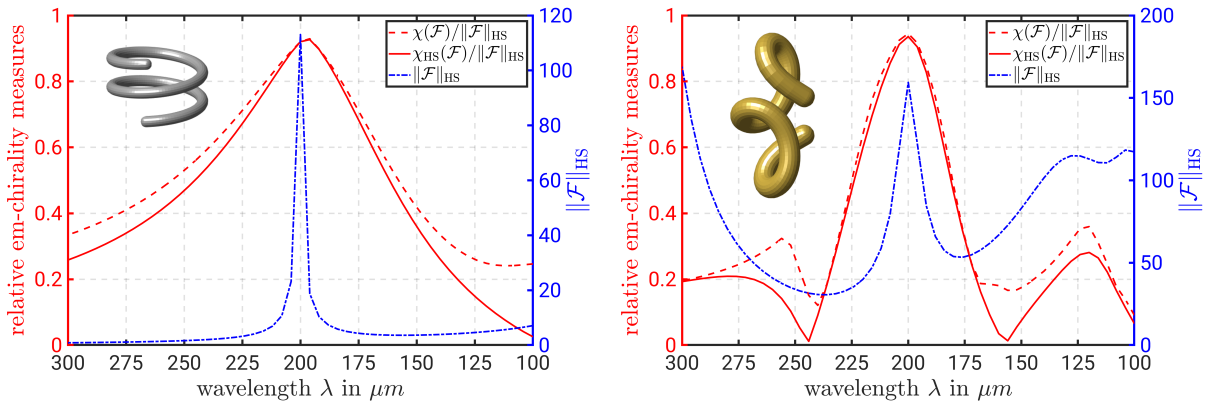

Figure 6.6. Frequency scans for wavelengths 100–300 µm. The corresponding objects are depicted in the top left corner each. The solid red line shows the relative em-chirality measure values. The dashed red line shows the relative non-modified em-chirality measure values that originally has been defined in [41]. The dash-dotted blue line shows the Hilbert–Schmidt norm $\|\mathcal{F}\|_{\mathrm{HS}}$ of the far-field operator.
Left: Frequency scan of the optimized silver helix from [41]. Here, we use a perfectly conducting helix, which is a reasonably good model for a silver helix for these wavelenghts. The helix has a relative modified em-chirality measure of approximately 92.04% for $\lambda = 200\,\mu\mathrm{m}$. *Right*: Frequency scan of the optimized perfectly conducting tubular object from Example 6.2 with a relative modified em-chirality of around 93.61% for $\lambda = 200\,\mu\mathrm{m}$. We can also nicely see that the peak of $\|\mathcal{F}\|_{\mathrm{HS}}$ is less narrow than for the helix. This could be advantageous when, e.g., counting in production error in potential practical realizations.

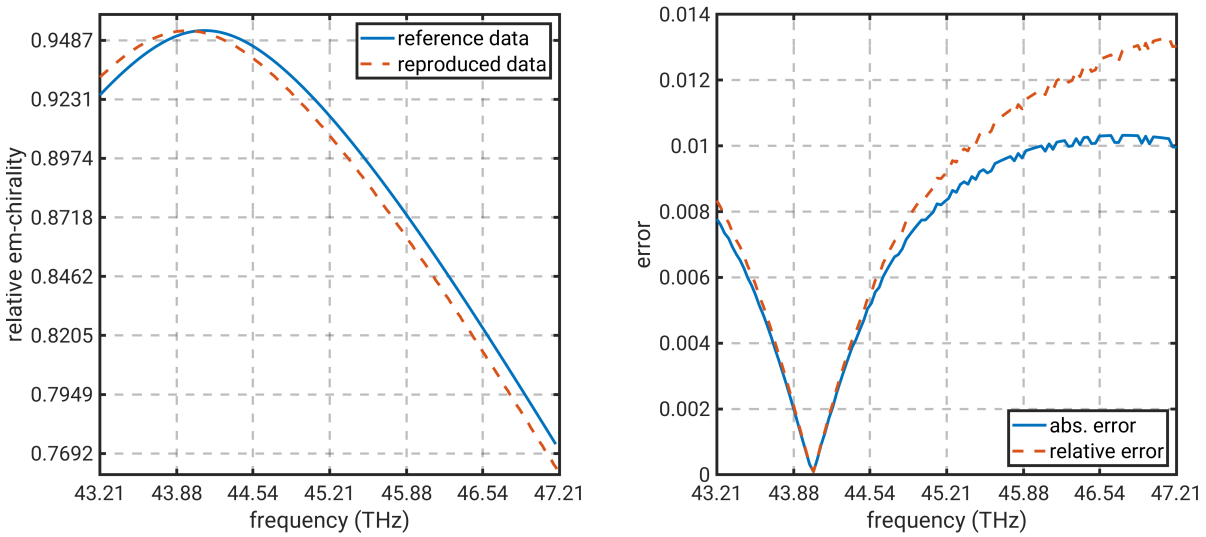

Figure 6.7. *Left*: Comparison of the reference data (blue) and the reproduction (orange) for the reference helix D_{ref} for $f \in [43.21\,\text{THz}, 47.21\,\text{THz}]$. *Right*: The corresponding absolute and relative errors.

6.2.2. Optimization of Silver Tubes

Next, as a reference object we use a silver helix from [97] – henceforth, referred to as the *reference helix* D_{ref} –, embedded in a homogeneous, isotropic, and non-absorbing medium with a relative permittivity $\varepsilon_{r,+} = 1.8912$, which is optimized for a target frequency of 44.21 THz – where it reaches $\chi(\mathcal{F})/\|\mathcal{F}\|_{\text{HS}} \approx 95.47\%$ – by the use of Bayesian optimization with Gaussian processes provided by the simulation software `JCMsuite`. In this frequency regime, the perfect conductor model fails to be accurate and, hence, we need to use the modified PMCHWT solver (5.18) for penetrable obstacles.

We start by modeling the reference helix, for which $r_{\text{minor}} = 53.32\,\text{nm}$, $r_{\text{major}} = 183\,\text{nm}$, $n_{\text{turns}} = 1.407$, and $p = 168.6\,\text{nm}$, see [97, Figure 1].

The material parameters for silver for wavelenghts 0.188–1.94 µm are interpolations of data from [62], for wavelengths 1.94–248 µm we use [54]. A convenient open-source database of optical constants with comprehensive user interface can be found on `https://refractiveindex.info`, see [91].

Then, we verify the results from [97, Figure 1] by using our BEM implementation. This also provides confirmation for us that the methods and scaling of the object have been conducted correctly. For this purpose, we received the reference data corresponding to [97, Figure 1] for frequencies $\widetilde{f} \in [43.21\,\text{THz}, 47.21\,\text{THz}]$ and compared the chirality properties to our results.

The frequency $f = 44.21\,\text{THz}$ corresponds to the vacuum wavelength $\lambda = c/f \approx 6.7811\,\mu\text{m}$, cf. (6.22). Thus, we can model silver objects, embedded in the same medium as the reference helix D_{ref}, by choosing $\varepsilon_{r,-} \approx -2475.44 + 349.93\text{i}$, $\varepsilon_{r,+} = 1.8912$, and $\mu \equiv 1$. Note that we have to

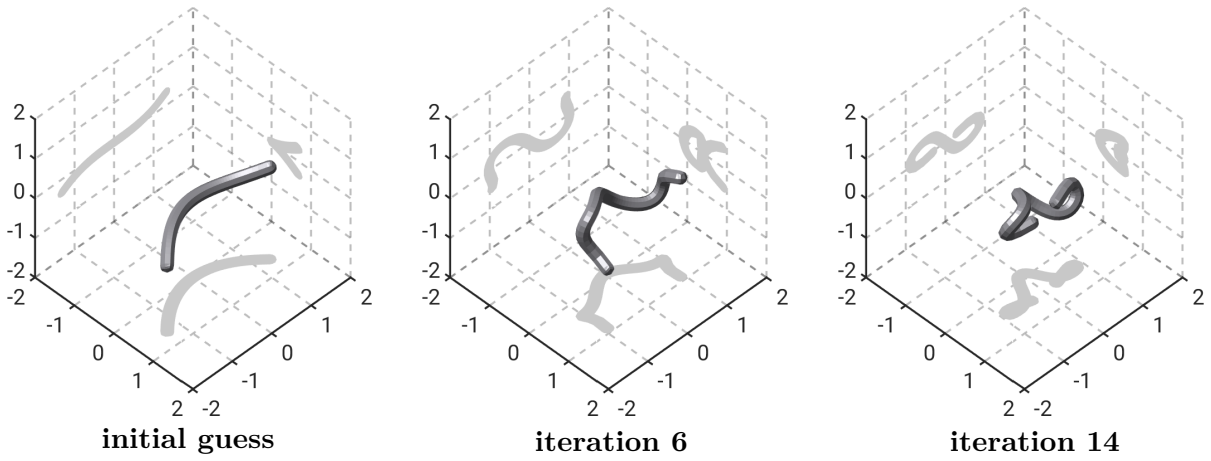

Figure 6.8. The initial guess, one excerpt and the final result from the optimization in Example 6.5.

scale the helix' true size by (6.24), thus,

$$\begin{aligned} \widehat{r}_{\text{major}} &= s_{\blacktriangle,f}(0.183) \approx 0.1696\,, \\ \widehat{r}_{\text{minor}} &= s_{\blacktriangle,f}(0.0533) \approx 0.0494\,, \\ \widehat{p} &= s_{\blacktriangle,f}(0.1686) \approx 0.1562\,. \end{aligned}$$

If we want to check different frequencies, we can also scale the object instead by multiplying the corresponding quantities with $\widetilde{f}/(44.21\,\text{THz})$, where $\widetilde{f}$ is the new target frequency. In doing so, we also obtain a new wavelength $\lambda = c/f$ and the associated relative interior electric permittivity $\varepsilon_{r,-}$ from [54], [91]. A resulting frequency scan for the frequencies $\widetilde{f} \in [43.21\,\text{THz}, 47.21\,\text{THz}]$ and a comparison to the reference data is depicted in Figure 6.7.

Next, we perform a free-form optimization of a silver tube with the same material parameters.

Example 6.5. We initiate the optimization scheme with a silver obstacle D defined by a third-degree B-spline curve with control points

$$\boldsymbol{c}_j = 3 \begin{pmatrix} (j/20 - 1/2)^2 \\ j/20 - 1/2 \\ (j/20 - 1/2)^3 \end{pmatrix}, \qquad j = 0, \ldots, 19\,.$$

The radius function is set constant to $r \equiv 0.13$. We choose the material parameters $\varepsilon_{r,-} \approx -2475.44 + 349.93\text{i}$, $\varepsilon_{r,+} = 1.8912$, $\mu \equiv 1$ and the angular frequency $\omega = 1$. Discretizing the surface leads to a mesh and a corresponding RWG finite element space with 13380 DOF. The regularization parameters are chosen as $\alpha_1 = 1\text{e}{-3}$, $\alpha_2 = 1\text{e}{-2}$. Moreover, we set $N = 3$. Starting with a relative modified em-chirality of approximately 1.2% the BFGS scheme terminates after 14 iterations, yielding an object with a relative modified em-chirality of around 79.33%. The results for the optimization are shown in Figure 6.8.

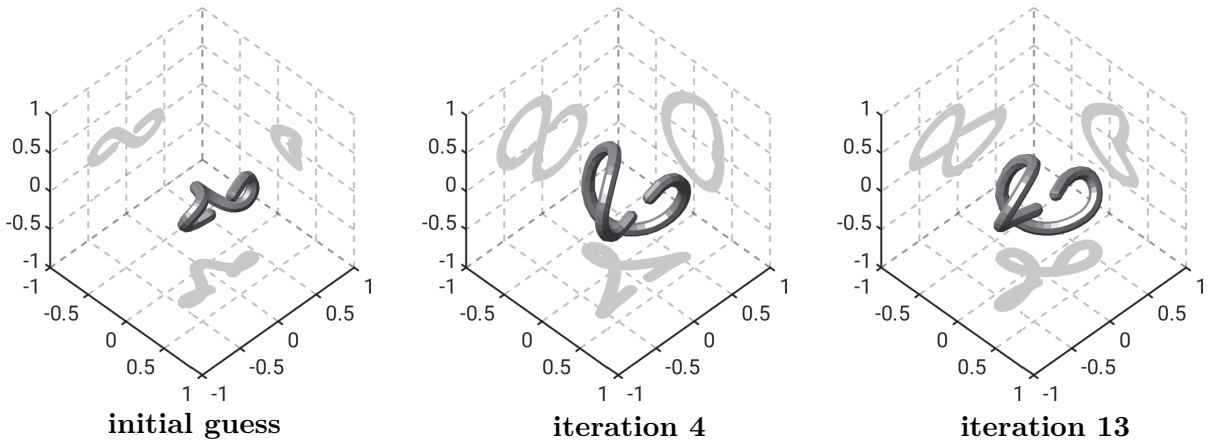

Figure 6.9. The initial guess, one excerpt and the final result from the optimization in Example 6.6.

We observe that the shape of the optimized silver object in Example 6.5 is similar to these of the optimized perfect conductors, cf., e.g., Figures 6.2 and 6.8. In the second example, we include this information by assuming that the initial guess already has such a shape. Hence, we start the optimization with a scaled version of the result from Example 6.5. The aim is to extend its flexibility by lowering the radius.

Example 6.6. We scale the optimized object from Example 6.5 down by a factor of two and restart the optimization process with the same material parameters and $\alpha_1 = 1\text{e}{-5},\ \alpha_2 = 1\text{e}{-2}$. Thus, the radius function is set constant to $r \equiv 0.13/2 = 6.5\text{e}{-2}$. Here, we start with a relative modified em-chirality of approximately 26.9% and the BFGS scheme terminates after 13 iterations, yielding an object with a relative modified em-chirality of around 88.57%. The results for the optimization are shown in Figure 6.9.

Note that in Examples 6.5 and 6.6, we specify the values of the relative *modified* em-chirality measure. The corresponding relative em-chirality values are approximately 84.51% for the final result from Example 6.5 and approximately 89.80% for the final result from Example 6.6. Recall the relative em-chirality of roughly 95.47% for the reference helix D_{ref}. Thus, in this case, the value of the optimized object does not exceed that of the reference object. However, they are of larger size again. In Figure 6.10, we provide a size comparison of the reference helix D_{ref} with the results from Examples 6.5 and 6.6. We also note that there potentially exist even larger scaled objects with such high chirality properties, however, recall that we have to solve $(2N^2 + 4N) \cdot (\#\,\text{perturbations})$ scattering problems to assemble one gradient for the BFGS, where N is the truncation parameter for the vector spherical harmonics expansion of the far-field operator. Hence, numerical computations quickly become unfeasible, because we need to align the truncation parameter to the object's size by $N \gtrsim kR$, see Remark 6.3.

Furthermore, in Figure 6.11, we show frequency scans for the objects from Examples 6.5 and 6.6 for frequencies in a range from 43.81 THz to 45.41 THz. Remarkably, we observe that despite being optimized for a frequency of 44.21 THz, both objects attain their maximum at a frequency smaller than 44 THz.

6.3. Conclusion

We have successfully optimized the shape of tubular objects, such that they reach high em-chirality values while being much bigger in size than the objects that have been considered optimal previously – cf. both the helices from [41], [97] and the rather complicated looking nanowires from [69, Subsection 5.6.3]. The reason for helical structures being the choice in, e.g., [41, Section VII], is motivated by geometrically optimized helical antennas for circular polarization from [112]. An explanation for the convenient behavior of helices can be found in [97, p. 2]. Nevertheless, the obvious disadvantage is that the shape cannot break out of the helical restraint – even if it would only be a small shear deformation of such a helix. Another drawback becomes apparent from the optimized helices, namely, they are restricted to objects of very small size, which makes them significantly challenging candidates for practical realizations.

The optimal nanowires from [69, Subsection 5.6.3] are free-form optimized structures that also have two disadvantages: on the one hand the smallness drawback applies here as well. On the other hand, they take on a rather unintuitive and complicated shape, which makes practical feasibility even more difficult.

In contrast, the objects that are optimized in Examples 6.1–6.6 reach very high em-chirality values while being bigger in size than the optimal helices and nanowires and still taking on a seemingly intuitive shape. We have no solid interpretation of why the optimal structures turn out as they do, however, one explanation could possibly be that the optimized object embodies a combination of multiple electric dipole antennas and coils achieving the desired – close to optimal – feedback behavior, as considered for two helices in [64].

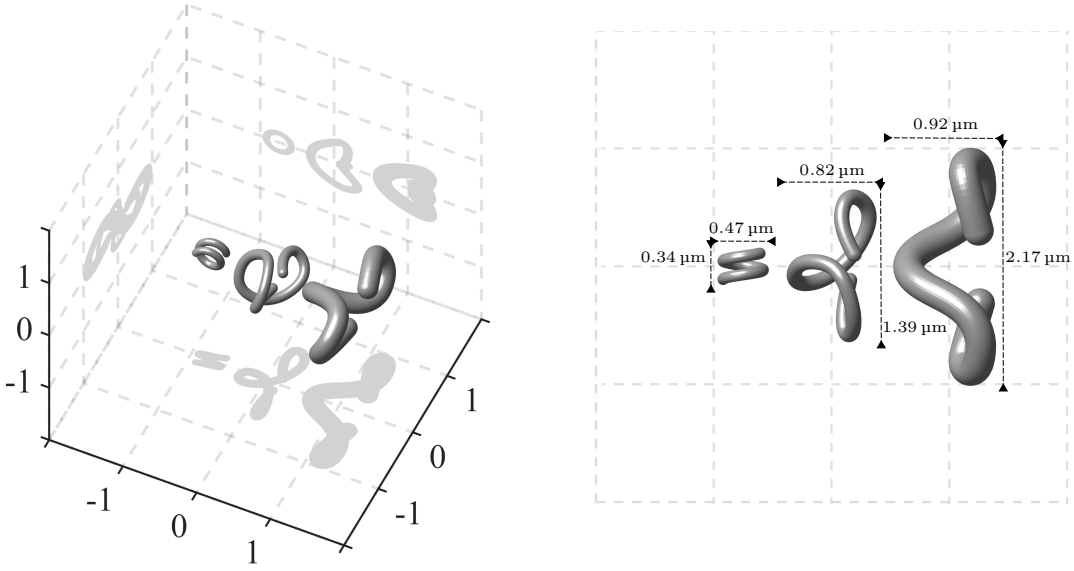

Figure 6.10. Size comparison of the optimized non-helical objects from Example 6.5 (right in both cases; radius $\approx 0.1403\,\mu\text{m}$), Example 6.6 (middle in both cases; radius $\approx 0.0702\,\mu\text{m}$), and the silver helix from [97] (left in both cases; radius $= 0.0533\,\mu\text{m}$).

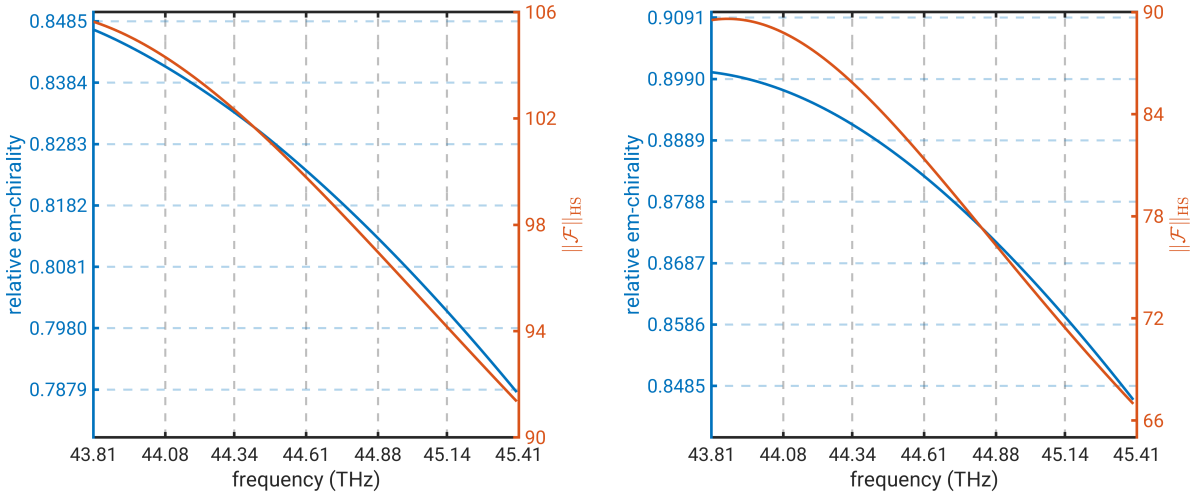

Figure 6.11. Frequency scans, showing the relative em-chirality (blue) and $\|\mathcal{F}\|_{\text{HS}}$ (orange) for $f \in [43.81\,\text{THz}, 45.41\,\text{THz}]$. On the vertical axis is the relative em-chirality (not modified). *Left*: Object from Example 6.5. *Right*: Object from Example 6.6.

APPENDIX A

FORMULARY

We consider sufficiently smooth scalar-valued functions $u, v\colon \mathbb{R}^3 \to \mathbb{C}$ and vector-valued functions $\boldsymbol{U}, \boldsymbol{V}\colon \mathbb{R}^3 \to \mathbb{C}^3$. There hold the following differentiation formulae:

$$\operatorname{div}(v\,\boldsymbol{U}) = v \operatorname{div}\boldsymbol{U} + \boldsymbol{\nabla} v \cdot \boldsymbol{U}\,, \tag{A.1a}$$

$$\operatorname{div}(\boldsymbol{U} \times \boldsymbol{V}) = \boldsymbol{V} \cdot \mathbf{curl}\,\boldsymbol{U} - \boldsymbol{U} \cdot \mathbf{curl}\,\boldsymbol{V}\,. \tag{A.1b}$$

Furthermore,

$$\mathbf{curl}\,\boldsymbol{\nabla} \equiv \mathbf{0}\,, \tag{A.2}$$

$$\operatorname{div}\mathbf{curl} \equiv 0\,. \tag{A.3}$$

Theorem A.1 (Gauss' Divergence Theorem)**.** *Let $D \subseteq \mathbb{R}^3$ be a Lipschitz domain and $\boldsymbol{U}\colon \mathbb{R}^n \to \mathbb{R}^n$ a C^1 vector field with compact support. Then it holds that*

$$\int_D \operatorname{div}\boldsymbol{U}(\boldsymbol{x})\,\mathrm{d}\boldsymbol{x} = \int_{\partial D} \boldsymbol{U}(\boldsymbol{x}) \cdot \boldsymbol{\nu}(\boldsymbol{x})\,\mathrm{d}s\,.$$

Proof. [80, Theorem 3.34] ∎

As a consequence of Theorem A.1 we obtain the following integral identities, see [68, Theorem A.11, Theorem A.13].

Lemma A.2 (Integral identities)**.** *Let $D \subseteq \mathbb{R}^3$ be a bounded Lipschitz domain and $\boldsymbol{U}, \boldsymbol{V} \in \boldsymbol{C}^1(D) \cap \boldsymbol{C}(\overline{D})$ as well as $u, v \in C^1(\overline{D})$. There hold*

$$\int_D v\,\boldsymbol{\nabla} u\,\mathrm{d}\boldsymbol{x} + \int_D u\,\boldsymbol{\nabla} v\,\mathrm{d}\boldsymbol{x} = \int_{\partial D} v\,u\,\boldsymbol{\nu}\,\mathrm{d}s\,, \tag{A.4a}$$

$$\int_D \mathbf{curl}\,\boldsymbol{U}\,\mathrm{d}\boldsymbol{x} = \int_{\partial D} \boldsymbol{\nu} \times \boldsymbol{U}\,\mathrm{d}s\,, \tag{A.4b}$$

$$\int_D u \operatorname{div}\boldsymbol{U} + \boldsymbol{U} \cdot \boldsymbol{\nabla} u\,\mathrm{d}\boldsymbol{x} = \int_{\partial D} u(\boldsymbol{\nu} \cdot \boldsymbol{U})\,\mathrm{d}s\,, \tag{A.4c}$$

$$\int_D \boldsymbol{V} \cdot \mathbf{curl}\,\boldsymbol{U} - \boldsymbol{U} \cdot \mathbf{curl}\,\boldsymbol{V}\,\mathrm{d}\boldsymbol{x} = \int_{\partial D} (\boldsymbol{U} \times \boldsymbol{V}) \cdot \boldsymbol{\nu}\,\mathrm{d}s\,. \tag{A.4d}$$

APPENDIX B

B-Spline Curves

B-spline (short for basis spline) curves have been introduced in [101], [102], [36] with truncated power functions. Another way to define them is through the so-called "blossoming" approach, see [94, Chapter E.18]. We use the reccurance formula proven in [37], since it is the most useful for numerical implementations. More about B-spline curves is summarized in [38, Chapter IX], [35], [89, Chapters 2 and 3]. A significant advantage – regarding shape optimization – of the B-spline curves over, e.g., the closely related Bézier curves, is the local control that allows changing individual portions of the curve, without changing the whole B-spline curve. Bézier curves use *Bernstein*[1] *basis polynomials* [8], see also [39, Chapter 3.2], which are strictly positive over the whole parameter interval (see [39, Theorem 3.2.1]) and, hence, imply global control. Thus, changing individual portions has influence on the whole Bézier curve's shape.

Let $\boldsymbol{P}^0, \ldots, \boldsymbol{P}^n \in \mathbb{R}^3$ denote some distinct *control points* and $t_0, \ldots, t_m \in [0,1]$ some *knots* such that $m - n - 1 \geq 0$ and $t_0 \leq \ldots \leq t_k \leq t_{k+1} \leq \ldots \leq t_m$. We call $p \coloneqq m - n - 1$ the *polynomial degree*.

Definition B.1. *For $t \in [0,1]$, we recursively define the kth basis functions $N_{k,j}$ of degree j by*

$$N_{k,0}(t) \coloneqq \begin{cases} 1\,, & t_k \leq t < t_{k+1}\,, \\ 0\,, & \textit{otherwise}\,, \end{cases} \qquad k \in \{0, \ldots, m-1\}\,,$$

as well as

$$N_{k,j}(t) \coloneqq \begin{cases} \dfrac{t - t_k}{t_{k+j} - t_k}\, N_{k,j-1}(t) + \dfrac{t_{k+j+1} - t}{t_{k+j+1} - t_{k+1}}\, N_{k+1,j-1}(t)\,, & t_{k+j} \neq t_k\,,\ t_{k+j+1} \neq t_{k+1}\,, \\ \dfrac{t_{k+j+1} - t}{t_{k+j+1} - t_{k+1}}\, N_{k+1,j-1}(t)\,, & t_{k+j} = t_k\,,\ t_{k+j+1} \neq t_{k+1}\,, \\ \dfrac{t - t_k}{t_{k+j} - t_k}\, N_{k,j-1}(t)\,, & t_{k+j} \neq t_k\,,\ t_{k+j+1} = t_{k+1}\,, \\ 0\,, & t_{k+j} = t_k\,,\ t_{k+j+1} = t_{k+1}\,, \end{cases}$$
$$j \in \{1, \ldots, p\}\,,\ k \in \{0, \ldots, m-j-1\}\,.$$

[1] Sergei Natanowitsch Bernstein (1880–1968)

Furthermore, we define a B-spline curve $\boldsymbol{z}\colon [0,1] \to \mathbb{R}^3$ *of degree* p *by*

$$\boldsymbol{z}(t) \coloneqq \sum_{k=0}^{n} N_{k,p}(t)\, \boldsymbol{P}^k\,, \qquad t \in [0,1]\,.$$

The functions $N_{k,j}$ are piecewise polynomials of degree p and vanish outside the interval $[t_k, t_{k+j}]$. Moreover, we have the following smoothness properties at the knots.

Theorem B.2. *Let* t_i, $i \in \{0,\dots,m\}$, *be a knot with multiplicity* $l < p$. *Then, the basis functions are in* $C^{p-l}((a,b),\mathbb{R})$ *in a neighborhood* (a,b) *of* t_i.

Proof. See [72, Theorem 4]. ■

Theorem B.2 immediately implies that on any open interval $(a,b) \subseteq [0,1]$ containing only simple knots, $\boldsymbol{z} \in \boldsymbol{C}^{p-1}((a,b),\mathbb{R}^3)$ for the corresponding B-spline $\boldsymbol{z}$.

Definition B.3. *A B-spline curve* $\boldsymbol{z}$ *is said to be* clamped *if* $t_0 = t_1 = \ldots = t_p$ *and* $t_{m-p} = t_{m-p+1} = \ldots = t_m$.

Theorem B.4. *Let* $t \in [0,1]$. *The derivative of the* k*th basis function* $N_{k,j}$ *of degree* j *is reccursively given by*

$$N'_{k,j}(t) = \begin{cases} \dfrac{j}{t_{k+j} - t_k}\, N_{k,j-1}(t) - \dfrac{j}{t_{k+j+1} - t_{k+1}}\, N_{k+1,j-1}(t)\,, & t_{k+j} \neq t_k\,,\ t_{k+j+1} \neq t_{k+1}\,, \\ -\dfrac{j}{t_{k+j+1} - t_{k+1}}\, N_{k+1,j-1}(t)\,, & t_{k+j} = t_k\,,\ t_{k+j+1} \neq t_{k+1}\,, \\ \dfrac{j}{t_{k+j} - t_k}\, N_{k,j-1}(t)\,, & t_{k+j} \neq t_k\,,\ t_{k+j+1} = t_{k+1}\,, \\ 0\,, & t_{k+j} = t_k\,,\ t_{k+j+1} = t_{k+1}\,, \end{cases}$$

$$j \in \{1,\dots,p\}\,,\ k \in \{0,\dots,m-j-1\}\,.$$

Next, let $\boldsymbol{z}$ *be a clamped B-spline curve of degree* $p \geq 1$. *By setting the control points*

$$\boldsymbol{Q}^k \coloneqq \frac{p}{t_{k+p+1} - t_{k+1}}\,(\boldsymbol{P}^{k+1} - \boldsymbol{P}^k)\,, \qquad k = 0,\dots,n-1\,,$$

we obtain the derivative $\boldsymbol{z}'$ *with*

$$\boldsymbol{z}'(t) = \sum_{k=0}^{n-1} N_{k+1,p-1}(t)\, \boldsymbol{Q}^k\,, \qquad t \in [0,1]\,.$$

Proof. Differentiation can be seen in [72, Theorem 3]. Now, let $\boldsymbol{z}$ be a clamped B-spline. Thus, for $t \in [0,1]$ it holds that

$$\boldsymbol{z}'(t) = \sum_{k=1}^{n} \frac{p}{t_{k+p} - t_k} N_{k,p-1}(t)\boldsymbol{P}^k - \sum_{k=0}^{n-1} \frac{p}{t_{k+p+1} - t_{k+1}} N_{k+1,p-1}(t)\boldsymbol{P}^k\,.$$

An index shift and defining

$$\boldsymbol{Q}^k \coloneqq \frac{p}{t_{k+p+1} - t_{k+1}} \left(\boldsymbol{P}^{k+1} - \boldsymbol{P}^k\right), \qquad k = 0, \dots, n-1,$$

yields the assertion. ■

Theorem B.5. *Denote by $\widetilde{N}_{k,j}$ the basis functions associated with the knots $t_1, \dots, t_{m-1}$. Then,*

$$N_{k+1,p-1} = \widetilde{N}_{k,p-1}.$$

Proof. This follows readily from Definition B.1. ■

Theorem B.5 provides that the derivative of a clamped B-spline curve $\boldsymbol{z}$ is given by

$$\boldsymbol{z}'(t) = \sum_{k=0}^{n} \widetilde{N}_{k,p-1}(t)\, \boldsymbol{Q}^k, \qquad t \in [0,1].$$

Thus, $\boldsymbol{z}'$ is itself a clamped B-spline curve of degree $p-1$ with the $n-1$ control points $\boldsymbol{Q}^k$ and the $m-1$ knots $t_1, \dots, t_{m-1}$. Finally, we note that for a clamped B-spline curve $\boldsymbol{z}$ there hold

$$\begin{aligned} \boldsymbol{z}(0) &= \boldsymbol{P}^0, & \boldsymbol{z}(1) &= \boldsymbol{P}^n, \\ \boldsymbol{z}'(0) &= \frac{p}{t_{p+1} - t_1} \left(\boldsymbol{P}^1 - \boldsymbol{P}^0\right), & \boldsymbol{z}'(1) &= \frac{p}{t_{m-1} - t_{m-p-1}} \left(\boldsymbol{P}^n - \boldsymbol{P}^{n-1}\right). \end{aligned}$$

APPENDIX C

The CFIE and PMCHWT Integral Equation

Let the electric and magnetic potentials $\boldsymbol{\mathcal{E}}_k$ and $\boldsymbol{\mathcal{H}}_k$ as well as the boundary operators $\mathbf{S}_k$ and $\mathbf{C}_k$ be defined as in Section 5.1. In addition to the indirect EFIE (5.8) (for the perfect conductor) as well as the modified PMCHWT (5.18) (for penetrable obstacles) we present an additional boundary integral equation for each problem. These have been used in [5, Section 4] and in our setting – using the BEM library `Bempp-cl` – they lead to significantly higher computation times than the indirect EFIE / modified PMCHWT. However, they can be used to generate the far-field data for the numerical examples of the inverse problem from Section 5.4, avoiding an inverse crime [31, p. 179].

C.1. Perfect conductor

Denote by $\boldsymbol{E}^s, \boldsymbol{H}^s$ a radiating solution of (2.24), (2.20). As in Section 5.1, we consider the Stratton–Chu representation formula for the scattered fields $\boldsymbol{E}^s, \boldsymbol{H}^s$ in $\mathbb{R}^3 \setminus \overline{D}$, i.e.,

$$\left.\begin{aligned} \boldsymbol{E}^s &= -\boldsymbol{\mathcal{E}}_k \, \boldsymbol{\gamma}_t^+ \boldsymbol{H}^s - \boldsymbol{\mathcal{H}}_k \, \boldsymbol{\gamma}_t^+ \boldsymbol{E}^s \\ \boldsymbol{H}^s &= \boldsymbol{\mathcal{E}}_k \, \boldsymbol{\gamma}_t^+ \boldsymbol{E}^s - \boldsymbol{\mathcal{H}}_k \, \boldsymbol{\gamma}_t^+ \boldsymbol{H}^s \end{aligned}\right\} \quad \text{in } \mathbb{R}^3 \setminus \overline{D}\,. \tag{C.1}$$

We choose the direct ansatz $\boldsymbol{\gamma}_t^+ \boldsymbol{H}^s = \boldsymbol{\Psi} \in \boldsymbol{H}^{-1/2}(\mathrm{Div}, \partial D)$. Then, we apply the trace operator $\boldsymbol{\gamma}_t$ on both equations of (C.1) and subsequently apply the jump relations (5.3), obtaining

$$\left.\begin{aligned} \boldsymbol{\gamma}_t^+ \boldsymbol{E}^s &= -\mathbf{S}_k \, \boldsymbol{\Psi} - \left(-\frac{1}{2} I + \mathbf{C}_k\right) \boldsymbol{\gamma}_t^+ \boldsymbol{E}^s \\ \boldsymbol{\Psi} &= \mathbf{S}_k \, \boldsymbol{\gamma}_t^+ \boldsymbol{E}^s - \left(-\frac{1}{2} I + \mathbf{C}_k\right) \boldsymbol{\Psi} \end{aligned}\right\} \quad \text{on } \partial D\,. \tag{C.2}$$

Next, we rearrange the equations from (C.2) to obtain the *direct electric field integral equation* (direct EFIE) and the *direct magnetic field integral equation* (direct MFIE)

$$\mathbf{S}_k \, \boldsymbol{\Psi} = -\left(\frac{1}{2} I + \mathbf{C}_k\right) \boldsymbol{\gamma}_t^+ \boldsymbol{E}^s \qquad \text{and} \qquad \left(\frac{1}{2} I + \mathbf{C}_k\right) \boldsymbol{\Psi} = \mathbf{S}_k \, \boldsymbol{\gamma}_t^+ \boldsymbol{E}^s\,, \tag{C.3}$$

respectively, on ∂D. A brief comparison of the direct EFIE and MFIE is outlined in [25]. In general, the direct EFIE suffers from ill-conditioning for high and low frequencies, and the direct MFIE from accuracy problems for very low frequencies, see [114] for the problem specification and a remedy. Furthermore, both integral equations can be subject to interior resonances, which have been identified in [77, §2] and illustrated – together with several remedies – in [88], see also [26]. One remedy is a so-called *combined field integral equation* (CFIE) [78], [81], which is assembled through linear combinations of the direct EFIE and MFIE. In the past decades, different variations of CFIEs have been proposed. We choose the CFIE from [32] that has the benefit of being well-conditioned as well as neither suffering from interior resonances nor having the low-frequency problem. However, with this CFIE we rely on smooth domains, which is no major drawback, since this is a restriction already imposed by the employment of domain derivatives. For a coercive CFIE on Lipschitz domains, see [20, Chapter 4].

Hence, we regularize the direct EFIE with the operator $\mathbf{S}_{\mathrm{i}k}$ and obtain the regularized direct EFIE

$$\mathbf{S}_{\mathrm{i}k}\,\mathbf{S}_k\,\boldsymbol{\Psi} = -\,\mathbf{S}_{\mathrm{i}k}\left(\frac{1}{2}I + \mathbf{C}_k\right)\boldsymbol{\gamma}_t^+\boldsymbol{E}^s\,. \tag{C.4}$$

We can replace the scattered fields $\boldsymbol{E}^s$ by the domain derivative $\boldsymbol{E}'$ in all those steps; note, however, that then also $\boldsymbol{\Psi} = \boldsymbol{\gamma}_T\boldsymbol{H}'$. Next, we combine the regularized direct EFIE and the direct MFIE by subtracting the former from the latter to arrive at the CFIE

$$\left(\frac{1}{2}I + \mathbf{C}_k - \mathbf{S}_{\mathrm{i}k}\,\mathbf{S}_k\right)\boldsymbol{\Psi} = \left(\mathbf{S}_k + \mathbf{S}_{\mathrm{i}k}\left(\frac{1}{2}I + \mathbf{C}_k\right)\right)\boldsymbol{f}\,, \tag{C.5}$$

where $\boldsymbol{f} = -\boldsymbol{\gamma}_t\boldsymbol{E}^i$ for the scattering problem (cf. (2.24b)) or $\boldsymbol{f} = \mathrm{i}\omega\mu_+\boldsymbol{h}_{\boldsymbol{\nu}}\,\boldsymbol{\gamma}_T\boldsymbol{H} - \mathbf{Curl}\,(\boldsymbol{h}_{\boldsymbol{\nu}}\boldsymbol{E}_{\boldsymbol{\nu}})$ for the domain derivative (cf. (3.15)). With (C.1), the corresponding scattered electric fields are given by $\boldsymbol{E}^s = -\,\boldsymbol{\mathcal{E}}_k\boldsymbol{\Psi} - \boldsymbol{\mathcal{H}}_k\boldsymbol{\gamma}_t^+\boldsymbol{E}^s$ in $\mathbb{R}^3 \setminus \overline{D}$ and the corresponding far-field patterns by $\boldsymbol{E}^\infty = -\,\boldsymbol{\mathcal{E}}_k^\infty\boldsymbol{\Psi} - \boldsymbol{\mathcal{H}}_k^\infty\boldsymbol{\gamma}_t^+\boldsymbol{E}^s$ on $\mathbb{S}^2$ (analogously for the domain derivative $\boldsymbol{E}'$).

C.2. Penetrable Obstacle

Recall the the definition of the multitrace operator

$$\mathbf{A}_k\colon (\boldsymbol{H}^{-1/2}(\mathrm{Div},\partial D))^2 \to (\boldsymbol{H}^{-1/2}(\mathrm{Div},\partial D))^2\,, \qquad \mathbf{A}_k = \begin{pmatrix} \mathbf{C}_k & \mathbf{S}_k \\ -\,\mathbf{S}_k & \mathbf{C}_k \end{pmatrix},$$

from Subsection 5.1.2. We use a variant of the well-known (direct) PMCHWT integral equation [90], which uses the exterior traces of the scattered electric and magnetic fields as the unknowns [19, Section 7.1] [21, Section 6.2]. As in Subsection 5.1.2, we can rewrite the Stratton–Chu formulae as

$$\begin{pmatrix} \boldsymbol{\gamma}_t^-\boldsymbol{E} \\ \boldsymbol{\gamma}_t^-\boldsymbol{H} \end{pmatrix} = \left(\frac{1}{2}\boldsymbol{I} + \mathbf{A}_{k_-}\right)\begin{pmatrix} \boldsymbol{\gamma}_t^-\boldsymbol{E} \\ \boldsymbol{\gamma}_t^-\boldsymbol{H} \end{pmatrix}, \qquad \begin{pmatrix} \boldsymbol{\gamma}_t^+\boldsymbol{E}^s \\ \boldsymbol{\gamma}_t^+\boldsymbol{H}^s \end{pmatrix} = \left(\frac{1}{2}\boldsymbol{I} - \mathbf{A}_{k_+}\right)\begin{pmatrix} \boldsymbol{\gamma}_t^+\boldsymbol{E}^s \\ \boldsymbol{\gamma}_t^+\boldsymbol{H}^s \end{pmatrix}, \tag{C.6}$$

respectively (see (5.14), (5.15), however, without employing an ansatz). Note that by definition (2.19), it holds that $\boldsymbol{E}^s = \boldsymbol{E}$ in D. Exploiting the interface condition (2.22b), i.e.,

$$\begin{pmatrix} \gamma_t^- \boldsymbol{E} \\ \gamma_t^- \boldsymbol{H} \end{pmatrix} = \begin{pmatrix} \gamma_t^+ \boldsymbol{E}^s \\ \gamma_t^+ \boldsymbol{H}^s \end{pmatrix} + \begin{pmatrix} \gamma_t \boldsymbol{E}^i \\ \gamma_t \boldsymbol{H}^i \end{pmatrix},$$

we find with (C.6) that

$$\begin{aligned} \left(\frac{1}{2}\boldsymbol{I} + \mathbf{A}_{k_-}\right) \left[\begin{pmatrix} \gamma_t^+ \boldsymbol{E}^s \\ \gamma_t^+ \boldsymbol{H}^s \end{pmatrix} + \begin{pmatrix} \gamma_t \boldsymbol{E}^i \\ \gamma_t \boldsymbol{H}^i \end{pmatrix} \right] &= \begin{pmatrix} \gamma_t^+ \boldsymbol{E}^s \\ \gamma_t^+ \boldsymbol{H}^s \end{pmatrix} + \begin{pmatrix} \gamma_t \boldsymbol{E}^i \\ \gamma_t \boldsymbol{H}^i \end{pmatrix} \\ &= \left(\frac{1}{2}\boldsymbol{I} - \mathbf{A}_{k_+}\right) \begin{pmatrix} \gamma_t^+ \boldsymbol{E}^s \\ \gamma_t^+ \boldsymbol{H}^s \end{pmatrix} + \begin{pmatrix} \gamma_t \boldsymbol{E}^i \\ \gamma_t \boldsymbol{H}^i \end{pmatrix}. \end{aligned} \tag{C.7}$$

In all of these considerations, we may replace the scattered fields $\boldsymbol{E}^s, \boldsymbol{H}^s$ by the domain derivatives $\boldsymbol{E}', \boldsymbol{H}'$, where we have to use the interface condition (3.14) instead of (2.22b). Then, rearranging (C.7), we eventually arrive at the PMCHWT integral formulation

$$\left(\mathbf{A}_{k_-} + \mathbf{A}_{k_+}\right) \begin{pmatrix} \boldsymbol{\Psi} \\ \boldsymbol{\Upsilon} \end{pmatrix} = \left(\mathbf{A}_{k_-} - \frac{1}{2}\boldsymbol{I}\right) \begin{pmatrix} \boldsymbol{f} \\ \boldsymbol{g} \end{pmatrix}, \tag{C.8}$$

with the functions $\boldsymbol{f}$, $\boldsymbol{g}$ given by the right hand sides of (2.22b) and (3.14) for the scattered field and the domain derivative, respectively. The integral equation is uniquely solvable (see [21, Corollary 6.4]), with the unknown functions given by

$$\begin{pmatrix} \boldsymbol{\Psi} \\ \boldsymbol{\Upsilon} \end{pmatrix} = \begin{pmatrix} \gamma_t^+ \boldsymbol{E}^s \\ \gamma_t^+ \boldsymbol{H}^s \end{pmatrix} \text{ for } \begin{pmatrix} \boldsymbol{f} \\ \boldsymbol{g} \end{pmatrix} \text{ as in (2.22b) and } \begin{pmatrix} \boldsymbol{\Psi} \\ \boldsymbol{\Upsilon} \end{pmatrix} = \begin{pmatrix} \gamma_t^+ \boldsymbol{E}' \\ \gamma_t^+ \boldsymbol{H}' \end{pmatrix} \text{ for } \begin{pmatrix} \boldsymbol{f} \\ \boldsymbol{g} \end{pmatrix} \text{ as in (3.14)}.$$

Furthermore, we apply the Calderón preconditioner $(\mathbf{A}_{k_-} + \mathbf{A}_{k_+})$ on equation (C.8), which yields a well-conditioned system, see [33].

APPENDIX D

Numerical Validation of the Fréchet Derivative

In what follows, we present the approach to verify that the Fréchet derivatives of the far-field map and operator are implemented correctly. It may also be interpreted as a numerical validation of the characterizations from Section 4.2. We construct an example, where we can easily check the definition of the domain derivative, i.e.,

$$\|F(\partial D_{\boldsymbol{h}}) - F(\partial D) - F'[\partial D]\boldsymbol{h}\|_{\boldsymbol{L}^2_t(\mathbb{S}^2)}$$
$$\text{and} \quad \left\| \frac{\chi_{\mathrm{HS}}(\mathcal{F}(\partial D_{\boldsymbol{h}}))}{\|\mathcal{F}(\partial D_{\boldsymbol{h}})\|_{\mathrm{HS}}} - \frac{\chi_{\mathrm{HS}}(\mathcal{F}(\partial D))}{\|\mathcal{F}(\partial D)\|_{\mathrm{HS}}} - \left(\frac{\chi_{\mathrm{HS}}}{\|\cdot\|_{\mathrm{HS}}}\right)'[\mathcal{F}(\partial D)]\boldsymbol{h} \right\|_{\mathrm{HS}}$$

should approach zero with convergence order two each as $\|\boldsymbol{h}\|_{\boldsymbol{C}^1} \to 0$.

To achieve this, we perturb the object by some $\widehat{\boldsymbol{h}}$ and calculate the corresponding Fréchet derivatives. Then, we consider the perturbation $\boldsymbol{h} = h\,\widehat{\boldsymbol{h}}$ for some $h > 0$. Using the linearity of the Fréchet derivatives, we can compute

$$F'[\partial D]\boldsymbol{h} = h\,F'[\partial D]\widehat{\boldsymbol{h}} \qquad \text{and} \qquad \left(\frac{\chi_{\mathrm{HS}}}{\|\cdot\|_{\mathrm{HS}}}\right)'[\mathcal{F}(\partial D)]\boldsymbol{h} = h\,\left(\frac{\chi_{\mathrm{HS}}}{\|\cdot\|_{\mathrm{HS}}}\right)'[\mathcal{F}(\partial D)]\widehat{\boldsymbol{h}}\,.$$

As an example, we consider a tubular object with B-spline spine curve $\boldsymbol{z}$ defined by 10 control points

$$\boldsymbol{c}_j = \begin{pmatrix} 3/4\cos(\pi\, j/18) \\ 3/4\sin(\pi\, j/18) \\ j/9 - 1/2 \end{pmatrix}, \qquad j \in \{0,\dots,9\}\,,$$

and constant radius function $r \equiv 3/2$. We implement a numerical evaluation of these domain derivatives as has been established in Chapters 5 and 6.

In Figure D.1, we illustrate three examples for the perfect conductor case. We plot the error

$$\frac{\chi_{\mathrm{HS}}(\mathcal{F}(\partial D_{\boldsymbol{h}}))}{\|\mathcal{F}(\partial D_{\boldsymbol{h}})\|_{\mathrm{HS}}} - \frac{\chi_{\mathrm{HS}}(\mathcal{F}(\partial D))}{\|\mathcal{F}(\partial D)\|_{\mathrm{HS}}} - h\,\left(\frac{\chi_{\mathrm{HS}}}{\|\cdot\|_{\mathrm{HS}}}\right)'[\mathcal{F}(\partial D)]\widehat{\boldsymbol{h}} \tag{D.1}$$

against h. We observe that we have convergence order two until h becomes significantly smaller than 1e−2. If we examine the sidelengths of the elements of the mesh that we use to discretize

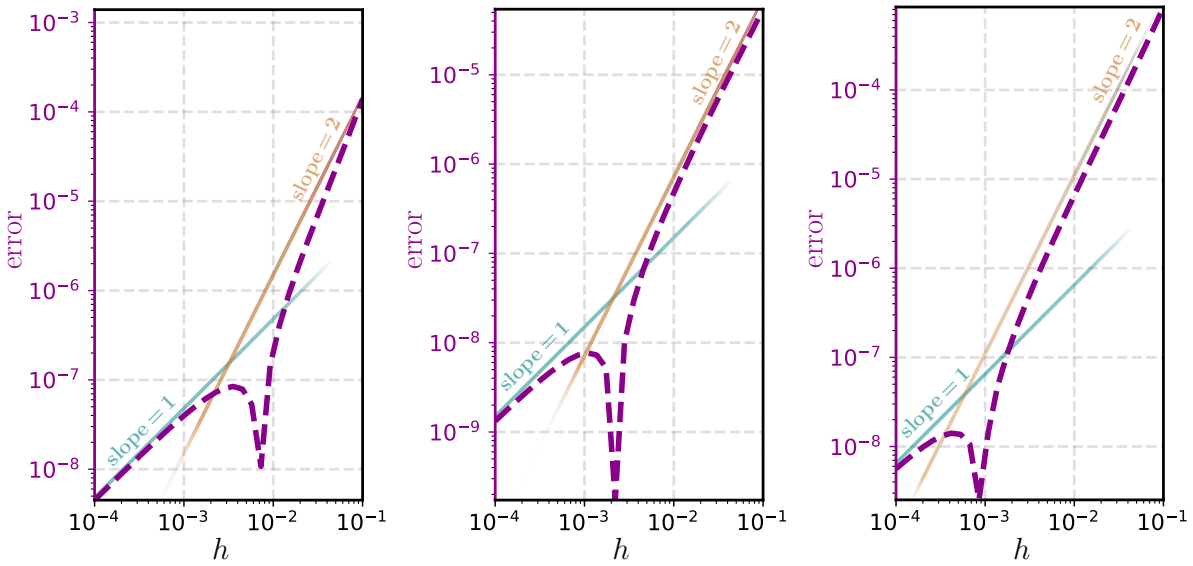

Figure D.1. Log–log plots of the difference (D.1) plotted against h for a perfectly conducting tube D for perturbations of the control points, the radius, or both. *Left*: Control points. *Middle*: Radius. *Right*: Control points and radius.

the tube, this becomes highly plausible, since they lie between 6.62e−3 and 3.92e−2, with mean 1.83e−2. Thus, if h becomes smaller than most of these triangles the error gets dominated by h, where the information from the domain derivative has less to no relevant influence on the convergence rate. Corresponding tests for penetrable obstacles and for the far-field map (for both perfect conductors and penetrable obstacles) yield similar results.

Bibliography

[1] T. Abboud and J.-C. Nédélec. Electromagnetic waves in an inhomogeneous medium. *J. Math. Anal. Appl.*, 164(1):40–58, 1992. URL: https://www.sciencedirect.com/science/article/pii/0022247X92901443, doi:10.1016/0022-247X(92)90144-3.

[2] H. Ammari, M. S. Vogelius, and D. Volkov. Asymptotic formulas for perturbations in the electromagnetic fields due to the presence of inhomogeneities of small diameter. II. The full Maxwell equations. *J. Math. Pures Appl. (9)*, 80(8):769–814, 2001. doi:10.1016/S0021-7824(01)01217-X.

[3] T. Arens, R. Griesmaier, and M. Knöller. Maximizing the electromagnetic chirality of thin dielectric tubes. *SIAM J. Appl. Math.*, 81(5):1979–2006, 2021. doi:10.1137/21M1393509.

[4] T. Arens, F. Hagemann, F. Hettlich, and A. Kirsch. The definition and measurement of electromagnetic chirality. *Math. Methods Appl. Sci.*, 41(2):559–572, 2018. doi:10.1002/mma.4628.

[5] T. Arens, M. Knöller, and R. Schurr. Inverse electromagnetic scattering problems for long tubular objects. *SIAM Journal on Scientific Computing*, 48(1):A185–A208, 2026. doi:10.1137/24M1687108.

[6] K. Atkinson and W. Han. *Theoretical numerical analysis*, volume 39 of *Texts in Applied Mathematics*. Springer, Dordrecht, third edition, 2009. A functional analysis framework. doi:10.1007/978-1-4419-0458-4.

[7] J. Baumeister. *Stable solution of inverse problems*. Advanced Lectures in Mathematics. Friedr. Vieweg & Sohn, Braunschweig, 1987. doi:10.1007/978-3-322-83967-1.

[8] S. Bernstein. Démonstration du théorème de weierstrass fondée sur le calcul des probabilités. *Communications of the Kharkov Mathematical Society*, 13:1–2, 1912/1913.

[9] T. Betcke and M. W. Scroggs. Bempp-cl: A fast Python based just-in-time compiling boundary element library. *Journal of Open Source Software*, 6(59):2879, 2021. doi:10.21105/joss.02879.

[10] R. L. Bishop. There is more than one way to frame a curve. *Amer. Math. Monthly*, 82:246–251, 1975. doi:10.2307/2319846.

[11] S. C. Brenner and L. R. Scott. *The mathematical theory of finite element methods*, volume 15 of *Texts in Applied Mathematics*. Springer, New York, third edition, 2008. doi:10.1007/978-0-387-75934-0.

[12] H. Brezis. *Functional analysis, Sobolev spaces and partial differential equations*. Universitext. Springer, New York, 2011.

[13] F. Brezzi and M. Fortin. *Mixed and hybrid finite element methods*, volume 15 of *Springer Series in Computational Mathematics*. Springer-Verlag, New York, 1991. doi:10.1007/978-1-4612-3172-1.

[14] C. G. Broyden. The convergence of a class of double-rank minimization algorithms 1. general considerations. *IMA Journal of Applied Mathematics*, 6(1):76–90, 03 1970. doi:10.1093/imamat/6.1.76.

[15] A. Buffa and S. H. Christiansen. The electric field integral equation on Lipschitz screens: definitions and numerical approximation. *Numer. Math.*, 94(2):229–267, 2003. doi:10.1007/s00211-002-0422-0.

[16] A. Buffa and S. H. Christiansen. A dual finite element complex on the barycentric refinement. *Math. Comp.*, 76(260):1743–1769, 2007. doi:10.1090/S0025-5718-07-01965-5.

[17] A. Buffa, M. Costabel, and C. Schwab. Boundary element methods for Maxwell's equations on non-smooth domains. *Numer. Math.*, 92(4):679–710, 2002. doi:10.1007/s002110100372.

[18] A. Buffa, M. Costabel, and D. Sheen. On traces for $H(\mathbf{curl}, \Omega)$ in Lipschitz domains. *J. Math. Anal. Appl.*, 276(2):845–867, 2002. doi:10.1016/S0022-247X(02)00455-9.

[19] A. Buffa and R. Hiptmair. Galerkin boundary element methods for electromagnetic scattering. *Topics in Computational Wave Propagation, Lect. Notes Comput. Sci. Eng*, 31:85–126, 01 2003. doi:10.1007/978-3-642-55483-4_3.

[20] A. Buffa and R. Hiptmair. A coercive combined field integral equation for electromagnetic scattering. *SIAM J. Numer. Anal.*, 42(2):621–640, 2004. doi:10.1137/S0036142903423393.

[21] A. Buffa, R. Hiptmair, T. v. Petersdorff, and C. Schwab. Boundary element methods for Maxwell transmission problems in Lipschitz domains. *Numer. Math.*, 95(3):459–485, 2003. doi:10.1007/s00211-002-0407-z.

[22] A. Buffa, R. Hiptmair, T. von Petersdorff, and C. Schwab. Boundary element methods for maxwell equations in lipschitz domains. *SAM Research Report 2001-05*, 2001. URL: https://doi.org/10.3929/ethz-a-004288266.

[23] Y. Capdeboscq, R. Griesmaier, and M. Knöller. An asymptotic representation formula for scattering by thin tubular structures and an application in inverse scattering. *Multiscale Model. Simul.*, 19(2):846–885, 2021. doi:10.1137/20M1369907.

[24] M. Cessenat. *Mathematical methods in electromagnetism*. Series on advances in mathematics for applied sciences. World Scientific, Singapore, 1996. Literaturverzeichnis: Seite 365-372. URL: https://zbmath.org/?q=an:0917.65099.

[25] W. C. Chew, C. P. Davis, K. F. Warnick, Z. P. Nie, J. Hu, S. Yan, and L. Gurel. Efie and mfie, why the difference? In *2008 IEEE Antennas and Propagation Society International Symposium*, pages 1–2, 2008. doi:10.1109/APS.2008.4619724.

[26] W. C. Chew and J. M. Song. Gedanken experiments to understand the internal resonance problems of electromagnetic scattering. *Electromagnetics*, 27(8):457–471, 2007. doi:10.1080/02726340701668039.

[27] S. H. Christiansen and J.-C. Nédélec. A preconditioner for the electric field integral equation based on Calderon formulas. *SIAM J. Numer. Anal.*, 40(3):1100–1135, 2002. doi:10.1137/S0036142901388731.

[28] D. Colton and R. Kress. *Inverse acoustic and electromagnetic scattering theory.* Applied mathematical sciences 93. Springer, Berlin, 2nd edition, 1998.

[29] D. Colton and R. Kress. On the denseness of Herglotz wave functions and electromagnetic Herglotz pairs in Sobolev spaces. *Math. Methods Appl. Sci.*, 24(16):1289–1303, 2001. doi:10.1002/mma.277.

[30] D. Colton and R. Kress. Looking back on inverse scattering theory. *SIAM Rev.*, 60(4):779–807, 2018. doi:10.1137/17M1144763.

[31] D. Colton and R. Kress. *Inverse acoustic and electromagnetic scattering theory*, volume 93 of *Applied Mathematical Sciences*. Springer, Cham, fourth edition, [2019] ©2019. doi:10.1007/978-3-030-30351-8.

[32] H. Contopanagos, B. Dembart, M. Epton, J. J. Ottusch, V. Rokhlin, J. L. Visher, and S. M. Wandzura. Well-conditioned boundary integral equations for three-dimensional electromagnetic scattering. *IEEE Trans. Antennas Propag.*, 50(12):1824–1830, 2002. doi:10.1109/TAP.2002.803956.

[33] K. Cools, F. P. Andriulli, and E. Michielssen. A Calderón multiplicative preconditioner for the PMCHWT integral equation. *IEEE Trans. Antennas and Propagation*, 59(12):4579–4587, 2011. doi:10.1109/TAP.2011.2165465.

[34] M. Costabel. Boundary integral operators on Lipschitz domains: elementary results. *SIAM J. Math. Anal.*, 19(3):613–626, 1988. doi:10.1137/0519043.

[35] M. G. Cox. The numerical evaluation of B-splines. *J. Inst. Math. Appl.*, 10:134–149, 1972.

[36] H. B. Curry and I. J. Schoenberg. On spline distributions and their limits: the Pólya distribution functions. In *Bulletin of the American Mathematical Society*, volume 53, pages 1114–1114. AMER MATHEMATICAL SOC 201 CHARLES ST, PROVIDENCE, RI 02940-2213, 1947.

[37] C. de Boor. On calculating with B-splines. *J. Approximation Theory*, 6:50–62, 1972. doi:10.1016/0021-9045(72)90080-9.

[38] C. de Boor. *A practical guide to splines*, volume 27 of *Applied Mathematical Sciences*. Springer-Verlag, New York, revised edition, 2001.

[39] J. de Villiers. *Mathematics of approximation*, volume 1 of *Mathematics Textbooks for Science and Engineering*. Atlantis Press, Paris, 2012. With a foreword by Charles K. Chui. doi:10.2991/978-94-91216-50-3.

[40] I. Fernandez-Corbaton, M. Fruhnert, and C. Rockstuhl. Objects of maximum electromagnetic chirality. *Phys. Rev. X*, 6(3), 2016. doi:10.1103/physrevx.6.031013.

[41] I. Fernandez-Corbaton, M. Fruhnert, and C. Rockstuhl. Objects of maximum electromagnetic chirality. *Phys. Rev. X*, 6:031013, July 2016. URL: https://link.aps.org/doi/10.1103/PhysRevX.6.031013, doi:10.1103/PhysRevX.6.031013.

[42] I. Fernandez-Corbaton, R. Griesmaier, M. Knöller, and C. Rockstuhl. Maximizing the electromagnetic chirality of thin metallic nanowires at optical frequencies. *J. Comput. Phys.*, 475:111854, 23, 2023. doi:10.1016/j.jcp.2022.111854.

[43] I. Fernandez-Corbaton, R. Griesmaier, M. Knöller, and C. Rockstuhl. Maximizing the electromagnetic chirality of thin metallic nanowires at optical frequencies. *J. Comput. Phys.*, 475:Paper No. 111854, 23, 2023. doi:10.1016/j.jcp.2022.111854.

[44] R. Fletcher. A new approach to variable metric algorithms. *The Computer Journal*, 13(3):317–322, 01 1970. doi:10.1093/comjnl/13.3.317.

[45] P. W. Fowler. Quantification of chirality: Attempting the impossible. *Symmetry: Culture and Science*, 16(4):321–334, 2005.

[46] X. Garcia-Santiago, M. Hammerschmidt, J. Sachs, S. Burger, H. Kwon, M. Knöller, T. Arens, P. Fischer, I. Fernandez-Corbaton, and C. Rockstuhl. Toward maximally electromagnetically chiral scatterers at optical frequencies. *ACS Photonics*, 9(6):1954–1964, 2022. doi:10.1021/acsphotonics.1c01887.

[47] D. Goldfarb. A family of variable-metric methods derived by variational means. *Math. Comp.*, 24:23–26, 1970. doi:10.2307/2004873.

[48] R. Griesmaier. A general perturbation formula for electromagnetic fields in presence of low volume scatterers. *ESAIM Math. Model. Numer. Anal.*, 45(6):1193–1218, 2011. doi:10.1051/m2an/2011015.

[49] R. Griesmaier and N. Hyvönen. A regularized newton method for locating thin tubular conductivity inhomogeneities. *Inverse Problems*, 27(11):115008, 2011. doi:10.1088/0266-5611/27/11/115008.

[50] R. Griesmaier and J. Sylvester. Uncertainty principles for inverse source problems for electromagnetic and elastic waves. *Inverse Problems*, 34(6):065003, 37, 2018. doi:10.1088/1361-6420/aab45c.

[51] F. Hagemann, T. Arens, T. Betcke, and F. Hettlich. Solving inverse electromagnetic scattering problems via domain derivatives. *Inverse Problems*, 35(8):084005, 2019. doi:10.1088/1361-6420/ab10cb.

[52] F. Hagemann and F. Hettlich. Application of the second domain derivative in inverse electromagnetic scattering. *Inverse Problems*, 36(12):125002, 34, 2020. doi:10.1088/1361-6420/abaa31.

[53] F. P. Hagemann. *Reconstructing the Shape and Measuring Chirality of Obstacles in Electromagnetic Scattering*. PhD thesis, Karlsruher Institut für Technologie (KIT), 2019. doi:10.5445/IR/1000100295.

[54] H.-J. Hagemann, W. Gudat, and C. Kunz. Optical constants from the far infrared to the x-ray region: Mg, al, cu, ag, au, bi, c, and al2o3. *J. Opt. Soc. Am.*, 65(6):742–744, Jun 1975. URL: https://opg.optica.org/abstract.cfm?URI=josa-65-6-742, doi:10.1364/JOSA.65.000742.

[55] F. Hettlich. Fréchet derivatives in inverse obstacle scattering. *Inverse Problems*, 11(2):371–382, 1995. doi:10.1088/0266-5611/11/2/007.

[56] F. Hettlich. Erratum: "Frechet derivatives in inverse obstacle scattering" [Inverse Problems **11** (1995), no. 2, 371–382; MR1324650 (95k:35217)]. *Inverse Problems*, 14(1):209–210, 1998. doi:10.1088/0266-5611/14/1/017.

[57] F. Hettlich. The domain derivative of time-harmonic electromagnetic waves at interfaces. *Math. Methods Appl. Sci.*, 35(14):1681–1689, 2012. doi:10.1002/mma.2548.

[58] G. Hu, L. Li, and J. Zou. Unique determination of a penetrable scatterer of rectangular type for inverse Maxwell equations by a single incoming wave. *Inverse Problems*, 35(3):035006, 17, 2019. doi:10.1088/1361-6420/aafe96.

[59] G. Hu, X. Liu, and B. Zhang. Unique determination of a perfectly conducting ball by a finite number of electric far field data. *J. Math. Anal. Appl.*, 352(2):861–871, 2009. doi:10.1016/j.jmaa.2008.09.016.

[60] G.-H. Hu, M. Vashisth, and J. Yang. Inverse time-harmonic electromagnetic scattering from coated polyhedral scatterers with a single far-field pattern. *SIAM J. Appl. Math.*, 81(1):25–46, 2021. doi:10.1137/20M1330798.

[61] J. D. Jackson. *Classical electrodynamics*. John Wiley & Sons, Inc., New York-London-Sydney, second edition, 1975.

[62] P. B. Johnson and R. W. Christy. Optical constants of the noble metals. *Phys. Rev. B*, 6:4370–4379, Dec 1972. URL: https://link.aps.org/doi/10.1103/PhysRevB.6.4370, doi:10.1103/PhysRevB.6.4370.

[63] B. Kaltenbacher, A. Neubauer, and O. Scherzer. *Iterative regularization methods for nonlinear ill-posed problems*, volume 6 of *Radon Series on Computational and Applied Mathematics*. Walter de Gruyter GmbH & Co. KG, Berlin, 2008. doi:10.1515/9783110208276.

[64] A. O. Karilainen and S. A. Tretyakov. Circularly polarized receiving antenna incorporating two helices to achieve low backscattering. *IEEE Transactions on Antennas and Propagation*, 60(7):3471–3475, 2012. doi:10.1109/TAP.2012.2196958.

[65] M. K.-H. Kiessling and A. S. Tahvildar-Zadeh. On the quantum-mechanics of a single photon. *Journal of Mathematical Physics*, 59(11), 2018. URL: http://dx.doi.org/10.1063/1.5021066, doi:10.1063/1.5021066.

[66] A. Kirsch. The domain derivative and two applications in inverse scattering theory. *Inverse Problems*, 9(1):81–96, 1993. doi:10.1088/0266-5611/9/1/005.

[67] A. Kirsch. On the existence of transmission eigenvalues. *Inverse Probl. Imaging*, 3(2):155–172, 2009. doi:10.3934/ipi.2009.3.155.

[68] A. Kirsch and F. Hettlich. *The mathematical theory of time-harmonic Maxwell's equations*, volume 190 of *Applied Mathematical Sciences*. Springer, Cham, 2015. Expansion-, integral-, and variational methods. doi:10.1007/978-3-319-11086-8.

[69] M. Knöller. *Electromagnetic scattering from thin tubular objects and an application in electromagnetic chirality*. PhD thesis, Karlsruher Institut für Technologie (KIT), 2023. doi:10.5445/IR/1000161368.

[70] R. Kress. *Linear integral equations*, volume 82 of *Applied Mathematical Sciences*. Springer, New York, 3rd edition, 2014. doi:10.1007/978-1-4614-9593-2.

[71] W. Kühnel. *Differentialgeometrie*. Aufbaukurs Mathematik. [Mathematics Course]. Springer Spektrum, Wiesbaden, updated edition, 2013. Kurven—Flächen—Mannigfaltigkeiten. [Curves—surfaces—manifolds]. doi:10.1007/978-3-658-00615-0.

[72] A. Kunoth, T. Lyche, G. Sangalli, and S. Serra-Capizzano. *Splines and PDEs: from approximation theory to numerical linear algebra*, volume 2219 of *Lecture Notes in Mathematics*. Springer, Cham; Fondazione C.I.M.E., Florence, 2018. Cetraro, Italy 2017, Lecture presented at the CIME Summer School held July 2–7, 2017, Fondazione CIME/CIME Foundation Subseries. doi:10.1007/978-3-319-94911-6.

[73] R. B. Kusner and J. M. Sullivan. *Möbius Energies for Knots and Links, Surfaces and Submainfolds*, volume 26. Citeseer, 1994.

[74] J. M. Lee. *Introduction to smooth manifolds*, volume 218 of *Graduate Texts in Mathematics*. Springer, New York, second edition, 2013.

[75] D.-H. Li and M. Fukushima. On the global convergence of the BFGS method for nonconvex unconstrained optimization problems. *SIAM J. Optim.*, 11(4):1054–1064, 2001. doi:10.1137/S1052623499354242.

[76] R. A. Litherland, J. Simon, O. Durumeric, and E. Rawdon. Thickness of knots. *Topology Appl.*, 91(3):233–244, 1999. doi:10.1016/S0166-8641(97)00210-1.

[77] A. Maue. On the formulation of a general scattering problem by means of an integral equation. *Z. Phys*, 126(7):601–618, 1949. doi:10.1007/BF01328780.

[78] J. R. Mautz and R. F. Harrington. H-field, e-field, and combined field solutions for bodies of revolution. Technical report, Syracuse University, 1977. URL: https://apps.dtic.mil/sti/tr/pdf/ADA040379.pdf.

[79] L. C. Maximon and F. W. J. Olver. *NIST Digital Library of Mathematical Functions, Chap. 10*. Release 1.1.6 of 2022-06-30. URL: http://dlmf.nist.gov/10.

[80] W. McLean. *Strongly elliptic systems and boundary integral equations*. Cambridge University Press, Cambridge, 2000.

[81] K. Mitzner. Numerical solution of the exterior scattering problem at eigenfrequencies of the interior problem. In *Radio Union Meeting, Boston, Mass*, 1968.

[82] P. Monk. *Finite element methods for Maxwell's equations*. Numerical Mathematics and Scientific Computation. Oxford University Press, New York, 2003. doi:10.1093/acprof:oso/9780198508885.001.0001.

[83] J.-C. Nédélec. Mixed finite elements in $\mathbf{R}^3$. *Numer. Math.*, 35(3):315–341, 1980. doi:10.1007/BF01396415.

[84] J.-C. Nédélec. *Acoustic and electromagnetic equations*, volume 144 of *Applied Mathematical Sciences*. Springer-Verlag, New York, 2001. Integral representations for harmonic problems. doi:10.1007/978-1-4757-4393-7.

[85] J. Nocedal and S. J. Wright. *Numerical optimization*. Springer Series in Operations Research and Financial Engineering. Springer, New York, second edition, 2006.

[86] J. O'Hara. Energy of a knot. *Topology*, 30(2):241–247, 1991. URL: https://www.sciencedirect.com/science/article/pii/0040938391900102, doi:10.1016/0040-9383(91)90010-2.

[87] W. K. H. Panofsky and M. Phillips. *Classical electricity and magnetism*. Courier Corporation, 2012.

[88] A. F. Peterson. The "interior resonance" problem associated with surface integral equations of electromagnetics: Numerical consequences and a survey of remedies. *Electromagnetics*, 10(3):293–312, 1990. arXiv:https://doi.org/10.1080/02726349008908245, doi:10.1080/02726349008908245.

[89] L. A. Piegl and W. Tiller. *The NURBS book*. Monographs in visual communications. Springer, Berlin, second edition, 1997. URL: https://zbmath.org/?q=an:0868.68106.

[90] A. J. Poggio and E. K. Miller. Integral equation solutions of three-dimensional scattering problems. In R. Mittra, editor, *Computer Techniques for Electromagnetics*, chapter 4, pages 159–264. Pergamon Press, Oxford / New York / Toronto, 1973. doi:10.1016/B978-0-08-016888-3.50008-8.

[91] M. N. Polyanskiy. Refractiveindex.info database of optical constants. *Scientific Data*, 11:94, 2024. doi:10.1038/s41597-023-02898-2.

[92] R. Potthast. Fréchet differentiability of boundary integral operators in inverse acoustic scattering. *Inverse Problems*, 10(2):431–447, 1994. doi:10.1088/0266-5611/10/2/016.

[93] R. Potthast. Domain derivatives in electromagnetic scattering. *Math. Methods Appl. Sci.*, 19(15):1157–1175, 1996. doi:10.1002/(SICI)1099-1476(199610)19:15<1157::AID-MMA814>3.3.CO;2-P.

[94] L. Ramshaw. *Blossoming: A connect-the-dots approach to splines*. Digital Equipment Corporation Palo Alto, 1987.

[95] S. M. Rao, D. R. Wilton, and A. W. Glisson. Electromagnetic scattering by surfaces of arbitrary shape. *IEEE Transactions on Antennas and Propagation*, 30(3):409 – 418, 1982. Cited by: 4835. URL: https://www.scopus.com/inward/record.uri?eid=2-s2.0-0020126542&doi=10.1109%2fTAP.1982.1142818&partnerID=40&md5=6f7710ae50bdfb70fe39945c1884f310, doi:10.1109/TAP.1982.1142818.

[96] P.-A. Raviart and J. M. Thomas. A mixed finite element method for 2nd order elliptic problems. In *Mathematical aspects of finite element methods (Proc. Conf., Consiglio Naz. delle Ricerche (C.N.R.), Rome, 1975)*, volume Vol. 606 of *Lecture Notes in Math.*, pages 292–315. Springer, Berlin-New York, 1977.

[97] L. Rebholz, C. Rockstuhl, and I. Fernandez-Corbaton. Chiral cavities made from lattices of highly electromagnetically-chiral scatterers. CRC 1173 Preprint 2025/35, Karlsruhe Institute of Technology, jul 2025. URL: https://www.waves.kit.edu/downloads/CRC1173_Preprint_2025-35.pdf, doi:10.5445/IR/1000183420.

[98] Y. Saad and M. H. Schultz. GMRES: a generalized minimal residual algorithm for solving nonsymmetric linear systems. *SIAM J. Sci. Statist. Comput.*, 7(3):856–869, 1986. doi:10.1137/0907058.

[99] F. Scheck. *Classical field theory*. Graduate Texts in Physics. Springer, Berlin, second edition, 2018. On electrodynamics, non-abelian gauge theories and gravitation. doi:10.1007/978-3-662-55579-8.

[100] P.-I. Schneider, X. Garcia Santiago, V. Soltwisch, M. Hammerschmidt, S. Burger, and C. Rockstuhl. Benchmarking five global optimization approaches for nano-optical shape optimization and parameter reconstruction. *ACS Photonics*, 6(11):2726–2733, 2019. doi:10.1021/acsphotonics.9b00706.

[101] I. J. Schoenberg. Contributions to the problem of approximation of equidistant data by analytic functions. Part A. On the problem of smoothing or graduation. A first class of analytic approximation formulae. *Quart. Appl. Math.*, 4:45–99, 1946. doi:10.1090/qam/15914.

[102] I. J. Schoenberg. Contributions to the problem of approximation of equidistant data by analytic functions. Part B. On the problem of osculatory interpolation. A second class of analytic approximation formulae. *Quart. Appl. Math.*, 4:112–141, 1946. doi:10.1090/qam/16705.

[103] M. W. Scroggs, T. Betcke, E. Burman, W. Śmigaj, and E. van 't Wout. Software frameworks for integral equations in electromagnetic scattering based on Calderón identities. *Comput. Math. Appl.*, 74(11):2897–2914, 2017. doi:10.1016/j.camwa.2017.07.049.

[104] D. F. Shanno. Conditioning of quasi-Newton methods for function minimization. *Math. Comp.*, 24:647–656, 1970. doi:10.2307/2004840.

[105] A. Sommerfeld. Die Greensche Funktion der Schwingungslgleichung. *Jahresbericht der Deutschen Mathematiker-Vereinigung*, 21:309–352, 1912. URL: https://gdz.sub.uni-goettingen.de/id/PPN37721857X_0021?tify={"view":"info","pages":[317]}.

[106] J. A. Stratton. *Electromagnetic theory*. John Wiley & Sons, 2007.

[107] E. Tiesinga, P. J. Mohr, D. B. Newell, and B. N. Taylor. *NIST Physical Measurement Laboratory: Values of Fundamental Physical Constants*. URL: https://physics.nist.gov/cuu/Constants/index.html.

[108] C. Villani. *Optimal transport*, volume 338 of *Grundlehren der mathematischen Wissenschaften [Fundamental Principles of Mathematical Sciences]*. Springer-Verlag, Berlin, 2009. Old and new. doi:10.1007/978-3-540-71050-9.

[109] H. F. Walker. Implementation of the GMRES method using Householder transformations. *SIAM J. Sci. Statist. Comput.*, 9(1):152–163, 1988. doi:10.1137/0909010.

[110] W. Wang, B. Jüttler, D. Zheng, and Y. Liu. Computation of rotation minimizing frames. *ACM Trans. Graph.*, 27:Article 2, 2008. doi:10.1145/1330511.1330513.

[111] D. Werner. *Funktionalanalysis*. Springer-Verlag, Berlin, 2nd edition, 1997.

[112] H. Wheeler. A helical antenna for circular polarization. *Proceedings of the IRE*, 35(12):1484–1488, 1947. doi:10.1109/JRPROC.1947.234573.

[113] A. Zangwill. *Modern electrodynamics*. Cambridge University Press, 2012.

[114] Y. Zhang, T. J. Cui, W. C. Chew, and J.-S. Zhao. Magnetic field integral equation at very low frequencies. *IEEE Transactions on Antennas and Propagation*, 51(8):1864–1871, 2003. doi:10.1109/TAP.2003.814753.

Notation

Basic notation

$\mathbb{N}$	natural numbers
$\mathbb{N}_0$	natural numbers including zero
$\mathbb{Z}$	integers
$\mathbb{R}^d$	d-dimensional real Euclidean space
$\mathbb{C}^d$	d-dimensional complex Euclidean space
$\boldsymbol{x}$	$\boldsymbol{x} = (x_1, x_2, x_3)^\top \in \mathbb{R}^3$
$\boldsymbol{x} \cdot \boldsymbol{y}$	dot product of $\boldsymbol{x}, \boldsymbol{y}$
$\boldsymbol{x} \times \boldsymbol{y}$	cross product of $\boldsymbol{x}, \boldsymbol{y}$
$\boldsymbol{x} \perp \boldsymbol{y}$	$\boldsymbol{x}$ is orthogonal to $\boldsymbol{y}$
$\lvert\boldsymbol{x}\rvert$	Euclidean norm of $\boldsymbol{x}$
D	open, bounded domain in $\mathbb{R}^3$
∂D	boundary of D
$\overline{D}$	closure of D
B_R	open ball in $\mathbb{R}^3$ with radius R, centered at zero
Ω	$B_R \setminus \overline{D}$
$\mathbb{S}^2$	unit sphere in $\mathbb{R}^3$
$\widehat{\boldsymbol{x}}$	direction $\boldsymbol{x}/\lvert\boldsymbol{x}\rvert \in \mathbb{S}^2$
$\boldsymbol{\nu}$	unit outward normal on ∂D
c	speed of light
ω	angular frequency
f	frequency
λ	wavelength
$k, k_\pm$	wave number
$\varepsilon, \varepsilon_\pm$	electric permitivitty
$\mu, \mu_\pm$	magnetic permeability
$\boldsymbol{z}, \boldsymbol{u}$	center curve parameterization and perturbation
r, δ	radius function and perturbation

Function spaces

$C^k(D), C^k(\partial D)$	space of k times continuously differentiable functions in D, ∂D
$C_0^k(D), C_0^k(\partial D)$	space of functions in $C^k(D)$, $C^k(\partial D)$ with compact support in D, ∂D
$C^k(\overline{D})$	space of functions in $C^k(D)$ with derivatives continuously extendable to $\overline{D}$
$L^2(D), L^2(\partial D)$	Lebesgue space of square integrable functions in D, ∂D
$\boldsymbol{X}(D), \boldsymbol{X}(\partial D)$	placeholder for spaces of vector-valued functions on D, ∂D
$\boldsymbol{X}_t(\partial D)$	spaces of tangential fields in $\boldsymbol{X}(\partial D)$
$\boldsymbol{X}_{\mathrm{loc}}(D)$	spaces of functions that are in $\boldsymbol{X}(K)$ for any open, bounded $K \subseteq D$
$H^s(D), H^s(\partial D)$	Sobolev spaces on D, ∂D
$\boldsymbol{H}(\mathbf{curl}, D)$	space of funtions in $\boldsymbol{L}^2(D)$ with weak **curl** in $\boldsymbol{L}^2(D)$
$\boldsymbol{H}^{-1/2}(\mathrm{Div}, D)$	Div-conforming trace space
$\boldsymbol{H}^{-1/2}(\mathrm{Curl}, D)$	Curl-conforming trace space

Functions

$\boldsymbol{E}^i, \boldsymbol{H}^i$	incident electric and magnetic field
$\boldsymbol{E}^s, \boldsymbol{H}^s$	scattered electric and magnetic field
$\boldsymbol{E}, \boldsymbol{H}$	total electric and magnetic field
$\boldsymbol{E}^\infty, \boldsymbol{H}^\infty$	electric and magnetic far-field pattern
$\boldsymbol{E}^i[\varphi], \boldsymbol{H}^i[\varphi]$	incident electric and magnetic Herglotz field
$\boldsymbol{E}^s[\varphi], \boldsymbol{H}^s[\varphi]$	scattered electric and magnetic Herglotz field
$\boldsymbol{E}[\varphi], \boldsymbol{H}[\varphi]$	total electric and magnetic Herglotz field
$\boldsymbol{E}^\infty[\varphi], \boldsymbol{H}^\infty[\varphi]$	electric and magnetic far-field pattern of $\boldsymbol{E}^s[\varphi], \boldsymbol{H}^s[\varphi]$
j_n	spherical Bessel function of the first kind
y_n	spherical Bessel function of the second kind
$h_n^{(1)}$	spherical Hankel function of the first kind
Y_n^m	spherical harmonics
$\boldsymbol{U}_n^m, \boldsymbol{V}_n^m$	vector spherical harmonics
$\boldsymbol{M}_n^m, 1/k\,\mathbf{curl}\,\boldsymbol{M}_n^m$	entire solutions of time-harmonic Maxwell system
$\boldsymbol{N}_n^m, 1/k\,\mathbf{curl}\,\boldsymbol{N}_n^m$	radiating entire solutions of time-harmonic Maxwell system

χ	chirality measure
χ_{HS}	modified chirality measure

Operators

$\boldsymbol{\nabla}, \mathbf{Grad}$	gradient, surface gradient
$\mathrm{div}, \mathrm{Div}$	divergence, surface divergence
$\mathbf{curl}, \mathrm{Curl}, \mathbf{Curl}$	curl, scalar surface curl, vectorial surface curl
$\boldsymbol{\gamma}_t$	tangential trace with range $\boldsymbol{H}^{-1/2}(\mathrm{Div}, \partial D)$
$\boldsymbol{\gamma}_T$	tangential trace with range $\boldsymbol{H}^{-1/2}(\mathrm{Curl}, \partial D)$
$\boldsymbol{\gamma}_N$	Neumann trace
$\boldsymbol{\Lambda}$	Calderón operator
$\mathrm{SL}_k, \mathbf{SL}_k$	scalar- and vector-valued single-layer potential
$\boldsymbol{\mathcal{E}}_k, \boldsymbol{\mathcal{H}}_k$	electric and magnetic potential
$\mathbf{S}_k, \mathbf{C}_k$	electric and magnetic boundary operator
$\mathbf{A}_k$	multitrace operator
F	far-field map
$\mathcal{F}$	far-field operator